

1124 3154

MONASH UNIVERSITY
THESIS ACCEPTED IN SATISFACTION OF THE
REQUIREMENTS FOR THE DEGREE OF
DOCTOR OF PHILOSOPHY
ON..... 12 April 2002

.....
Sec. Research Graduate School Committee

Under the copyright Act 1968, this thesis must be used only under the normal conditions of scholarly fair dealing for the purposes of research, criticism or review. In particular no results or conclusions should be extracted from it, nor should it be copied or closely paraphrased in whole or in part without the written consent of the author. Proper written acknowledgement should be made for any assistance obtained from this thesis.

MONITORING OF PIPELINE USING SMART SENSORS

A thesis submitted in accordance with the regulations of Monash University
in partial fulfilment of the requirements for degree of
Doctor of Philosophy

by

Wibowo Harso Nugroho

Ir., MSc.

Department of Mechanical Engineering

Monash University

Melbourne, Victoria, Australia

January 2001

TABLE OF CONTENTS

TABLE OF CONTENTS

SUMMARY

DECLARATION

ACKNOWLEDGMENTS

NOMENCLATURE

LIST OF FIGURES

LIST OF TABLES

1. INTRODUCTION	1
2. LITERATURE REVIEW	4
2.1. Prediction of Failure in Pipelines	4
2.2. In service Monitoring of Pipelines	9
2.3. Concluding Remarks	16
3. ACTUATOR - SENSOR AND BONDING SYSTEM DURABILITY	18
3.1. Load Design for Experimental Investigation	18
3.2. Experimental Investigation	21
3.3. Results and Discussion	26
3.4. Concluding Remarks	29

4. NUMERICAL INVESTIGATION OF THE DETECTION OF A FLAW IN THE SYSTEM	30
4.1. Transfer Function Method	30
4.2. FE Modelling of the Structure	35
4.3. Numerical Simulation Results and Discussion	37
4.3.1. Transfer Function Results	38
4.3.2. R-Curve Results	60
4.4. Concluding Remarks	77
5. EXPERIMENTAL INVESTIGATION OF THE DETECTION OF A FLAW IN THE SYSTEM	79
5.1. Experimental Investigation of the Clamped Plate with the Artificial Crack Growth	79
5.2. Results and Discussions	83
5.3. Experimental Investigation of the Clamped Plate with the Real Crack Growth	101
5.4. Results and Discussions	103
5.5. Concluding Remarks	119
6. THE USE OF AN ARRAY OF SENSORS FOR STRESS-FIELD CONSTRUCTION	120
6.1. 2-D Stress Function for Stress Field Construction	121
6.1.1. Determination of Criticality	124
6.1.2. Numerical Investigation	127
6.1.3. Results and Discussions	130
6.1.4. Experimental Investigation	140
6.1.5. Results and Discussions	142

6.2. 3-D Stress Function for Stress Field Construction	150
6.2.1. Derivation of the Components of the 3-D Stress	
Function	150
6.2.2. Numerical Investigation	155
6.2.3 Results and Discussion	158
 6.3. Concluding Remarks	 175

7. CONCLUSIONS AND RECOMMENDATIONS FOR FUTURE WORK .177

REFERENCES	181
-------------------------	------------

APPENDICES

APPENDIX A. The PZT T107-A4E-602 Properties

APPENDIX B. The PIPELINE DESIGN Properties

**APPENDIX C. The Comparisons of the Strain Fields Inside the Array of
Sensors Between Strain Gauge Reading and the 2-D Stress Function**

**APPENDIX D. On the use of the 3D-Stress Function to Monitor an
Embedded Semi-Elliptical Crack in a Thick plate**

APPENDIX E. List of Publications

BIOGRAPHICAL NOTE

SUMMARY

This “ **MONITORING OF PIPELINE USING SMART SENSORS** ” research consists of:

1. **Durability Test of the PZT Sensors-Actuators and their Bonding System.**
2. **Numerical and Experimental Investigation of Determination for Existence of Damage (Cracks) Using Smart Material Lead Zirconate Titanate (PZT) as Array of Sensors-Actuators.**
3. **The Stress Field Reconstruction by a Suitable Stress Function Using Data Provided from the Array of Displacement Sensors and the Determination of the Criticality of the Structural Component.**

The first stage of this research will demonstrate the feasibility of the PZT sensor-actuator and their bonding system with respect to the loads that are commonly experienced in the pipeline. Based on the findings the PZT will be used in this research to detect damage in a structural component.

The second part of this research will be conducted to demonstrate how this PZT actuator-sensor pair can be used to detect, and approximately, to locate damage in a structure. This approach will examine the possibility of using an array of piezoelectric transducers attached to the structure for both actuation and sensing. The results from a set of numerical and experimental investigations will show that the use of an array of PZT sensor-actuator can be used satisfactorily to locate the damage and to monitor the growth of the damage.

In the last stage of this research, a method to assess the integrity of the structure will be conducted. To assess the integrity of the structure it is proposed to construct the stress field from point measurements from the array of sensors by using an algorithm based on a suitable stress function. A technique to determine the location of the crack tip will refine the results from the previous stage of research. With the knowledge of this crack tip location and stress field around it, the mode I Stress Intensity Factor (SIF), K_I can be determined. This numerical investigation of the 2D stress function will be substantiated with a set of experimental results. Based on these results the fracture stress of a structural component will also be calculated. To apply this stress function application to a thick structure a suitable 3D-stress function, which satisfies the embedded semi-elliptical crack condition, will be derived. The derived 3D-stress function will then be used to construct the stress field at the back surface of the plate with an embedded semi-elliptical crack.

In conclusion, this project will demonstrate a potential technique of pipeline monitoring which combines:

- An active system for in-situ monitoring, using an active element PZT as a sensor/actuator, in conjunction with a passive sensor such as a strain gauge.
- A suitable stress function based algorithm that detects and assesses the damage levels present in the structure by evaluating structural response data acquired from bonded sensors such as PZT patches and strain gauges.

DECLARATION

To the best of my knowledge and belief, this thesis contains no material;

- (i) Previously published or written by another person except where due reference is made in the text of this thesis.**
- (ii) Which has been accepted for the award of a degree or diploma in this or any other educational institution.**

Wibowo Harso Nugroho



January, 2001

Acknowledgements

In the name of GOD the most beneficent and merciful. Praise be to GOD the Lord of the universe.

The author wishes to thank whole-heartedly those people and organizations whose advice, support and encouragement contributed to the presentation of this work.

Foremost, I am indebted to my sole supervisor A/Professor W. K. Chiu for his assistance and enthusiasm. The assistance from him in numerical and experimental investigation of the smart material/structure is highly appreciated.

The quality support from technical staff from the Department of Mechanical Engineering is sincerely appreciated. I am grateful to Mr. Ron Laemmle for the specimen preparation.

Many thanks to Ms. Jane Moodie of Language and Learning Services (LLS) Engineering faculty for her assistance in the beginning of the writing process.

The financial supports from Government of Indonesia of Science Technology and Industrial Development (STAID) is gratefully acknowledged.

This dissertation is dedicated to my parents, who encouraged me to do the best I could. Especially for my father who passed away at the beginning of this PHD study. Thanks Mum and Dad.

Finally to my lovely wife Leily Rahmawati. I thank you for your understanding, support and your cheerful personality, which catalyzed this work.

NOMENCLATURE

a	Half of the crack length (mm), semi-major axis of the semi-elliptical crack (Section 6.2)
A	Cross sectional area (mm ²)
A _k	Amplitude of the spectrum (Volt)
b	Semi-minor axis of the semi-elliptical crack (Section 6.2)
d	Depth of the seabed from the sea surface
d ₃₁	Electrical coupling coefficient of the PZT(m/Volt)
D	Diameter of the pipe (mm)
E	Youngs modulus of a material (GPA)
F	Applied force (N)
g	Earth constant gravity (m/s ²)
G	Shear Modulus (MPa)
h	Thickness of the pipe (mm)
k	Stiffness (N/m)
K _I	Stress Intensity Factor (SIF) mode I (MPa√m)
K _{Ic}	Fracture Toughness (MPa√m)
l	Length of the cross sectional area (mm)
L	Length of PZT under voltage excitation (m)
PZT	Lead Zirconate Titanate (Piezoceramics)
r _p	Plasticity zone size(m)
t	Thickness (mm)
TF	Transfer Function
V	Applied electrical field (Volt)
V _k	Vibration spectrum
V _{ks}	Vibration spectrum from the sensor
V _{kact}	Vibration spectrum from the actuator

ΔL	Induced length of PZT under voltage excitation (m)
ϵ	Strain
ϵ_{\max}	Maximum strain
θ_k	Phase angle (rad)
ν	Poisson ratio
ρ	Density (g/cm ³)
σ	Stress (MPa)
σ_c	Fracture (residual) stress (MPa)
σ_y	Yield strength of a material (MPa)
σ_u	Ultimate tensile stress of a material (MPa)
σ_0	Stress flow or the average of the σ_u and σ_y (MPa)
σ_{mhoop}	Maximum hoop stress (MPa)
σ_{xx}	Stress component in the X- direction (MPa)
σ_{yy}	Stress component in the Y- direction (MPa)
σ_{zz}	Stress component in the Z- direction (MPa)
τ_{xy}	Shear stress component in the X-Y direction (MPa)
τ_{xz}	Shear stress component in the X-Z direction (MPa)
ω	Frequency (Hz)

LIST OF FIGURES

Figure 1.1. A flow chart of the research	3
Figure 2.1. Structural integrity diagram	6
Figure 2.2. Flow chart of FAMED for evaluating critical flaw size and fatigue life.....	8
Figure 2.3. A smart structure concept	11
Figure 3.1a. Aluminum Bars for Sensor-Actuator Degradation Investigation.....	22
Figure 3.1b. A schematic sensor - actuator degradation test-specimen	22
Figure 3.2. Material Testing System	24
Figure 3.3. Control System of MTS	24
Figure 3.4. Schematic diagram of the experimental set-up	25
Figure 3.5. Degradation chart of PZT under loads of 1500, 2000, 3000, 4000 microstrains	27
Figure 3.6. Strain gauge reading on different strain loads.....	28
Figure 4.1a. A thin aluminium plate clamped on the 2 shorter edges with distributed PZT actuator and sensors	33
Figure 4.1b. Detailed Configuration of the Actuator-Sensor Pairs	33
Figure 4.2. A schematic mechanical model of the system	34
Figure 4.3. Schematic of test plate arrangement	36
Figure 4.4a. TF Amplitude of A1B1	40
Figure 4.4b TF Phase Angle of A1B1	40
Figure 4.5a. TF Amplitude of A2B2	41
Figure 4.5b TF Phase Angle of A2B2	41
Figure 4.6a. TF Amplitude of A3B3	42
Figure 4.6b TF Phase Angle of A3B3	42
Figure 4.7a. TF Amplitude of A4B4	43
Figure 4.7b TF Phase Angle of A4B4	43
Figure 4.8a. TF Amplitude of A5B5	44
Figure 4.8b TF Phase Angle of A5B5	44
Figure 4.9a. TF Amplitude of A6B6	45
Figure 4.9b TF Phase Angle of A6B6	45
Figure 4.10a. TF Amplitude of B1C1.....	48
Figure 4.10b. TF Phase Angle of B1C1	48
Figure 4.11a. TF Amplitude of B2C2.....	49
Figure 4.11b. TF Phase Angle of B2C2	49

Figure 4.12a. TF Amplitude of B3C3	50
Figure 4.12b. TF Phase Angle of B3C3	50
Figure 4.13a. TF Amplitude of B4C4	51
Figure 4.13b. TF Phase Angle of B4C4	51
Figure 4.14a. TF Amplitude of B5C5.....	52
Figure 4.14b. TF Phase Angle of B5C5	52
Figure 4.15a. TF Amplitude of B6C6	53
Figure 4.15b. TF Phase Angle of B6C6	53
Figure 4.16a. TF Amplitude of A1B2	55
Figure 4.16b. TF Phase Angle of A1B2	55
Figure 4.17a. TF Amplitude of A2B3	56
Figure 4.17b. TF Phase Angle of A2B3	56
Figure 4.18a. TF Amplitude of A3B4	57
Figure 4.18b. TF Phase Angle of A3B4	57
Figure 4.19a. TF Amplitude of A4B5	58
Figure 4.19b. TF Phase Angle of A4B5	58
Figure 4.20a. TF Amplitude of A5B6	59
Figure 4.20b. TF Phase Angle of A5B6	59
Figure 4.21. Typical Experimental Transfer Function Amplitude	61
Figure 4.22. TF-data of the area under the frequency spectrum of the pair A1B1 for every damage condition (numerical)	63
Figure 4.23. TF-data of the area under the frequency spectrum of the pair A2B2 for every damage condition(numerical)..	64
Figure 4.24. TF-data of the area under the frequency spectrum of the pair A3B3 for every damage condition.(numerical)	64
Figure 4.25. TF-data of the area under the frequency spectrum of the pair A4B4 for every damage condition.(numerical).....	65
Figure 4.26. TF-data of the area under the frequency spectrum of the pair A5B5 for every damage condition (numerical).....	65
Figure 4.27. TF-data of the area under the frequency spectrum of the pair A6B6 for every damage condition (numerical)	66
Figure 4.28. TF-data of the area under the frequency spectrum of the pair B1C1 for every damage condition (numerical)	67
Figure 4.29. TF-data of the area under the frequency spectrum of the pair B2C2 for every damage condition (numerical)	68
Figure 4.30. TF-data of the area under the frequency spectrum of the pair B3C3 for every damage condition (numerical).....	68

Figure 4.31. TF-data of the area under the frequency spectrum of the pair B4C4 for every damage condition (numerical)	69
Figure 4.32. TF-data of the area under the frequency spectrum of the pair B5C5 for every damage condition (numerical)	69
Figure 4.33. TF-data of the area under the frequency spectrum of the pair B6C6 for every damage condition (numerical)	70
Figure 4.34. TF-data of the area under the frequency spectrum of the pair A1B2 for every damage condition (numerical)	74
Figure 4.35. TF-data of the area under the frequency spectrum of the pair A2B3 for every damage condition (numerical)	74
Figure 4.36. TF-data of the area under the frequency spectrum of the pair A3B4 for every damage condition (numerical)	75
Figure 4.37. TF-data of the area under the frequency spectrum of the pair A4B5 for every damage condition (numerical)	76
Figure 4.38. TF-data of the area under the frequency spectrum of the pair A5B6 for every damage condition (numerical).....	77
Figure 5.1a. The specimen for Transfer Function Investigation	80
Figure 5.1b. Detailed Configuration of the Actuator-Sensor Pairs.....	80
Figure 5.2a. The specimen - Oscilloscope - Signal generator set-up	82
Figure 5.2b. A Schematic diagram of the Signal generator – oscilloscope -specimen set-up.....	82
Figure 5.3a. The specimen - FFT analyzer - Signal generator set – up.....	84
Figure 5.3b. A Schematic Diagram of the Signal generator - FFT analyser - specimen set-up	84
Figure 5.4. TF-data of the area under the frequency spectrum of the pair A1B1 for every damage condition (saw cut)	87
Figure 5.5. TF-data of the area under the frequency spectrum of the pair A2B2 for every damage condition (saw cut)	87
Figure 5.6. TF-data of the area under the frequency spectrum of the pair A3B3 for every damage condition. (saw cut)	88
Figure 5.7. TF-data of the area under the frequency spectrum of the pair A4B4 for every damage condition.(saw cut)	88
Figure 5.8. TF-data of the area under the frequency spectrum of the pair A5B5 for every damage condition (saw cut).....	89
Figure 5.9. TF-data of the area under the frequency spectrum of the pair A6B6 for every damage condition (saw cut)	89

Figure 5.10. TF-data of the area under the frequency spectrum of the pair B1C1 for every damage condition (saw cut)	91
Figure 5.11. TF-data of the area under the frequency spectrum of the pair B2C2 for every damage condition (saw cut)	91
Figure 5.12. TF-data of the area under the frequency spectrum of the pair B3C3 for every damage condition (saw cut)	92
Figure 5.13. TF-data of the area under the frequency spectrum of the pair B4C4 for every damage condition (saw cut)	92
Figure 5.14. TF-data of the area under the frequency spectrum of the pair B5C5 for every damage condition (saw cut)	93
Figure 5.15. TF-data of the area under the frequency spectrum of the pair B6C6 for every damage condition (saw cut)	93
Figure 5.16. TF-data of the area under the frequency spectrum of the pair A1B2 for every damage condition (saw cut)	97
Figure 5.17. TF-data of the area under the frequency spectrum of the pair A2B3 for every damage condition (saw cut)	98
Figure 5.18. TF-data of the area under the frequency spectrum of the pair A3B4 for every damage condition (saw cut)	98
Figure 5.19. TF-data of the area under the frequency spectrum of the pair A4B5 for every damage condition (saw cut)	99
Figure 5.20. TF-data of the area under the frequency spectrum of the pair A5B6 for every damage condition (saw cut)	99
Figure 5.21. The plate specimen that is clamped on the MTS machine	102
Figure 5.22. A Halec Eddy current crack detector	102
Figure 5.23. Schematic diagram of Transfer Function method for a detection of the fatigue crack	103
Figure 5.24. Detailed position of the occurred fatigue cracks in the test Plate	104
Figure 5.25. TF-data of the area under the frequency spectrum of the pair A1B1 for every damage condition (fatigue crack).....	105
Figure 5.26. TF-data of the area under the frequency spectrum of the pair A2B2 for every damage condition (fatigue crack)	106
Figure 5.27. TF-data of the area under the frequency spectrum of the pair A3B3 for every damage condition. (fatigue crack)	106
Figure 5.28. TF-data of the area under the frequency spectrum of the pair A4B4 for every damage condition.(fatigue crack)	107
Figure 5.29. TF-data of the area under the frequency spectrum of the pair A5B5	

for every damage condition (fatigue crack)	107
Figure 5.30. TF-data of the area under the frequency spectrum of the pair A6B6	
for every damage condition (numerical)	108
Figure 5.31. TF-data of the area under the frequency spectrum of the pair B1C1	
for every damage condition (fatigue crack)	109
Figure 5.32. TF-data of the area under the frequency spectrum of the pair B2C2	
for every damage condition (fatigue crack)	109
Figure 5.33. TF-data of the area under the frequency spectrum of the pair B3C3	
for every damage condition (fatigue crack)	110
Figure 5.34. TF-data of the area under the frequency spectrum of the pair B4C4	
for every damage condition (fatigue crack)	110
Figure 5.35. TF-data of the area under the frequency spectrum of the pair B5C5	
for every damage condition (fatigue crack)	111
Figure 5.36. TF-data of the area under the frequency spectrum of the pair B6C6	
for every damage condition (fatigue crack)	111
Figure 5.37. TF-data of the area under the frequency spectrum of the pair A1B2	
for every damage condition (fatigue crack)	115
Figure 5.38. TF-data of the area under the frequency spectrum of the pair A2B3	
for every damage condition (fatigue crack)	115
Figure 5.39. TF-data of the area under the frequency spectrum of the pair A3B4	
for every damage condition (fatigue crack)	116
Figure 5.40. TF-data of the area under the frequency spectrum of the pair A4B5	
for every damage condition (fatigue crack)	116
Figure 5.41. TF-data of the area under the frequency spectrum of the pair A5B6	
for every damage condition (fatigue crack)	117
Figure 6.1. Geometry of the crack on an elastic sheet	121
Figure 6.2. Geometry of the left hand crack tip	123
Figure 6.3. Crack tip region and geometry of the problem	124
Figure 6.4. An array of sensors (12 rows x 12 columns), which applied	
on the region at some distance away from of the crack	128
Figure 6.4a. Detail A, the position of the sensor point measurement	
on the plate in numerical investigation	128
Figure 6.5. Two identical arrays of sensors (each is 6rows x 12 columns)	
with a crack in between them	129
Figure 6.5a. Detail B, the position of the sensor point measurement	
on the plate in numerical investigation	129

Figure 6.6. Sensors position with a crack is on equidistant line & The mode I SIF, K_I calculation point is in region II .	131
Figure.6.7. Sensors position with a crack is on equidistant line & The mode I SIF, K_I calculation point is in region I	131
Figure 6.8. Sensors position with a crack position is not on equidistant line & The mode I SIF, K_I calculation point is in region II.	132
Figure 6.9. Sensors position with a crack position is not on equidistant line & The mode I SIF, K_I calculation point is in region I	132
Figure 6.10. An array of sensors to predict the crack & The mode I SIF, K_I calculation point is in region II	133
Figure 6.11. An array of sensors to predict the crack & The mode I SIF, K_I calculation point is in region close to crack tip(region I)	133
Figure 6.12. The error plot of the plate with a 25mm simple crack	135
Figure 6.13. The stress field in y-direction σ_{yy} constructed by the Stress Function (equidistant)	136
Figure 6. 14. The stress field in y-direction σ_{yy} calculated by FEM (equidistant).....	136
Figure 6.13. The stress field in y-direction σ_{yy} constructed by the Stress Function (not equidistant).....	137
Figure 6. 14. The stress field in y-direction σ_{yy} calculated by FEM(not equidistant) ...	137
Figure 6.13. The stress field in y-direction σ_{yy} constructed by the Stress Function (one array)	138
Figure 6. 14. The stress field in y-direction σ_{yy} calculated by FEM (one array)	138
Figure 6.19. Schematic diagram of the experimental investigation of the (200x400x2)mm ³ plate with an initial center crack	141
Figure 6.19a. Detail C, the position of the array of strain gauges mounted on the plate in the experimental investigation	141
Figure 6.20. The plate specimen of this experimental investigation	142
Figure 6.21. The plot of error of 10mm crack	143
Figure 6.22. Plot of error of 16mm crack	144
Figure 6.23. Plot of error of 28-mm crack	144
Figure 6.24. Schematic diagram of the experimental mode I SIF. K_I calculation point	146
Figure 6.25. Relationship between the residual strength σ_r and the crack length $2a$	149
Figure 6.26. A plate with a semi-elliptical crack under tension	150
Figure 6.27. Half plate 3D FE model of the investigation	156

Figure 6.27a. Detailed element of the surface crack	156
Figure 6.28. Two identical arrays of sensors (each is 6 rows x 12 columns) at the back surface of the plate with an embedded semi-elliptical crack in between them	157
Figure 6.28a. Detail D, the position of the sensor point measurement on the plate in numerical investigation	157
Figure 6.29. Stress field in Z-direction σ_{zz} for $b/a=0.2$, $b/t=0.1$, calculated from FEM	159
Figure 6.30. Stress field in Z-direction σ_{zz} for $b/a=0.2$, $b/t=0.1$, constructed from The Stress Function	159
Figure 6.31. Stress field in Z-direction σ_{zz} for $b/a=0.2$, $b/t=0.2$, calculated from FEM	160
Figure 6.32. Stress field in Z-direction σ_{zz} for $b/a=0.2$, $b/t=0.2$, constructed from The Stress Function	160
Figure 6.33. Stress field in Z-direction σ_{zz} for $b/a=0.2$, $b/t=0.4$, calculated from FEM	161
Figure 6.34. Stress field in Z-direction σ_{zz} for $b/a=0.2$, $b/t=0.4$, constructed from The Stress Function	161
Figure 6.35. Stress field in Z-direction σ_{zz} for $b/a=0.2$, $b/t=0.5$, calculated from FEM	162
Figure 6.36. Stress field in Z-direction σ_{zz} for $b/a=0.2$, $b/t=0.5$, constructed from The Stress Function	162
Figure 6.37. Stress field in Z-direction σ_{zz} for $b/a=0.4$, $b/t=0.1$, calculated from FEM	163
Figure 6.38. Stress field in Z-direction σ_{zz} for $b/a=0.4$, $b/t=0.1$, constructed from The Stress Function	163
Figure 6.39. Stress field in Z-direction σ_{zz} for $b/a=0.4$, $b/t=0.2$, calculated from FEM	165
Figure 6.40. Stress field in Z-direction σ_{zz} for $b/a=0.4$, $b/t=0.2$, constructed from The Stress Function	165
Figure 6.41. Stress field in Z-direction σ_{zz} for $b/a=0.4$, $b/t=0.4$, calculated from FEM	166
Figure 6.42. Stress field in Z-direction σ_{zz} for $b/a=0.4$, $b/t=0.4$, constructed from The Stress Function	166
Figure 6.43. Stress field in Z-direction σ_{zz} for $b/a=0.4$, $b/t=0.5$, calculated from FEM	167

LIST OF TABLES

Table 2.1. Integrity Management Program.....	9
Table 2.2. Strain and Displacement Sensors: The Principal Options for Structural Monitoring	12
Table 3.1. Mechanical properties of API X-65 and X-80.....	19
Table 3.2. Constants for calculating the maximum pressure P_{max}	19
Table 4.1. The Material Properties of the Al plate and PZT	36
Table 4.2. Percentage of reduction of R-value from no-damage condition using a direct-TF (numerical).....	71
Table 4.3. Percentage of reduction of R-value from no-damage condition using a cross-TF (numerical)	76
Table 5.1. Percentage of reduction of R-value from no-damage condition using a direct-TF (saw-cut)	94
Table 5.2. Percentage of reduction of R-value from no-damage condition using a cross-TF (saw-cut)	100
Table 5.3. Percentage of reduction of R-Value from no-damage condition using a direct-TF (Fatigue crack)	113
Table 5.4. Percentage of reduction of R-value from no-damage condition using a cross TF (fatigue crack)	117
Table 6.1. Mode I Stress Intensity Factor from the numerical investigation	139
Table 6.2. The Crack Tip Location	145
Table 6.3. Mode I Stress Intensity Factor from the experimental investigation	147
Table 6.4. Percentage differences of the maximum stresses σ_{zz} s calculated from FEM and reconstructed from the stress function	174

...,and GOD sent down iron, which is (material for) mighty war, as well as many benefits for mankind,...

The Iron (Quran 57:25)

CHAPTER 1. INTRODUCTION

A pipeline is built for transporting either compressible or incompressible fluids or sometimes a mixture of them. Steel pipelines are most commonly used for this purpose. Many of these pipeline systems have been constructed for transporting these fluids over long distances. One of the important maintenance issues of pipeline systems is failure prevention, as such a failure would not only affect production but could have significant impact on public safety and the environment.

Failure of the pipeline structure is commonly caused by crack growth, and thus detection of the early stage of the crack is critical. This crack detection can only be achieved by monitoring the pipeline. The continuous monitoring of the pipeline system is a helpful tool for assessing the integrity of the system. In this method the engineering data, such as strains or displacements in relation to stresses that occur on the pipe wall, are recorded and processed to have a clear description of the system performance.

Smart active sensors are pairs of sensor-actuator and can be used to accomplish continuous monitoring of the pipeline. A smart pipeline is very appropriate since pipelines can be located in the regions hardly accessible to humans, such as in the jungle or on the seabed.

This smart structure methodology requires sensors to measure the stress values on a particular structure. Arrays of smart sensors can be used to measure the strains or displacements on a structure. Hookes' law can then be applied to find the stresses. In these strain or displacement measurement sensors must be attached or embedded on the structure.

This research program seeks to extend active smart sensor technology, which is currently used predominantly in the aircraft industries (Irving, 1996)¹, to the oil and gas industries. The PZT (Lead Zirconate Titanate) is a commonly used smart material that can act both as the sensor and the actuator. This material will generate a voltage when a mechanical force is applied, and will generate a force with an applied voltage.

To date, an extensive literature search has revealed that whilst there are significant developments in the field of fracture mechanics, smart structures and sensing, and stress analysis, there is little work reported on the use of these tools in an integrated manner for the determination of the integrity of pipeline structures.

This research seeks to combine the recent developments in smart structure technology with fracture mechanics for a "smart" system in pipeline integrity assessment. This smart pipeline concept is to improve maintenance scheduling and to prevent failure under operational conditions.

The aims of this smart pipeline concept are:

- 1) To determine the presence of any existing or developing flaws
- 2) To assess the criticality of the flaw

To achieve the above aims a series investigation will be conducted in this research. These can be summarised in the flow chart shown in Figure 1.1.

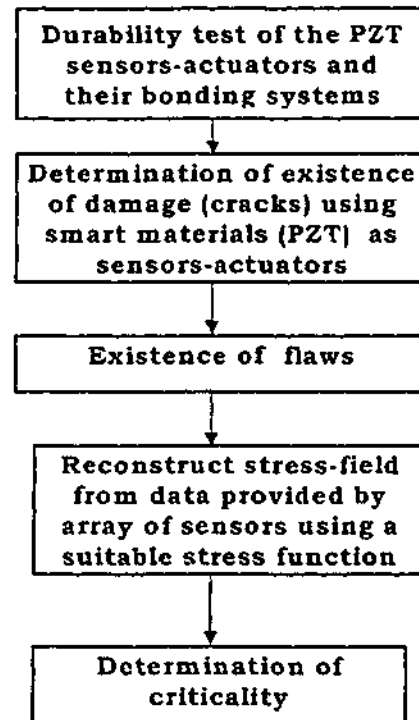


Figure 1.1. A flow chart of the research

In this thesis, a review of failure prediction in pipeline and in service monitoring of pipeline is presented in Chapter 2. In Chapter 3, experimental investigation of sensor-actuator and bonding system durability is reported. Then, in Chapter 4, the numerical investigation of the detection of existing/developing flaw in system is outlined which is followed immediately with the experimental investigation in Chapter 5. In Chapter 6, the ability of the developed algorithm to reconstruct stress field and determine the criticality of the flaw by using an array of sensors is presented. Finally, the significant findings of this research are summarised in Chapter 7.

CHAPTER 2. LITERATURE REVIEW

This literature review consists of two sections. First, it reviews prediction methods that can be used to design and/or prevent the failure of the pipeline. Second, it reviews some studies of the monitoring of pipelines with introduction of smart structure concept and successful applications of the passive sensor on the pipe-structure.

2.1. Prediction of failure in pipelines

Prediction of failure in pipelines has been investigated by many researchers. The predictive method for such rupture event in on or off shore systems can be useful for the designer. Venzi et al (1993)² reviewed current theories for predicting the ductile fracture propagation in high-pressure pipelines. This report contained a comprehensive survey of predictive methods. The review began in the 1970s when many countries took initiatives in clarifying certain important aspects of the ductile fracture phenomenon. Significant results were produced by these studies in the early 1980s. At the start of the 1990s the procedures of predictive methods were based on:

- 1) A continuation of the semi empirical approach by developing the test database of high-grade pipe.
- 2) The initiation of theoretical models based on fracture mechanics methodology by performing the computational model.

Venzi's review indicated that future research should be directed at determining the relationship between toughness and maximum permissible crack length.

In 1992 Emery et al³ developed a numerical method to predict the occurrence of crack arrest and the arrest length for full-scale pipe rupture. The pipe rupture was simulated in a computer and the pipe was

represented by a series of discontinuous split rings that deform elasto-plastically under fluid pressure and inertial loads. Pressures and pipe material characteristics, that were found experimentally, were used as inputs. Comparisons of measured opening axial shapes and those predicted by the simple ring model were in good agreement. The model was also successful in predicting the occurrence of crack arrest and the arrest length.

Kanninen et al (1994)⁴ described a user-oriented methodology in a recent report. This methodology can be used for assessing the risk of ductile fracture propagation in the full range of design and operating conditions that possibly occur on their gas transmission pipeline system. This predictive methodology is unique and at the leading edge of the technology since:

- 1) The bound of the full range of rich gas decompression completed the parametric calculations of crack tip pressure versus wave speed.
- 2) The assessment of the predictive method that was based on these calculations proved to be more accurate in predicting propagation and arrest of ductile fracture in pipeline steel than other alternative empirical procedures. This assessment can be done in two general ways: (2.a) For a new design, a minimum acceptable value of the pipeline steel toughness property can be determined by specifying the pipe size and the line pressure. (2.b) For an existing pipeline, calculating the critical pressure that may lead to rupture can prevent the long propagating fracture.

The failure of the pipeline is usually caused by crack growth. The crack will reduce the thickness of pipe wall and increase the hoop stress. Fortunately, before the pipe burst it leaks. This phenomenon is called a leak before breaks (LBB) and was described by Setz et al (1990)⁵ when determining the tolerable flaws of the pressurized components. This

research established the requirements of the tolerable flaws to meet the LBB criterion which were; (1) non-significant growth of part-through cracks; (2) the behavior of the LBB for excessive loading conditions must be knowledgeable (stable or unstable); (3) the leak can be detected in time. The investigation demonstrated an example of application of a fracture mechanics concept for tolerable embedded and surface flaws.

To make the LBB assessment easier Sharples and Clayton (1990)⁶ drew the structural integrity diagram of the pressure-vessel. This diagram is a plot of crack depth against crack length. They defined three regions for the structural integrity diagram (see Figure 2.1). *Region 1* is for cracks, which remain below the initiation size and only grow by fatigue through the wall. *Region 2*, is for cracks, which undergo combined fatigue and tearing before breakthrough occurs, but which finally break through by the same ligament failure as in Region 1. This region can lead to very extensive stable crack extension. *Region 3* is for cracks that may begin as fatigue cracks, then undergo combined fatigue and tearing, but which fail by crack instability, causing rapid breakthrough with possible dynamics effects.

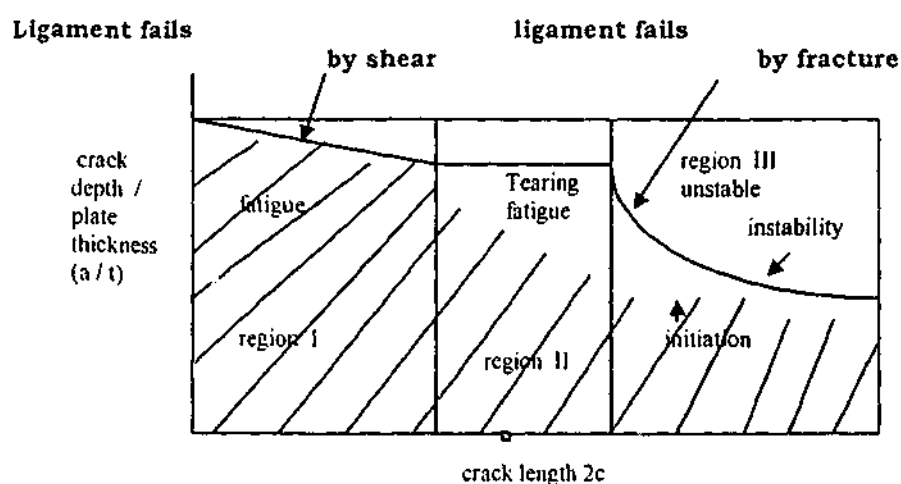


Figure 2.1. Structural integrity diagram

These cracks, once they reach the unstable condition, must be considered as unsafe. For some very long cracks, the time period between initiation and instability may be very small (due to the rapid rise in stress intensity factor with depth) and a safety margin on initiation may be needed in practice. The use of the structural integrity diagram in Figure 2.1 above requires a model of crack shape development as a crack grows through the wall of the vessel up to the stage at which the deepest part of the crack breaks through the wall, and this is considered for a number of growth mechanisms.

The failure of the pipeline is usually caused by crack growth that minimizes the fatigue life of the structure. In 1995, Lee and Liebowitz⁷ made an expert system that allowed the designer to evaluate critical flaw size in structural components subjected to fatigue loads. Specimen/size, load amplitude and mean stress and material type could be varied such that their combined effects could be accounted for in determining the condition of global instability. This corresponded to the onset of rapid crack propagation. This expert system would enable engineers to design more sophisticated components than their previous capability. The flowchart of the Fracture Analysis Material Evaluation Database (FAMED) of that system is shown in Figure 2.2. In this flowchart, the user selects the material type according to the number 1, 2 or 3, then the mean stress $\bar{\sigma}$ and stress amplitude $\Delta\sigma$ is decided from the Roman numeral between I and III. If the fatigue loads falls outside of I.II.III, the user may obtain three answers and find the answer by interpolation. With this system one could select the material and change the geometry design quickly to suit with the design requirements.

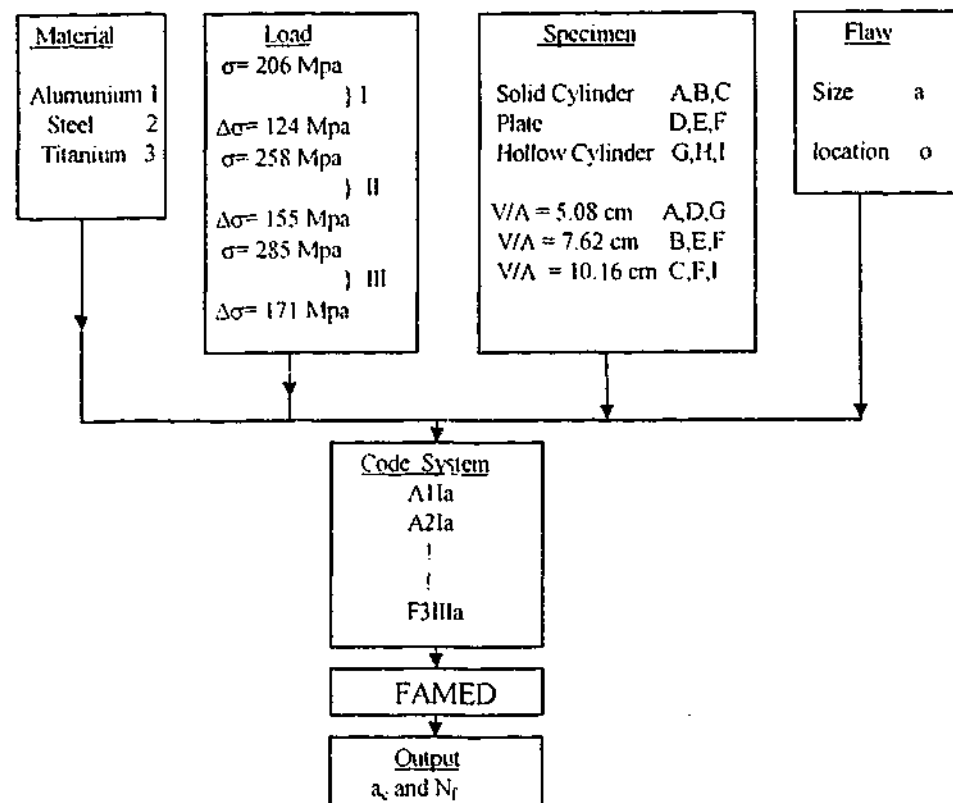


Figure 2.2. Flow chart of FAMED for evaluating critical flaw size and fatigue life

In the case of sub-sea pipelines a prediction of fatigue life was carried out during the design of Transmediterranean Pipeline and reported by Celant et al (1982)⁸. The fatigue life of this underwater pipeline was not only affected by the stress level imposed by supports configuration, pipeline weight, external hydrostatic pressure, weight-pressure-temperature of the internal fluid but also the cyclic load resulting from hydro-elastic phenomena of interaction between spanning pipe and sea bottom current. The design choices have been affected by the results of this research. From route selection, particularly, they were aiming at the determination of the intervention works on the sea bottom before pipe laying, and the possible installation of over-weights or pipe supports in order to avoid free spans of unacceptable length, to determination the interval between periodic inspections.

From these reviews it can be noticed that all the prediction methods of failure of a pipeline are based on fracture mechanics approach. This approach is well established. However, since a pipeline operates for long

time, a continuous inspection is needed to warn of any failure under normal operations. The next section will give some reviews of this topic.

2.2. In-Service Monitoring of Pipelines

The basis of the Integrity Management program is an understanding of the hazards and risks that a pipeline is exposed to, and the associated business and safety consequences. Ronsky and Trefanenko (1992)⁹ on their paper split the Integrity Management of the pipelines, which is the process by which pipeline owners ensure the long term, safe and reliable operation of their systems, into four phases (see table below)

Table 2. 1. Integrity Management Program

PIPELINE	INSPECTION	DEFECT AND	REHABILITATION
ASSESSMENT	MANAGEMENT	ASSESSMENT	& MAINTENANCE
			MANAGEMENT
Pipeline Prioritizing	Method Assessment	Data Interpretation	Field Inspection and
Risk Identification	Contract specifications	Defect Assessment	Coordination
Procedures Audit	Vendor Selection	Repair Prioritization	Field Services
Safety Audit	Pipeline Modifications	Repair Alternatives	Specifications
	Inspection Procedures	Repair Procedures	Contract
	Field Supervision	and Specifications	Contractor Selection
	Data Verification		Maintenance Programs

The integrity management program above highlights the importance of in-service continuous monitoring techniques for the systems. These techniques can be divided into three categories. Firstly, the companies have their maintenance schedules, then monitor the systems based on the schedule. Secondly, the company installs the equipment that can record or read the system performance. Data can be in form of strains or displacements in relation with stresses that occur on the pipeline wall. That means the companies can monitor the systems in real time. This will constitute the concept of a smart pipeline. Thirdly, it is a combination of the two previous categories.

Since pipeline systems can be located in regions hardly accessible by humans, such as in the jungle or on the seabed, continuous monitoring of the pipeline is a seemingly good option. This smart pipeline concept raises the possibility of remote inspection, which could reduce maintenance costs.

To know how a smart structure concept works a definition of the term is necessary. The comprehensive survey was carried out by Spillman Jr, W.B et al (1996)¹⁰ in Europe, US and Japan to define smart material and structures. When the survey was conducted in Europe the respondents were divided into three groups. The groups were marine engineering, civil engineering and aerospace engineering. Each group had their own definition on the smart structure/ material. The marine engineering group defined the smart structures as "*structures, which react in a pre-defined manner to provide a desired response to their environment either through (1) inherent material properties or (2) engineered control*". The definition of smart structure from the civil engineering group is "*smart structures provide some useful tangible benefit to the civil engineer and end user which is achieved through adaptability, knowledge of known limits and constraints, compatibility with existing design methodologies and ability to learn*". The last group stated "*in smart materials, everything is integrated, while in smart structures, the sensors and actuators are separated*".

The survey in North American resulted in a definition of a smart material and/or structure as a system that is designed for a specific functional purpose, and in fulfilling this purpose, it operates at a higher level of performance than its conventional counterpart. The system senses its internal state and external environment, and makes decisions and/or responds based on the data obtained to meet the functional requirements. Finally, the surveys succeeded to have a formal definition of a smart structure, which is "*a non-biological physical structure having*

the following attributes: (1) a definite purposes; (2) means and imperative to achieve that purpose; (3) a biological pattern of functioning". The smart structure concept is shown on the Figure 2.3

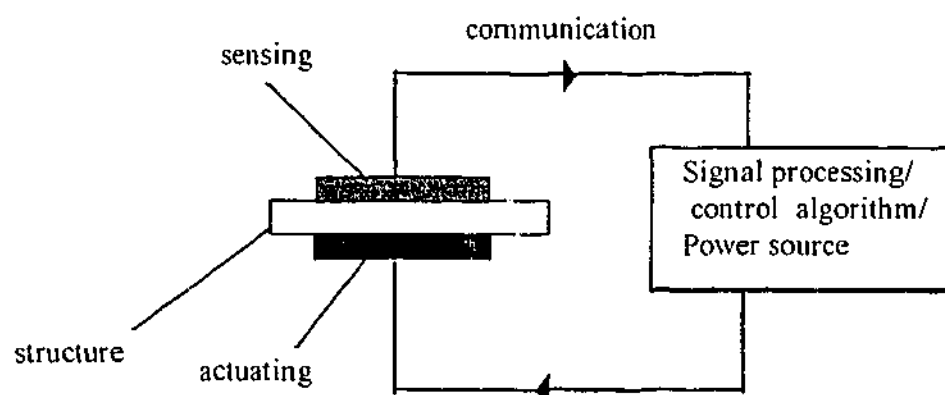


Figure 2.3. A smart structure concept

Culshaw (1996)¹¹ has tabulated a range of strain and displacement sensors that can be used as principal option for structural monitoring. These sensors are foil (such as the traditional strain gauge), semiconductor, LVDT, vibrating wire, PZT Film, PZT ceramic, optical fiber, photogrammetry (see Table 2.2).

Table 2.2. Strain and Displacement Sensors: The Principal Options for Structural Monitoring

Type	Foil	Semiconductor	LVDT	Vibrating Wire	PZT Film	PZT Ceramic	Optical Fiber	Photogrammetry	Comments
Typical Sensitivity	10 V/ ϵ	1000 V/ ϵ	-1 V/ μ d	± 2 in. frequency for 0.1 % ϵ	10 000 V/ ϵ	20 000 V/ ϵ	2 fringes/ μ 10 ⁻⁶ (10) fringe detectable Can be either	100 μ or better	10 μ is typical structural need
Point/Integral	Point (integrated to 0.1 m)	Point	Displacement	Point over short gauge length	Can integrate using large films	Point		Surface or volume measurement	Relative merits of point and integrated sensing complex
Gauge Lengths	0.5 mm to 100 mm	1 mm ^{1,2}	0.5 mm to 500 mm (displacement)	From millimeters to centimeters	From millimeters to a few meters	From millimeters to centimeters	From millimeters to hundreds of meters	To a few meters	
Bandwidth	-10 kHz	-100 kHz	< 100 Hz	-100 Hz	AC (few Hz) to 100 MHz	AC (few Hz) to 100 MHz	DC to 100 MHz	Essentially DC because of processing need	High values needed for ultrasonic probes
Distributed Measurement Potential	No	No	No	No	Possible, not demonstrated, and requires multiple connections	No	Yes - relatively straight-forward	Inherent but needs markers	Distributed measurement capability is virtually essential in online, continuous structural monitoring for test and evaluation, can tolerate using wiring harnesses
Multiplexing Feasibility	Difficult field bus	Difficult field bus	Difficult field bus	Difficult field bus	Can be integrated into film layout Readout difficult not demonstrated	Difficult field bus	Can be integrated into fibre design Readout demonstrated for many systems	Not applicable	
Chemical material compatibility	Poor	Good can be passivated	Poor	Poor but can be packaged and has been used in concrete	Poor-low temperature Curie point	Poor brittle	Excellent, withstands many processes	Inherent because non-contact	
Dynamic Range	10 % ϵ	to 0.5 % ϵ	0.3 % off set	-0.1 % ϵ	-0.5 % ϵ	-0.1 % ϵ	to 5 % ϵ only useful in tension	Not applicable	Large dynamic ranges needed in, e.g., composites. Some materials, e.g., concrete often operate in compression
Comments	The traditional strain gauge	Excellent for point measurements	Excellent, well characterized displacement measuring device, though large	Already in use to monitor some concrete structures, VWG's are large (relatively)	Low Curie temperature restricts applications (20 deg) Excellent potential as distributed gauge		For many, the most promising technology Distributed capability very powerful	Relatively little applied to date Good for inspection if define markers on structure and solve complex processing issues	

There are reported works, which describe attempts to use passive sensors to monitor pipelines. Shannon (1973)¹² described a monitoring procedure for thick-walled cylinder in Northern Ireland, U.K. The experiment was found that a relatively simple technique could be used for monitoring the extension of the radial crack in the thick-walled cylinder. The reason for this experiment was also to solve the difficulty of the ultrasonic crack detection in a simple geometry such as thick walled cylinder. In this detection, the measurements of radial cracks emanating from the bore surface can be hindered in small diameter cylinders by the curvature of the outer surface, and for all sizes of vessel, with a ratio of outer to inner diameters of approximately 2.0 and by the low sensitivity of both normal and shear waves. In this case, a passive sensor strain gauge was used on that experiment to read the local changes, which were induced in the external strain pattern by the presence of the cracks. This strain pattern was used as a means of sensing the depth of the radial crack. The result from that experiment was the development of an approximation for stress and strain in cylinder with internal longitudinal straight-fronted crack.

The other application of using an instrumented pipe was conducted by the Association of American Railways Laboratories (1964)¹³. That experiment was required to provide experimental data for evaluating the problem of uncased pipeline crossing. The uncased pipeline was supposed to withstand the loads from both internal pressure and external loads imposed on the pipe by trucks or railway trains passing over the pipeline. The experiment was conducted in the engineering laboratories where the test specimen was made on a length 28 in, OD by 12.75 in and measured thickness between 0.253 to 0.259 in. The stresses were calculated from strain-gauge readings and used by engineers to design the crossing. This paper covered the conversion of the measured strains into stresses and the analysis of the stresses (for the 12-inch pipe only) in

relation to (1) internal pressure; (2) external load; (3) location of high stresses in pipe with regard to point of load application; (4) interactions between stresses produced by internal pressure and external load; and (5) effect of cyclic loading.

Some researches of the instrumented structure in underwater environment also showed encouraging results. The experiment for a cylindrical structure in underwater environment was performed in Garden Banks 388 in the Gulf of Mexico and reported by Thrall et al (1995)¹⁴. The purpose of the experiment was to obtain information on the riser response to environmental loads for successful and reliable continued operation. The monitoring system consisted of two monitoring parts; structural and environmental. A riser was instrumented with strain gauges, inclinometer, and accelerometer to monitor its tension, bending, orientation and a motion. The stress data obtained from the bonded resistance strain gauges were used to calculate the remaining operational fatigue life.

The successful method for locating a blockage in a marine pipeline was reported by Rogers (1995)¹⁵. That method was based on measuring the changes of the hoop stress on a blockage area of the pipeline by using strain sensing. The changes in the hoop strain in the pipe are due to changes in the internal pressure when the oil blockage occurred. The device was made to convert radial extension or compression of the pipe into axial compression or tension respectively of a load cell. By pressurizing the pipe at position upstream and down stream of the blockage and measuring the resulting hoop strain, the boundaries of the blockage can be accurately defined. That device can be installed and recovered by ROV.

To place strain sensors in a harsh environment is another challenge for a smart structure concept to be applied. The sensors have to survive in that environment. Khan and Chen (1982)¹⁶ have conducted the potential use of strain gauges on the hostile environment such as high-pressure water. The coated strain gauges used on that study were able to withstand 80 MPa under water pressure. The comparison of the pressure effect was made between the coated strain gauge in a water environment and uncoated strain gages in an oil environment of the previously conducted study. This experimental study found a better technique for protecting the gauge under harsh environment and new compensating method to account for the effects of pressure and temperature simultaneously was necessary.

Marshall et al (1983)¹⁷ reported long-term exposures of strain sensors under hostile environment that performed on The Cognag Platform. The instrumentation system was installed in 1979 and runs to the year 1998. Some selected braces on 170 feet below sea level of that platform had been instrumented with strain gauges. One of the instrumented braces also carried an array of pre-cracked and as-welded fatigue specimens. When the first two sets of specimens were removed in 1979 and 1981, the platform had experienced three hurricanes Bob, Frederick and Allen. The strain gauges were be able to measure the stresses at the time of those hurricanes. That experiment succeeded in monitoring the health of the structure. The data from these measurements can therefore be used for estimating the remaining fatigue life as well as making the platform maintenance program of the structure.

Bullwinkle Platform was another platform that was instrumented following the success of Cognag experiments with more sophisticated data acquisition system. Swanson and Baxter (1989)¹⁸ reported the instrumentation system on that platform. Two major objectives of the Bullwinkle instrumentation system were: (1) Monitoring platform response to measured environmental conditions with particular emphasis on fatigue and platform maintenance (2) Acquiring data that will lead to a better understanding of the nature of forces due to combined waves and currents, particularly in the velocity field near the platform. The data were acquired with two microwave linked computer systems. The monitoring was done from on-shore with minimum operator intervention

This section has shown the use of the passive sensors to monitor the response of a structure under operational load. The durability of these sensors to withstand a harsh environment has also been reported.

2.3. Concluding Remarks

These reviews in this chapter have shown that the failure prediction of the pipeline by fracture mechanics concepts is well established. However, this approach needs knowledge of an initial defect or damage for assessing the pipe structure. Hence such a monitoring method that can detect and/or quantify the damage is required.

These reviews have shown monitoring in a pipeline using only passive sensors. These passive sensors only determine the response of the structure without the capability of actively monitoring the structure integrity in with a predetermined input.

The ability of the passive sensor e.g. strain gauge, that is bonded on the structure, to be used for a damage assessment in a harsh environmental condition indicates that degradation of the bond may not be critical.

The review reported in the above showed the importance and the relevance of on-line monitoring of a pipeline system. In the attempt to develop an on-line monitoring technique it is proposed that:

- An active system for in-situ monitoring, by using the active element Lead Zirconate Titanate (PZT) as sensor/actuator, incorporated with the existing passive sensor e.g. strain gauge.
- An algorithm that can be used to detect and assess the damage by evaluating the structural response data from the sensors (PZT and strain gauge).

The proposal above can be achieved by firstly establishing the knowledge of the feasibility of the PZT actuator-sensor and their bonding system with respect to typical loads on the pipeline. This will be reported in the next chapter.

CHAPTER 3. ACTUATOR - SENSOR AND BONDING SYSTEM DURABILITY

The durability of the actuator-sensor and the durability of the bonding system on a smart structure are critical to the user. Knowledge of these properties will ensure that the actuator-sensor of the system describes the true condition of the structure. This is because unbonded or improper attachment of the actuator-sensor and or an actuator or sensor degraded due to fatigue can lead to an incorrect assessment of the criticality of the structure being monitored.

In this chapter, an experimental investigation of the durability of a Lead Zirconate Titanate (PZT) actuator-sensor and its bonding system is reported. This chapter consists of four sections. The first section describes calculation of the load for the experimental work. The second section describes the experimental method, while the third presents the results and discussion. The last section highlights the significant findings of this investigation.

3.1. Load Design for Experimental Investigation

The ultimate application of this proposed technique is to monitor the condition of pipeline, and hence the PZT has to experience the range of loads typically experienced by the pipeline. To determine the various loads that would be applied to the specimens, the feasible maximum strain in the actual pipeline was calculated. The procedure for the calculation, which was based on typical pipeline design data, is given below.

The design data are:

1. The pipeline will be located on the seabed at a depth of 145m¹⁹.
2. The materials to be used for the pipeline are²⁰:
 - a) API L X-65 outer diameter 965.2 mm and wall thickness 31.75 mm
 - b) API L X-80 outer diameter 762 mm and wall thickness 19.05 mm

The mechanical properties of the pipe-steel are given in table 3.1²¹:

Table 3.1. Mechanical properties of API X-65 and X-80

Grade of steel	σ_y (MPa) Yield Strength	σ_u (MPa) Ultimate Tensile Stress	Charpy Energy (J/mm ²)	DWTT Energy (J/mm ²)	Modulus E (GPa)	CTOA _c (critical Crack Tip Opening Angle)
X-65	447	596	0.96	3.55	200	8.68
X-80	541	658	2.01	7.06	200	11.13

To minimize the possibility of ductile fracture, the pressure should not exceed a maximum, which can be calculated using the following formula⁴:

$$P_{\max} = (2h/D)(CTOA_c / C)^{\alpha} (E^{\beta} \sigma_0^{\delta}) / (D/h)^{\epsilon} \quad (3.1)$$

where P_{\max} has the same units as Youngs' modulus E , D is the diameter of the pipe, h is the thickness of the pipe, σ_0 is the stress flow or the average of the yield and ultimate strengths σ_y and σ_u , and other constants are provided in table 3.2⁴:

Table 3.2. Constants for calculating the maximum pressure P_{\max}

Parameter	Lower Bound (Methane)	Upper Bound (Rich Gas)
C	106	670
α	0.653	0.551
β	0.492	0.649
δ	0.508	0.351
ϵ	0.425	0.535

Because the pipeline will be on the seabed, the maximum pressure is reduced by the hydrostatic pressure P_{hyd} of:

$$P_{hyd} = \rho g d \quad (3.2)$$

where ρ is the density of seawater, g is the earth constant gravity and d is the depth of the seabed from the sea surface.

Hence, the corrected maximum pressure is

$$P_{mcorr} = P_{max} - P_{hyd} \quad (3.3)$$

The maximum hoop stress σ_{mhoop} in a thin cylinder (the ratio R/t is greater than 10) can be calculated using the following formula²³:

$$\sigma_{mhoop} = \frac{P_{mcorr} R}{t} \quad (3.4)$$

where R the radius and t the thickness of the pipe.

Hence, the maximum strain ϵ_{max} can be found by using Hooke's law

$$\epsilon_{max} = \frac{\sigma_{mhoop}}{E} \quad (3.5)$$

where E is the Youngs modulus of the pipe material.

From the calculation that is shown on Appendix B, the maximum strain that will be experienced by the pipeline is in a range of 1800 to 2700 microstrains.

3.2. Experimental Investigation

This experimental investigation was carried out to assess the life of the PZT actuator - sensor and bonding system of the pipeline, which will experience the load in range of 1800 to 2700 microstrains. Hence, strains of 1500, 2000, 3000, 4000 micro strains were applied to 4 different specimens in order to establish the durability of the PZT in the range 1500 to 4000 microstrains. A number of specimens were made from aluminum bars. Aluminum is used in order to reduce the magnitude of the loading required to achieve the desired strains. A PZT T107-A4E-602 patch (the material properties are shown on Appendix A) and a small aluminum (Al) film with a strain gauge were mounted on every specimen (see Figure 3.1a and b). For this condition, for the PZT patch and Al film the strains ϵ must be equal:

$$\epsilon_{PZT} = \epsilon_{Alfilm} \quad (3.6)$$

Using Hookes' law, this equation can be expressed as:

$$\frac{\sigma_{PZT}}{E_{PZT}} = \frac{\sigma_{Alfilm}}{E_{Alfilm}}$$

where σ and E are the stress and Young's modulus

Since these materials experience the same force F , applying Pascal's law leads to the following relationship;

$$\frac{F}{A_{PZT}E_{PZT}} = \frac{F}{A_{Alfilm}E_{Alfilm}}$$

where A is the cross sectional area

So,

$$l_{Alfilm}t_{Alfilm}E_{Alfilm} = l_{PZT}t_{PZT}E_{PZT}$$

where l the length and t the thickness of the cross sectional area.

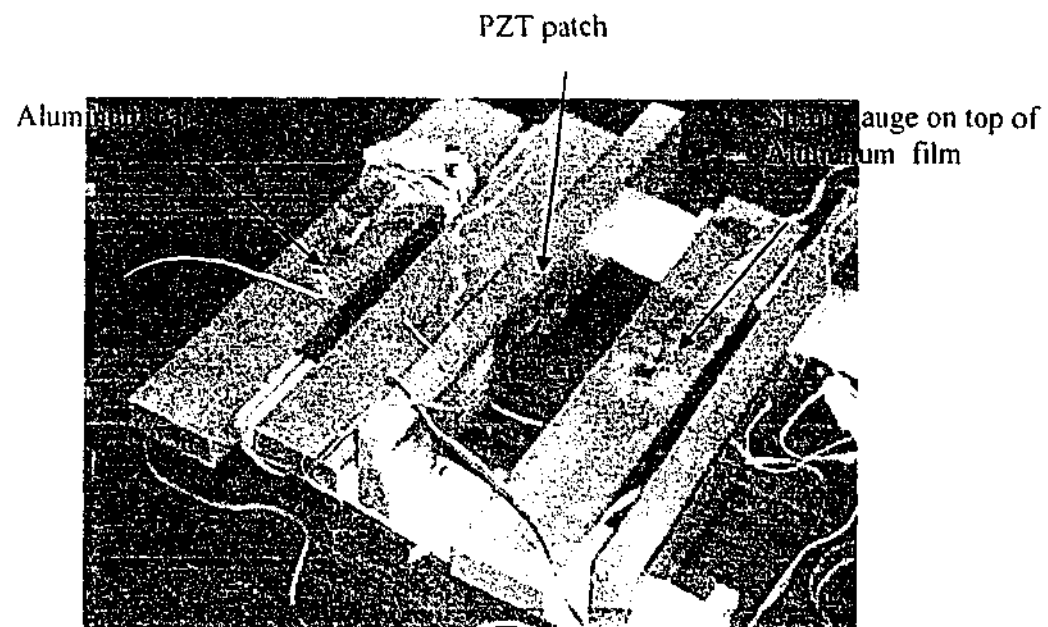


Figure 3.1a. Aluminum Bars for Sensor-Actuator Degradation Investigation

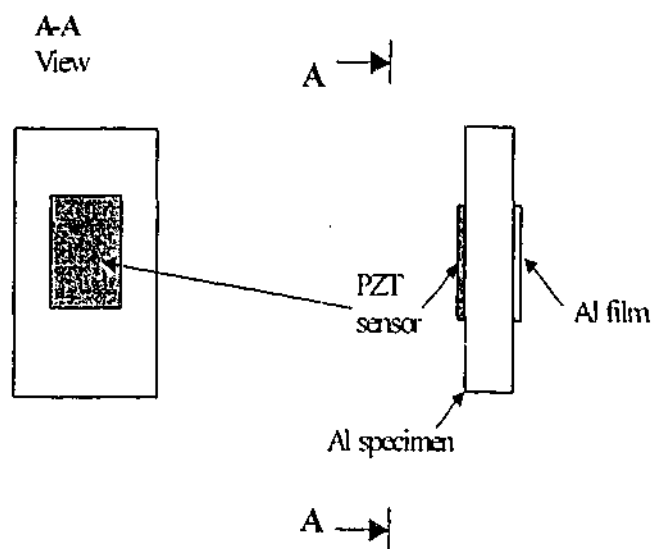


Figure 3.1b. A schematic sensor-actuator degradation test-specimen

Since the length of both materials is the same, equation (3.6) becomes:

$$t_{Alfilm} E_{Alfilm} = t_{PZT} E_{PZT} \quad (3.7)$$

or

$$K_{Alfilm} = K_{PZT} \quad (3.7a)$$

where K is the stiffness of the material.

The equivalence of the stiffness between the PZT patch and the Al film is very important since it ensures that the patch and film experience the same condition of any load to the specimen.

The test equipment consisted of a material testing machine MTS 810 (see Figure 3.2), a dual channel oscilloscope GOS-622G 20 Mhz, a computer which had the software Testware-SX version 3.1 (see Figure 3.3), a multiple channel 350 Ohm strain gauge amplifier ME823 with an adapter, a dual channel strip chart recorder and a bar specimen of dimensions 300x50x20 mm³ to which a PZT patch and an aluminum film with a strain gauge were attached. Araldite superstrength glue was used for bonding the PZT patch and Al film to the aluminum bar while Micromasurement M-BOND 2000 strain gauge glue was used for bonding the strain gauge to the Al film. Figure 3.4 shows this schematic diagram of experimental set-up.

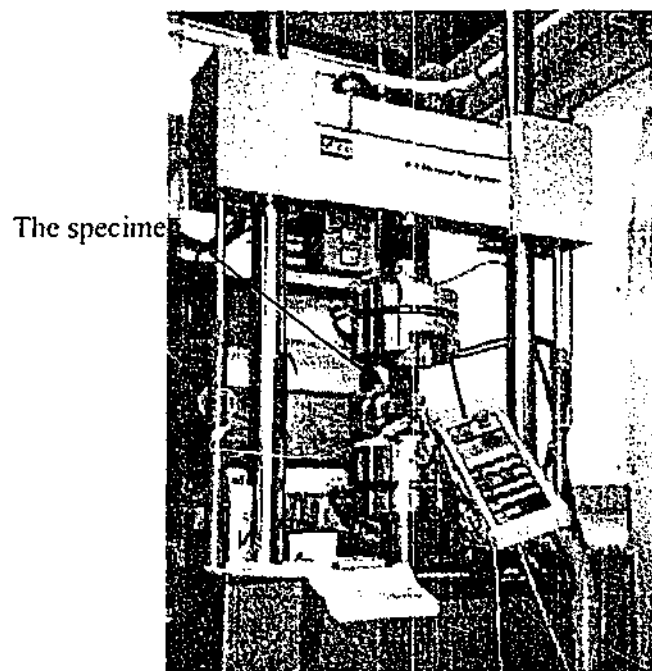


Figure 3.2. Material Testing System

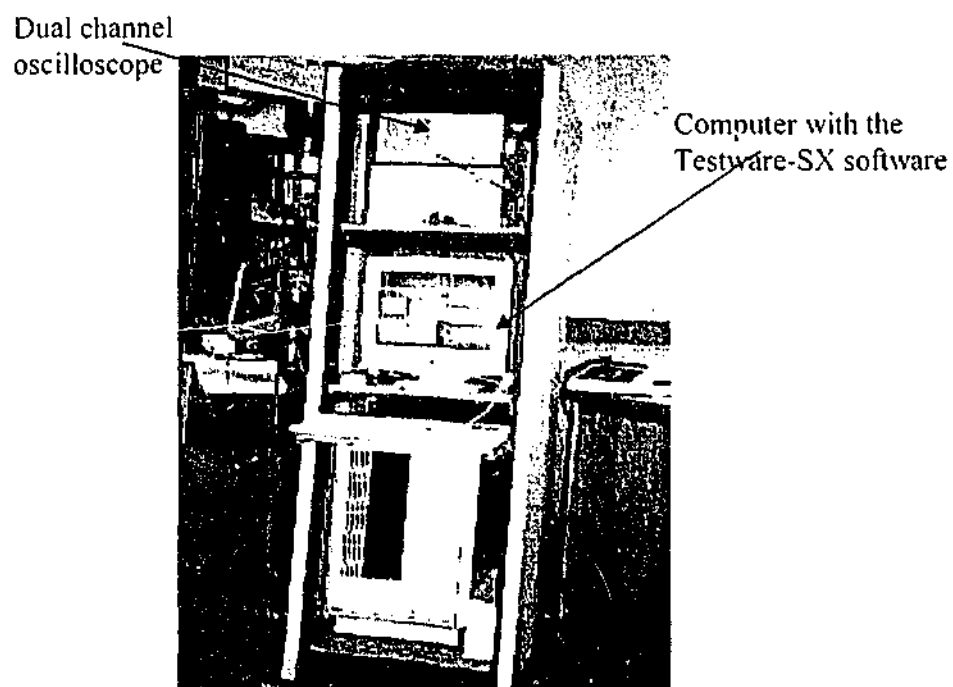


Figure 3.3. Control System of MTS

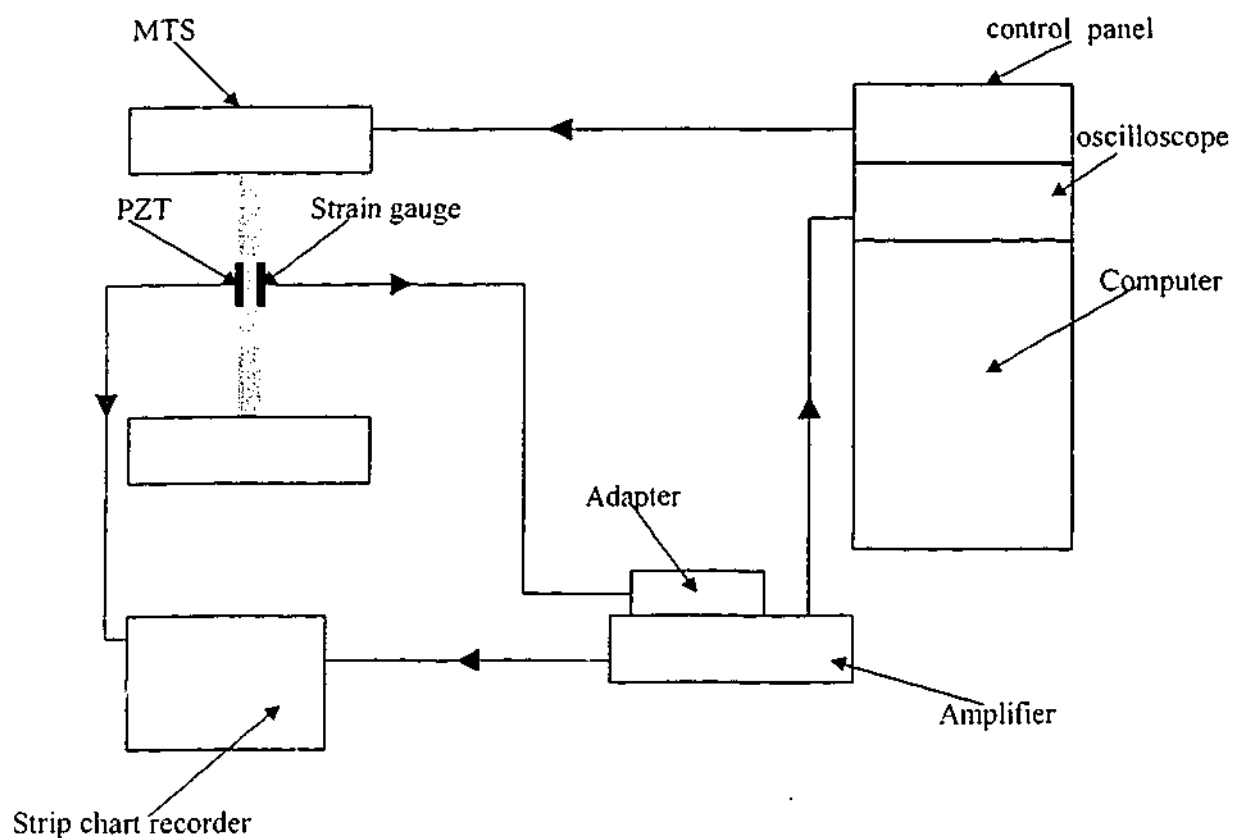


Figure 3.4. Schematic diagram of the experimental set-up

Strains of 1500, 2000, 3000, 4000 micro strains were applied to 4 different specimens in order to establish the durability of the PZT in the range 1500 to 4000 microstrains. The loads that were experienced by the specimens were calculated by using Hooke's law and Pascal's stress law. These calculations were also to ensure that the stress value was below the yield stress σ_y of the specimens to avoid breaking the specimen in one execution of load.

A dynamic load, which was based on these calculated strains and stresses, was applied to the specimen by the MTS 810. The MTS machine produced continuously cyclic load until the specimen was broken or the response signal from the PZT patch and/or the Al film became irregular. The load was inputted and controlled by software Testware - SX version 3.1 in the computer.

The structural response of the film was measured by the strain gauge and the PZT patch. The measurements from the strain gauge were sent to the strain gauge adapter, which was a Wheatstones bridge circuit. This circuit was designed to detect the change in the resistance of the gauge⁵. To amplify the signal an excitation voltage was added by the strain gauge amplifier. Two-channel output was selected from the amplifier with one channel connected to the oscilloscope to ensure that the measured strain was matched with the calculated strain. The voltage response signal from the amplifier, which was displayed on the oscilloscope, was calculated by the following formula:

$$V = 1/4 \times \text{Excitation Voltage} \times \text{Gauge Factor} \times \text{gain} \times \text{strain} \quad (3.10)$$

where the excitation voltage was chosen to be 10 V, the gauge factor was 3.28, which was specified by the manufacturer, the gain was chosen to be 30 and the strain was the calculated strain.

Another channel from the strain gauge amplifier was connected to the strip chart recorder. The structural response, which was experienced by the PZT patch, was directly sent to another channel of the strip chart recorder. The recorder plotted the response signal voltage of the PZT and strain gauge as a function of a number of cycles of load.

3.3. Result and Discussion

The results from this experimental investigation are shown in Figure 3.5. This figure represents the number of cycles N in x-axis versus the normalized voltages in y- axis that produced by the PZT patch under different strain loads.

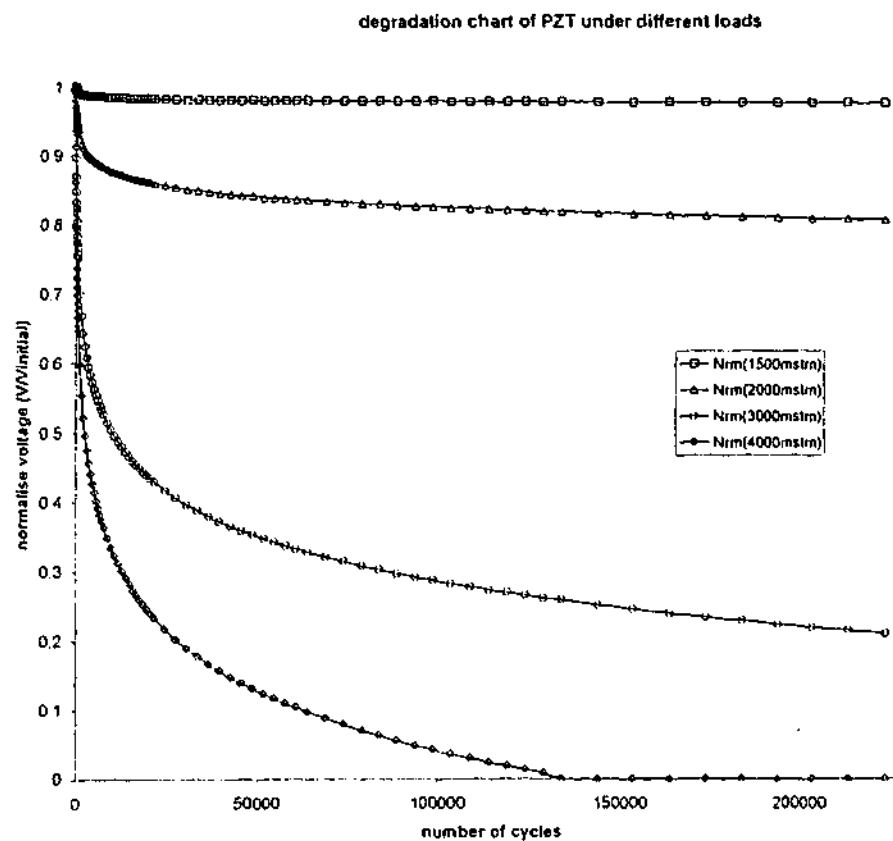


Figure 3.5. Degradation chart of PZT under loads of 1500, 2000, 3000, 4000 microstrains

It can be seen from the Figure 3.5 that at 3000 and 4000 microstrains the voltage decreases with the increasing of number of cycles. At 4000 microstrains, the PZT patch does not generate any voltage after 100000 cycles. At 3000 microstrains, the voltage that is generated by the PZT decrease at slower rate than the 4000 microstrains. Stable condition appears to be found at 1500 and 2000 microstrains. Based on these findings, all the experimental work in this thesis was conducted below 2000 microstrains. It is recommended not to use the PZT T107-A4E-602 patch for load above 3000 microstrains.

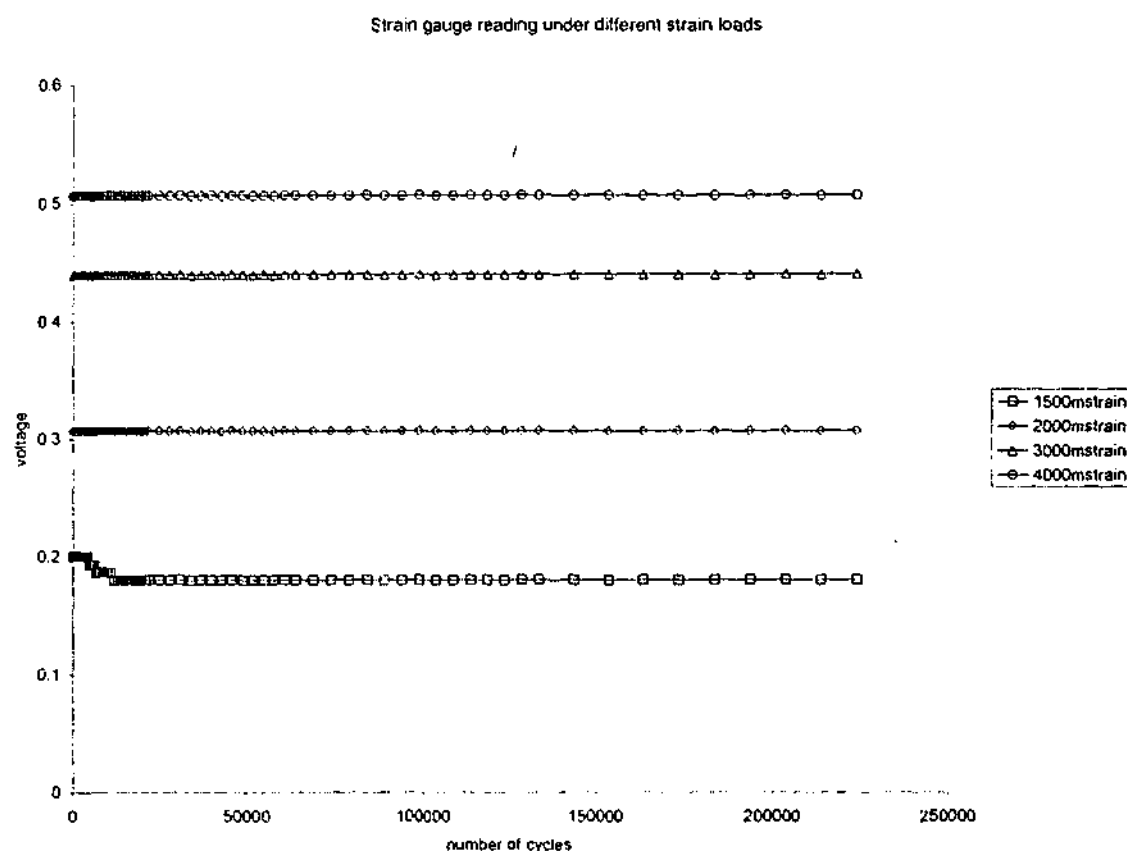


Figure 3.6. Strain gauge reading on different strain loads

The results from the strain gauges are shown in Figure 3.6. The constant strains recorded as a function of the number of cycles performed by the specimens showed that the bonding system has not degraded. This infers that the voltage reduction that was produced by a PZT patch at a particular strain load is purely due to the degradation of the PZT material after certain number of the cycles. Based on these results the bonding system i.e. Araldite superstrength glue will be used to bond PZTs on future test specimens and the Micromasurement M-BOND 2000 strain gauge glue was used for bonding the strain gauge onto test specimens.

3.4. Concluding Remarks

This experimental investigation demonstrated the feasibility of the PZT actuator-sensor and their bonding system with respect to typical loads on the pipeline. In this investigation the findings reported are applied to PZT T107-A4E-602 patch at ambient condition. In general, the results of this part of the research can be used as a reference to discriminate structural damage from sensor degradation at a particular strain load after a certain number of cycles. Based on the findings the PZT will be used on this research to detect damage in a structural component. The numerical investigation of this damage detection using the PZT will be conducted in next chapter.

CHAPTER 4. NUMERICAL INVESTIGATION OF THE DETECTION OF A FLAW IN THE SYSTEM

The results from Chapter 3 show that PZT material can be used on the proposed pipeline as the actuator-sensor pair. In this chapter, the use of PZT actuator-sensor pair for damage detection in a structure is simulated numerically. This approach examines the possibility of using an array of piezoelectric transducers attached to the structure for both actuation and sensing. To help in this development work, this research will initially focus on thin-walled pipeline system. Here, the piezoelectric actuators can be used to generate the elastic-waves on the test material i.e. plate. An array of piezoelectric actuators will be used to provide a broadband excitation across the desired frequency range to the structure. Another array of sensors in front of the actuator array will detect the structural response resulting from the broadband input. In this thesis the Active Damage Interrogation (ADI) method which was developed by Lichtenwalner et al (1997)²³ for detecting delamination in a composite material will be extended for the detection of a crack in an aluminum plate.

The first section of this chapter presents the transfer function (TF) method. Then, the numerical modeling for detecting a crack in an aluminum plate will be presented in the second section. The results from these investigations will be presented and discussed.

4.1. Transfer Function Method

This section describes the basic equations and underlying assumptions that are used in both the numerical and experimental work to calculate the Transfer Function. When the mounted PZT patch is actuated using an electrical field, it produces strain. This strain is also experienced by

the host structure. The in-plane actuation or sensing strain ε of the PZT is proportional to the mechanical and electrical coupling coefficient d_{31} of the ceramic and an applied electric field V , from Crawley et al (1991)²⁴ it can be expressed as:

$$\varepsilon = d_{31}V \quad (4.1)$$

If the bonding layers are thin and stiff, the strain of the PZT patch acting as an actuator is equal to the strain of the corresponding area of the plate below. This is also true for the patch that acts as a sensor. This situation in Crawley et al (1987)²⁵ is called a perfectly bonded actuator or sensor. The strain equation can then be written as:

$$\varepsilon_{pzt} = \varepsilon_{structure} \quad (4.2)$$

The PZT patch has three directional motions. Since the PZT patch that is used in this investigation is thin, the motion through the thickness direction is insignificant compared to the others and can be ignored. Hence, from Ha et al (1992)²⁶ the relationship of the strain-displacement for small deformation and pure extension is:

$$\varepsilon = \Delta L / L \quad (4.3)$$

where ΔL and L are an induced length and a length of PZT patch under force or voltage excitation

On any actuator-sensor pair, a broadband input voltage is applied to the actuator and the sensor detects the structural response to this input. The Transfer Function (TF) between the pair is then computed using equation (4.4):

$$TF = \frac{V_{ks}}{V_{kact}} \quad (4.4)$$

where V_{ks} is a vibration spectrum from the sensor and V_{kact} is a vibration spectrum from the actuator

The vibration spectrum V is defined as:

$$V_k(\omega) = A_k(\omega)e^{i\theta_k(\omega)} \quad (4.5)$$

where ω is a frequency, θ_k is a phase angle and A_k is an amplitude

In the experimental investigation, this vibration spectrum is measured with a frequency analyser. In the numerical investigation, the TF can be calculated using equation (4.1) to (4.4). The main purpose of this study is to determine if the TF obtained by equation (4.4) can be used to monitor the development of a crack on a structure.

In the numerical investigation, a thin aluminium plate, which was clamped on the shorter edges, was selected. The plate, which is shown in Figure 4.1a, has a dimension of 200 x 400 x 2 mm³. The arrays of actuators and sensors, denoted as rows of A, B and C, were bonded on the surface of the plate. The detailed configuration of the actuator-sensor pairs is shown in Figure 4.1b. The Transfer Function was measured from each actuator-sensor pair. Actuator-sensor pairs were combined in two ways to produce the transfer function: (a) A direct-TF measurement i.e. A_nB_n , B_nC_n ($n = 1 \dots 11$), (b) A cross-TF measurement i.e. A_nB_{n+1} , $A_{n+1}B_n$ ($n = 1 \dots 10$). In the A_nB_n , A_nB_{n+1} , $A_{n+1}B_n$ combinations, row A was an array of sensors while row B was an array of actuators. In B_nC_n combinations, row B was an array of sensors while row C was an array of actuators. Three-damage conditions in the structure, damage1 (with a 10mm crack), damage2 (with a 20mm crack) and damage3 (with a 30mm crack) were used in order to identify changes in the TF for each damage state. A no-damage (no-crack) case was also considered.

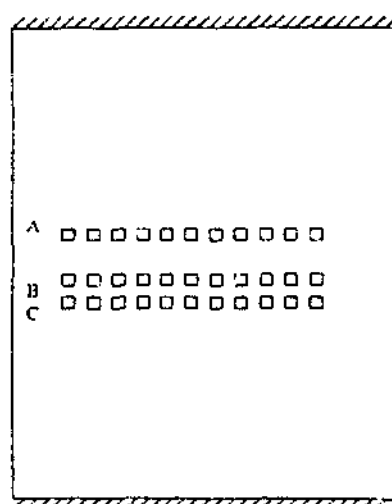


Figure 4.1a. A thin aluminium plate clamped on the 2 shorter edges with distributed PZT actuator and sensors

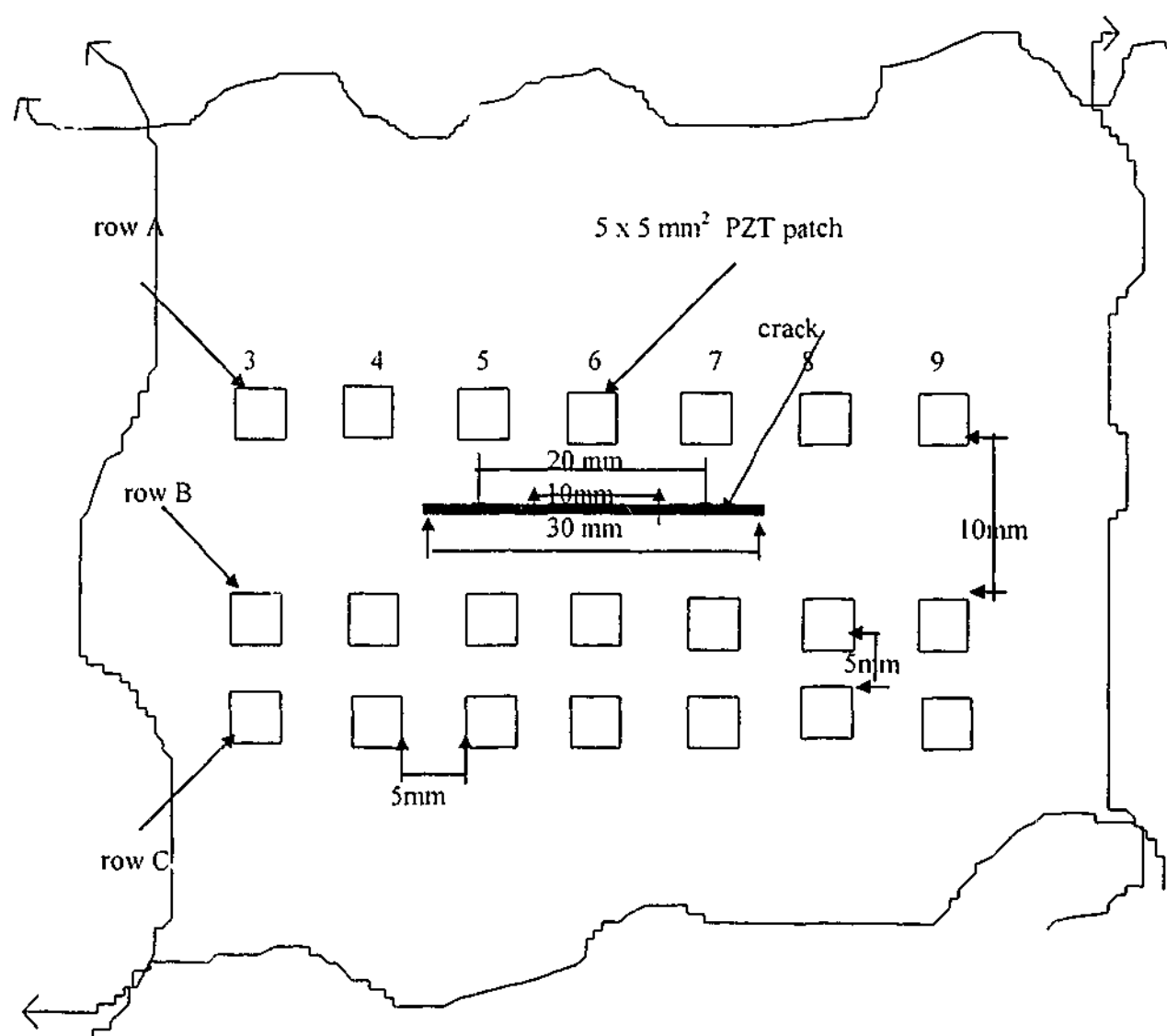


Figure 4.1b. Detailed Configuration of the Actuator-Sensor Pairs

The placement of distributed PZT patches in the configuration shown in Figure 4.1a and 4.1b was designed to answer these following questions:

- 1) Can the crack be predicted when it is located between rows A and B?
- 2) How sensitive are the rows B and C to the occurrence of a crack in between rows A and B?
- 3) Can the crack tip location be approximately determined?

Figure 4.1a and 4.1b show that the array of sensors-actuators consists of 3 rows (A, B and C) and 11 columns (1 ... 11). Figure 4.2 shows a schematic mechanical model of the system

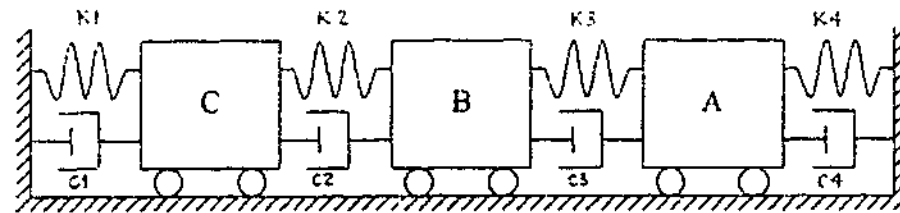


Figure 4.2. A schematic mechanical model of the system

The motion equation of the system above can be written as²⁷

$$\begin{bmatrix} m_1 & 0 & 0 \\ 0 & m_2 & 0 \\ 0 & 0 & m_3 \end{bmatrix} \begin{bmatrix} \ddot{x}_1 \\ \ddot{x}_2 \\ \ddot{x}_3 \end{bmatrix} + \begin{bmatrix} (c_1 + c_2) & (-c_2) & (-c_3) \\ (-c_2) & (c_2 + c_3) & (-c_4) \\ (-c_3) & (-c_4) & (c_3 + c_4) \end{bmatrix} \begin{bmatrix} \dot{x}_1 \\ \dot{x}_2 \\ \dot{x}_3 \end{bmatrix} + \begin{bmatrix} (k_1 + k_2) & (-k_2) & (-k_3) \\ (-k_2) & (k_2 + k_3) & (-k_4) \\ (-k_3) & (-k_4) & (k_3 + k_4) \end{bmatrix} \begin{bmatrix} x_1 \\ x_2 \\ x_3 \end{bmatrix} = \begin{bmatrix} f_C \\ f_B \\ f_A \end{bmatrix} \quad (4.6)$$

It must be emphasised at this stage that the work presented in this thesis will focus on the use of the change in the stiffness k of the structure to provide an indication of the presence of a crack. In this respect the work presented will focus on the "stiffness-based" approach and will focus on the analysis of the part of the spectrum that is not dominated by resonance.

In Equation (4.6), if the actuation is on f_B and the response is measured by f_A , then by applying equation (4.4) we can find the transfer function of AB. When the local damping c_3 and stiffness k_3 change because the crack is located between B and A, these terms can contribute significantly and can affect the TF calculation. However, when we excite the body C (i.e. f_C) and sense the response on body B (i.e. f_B), the contribution of stiffness k_3 to the overall response will be investigated. This will allow determining if the damage, which is located between A and B, can be detected by monitoring the response of B when C is excited.

4.2. Finite Element (FE) Modelling of the Structure

In this investigation a plate model was discretised into 1122 eight-node shell elements. A finite element model of the plate was made for every condition of testing (i.e. non-damage, and damage with a crack 10mm, 20mm, and 30mm). Figure 4.3 schematically shows how the crack was simulated on the plate. The material properties of the plate and PZT that was used in this FE model are shown in Table 4.1. It is important to take these material properties into consideration especially at the location where the PZT patches were attached. At that location, for every PZT patch the following relationship between the forces must be satisfied:

$$F_{\text{tot}} = F_{\text{PZT}} + F_{\text{Al}} \quad (4.7)$$

where F_{tot} is the total force from the PZT patches and aluminium plate underneath it. From Pascal's stress law,

$$(\sigma A)_{\text{tot}} = (\sigma A)_{\text{PZT}} + (\sigma A)_{\text{Al}} \quad (4.7a)$$

where σ and A are the stress and the area.

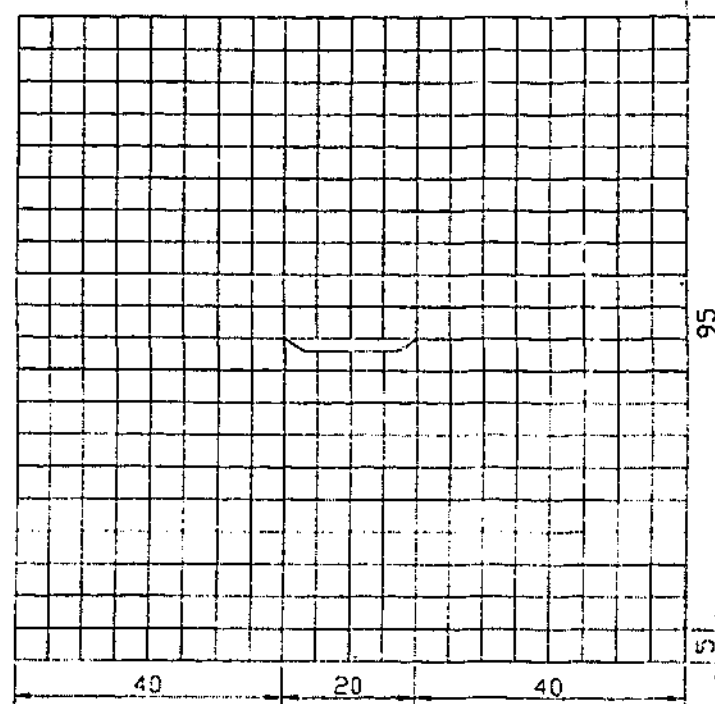


Figure 4.3. Schematic of test plate arrangement (this is not an FE mesh)

Table 4.1. The Material Properties of the Al plate and PZT^{28, 29, 30}

Material	Young's modulus(GPa)	Density (kg m ⁻³)	Poisson's ratio
Aluminium	68.5	2695	0.33
PZT - 5A	52	7800	0.33

By applying the stress-strain relationship (Hooke's law) equation (4.7a) becomes:

$$(\epsilon EA)_{\text{tot}} = (\epsilon EA)_{\text{PZT}} + (\epsilon EA)_{\text{Al}} \quad (4.7b)$$

where ϵ means the strain and E means Young's modulus.

From equation (4.2) and because the length of the stress working area of the PZT patch is equal to the length of the plate attached underneath, the following relationship holds:

$$E_{\text{tot}} = ((Et)_{\text{PZT}} + (Et)_{\text{Al}}) / t_{\text{tot}} \quad (4.8)$$

where t is the thickness.

Using a similar approach to the volume of the PZT and Al the relationship below is obtained:

$$\rho_{\text{tot}} = ((\rho t)_{\text{PZT}} + (\rho t)_{\text{Al}}) / t_{\text{tot}} \quad (4.9)$$

where t_{tot} is $(t_{\text{PZT}} + t_{\text{Al}})$ and ρ is the density

These combined material properties i.e. Equation (4.8) and (4.9) were used on the elements where the PZT patches were placed. In these regions the dimensions of an element were equal to the size of a PZT patch. The nodes on that element were selected to be excited or calculated when the element acted as an actuator or a sensor. The magnitude of the force was 10 Newton in a range of 250 to 100000 Hz. All calculations of a FE model including mesh generation were done at a SGI workstation. The TF calculations were performed in a P.C with results obtained from the finite element analysis.

4.3. Numerical Simulation Results and Discussions

The results of this investigation are presented in two subsections. First, it presents and discusses the results from the transfer function method. Second, it shows the results and the discussion of using the R-curve

method (to be defined later), which is similar to Lichtenwalner's work (1997).

4.3.1. Transfer Function (TF) Results

The number of pairs to be analysed in the numerical simulation was reduced because of symmetry. For the purpose of this investigation the pairs A_nB_n , B_nC_n ($n=1...6$), and the cross pairs A_nB_{n+1} ($n=1...5$), under the three damage conditions (with 10mm, 20mm and 30mm crack) including a no damage condition are presented below. All TF results that are presented here consist of the amplitude and phase differences for all the damage conditions.

Analysis of the TF of A_nB_n pairs

The amplitude and phase angles of the TF for the pair A_1B_1 are presented in Figure 4.4a and 4.4b. The results for all damage conditions are similar. This is because they are located far away from the crack region. The similarity of the TF results for every damage condition appears also on pairs A_2B_2 and A_3B_3 in Figure 4.5a&b and 4.6a&b. These indicate that the crack is still located relatively far away from these A_2B_2 and A_3B_3 pairs.

Figure 4.7a and 4.7b show the results obtained when sensor-actuator pair A_4B_4 was used. These results show that the TF began to shift to the left for the case with a 20mm crack. The 30mm crack presented a more distinct shift. This can be explained by the fact that when the crack approaches the sensor-actuator pair, the reduction in the stiffness resulted in a decrease in the natural frequency of the system.

Figure 4.8a and 4.8b showed the results obtained for the sensor-actuator pair A_5B_5 , the existence of a 10mm crack resulted in shifting of

the peak response from approximately 63 kHz to 60 kHz. A further increase in crack length (i.e. 20mm) resulted in a further reduction in the frequency of the peak response of the system (i.e. to approximately 50 kHz). At this crack length, a new peak in the frequency response (approximately 90 kHz) was introduced due to the reduction in systems stiffness. The frequency of this newly introduced mode was further reduced when the crack was further increased to 30mm.

In Figure 4.9a and 4.9b, shows the TF of the pair A6B6. At a 10mm crack the shift began to occur from the frequency region between approximately 70 kHz and 75 kHz to 58 kHz and 65 kHz, and a new peak was introduced into the frequency region between 90 kHz and 100 kHz. This is similar to those seen in Figure 4.8a and 4.8b. At the 20mm crack the new mode shifts from the frequency region between approximately 90 kHz and 100kHz to 80 kHz and 90 kHz, and the old modes were shifted to the frequency region approximately between 42kHz and 48 kHz. When the crack was increased to 30mm the higher mode shifted only a little, and the previous mode for 20mm continues to move down the frequency region to approximately between 35 kHz and 40 kHz. This insignificant shift in the higher mode with the larger crack length is due to the fact that stiffness in the structure between the sensor-actuator pair is not further reduced by any further increase in the crack length.

Summary for AnBn pairs TF results

From these results above, it is clear that the sensor actuator pair A6B6 that is close to the area of the damage can be used for detection of the damage (i.e. the 10mm crack). When the damage has propagated (i.e. grown to 20 and 30mm cracks) the detection can be successfully done not only by the pair A6B6 but by the pair A4B4 and A5B5 as well.

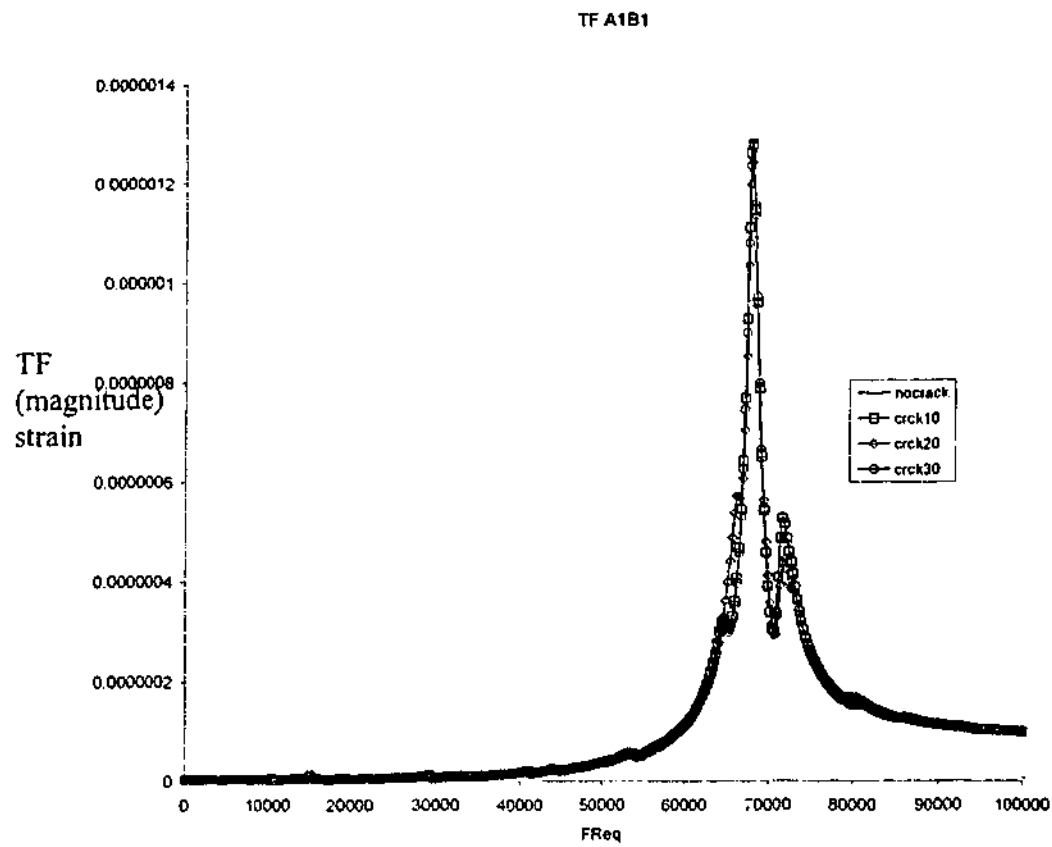


Figure 4.4a. TF Amplitude of A1B1

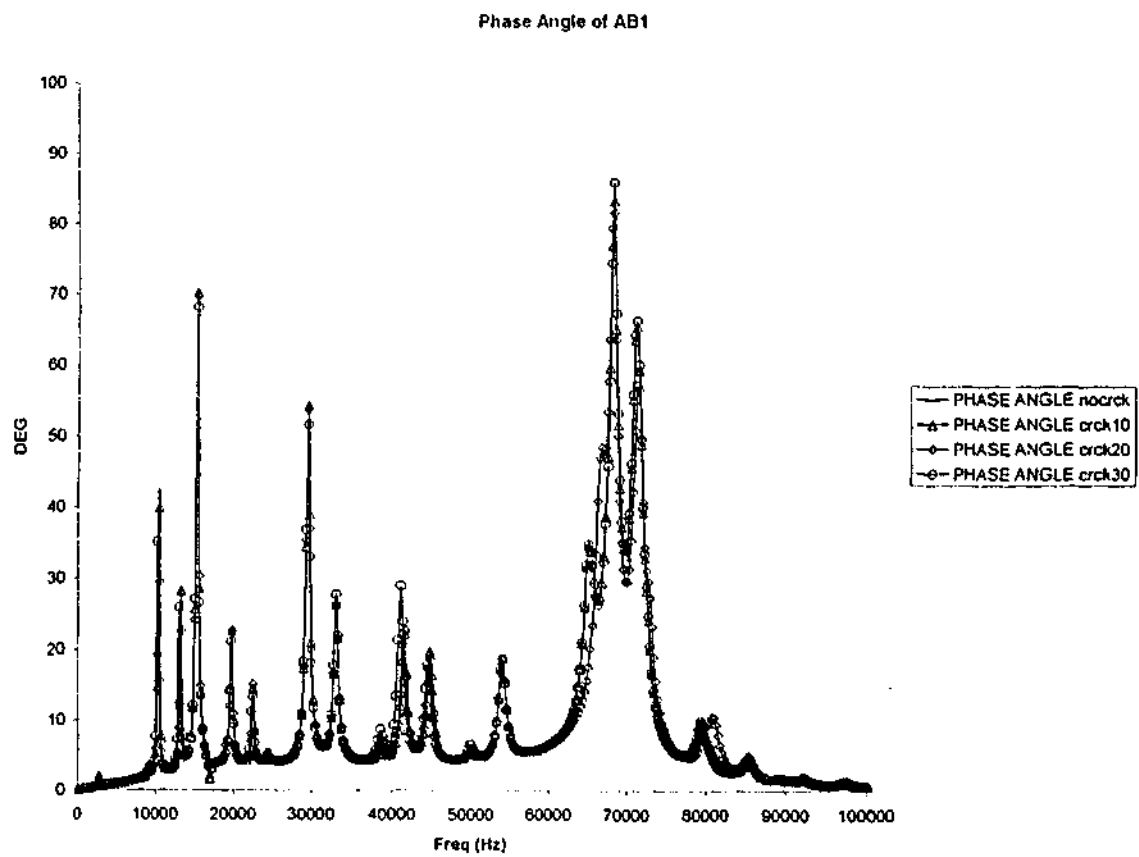


Figure 4.4b TF Phase Angle of A1B1

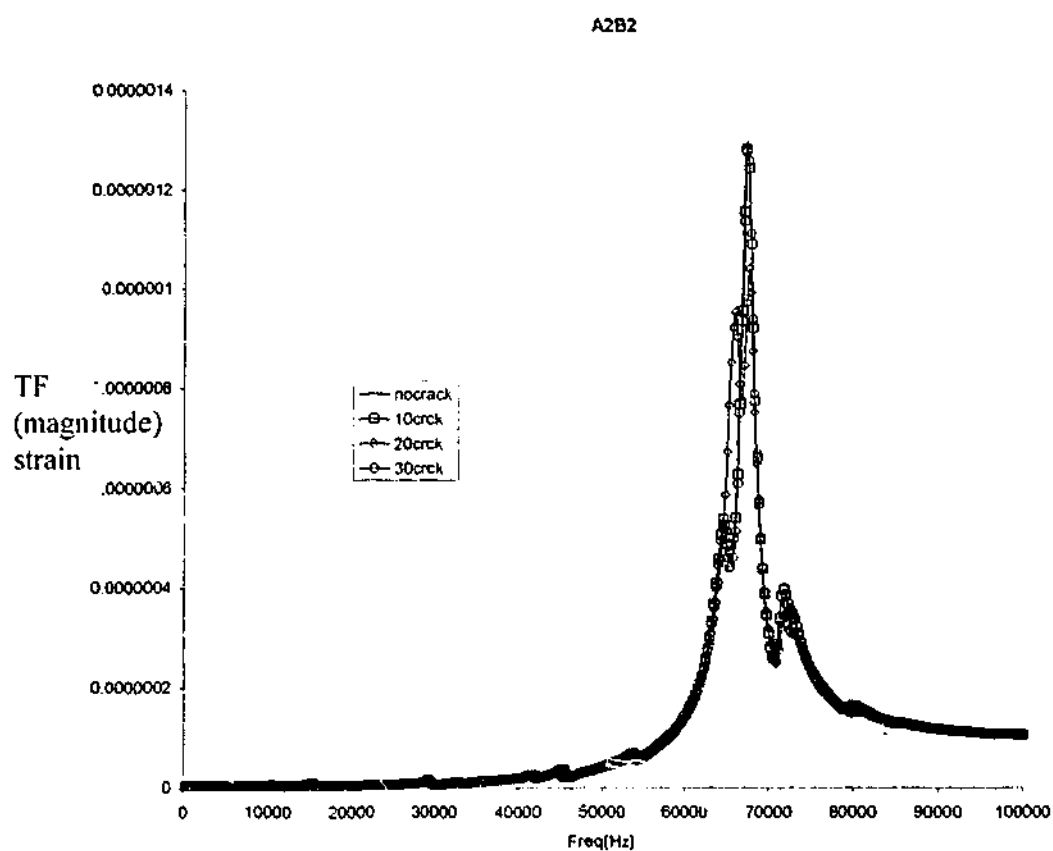


Figure 4.5a. TF Amplitude of A2B2

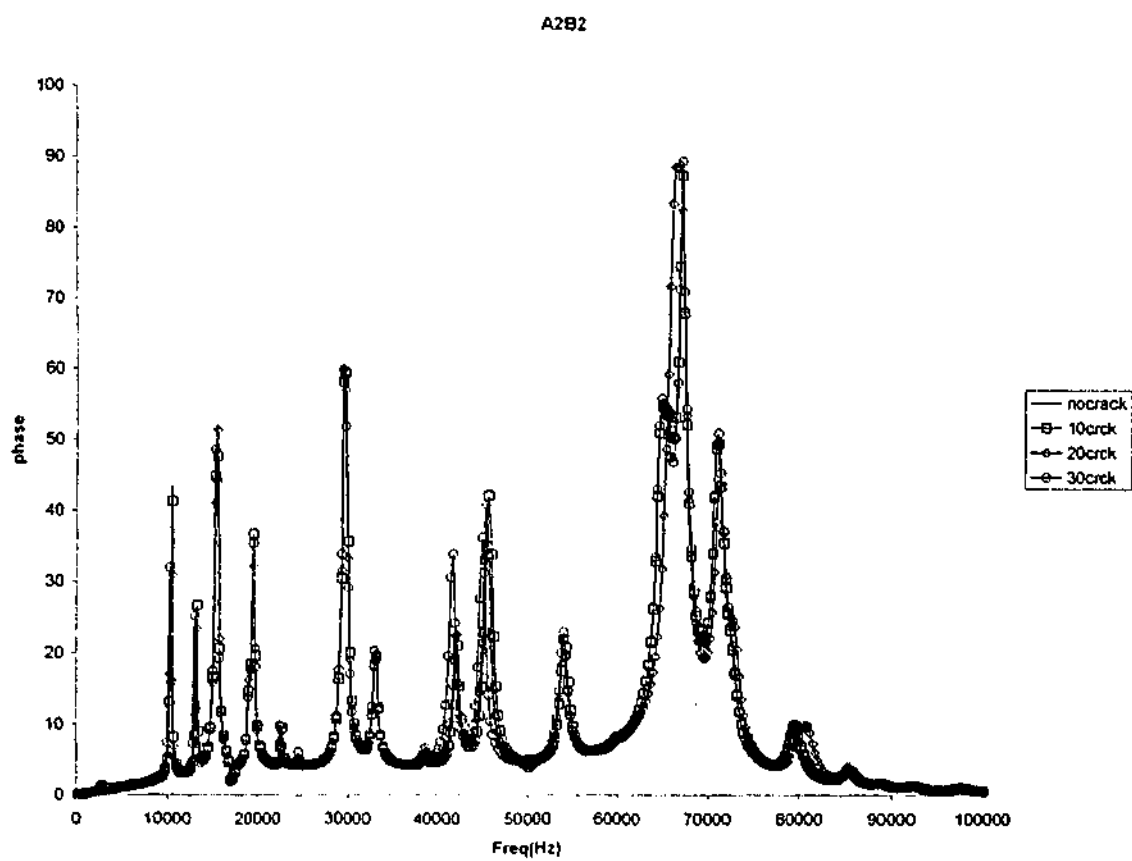


Figure 4.5b TF Phase Angle of A2B2

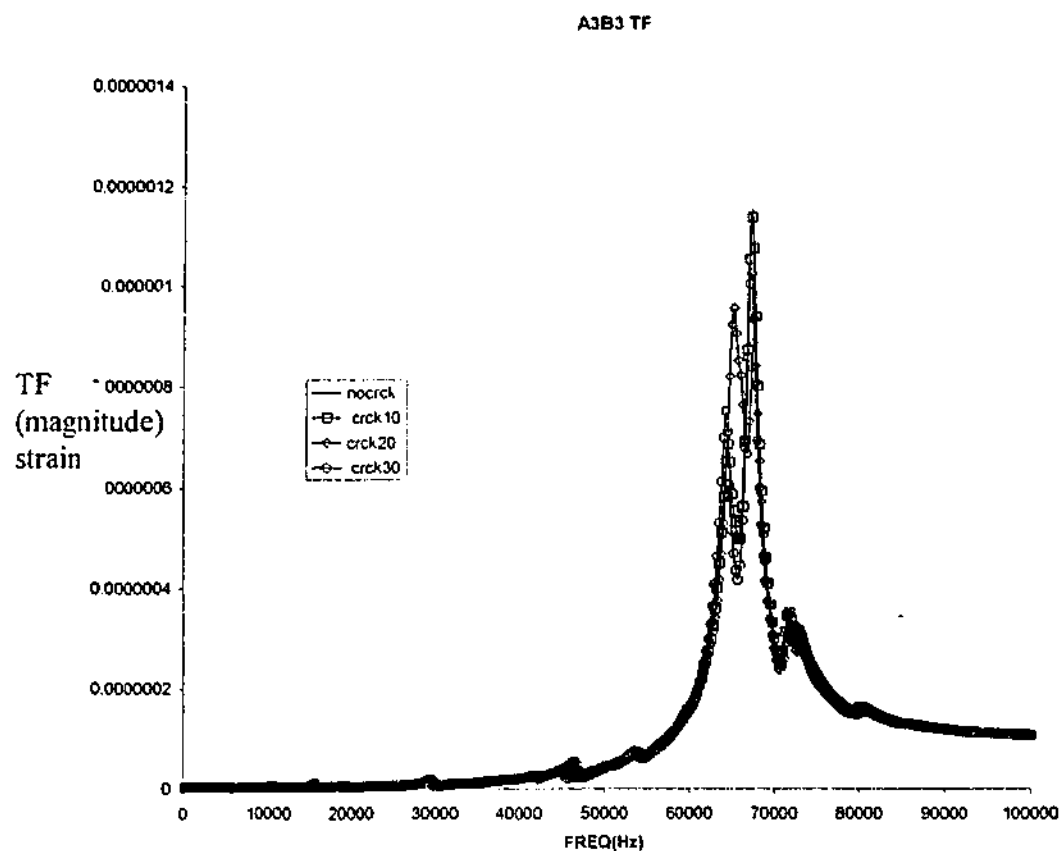


Figure 4.6a. TF Amplitude of A3B3

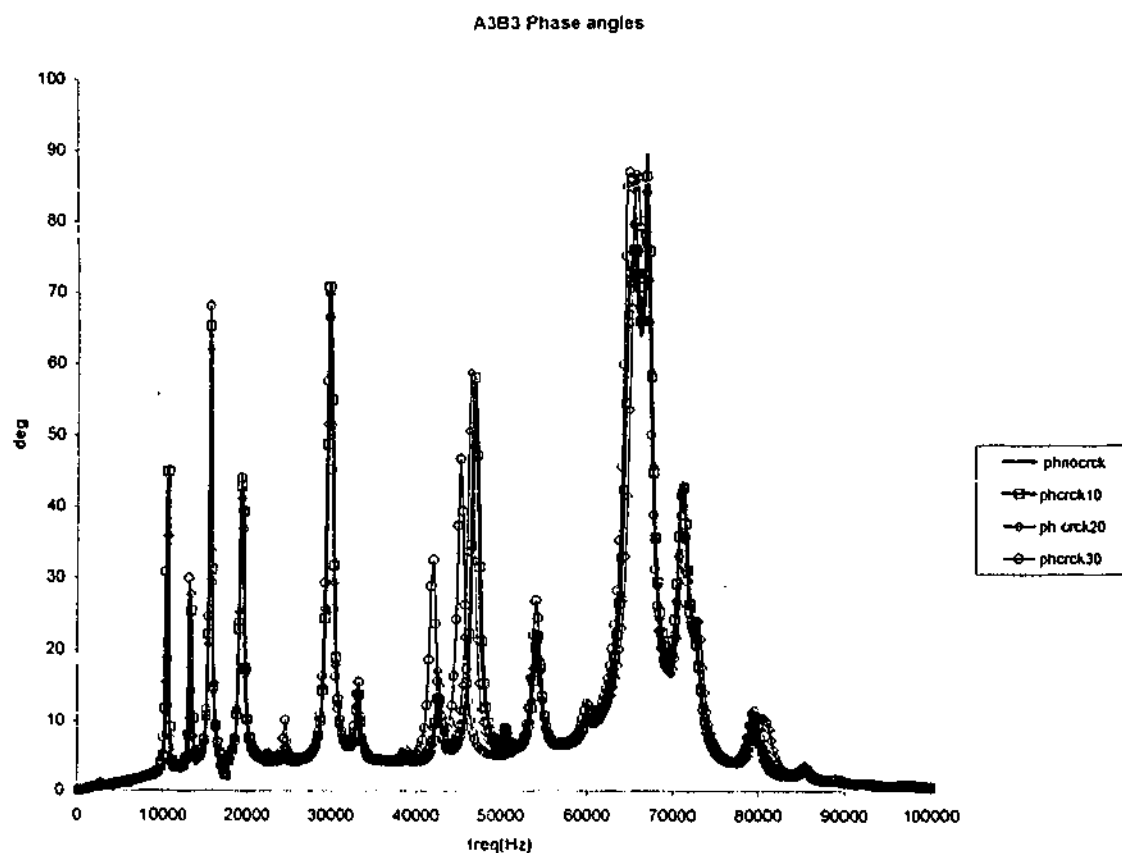


Figure 4.6b TF Phase Angle of A3B3

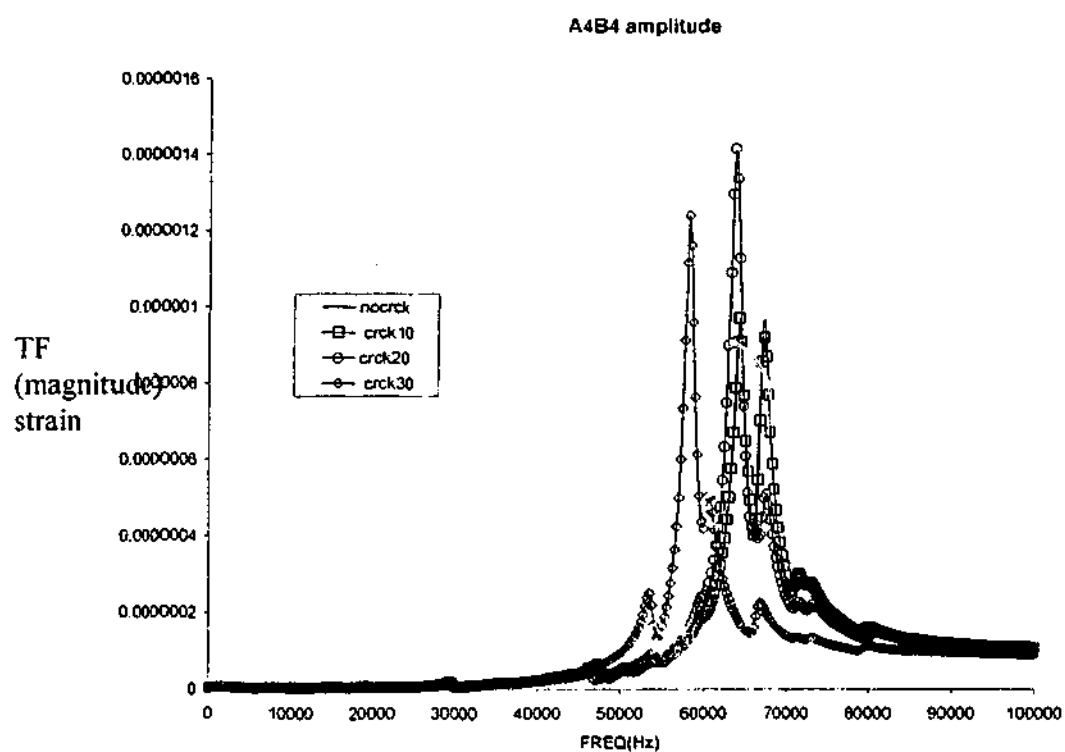


Figure 4.7a. TF Amplitude of A4B4

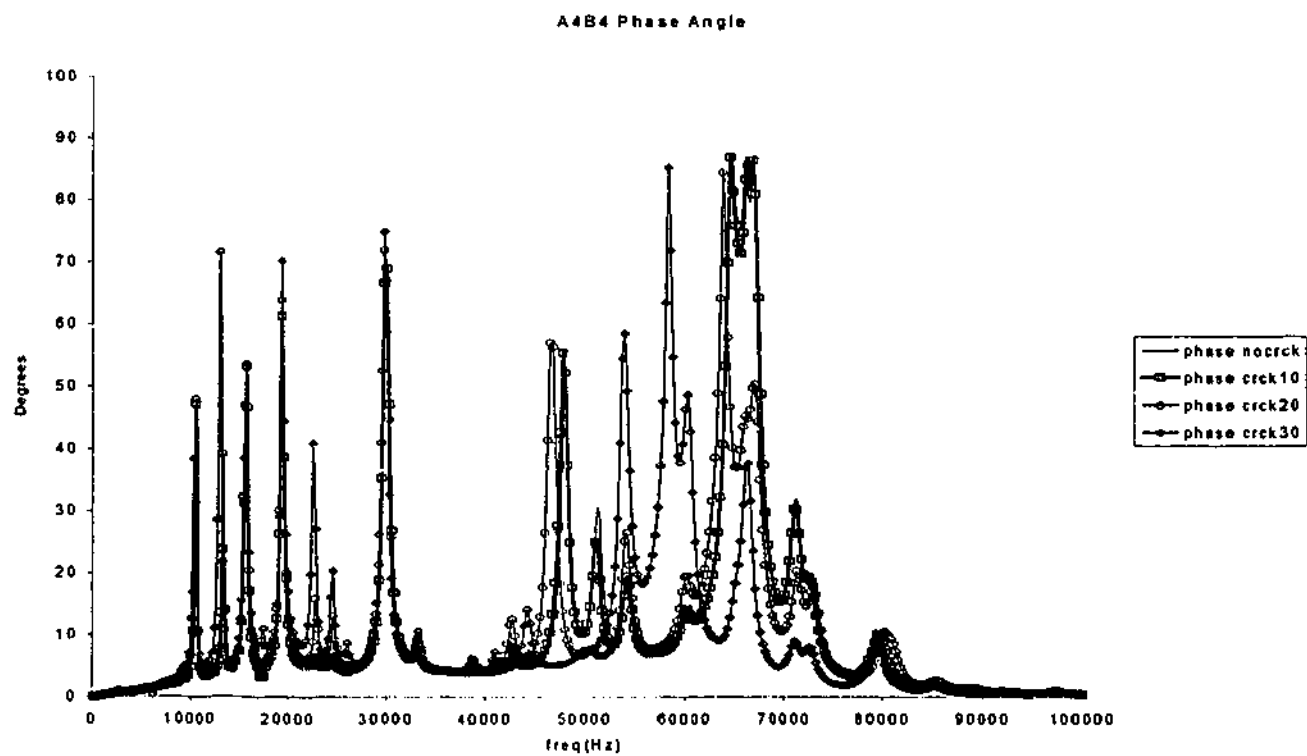


Figure 4.7b. TF Phase Angle of A4B4

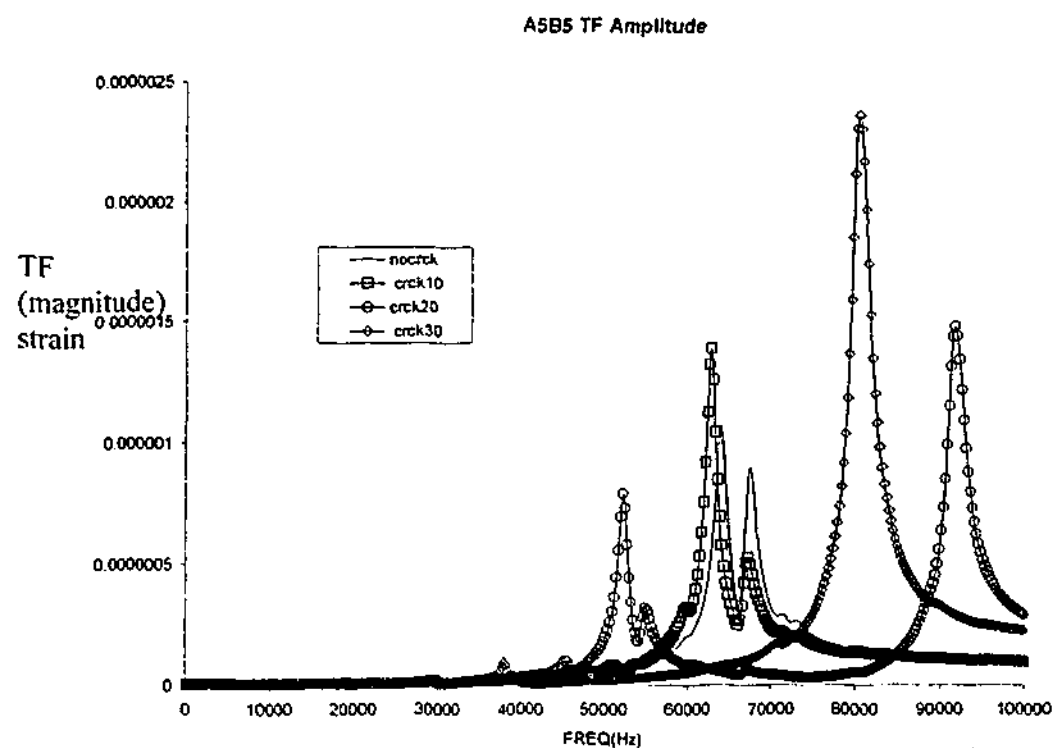


Figure 4.8a. TF Amplitude of A5B5

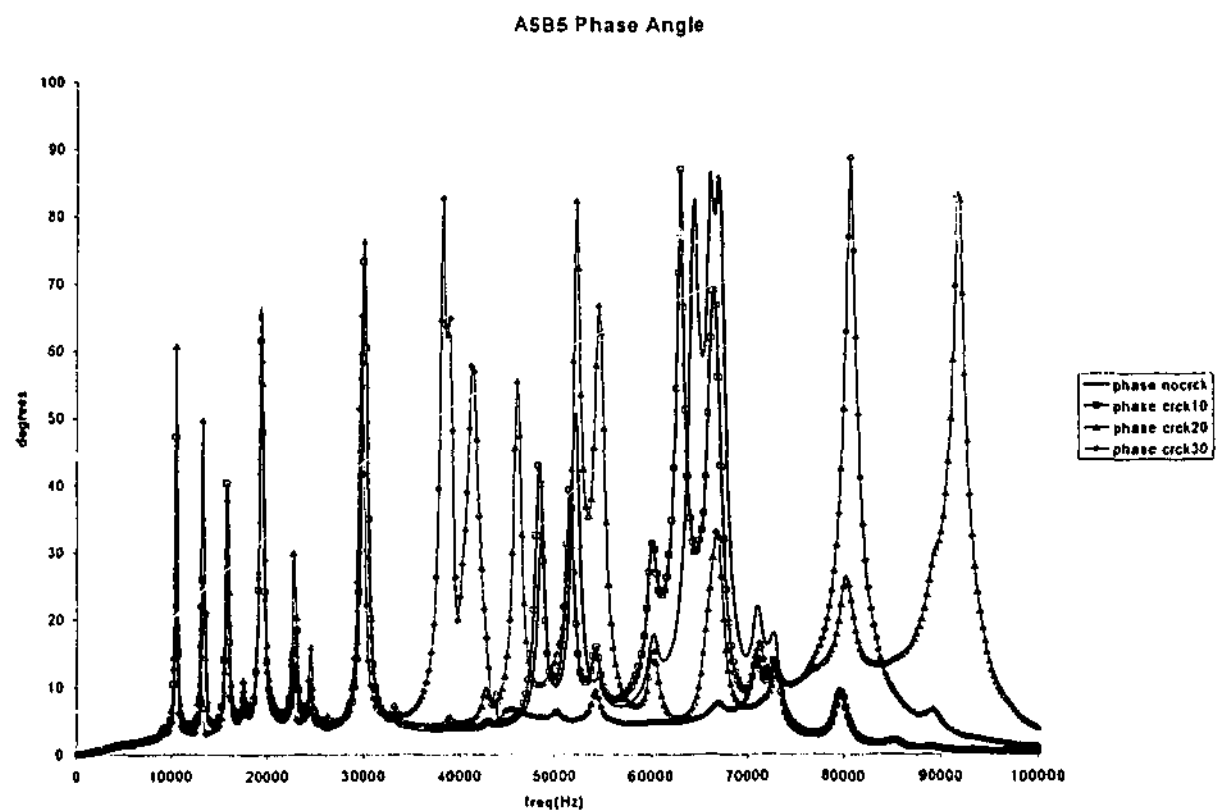


Figure 4.8b. TF Phase Angle of A5B5

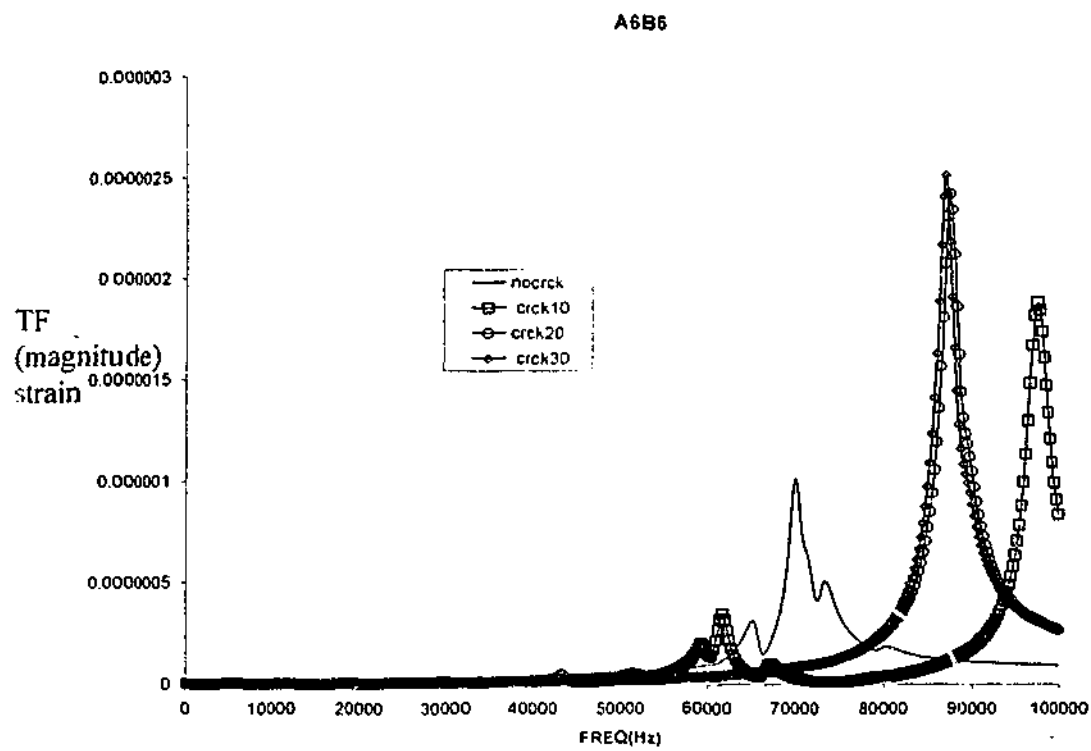


Figure 4.9a. TF Amplitude of A6B6

Figure 10 : A6B6 Phase Angle

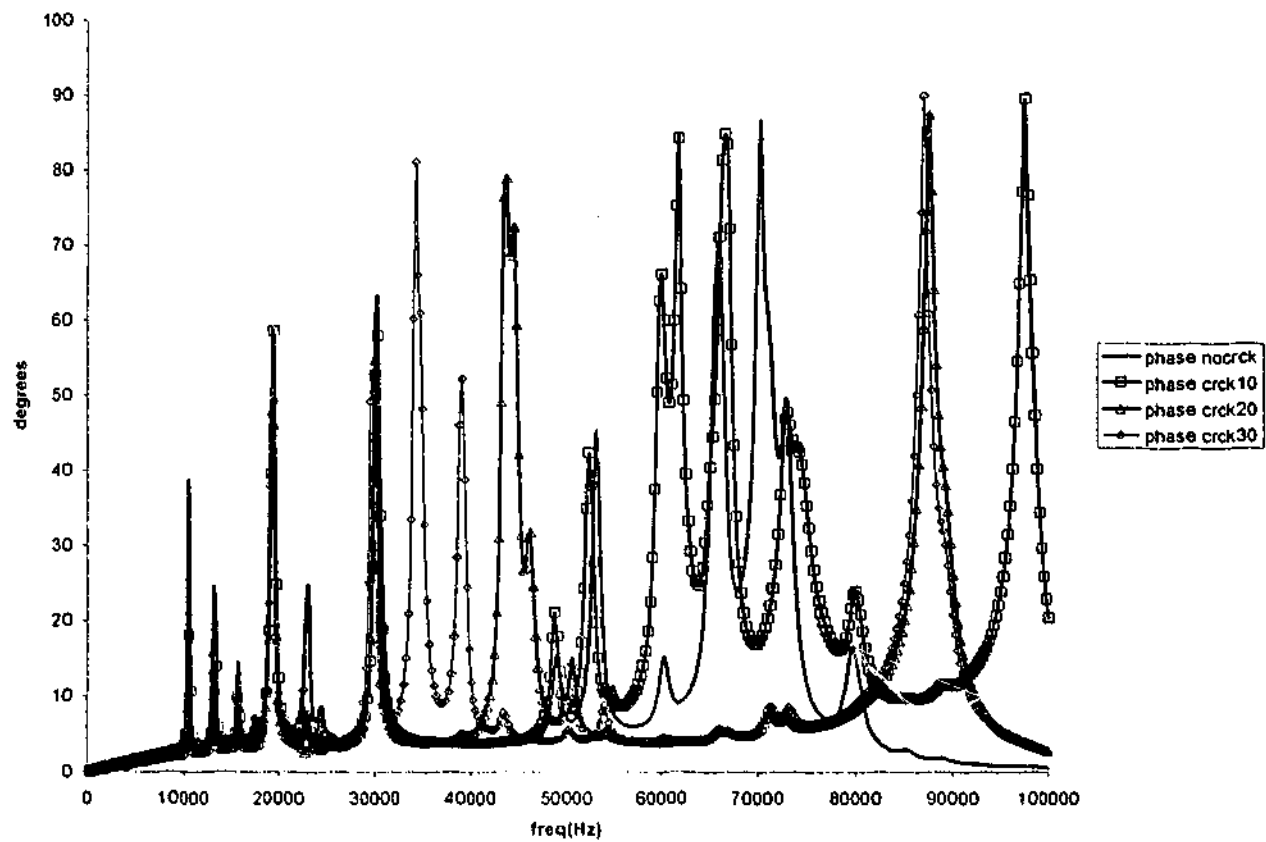


Figure 4.9b. TF Phase Angle of A6B6

Analysis of the TF of BnCn Pairs

The amplitudes and phase angles of the TF for the pair B1C1 that are under all damage conditions are presented in Figure 4.10a and 4.10b respectively. Since this pair is far away from the crack there is no shift occurring for every condition of the damage. The similarity of the TF results for every damage condition appears also on pairs B2C2 and B3C3 in Figure 4.11a&b and 4.12a&b. These indicate that the crack is still located relatively far away from these B2C2 and B3C3 pairs.

The TF for the pair B4C4 that are presented in Figure 4.12a and 4.12b do not change much for all damage conditions except for the 30mm crack case. Here, with the peak response shifting occurs from the frequency region between approximately 60 kHz and 65 kHz to 55 kHz and 60 kHz. This situation shows that the pair B4C4 is less sensitive than the pair A4B4 where the shift began at 20mm crack.

In Figure 4.13a and 4.13b, the TF for the pair B5C5 showed that at the 20mm crack the TF began to change. This situation shows also that this pair B5C5 is less sensitive than the pair A5B5. Interestingly the shift moved to the higher frequency region from the frequency region between approximately 70kHz to 72 kHz. At the 30mm crack the shift again moved to the higher frequency from the frequency region 65KHz to 67 kHz and 72 kHz to 75Khz. This different behaviour of the modal response may due to the fact that the crack has grown large and passed the fifth column of the sensor-actuator pair (i.e. B5C5). When the crack has developed past B5C5, (see Figure 4.1b), the local dynamics of the plate may have changed due to a change in the boundary condition. In this situation, the region ahead of B5C5 where the crack is located is now stress free.

Figure 4.15a and 4.15b show the results obtained for the sensor-actuator pair B6C6. These results show the peaks of the three damage conditions i.e. 10mm, 20mm, 30mm move to the same higher frequency region from between approximately 75KHz and 78KHz to 80KHz and 90KHz. This situation is similar to the pair B5C5 where the crack has grown large and passed the sixth column of sensor-actuator pairs.

Summary for BnCn pairs TF results

The overall finding of this section is similar to that obtained from the sensor-actuator pairs of AnBn. It appears that the BnCn pair can also be used to detect the presence of the crack. This appears to address the question posed earlier in this chapter. The responses of the TF obtained for the BnCn are quite different from the AnBn pairs. Whilst the "resonant" frequency for the AnBn pairs was reported to decrease with increasing damage size due to a reduction in the system stiffness between A and B, the "resonant" frequency of the BnCn pairs was found to increase with increasing damage sizes. The difference in the TF response allows one to infer that the crack must be located between rows A and B.

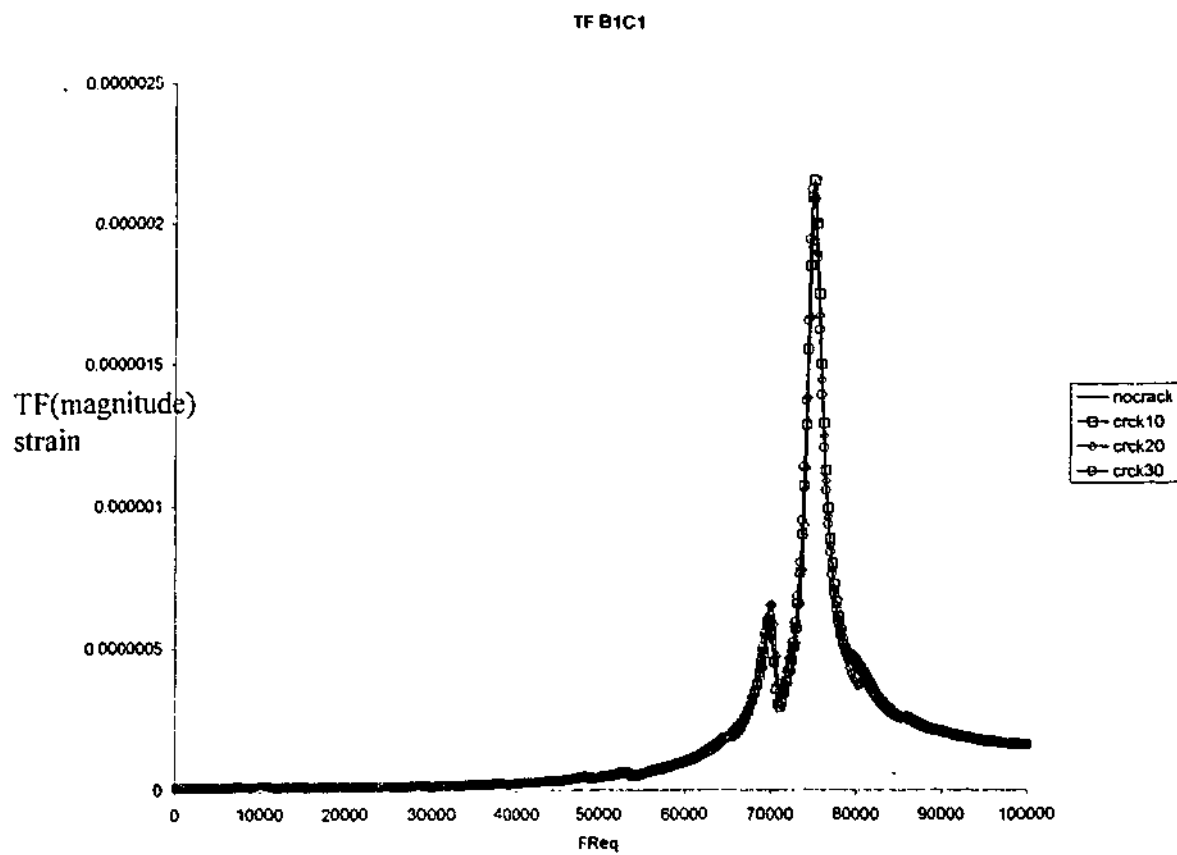


Figure 4.10a. TF Amplitude of B1C1

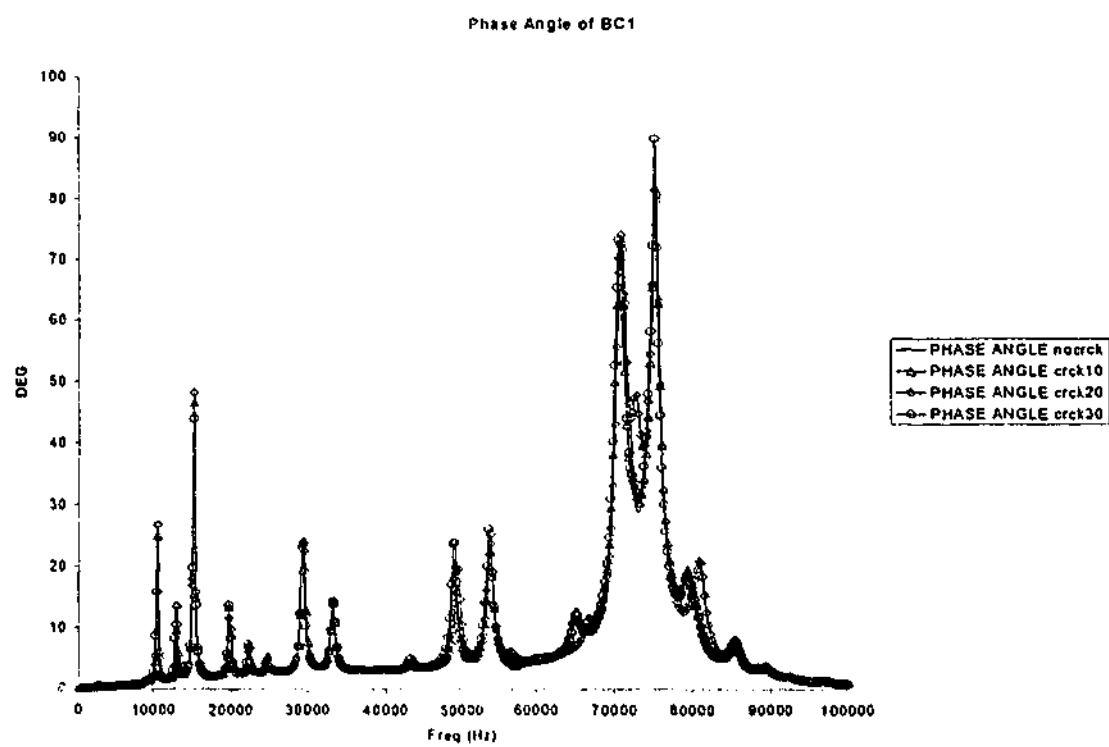


Figure 4.10b. TF Phase Angle of B1C1

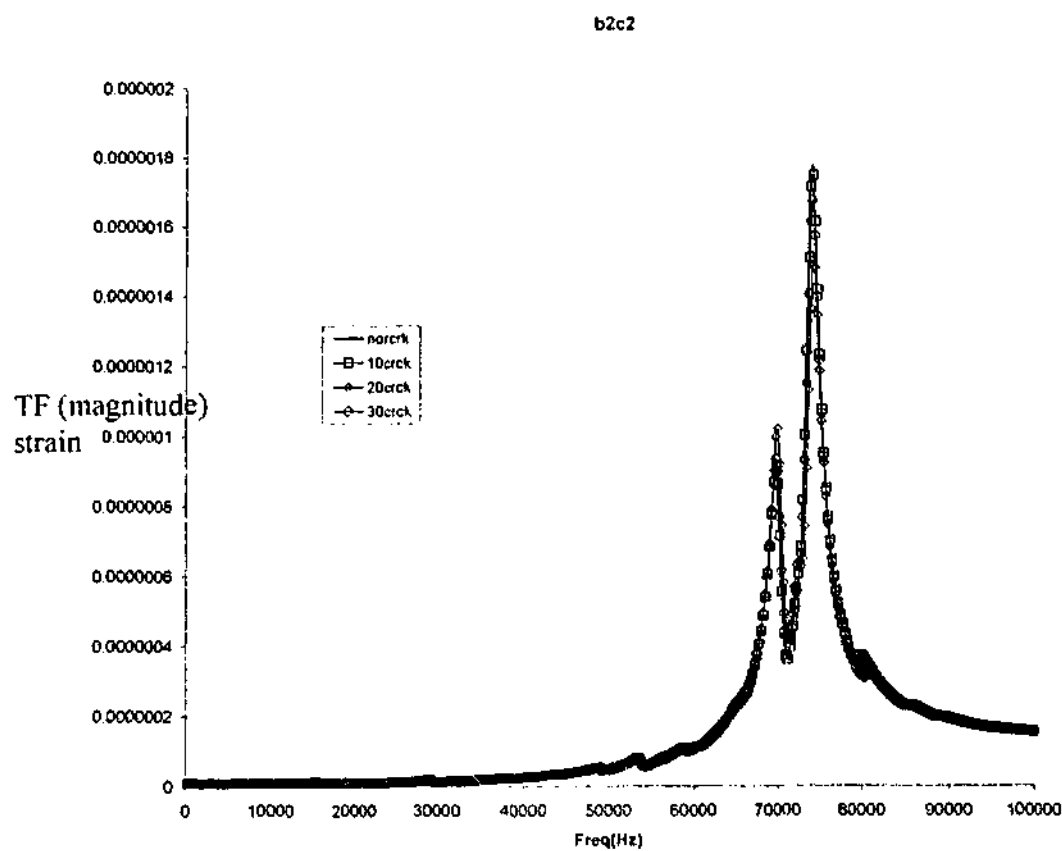


Figure 4.11a. TF Amplitude of B2C2

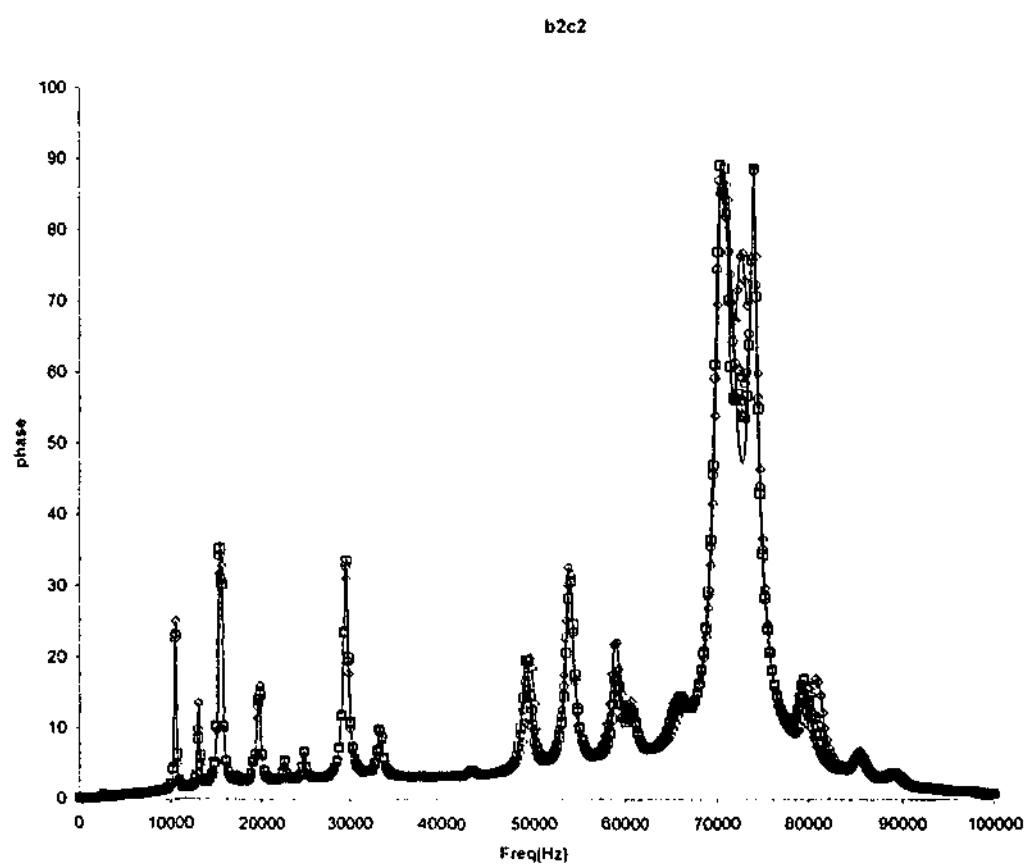


Figure 4.11b. TF Phase Angle of B2C2

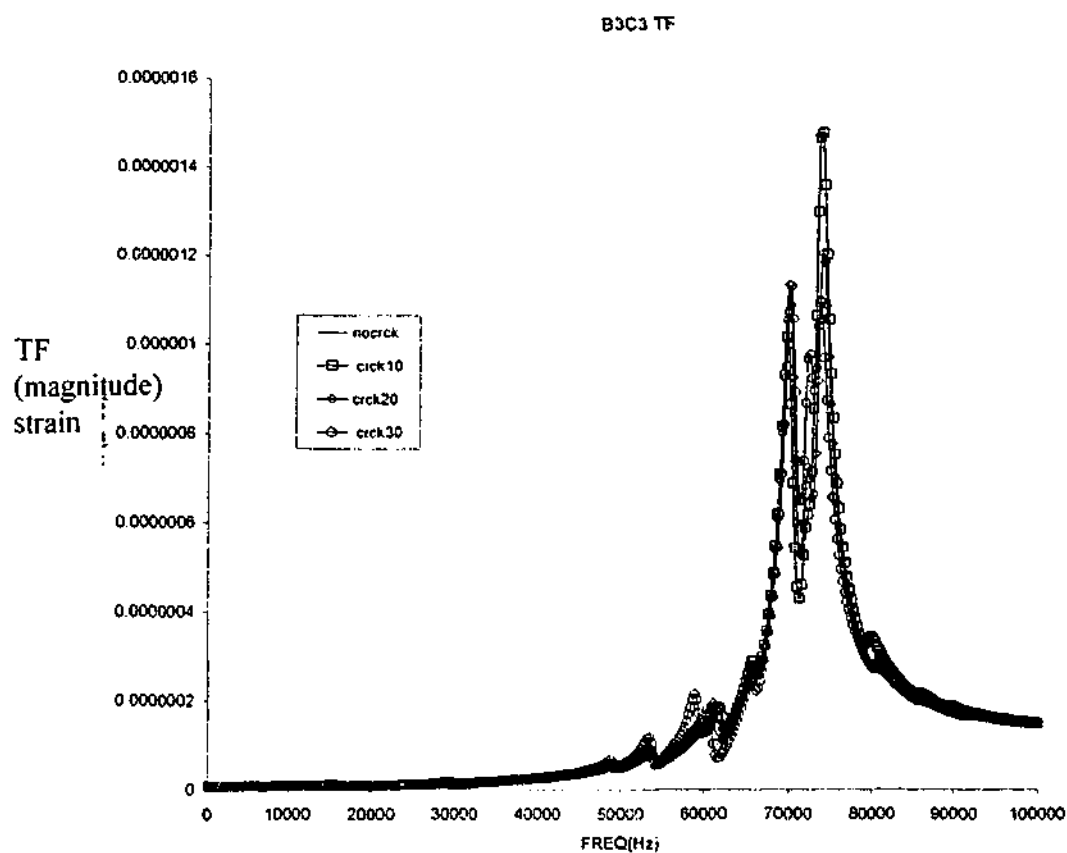


Figure 4.12a. TF Amplitude of B3C3

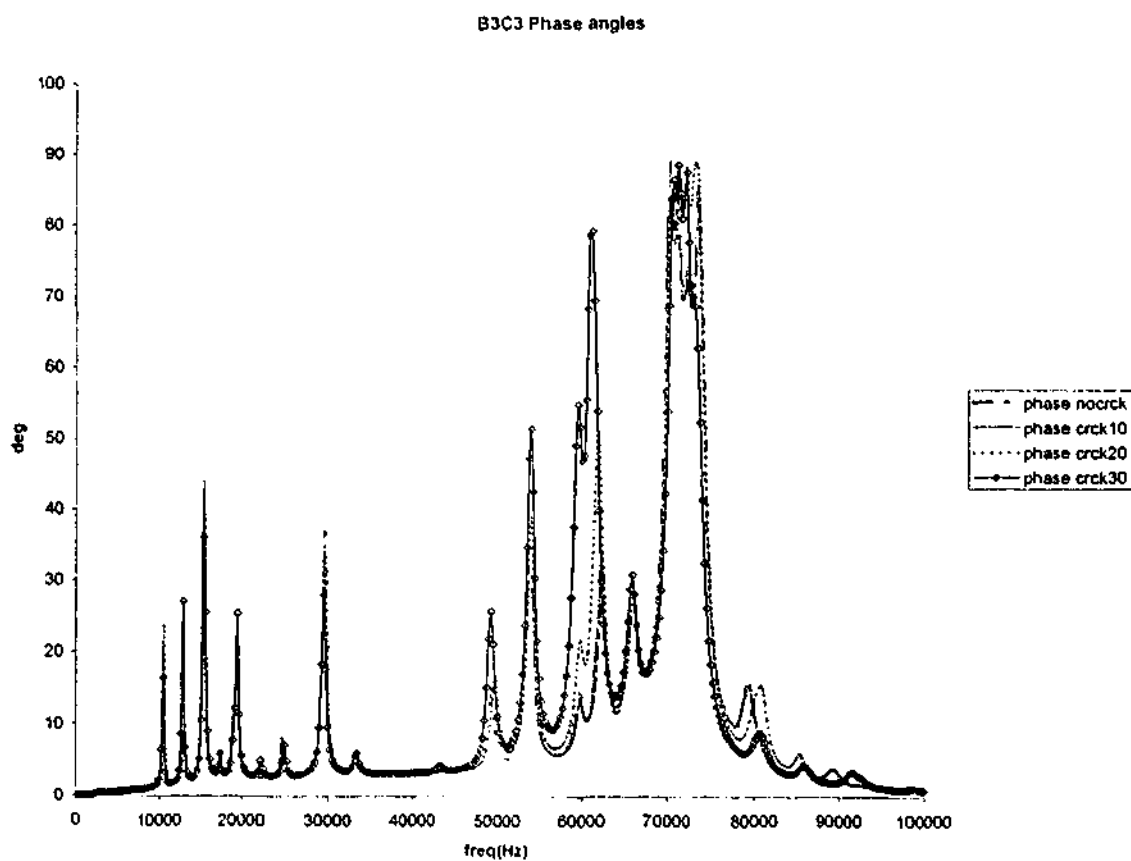


Figure 4.12b. TF Phase Angle of B3C3

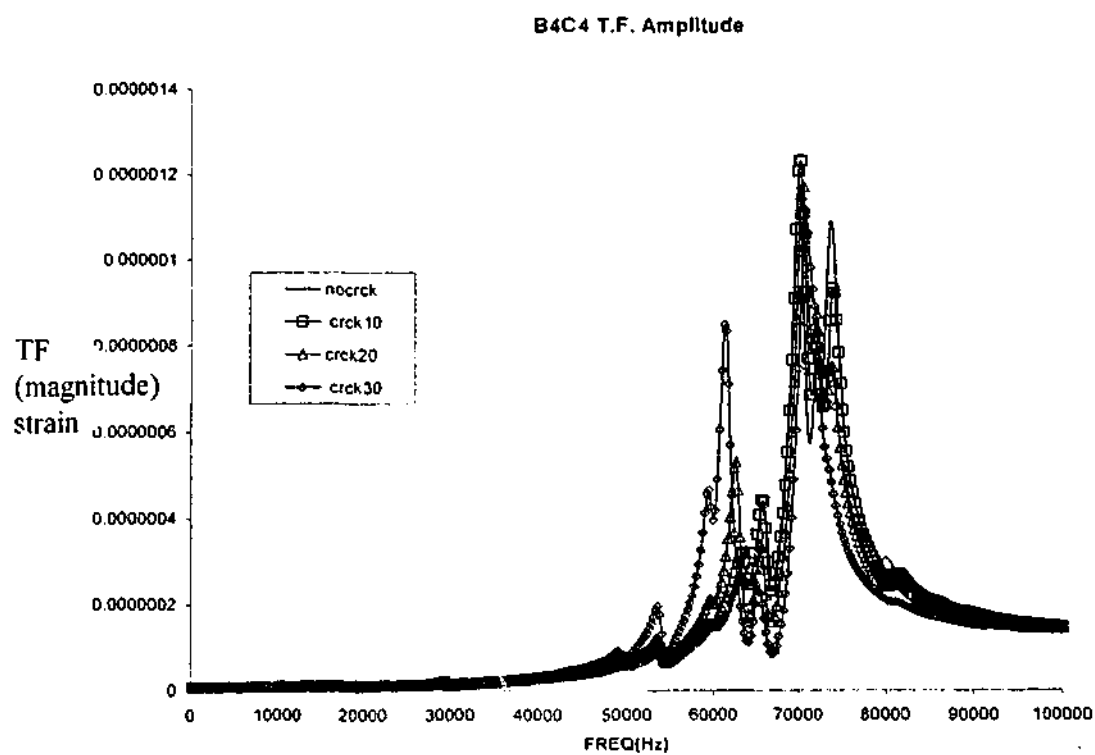


Figure 4.13a. TF Amplitude of B4C4

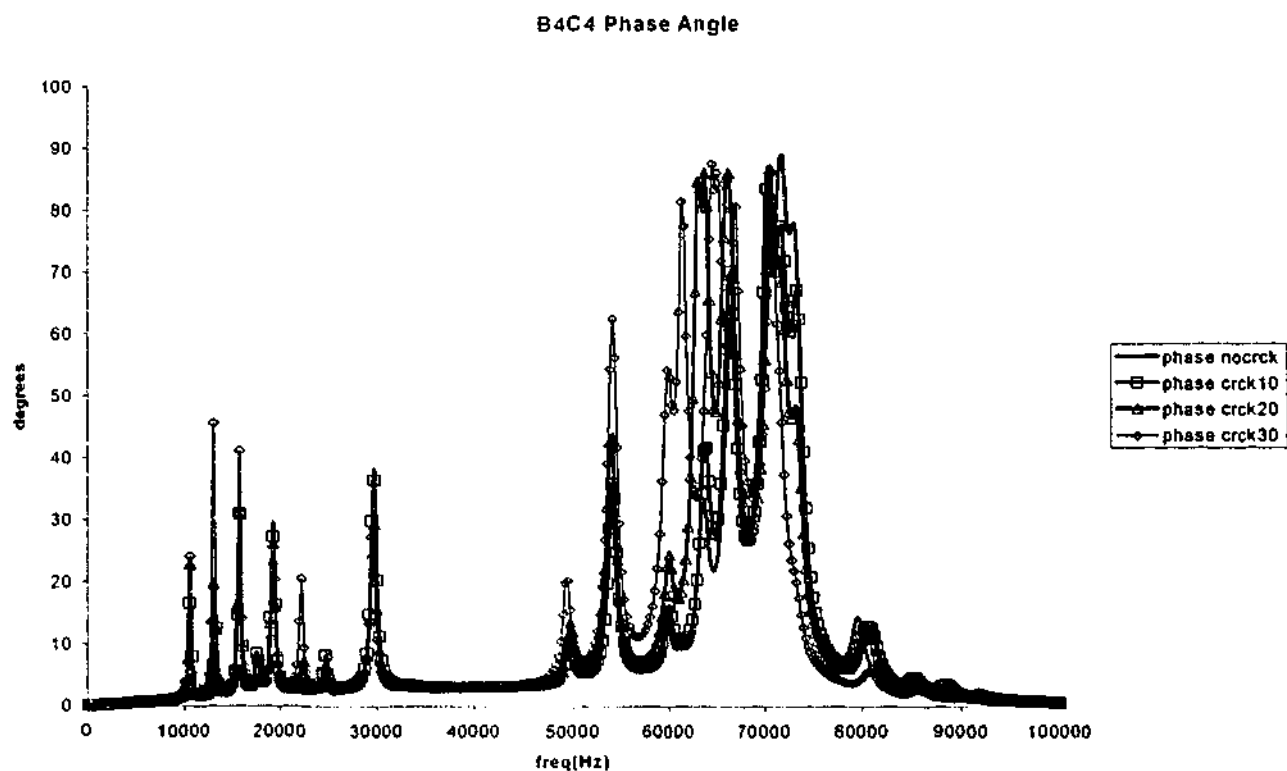


Figure 4.13b. TF Phase Angle of B4C4

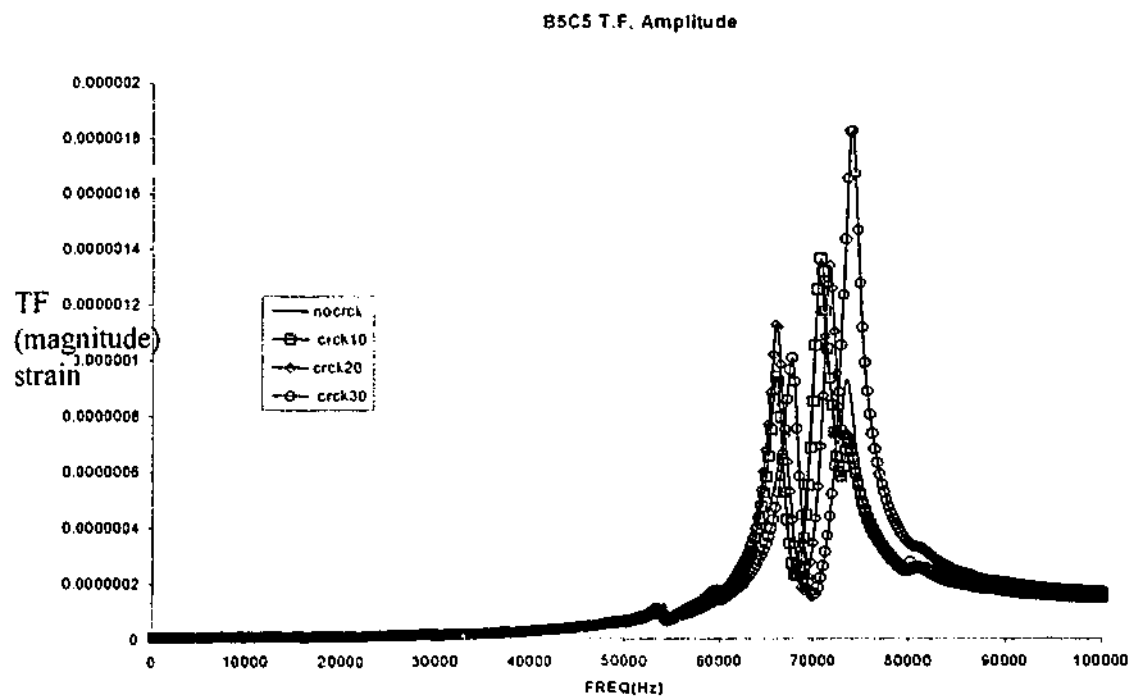


Figure 4.14a. TF Amplitude of B5C5

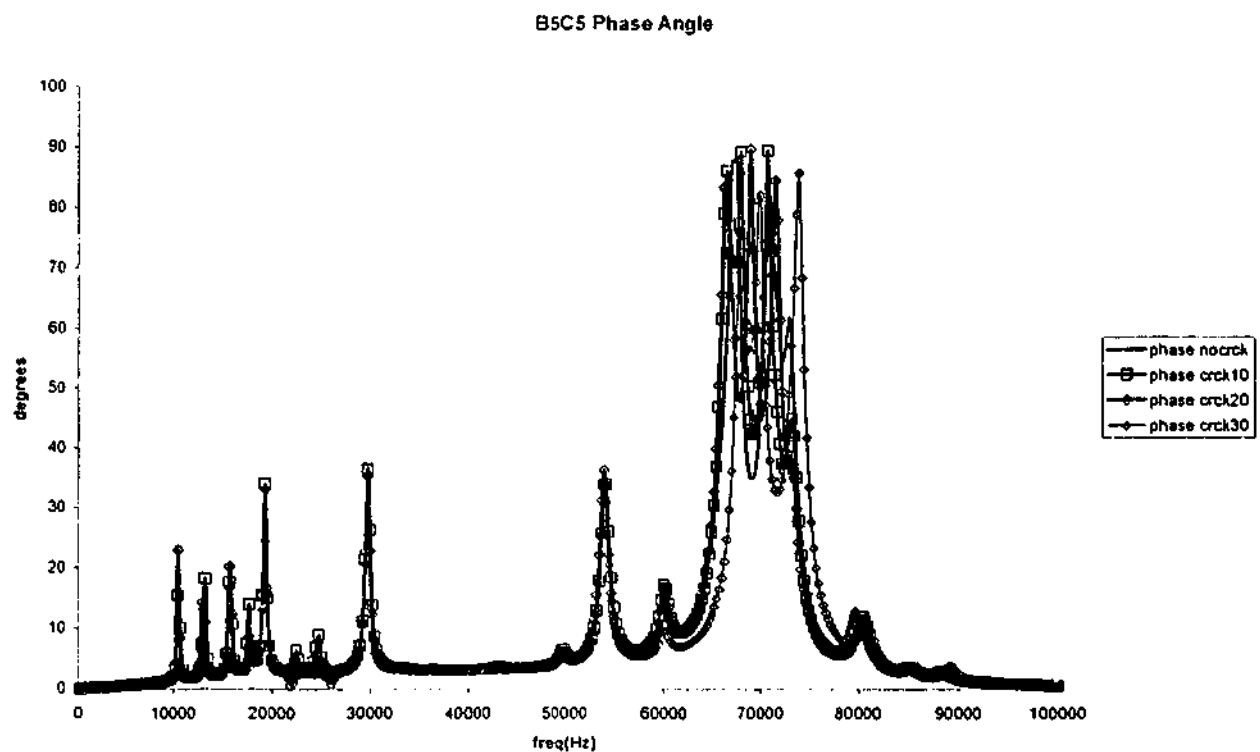


Figure 4.14b. TF Phase Angle of B5C5

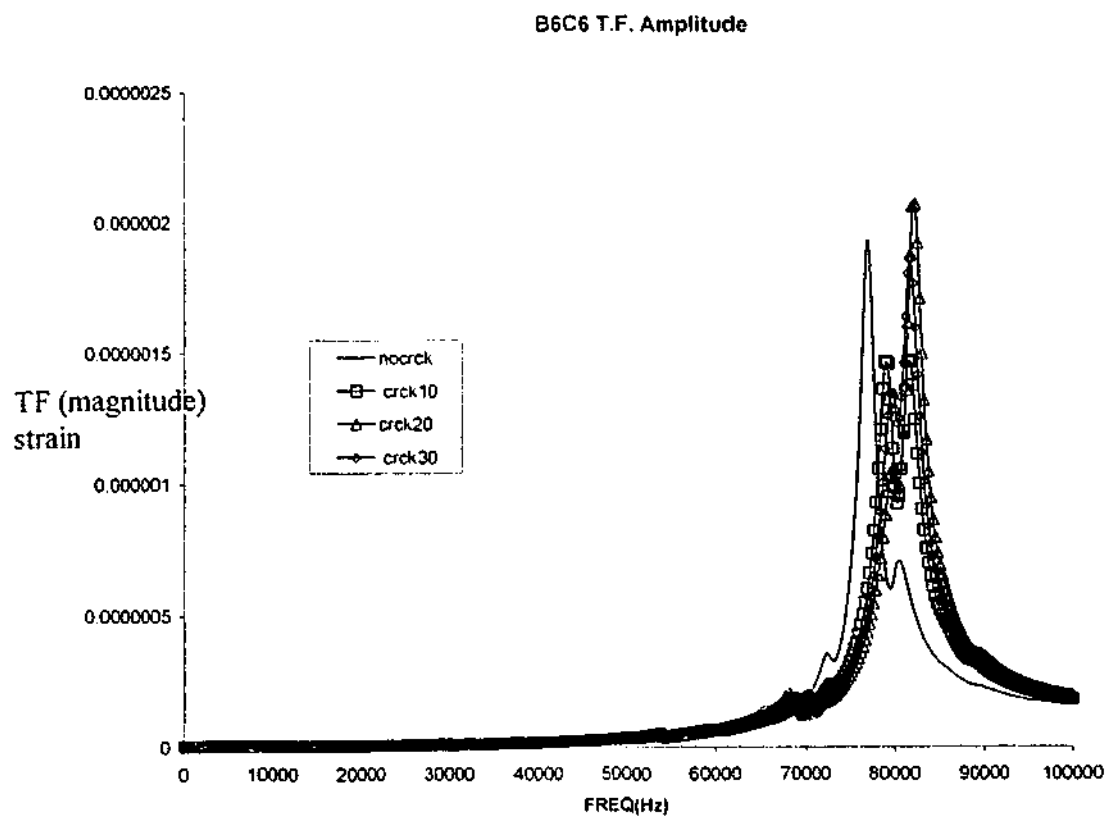


Figure 4.15a. TF Amplitude of B6C6

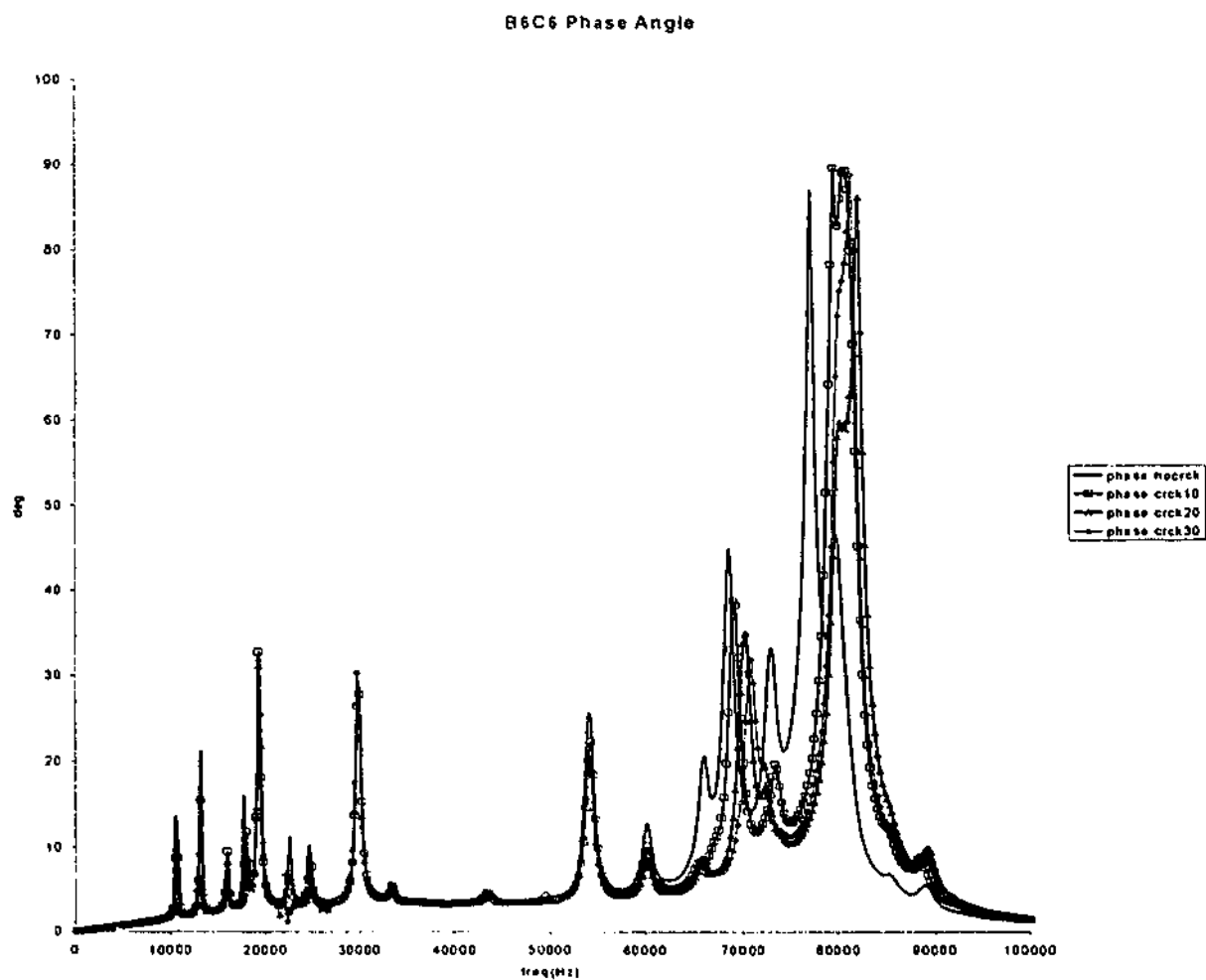


Figure 4.15b. TF Phase Angle of B6C6

Analysis of the TF of Cross-Pair A_nB_{n+1}

The amplitudes and phase angles of the TF for the pair A1B2 that are under all damage conditions including the no damage condition are presented in Figure 4.16a and 4.16b respectively. Since this pair is far away from the crack there is no shift occurring for every condition of the damage. Similar TF results for every damage condition appears also on pairs A2B3 and A3B4 in Figure 4.17a&b and 4.18a&b. These indicate that the crack is still located relatively far away from these A2B3 and A3B4 pairs.

The TF for the sensor-actuator pair A4B5 that are presented in Figure 4.19a and 4.19b show at the 30mm crack a shift occurred from the frequency region approximately 88 kHz to 86 kHz. The shift occurrence at this 30mm crack indicates that the crack tip is approximately located between this A4B5 pair (see Figure 4.1b). In Figure 4.20a and 4.20b, the TF for the pair A5B6 shows that at the 20mm crack a distinct shift of the peak occurs from the frequency region approximately 95 kHz to 88 kHz. At the 30mm crack the shift is more distinct from the frequency region approximately 88kHz to 84 kHz.

Summary for Cross-pair A_nB_{n+1} TF results

The results from this cross-pair showed the 30mm crack tip could be approximately located by looking at the shift, which occurred first on pair A4B5. However, in case of early damage (10mm crack), the A5B6 pair is not be able to detect the shift. This may be due to the change of local stiffness between this pair has not been detected by this pair. The detection of the shift at 20mm crack by the A5B6 but not by the A4B5 pair indicates that the 20mm crack tip is approximately located in front of A5B6 pair and has not passed this pair.

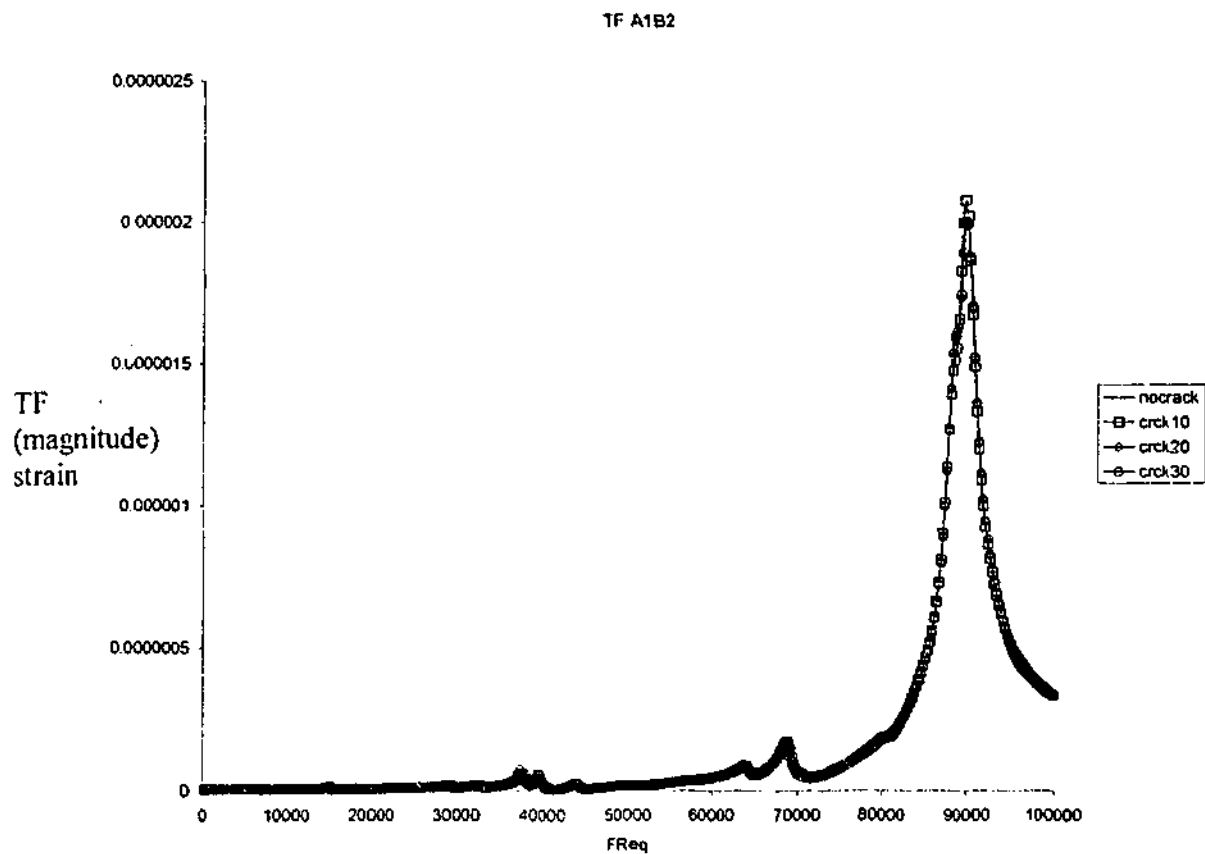


Figure 4.16a. TF Amplitude of A1B2

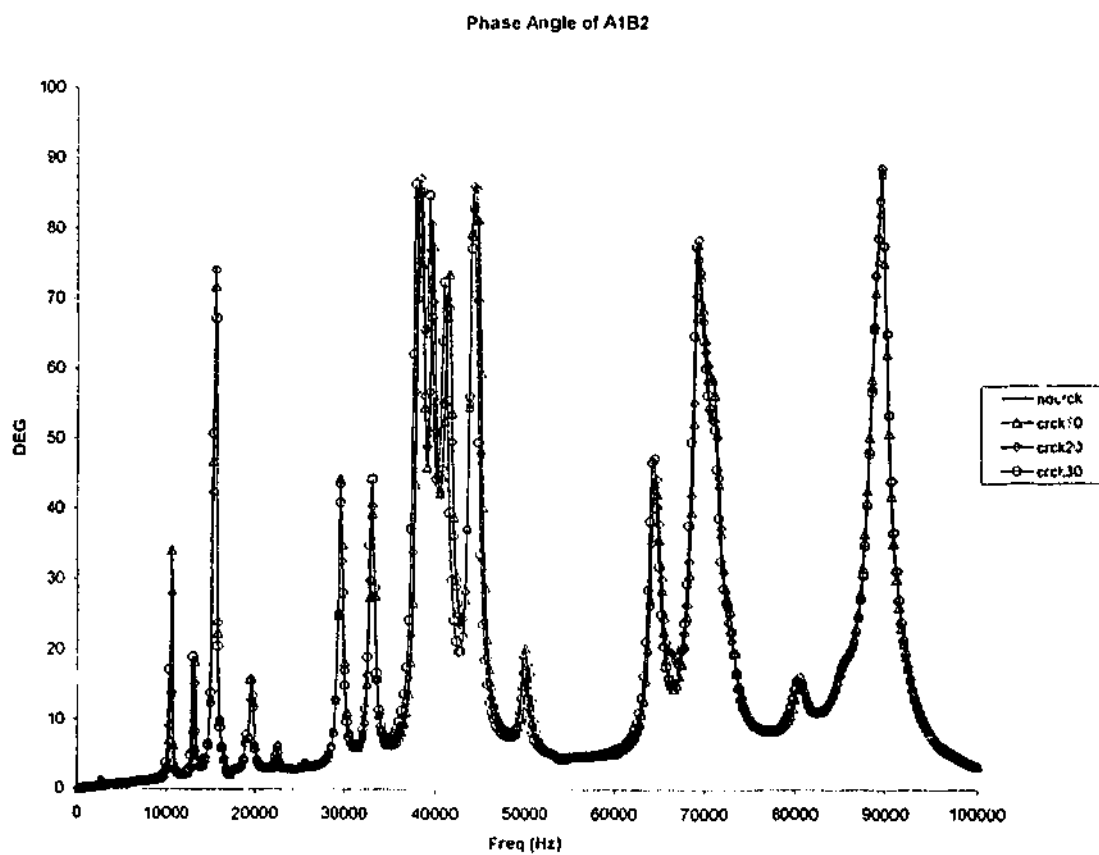


Figure 4.16b. TF Phase Angle of A1B2

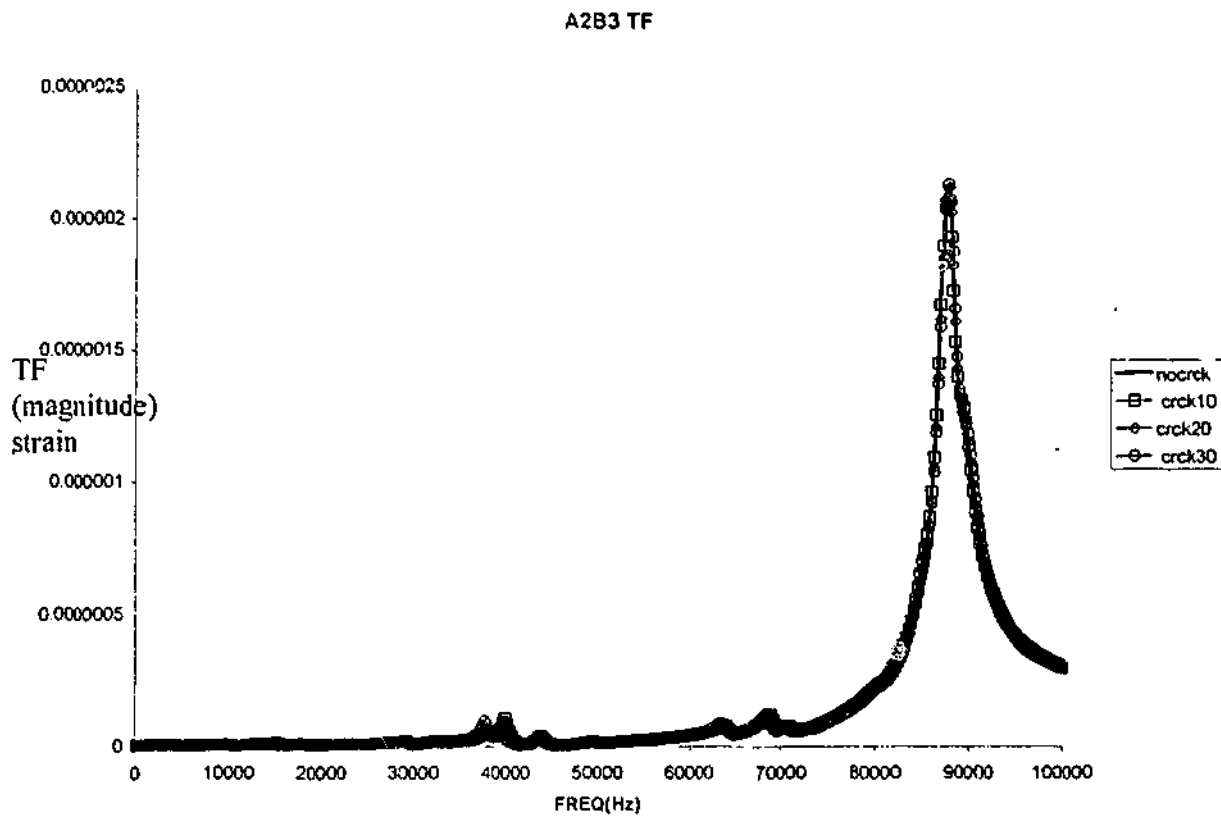


Figure 4.17a. TF Amplitude of A2B3

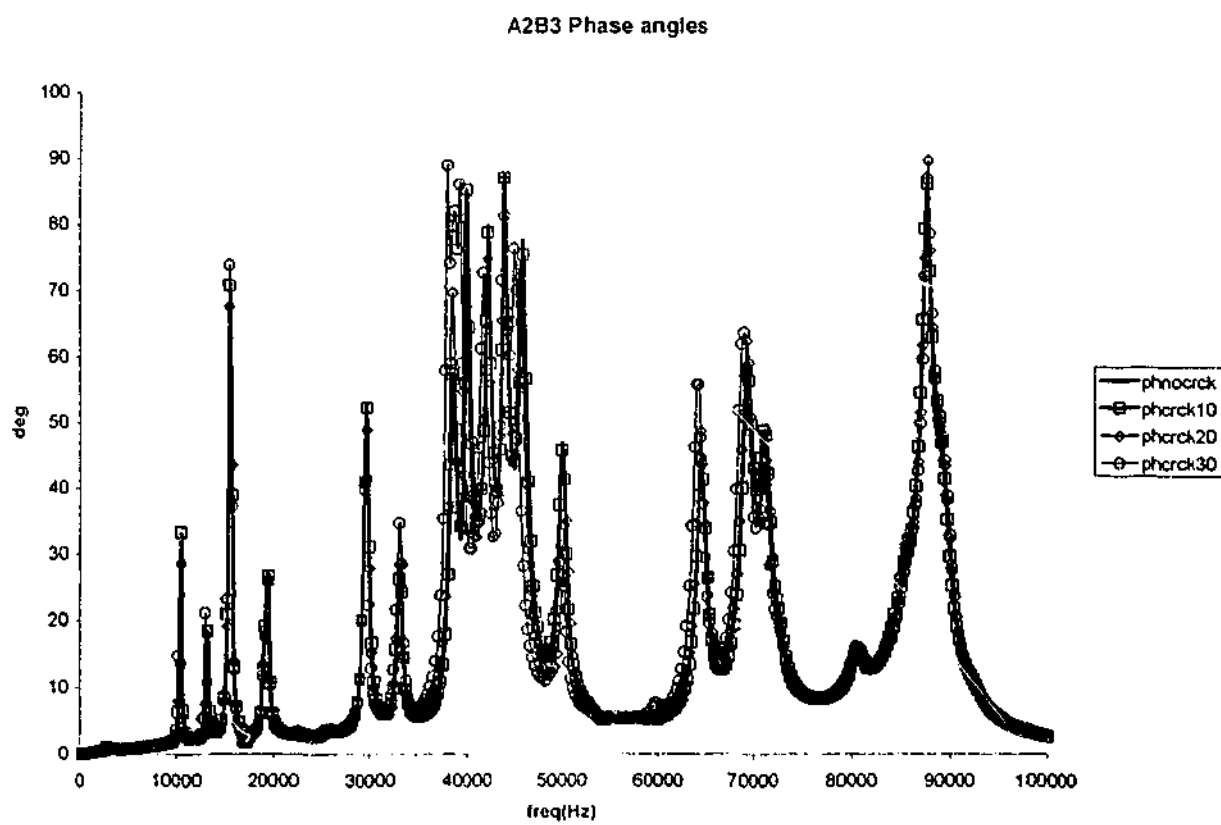


Figure 4.17b. TF Phase Angle of A2B3

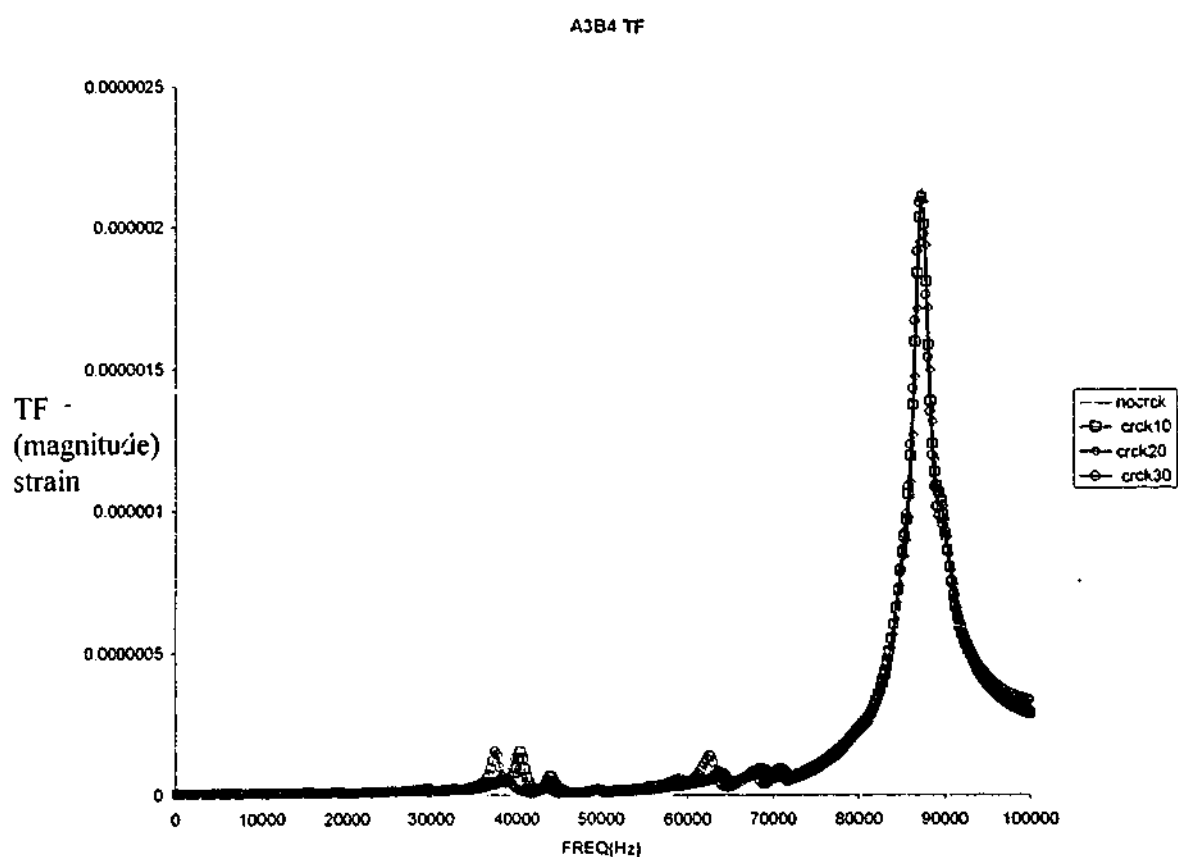


Figure 4.18a. TF Amplitude of A3B4

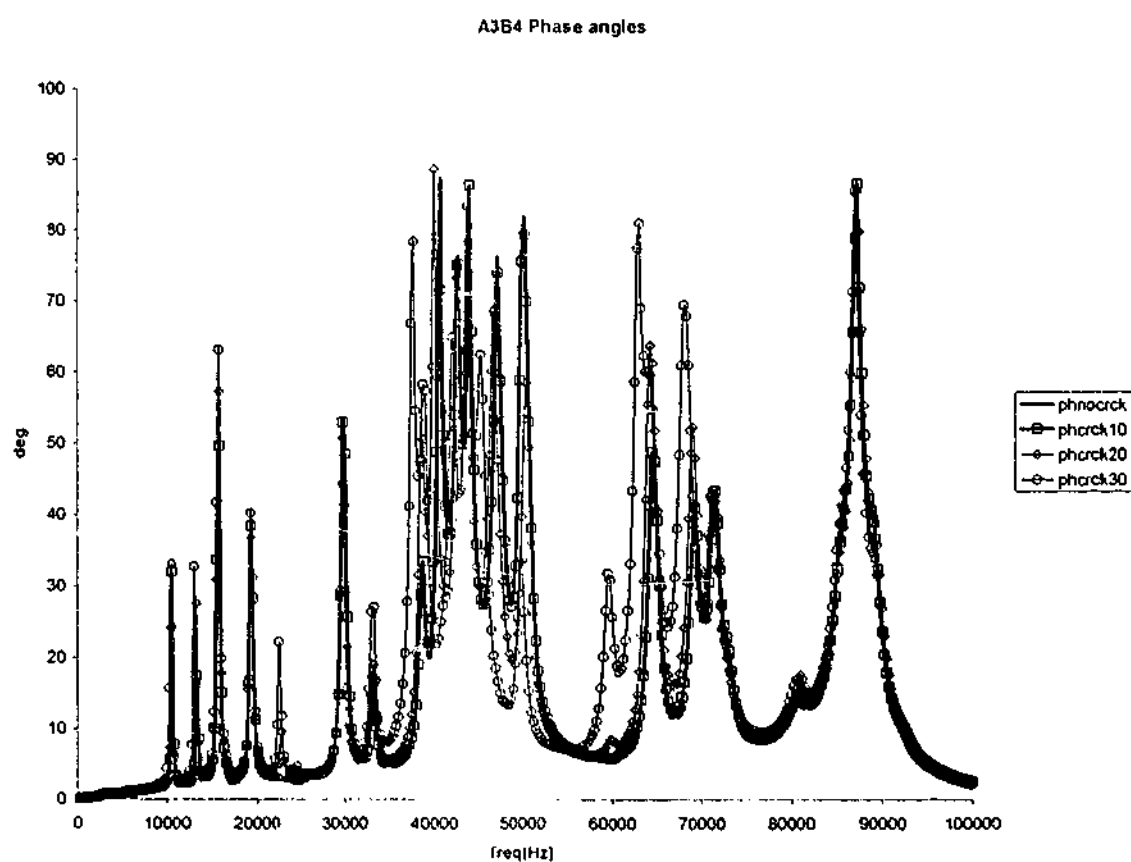


Figure 4.18b. TF Phase Angle of A3B4

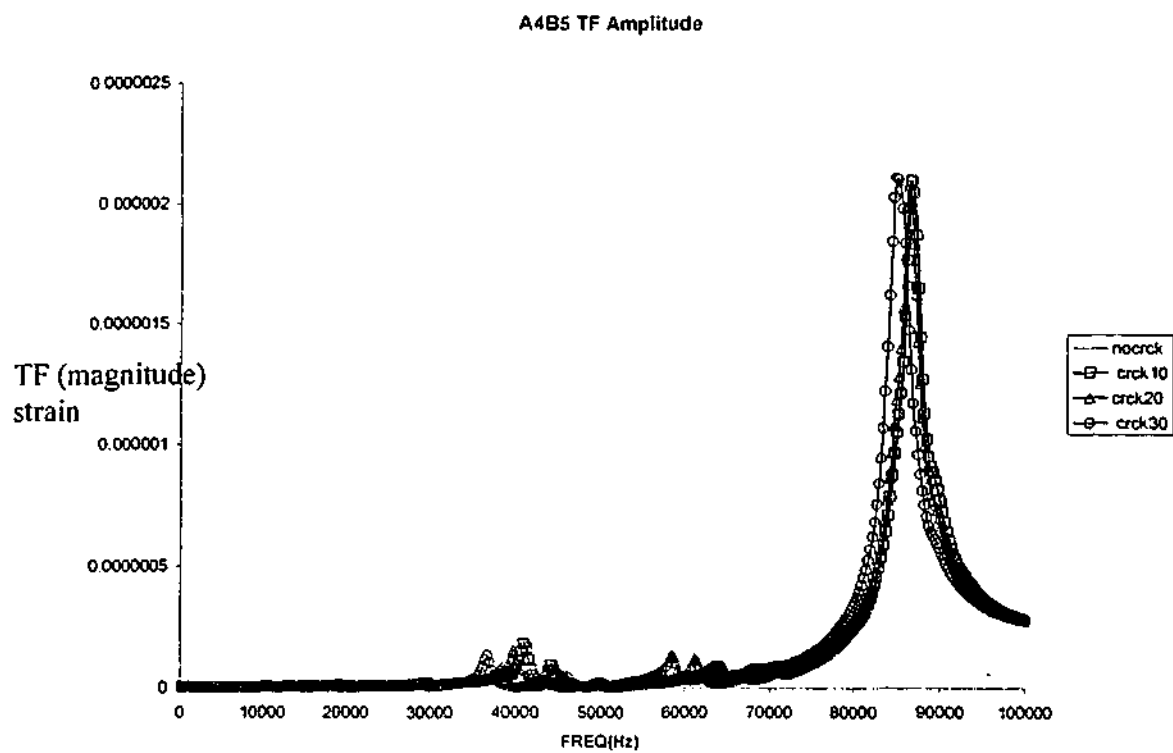


Figure 4.19a. TF Amplitude of A4B5

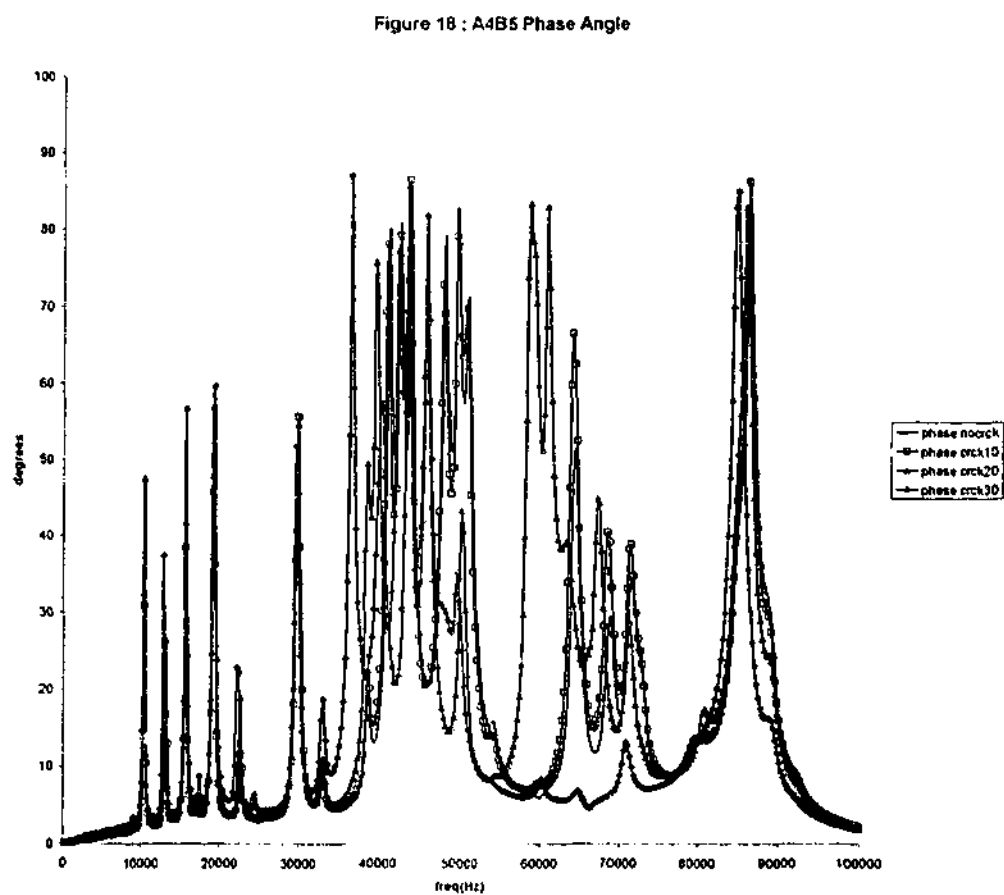


Figure 4.19b. TF Phase Angle of A4B5

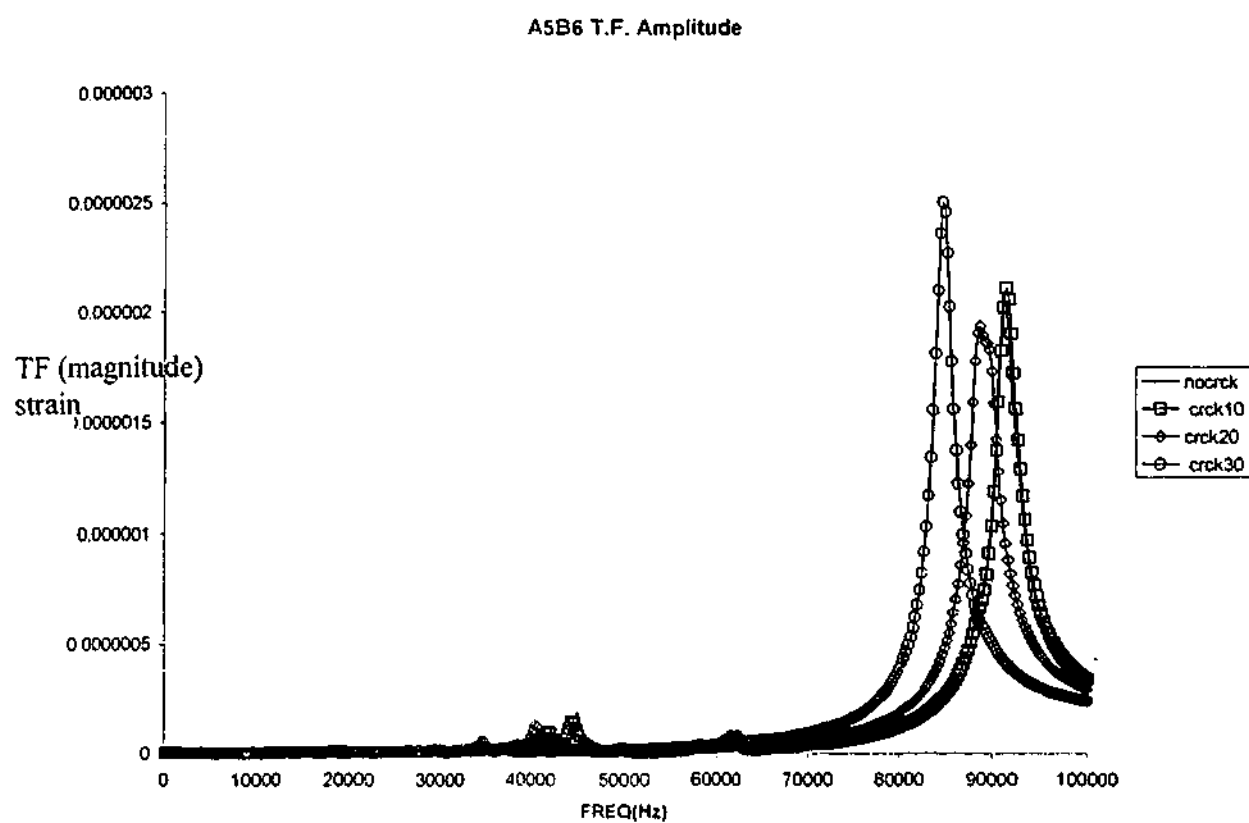


Figure 4.20a. TF Amplitude of A5B6

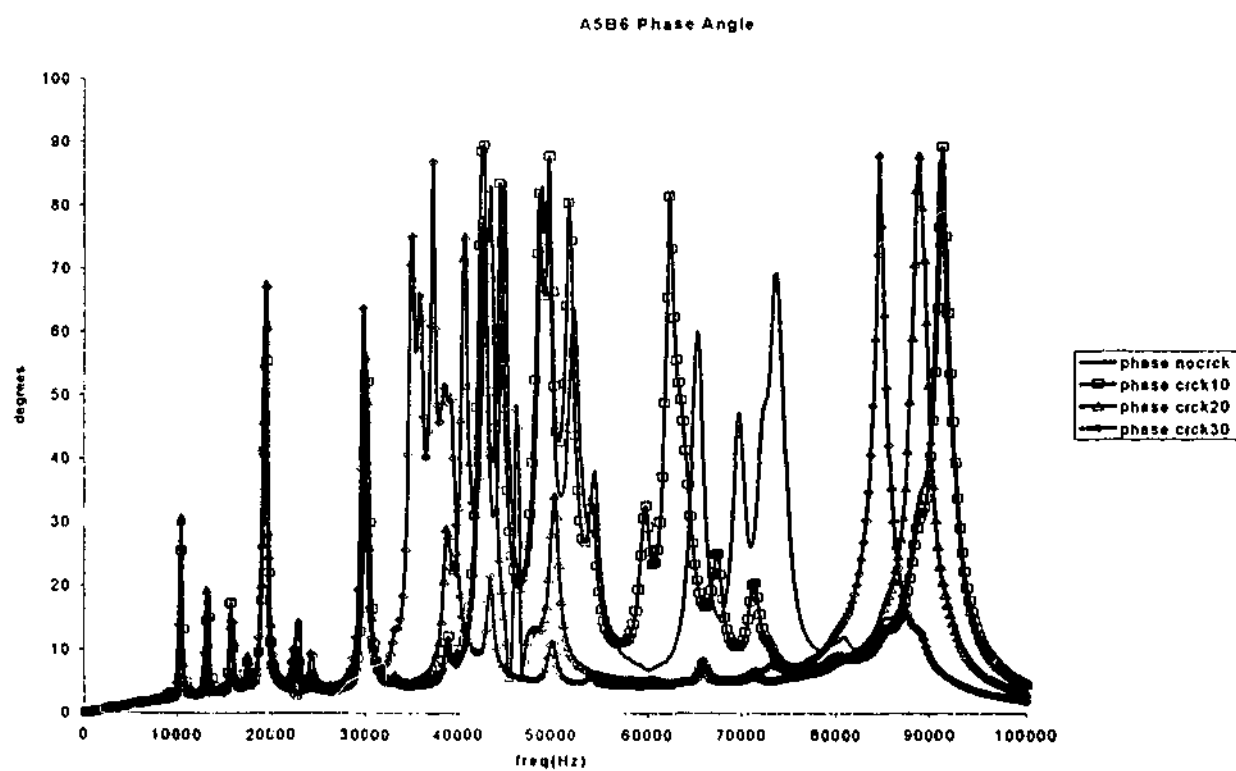


Figure 4.20b. TF Phase Angle of A5B6

Summary of Transfer Function Results

The above results based on a shift of frequency response can be summarized as follows:

- Equation (4.6) proposed to model the crack in the structure shows a shift on the natural frequencies due to the reduction of the local stiffness resulting from the crack. This is verified by the results presented.
- The results presented showed that it is possible to determine the presence of a crack by the shift of the modal frequency when the crack occurs between the sensor and the actuator.
- This work also proposes to use a series of sensor-actuator configuration to confirm the existence of the crack.
- These results also show that the investigation has to be conducted at a sufficiently high frequency range (i.e. up to 100KHz) to allow for the tracking of the reduction of the frequency in the higher modes.
- However, a major disadvantage of this technique is the reliance on the peaks on the frequency spectrum for the damage detection. It is likely that the spectrum obtained on any experiment in practice to exhibit noise in the spectrum. To address this concern we wish to introduce the concept of the R-curve (this is similar to the concept reported by Lichtenwalner et al (1997)).

4.3.2. R-Curve Results

In the numerical results above the peaks in the TF were easily identified. And the movement of these peaks was also easy to track. However, in the experimental results it is unlikely that the signal produced will be as clear as the numerical results (see Figure 4.21). This vibration spectrum is often "noisy" which can make it difficult to use the frequency response

function to analyse any change in the signal pattern. To overcome this problem, the concept of the R-curve is introduced. This is similar to the technique proposed by Lichtenwalner et.al (1997) ²³.

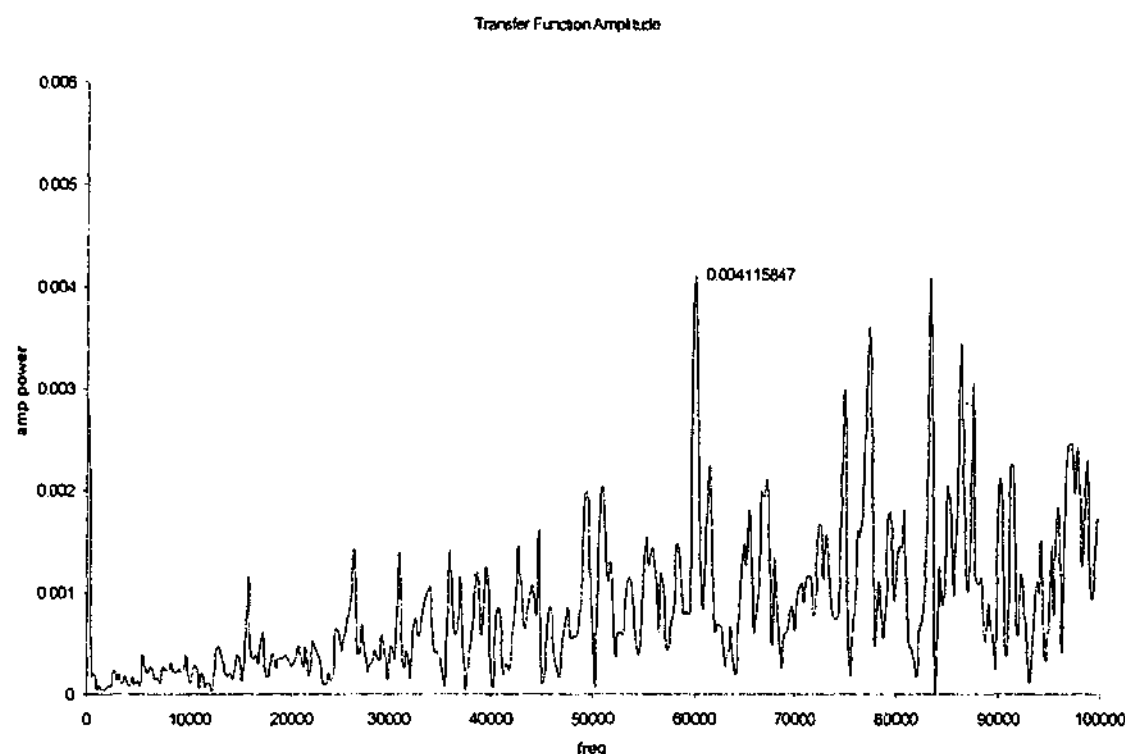


Figure 4.21. Typical Experimental Transfer Function Amplitude

Lichtenwalner and his co-workers proposed a concept of damage detection based on the integral of the transfer function over a given range of frequency. Here, this integral is defined as R . This area R under the TF frequency spectrum in a certain frequency range f_0 and f_n is calculated by this following formula:

$$R = \int_{f_0}^{f_n} A_{TF} df \quad [4.10]$$

where A_{TF} is the amplitude of the TF frequency spectrum

This R-Curve method (equation 4.10) was applied to the numerical results that were discussed above. The results are in the form of a

comparison of the area under the TF frequency spectrum for all the damage conditions, no damage, and 10mm, 20mm, 30mm cracks.

Analysis of the R-Curve of AnBn Pairs

Figure 4.22 and 4.23 shows the R- value in equation [4.10] of the TF-data for the pair A1B1 and A2B2 for every damage condition. The results show that there are no significant changes in the R-value for the various damage conditions. This is because the crack is located far away from these pairs. The R-values for every damage condition appear unchanged on pairs A3B3 in Figure 4.24, except for 30mm crack case. It appears that the A3B3 pair starts to sense the damage. This indicates that the 30mm crack is located relatively close to this A3B3 pair. In Figure 4.25, it presents results obtained from the pair A4B4 for every damage condition. For the 20, 30 mm crack case (see Figure 4.1.b), as the crack has developed closer to the pair A4B4, the area under the frequency spectrum appears to decrease with increasing crack lengths.

The results showed in Figure 4.26 for A5B5 are particularly interesting. Here it is observed that the R-value decreases appropriately with increasing crack size over a frequency range up to 20KHz. At a frequency approximately 20kHz the change in gradient in the R-value appears to affect the results. It appears that this is in the vicinity of the first dominant mode of the natural frequency of the plate. Since an increase in the crack size will result in the decrease in the natural frequency, this reduction seems to have affected the overall characteristics of the R-values. Base on this finding, it can be hypothesised that a limiting factor of the proposed R-value technique is that the frequency band to be analysed should not include the first dominant natural frequency.

Figure 4.26 showed also that as the 10mm crack grows towards the pair A5B5 (See Figure 4.1b) the R-value starts to change. As the crack increases and develops pass the pair A5B5, for 20 and 30 mm length (see Figure 4.1b), the area under the frequency spectrum appears to decrease with further increase in crack length. It can be noticed that from the reduction in R-value the pair A5B5 is more sensitive to the presence of the damage than pair A4B4. Figure 4.27 shows the results obtained from the sensor-actuator pair A6B6. Note that at 10mm crack the R-Value decrease significantly. It is interesting to note that as the crack pass the pair A6B6 in length of 20 and 30mm the R-curve starts to behave differently. This situation may indicate the crack is large and has passed the particular sensor-actuator pair. As discussed in the previous section the larger crack sizes i.e. 20&30mm have lead to a change in the dynamics of the local response as recorded by pair A6B6.

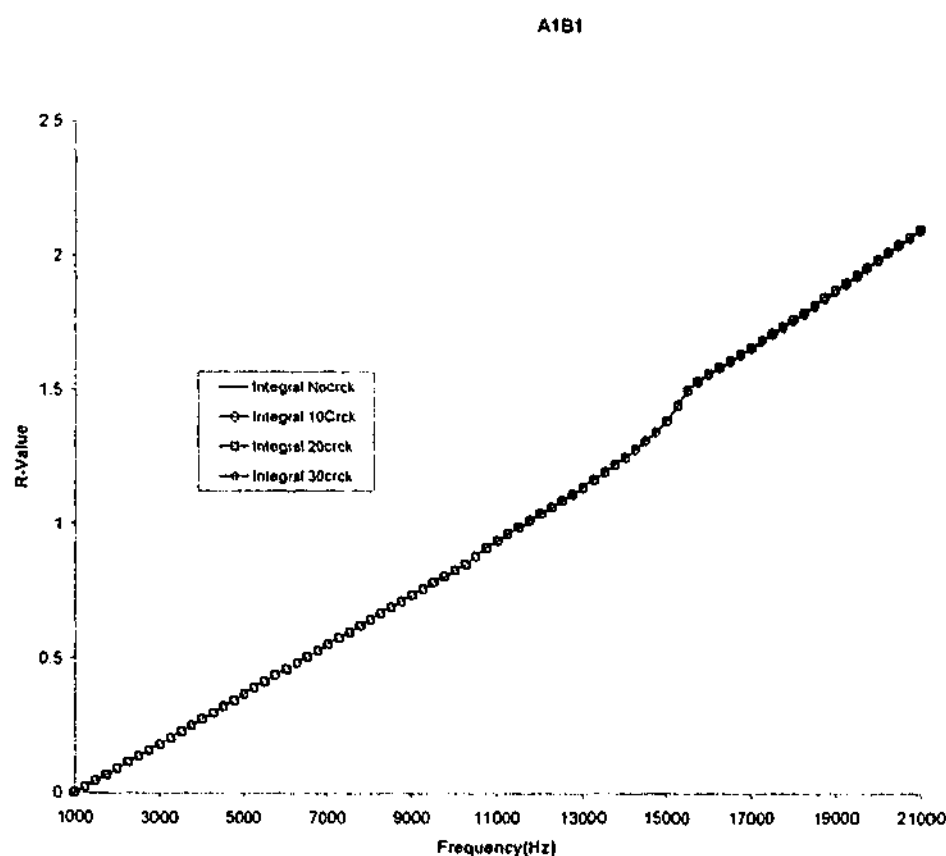


Figure 4.22. TF-data of the area under the frequency spectrum of the pair A1B1 for every damage condition

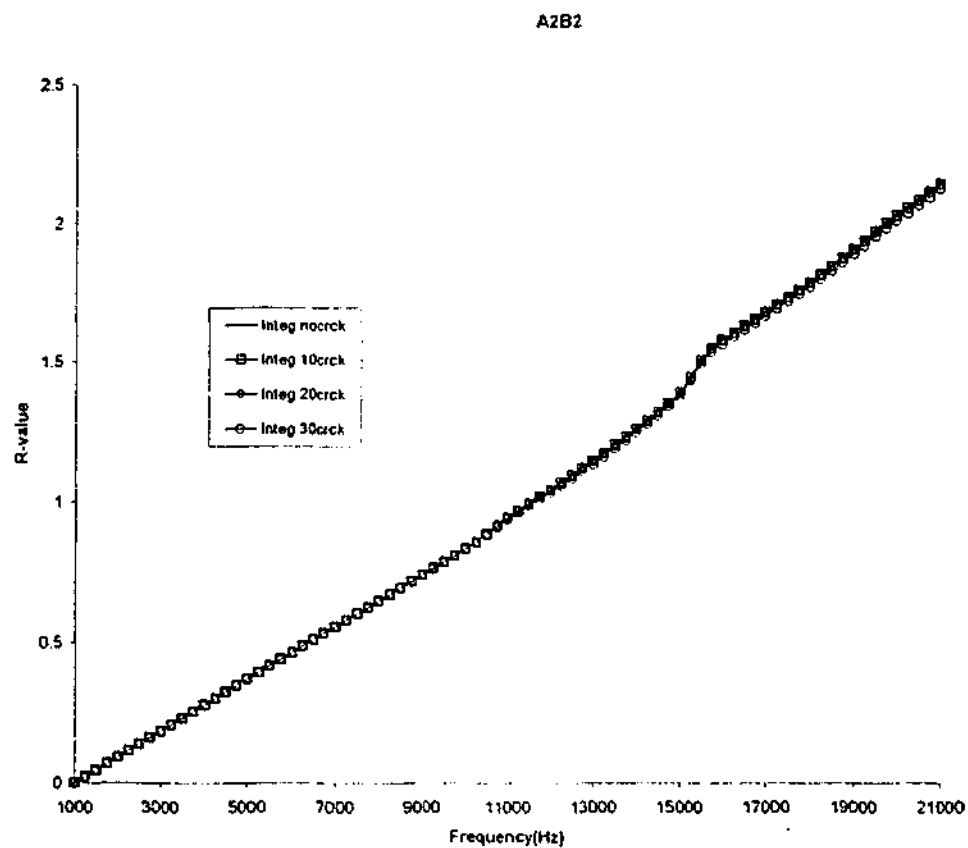


Figure 4.23. TF-data of the area under the frequency spectrum of the pair A2B2 for every damage condition

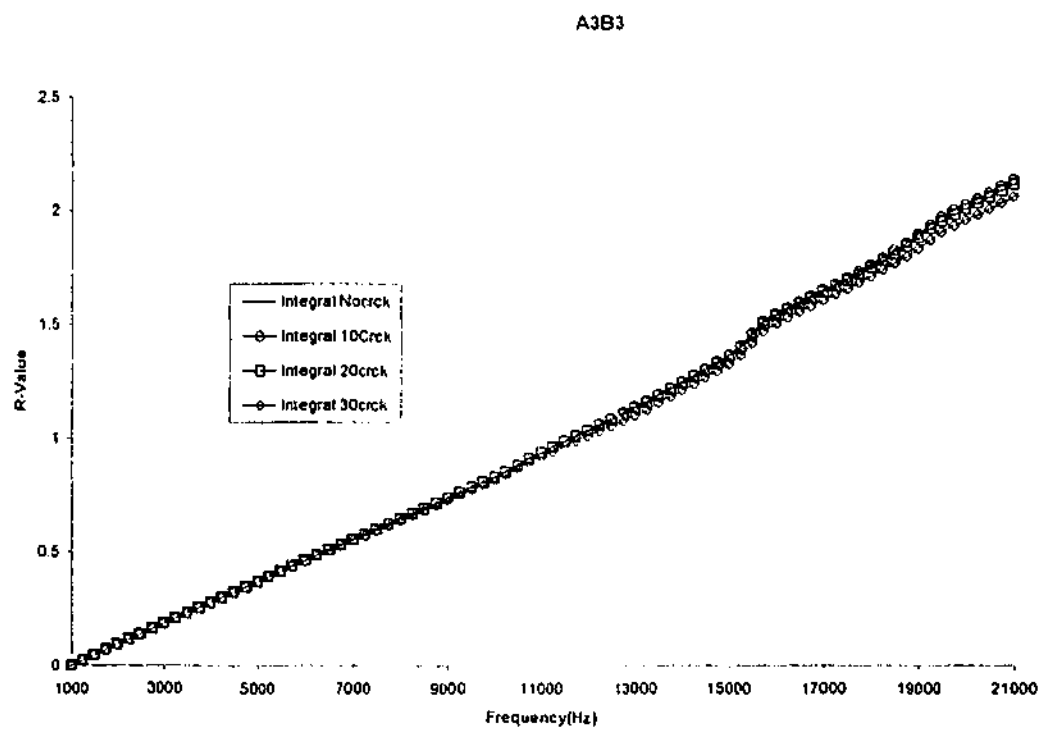


Figure 4.24. TF-data of the area under the frequency spectrum of the pair A3B3 for every damage condition

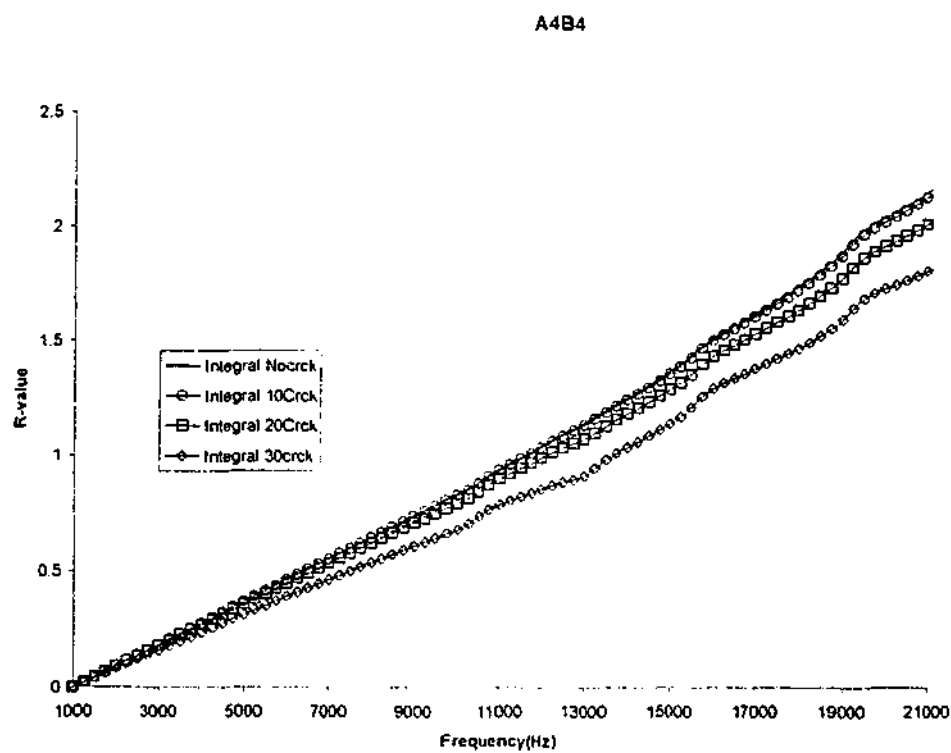


Figure 4.25. TF-data of the area under the frequency spectrum of the pair A4B4 for every damage condition

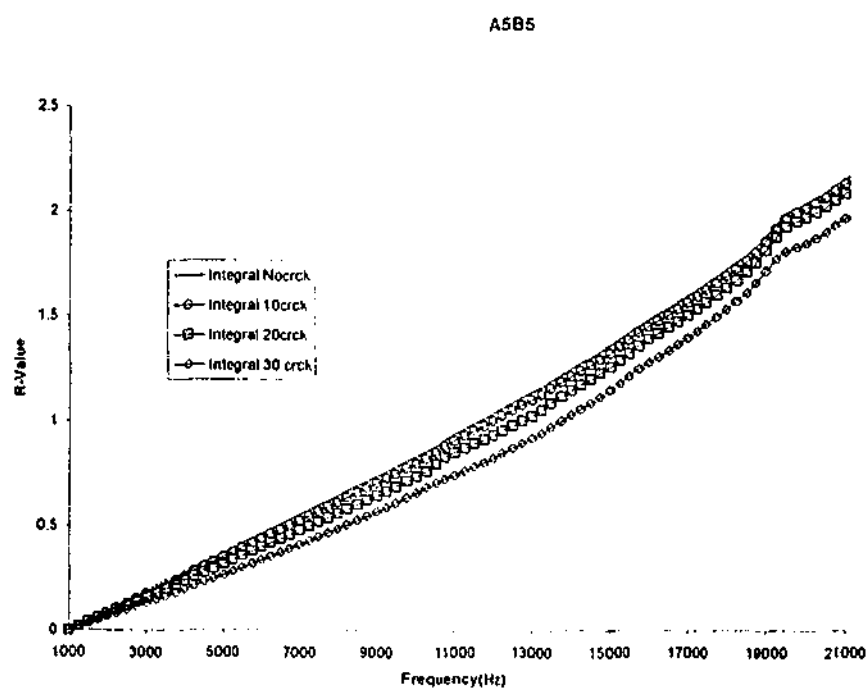


Figure 4.26. TF-data of the area under the frequency spectrum of the pair A5B5 for every damage condition

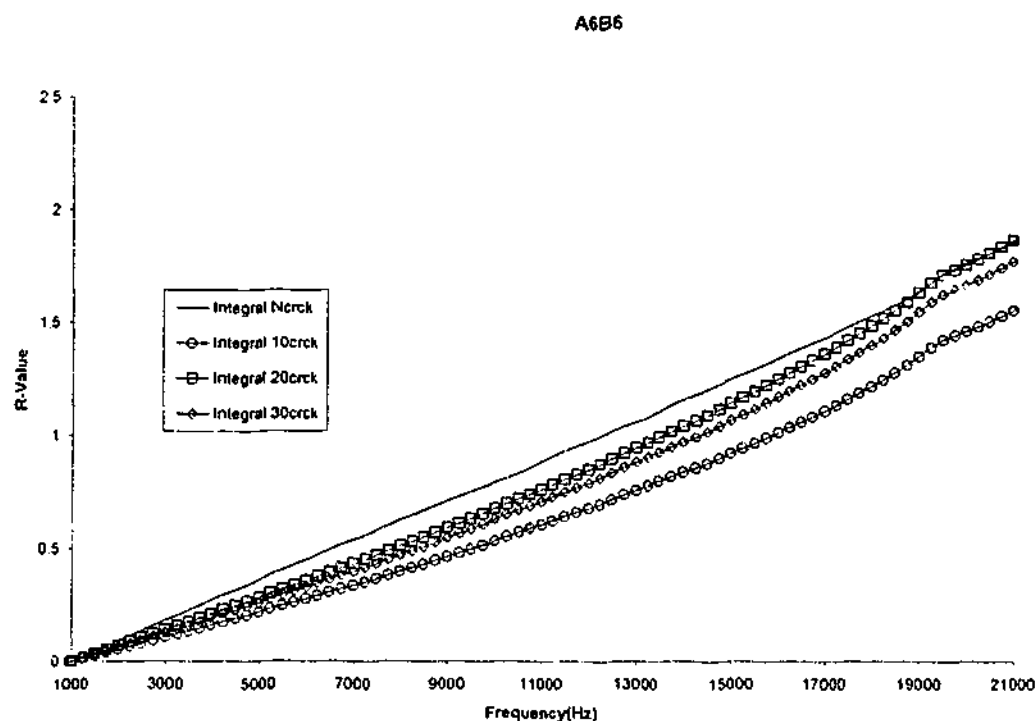


Figure 4.27. TF-data of the area under the frequency spectrum of the pair A6B6 for every damage condition

Analysis of the R-Curve of BnCn Pairs

Figure 4.28 shows the R-values of the pair B1C1 for every damage condition. The area of the pair does not change for all damage conditions. This is because the crack is located far away from the pair. The no-change of the R-values for every damage condition appears also on pairs B2C2 and B3C3 in Figure 4.29 and 4.30. These indicate that the crack is still located relatively far away from these B2C2 and B3C3 pairs.

However, unlike the pair A4B4, in Figure 4.31, the R-values of the pair B4C4 also does not change for every damage condition, in this case it appears the pair B4C4 is less sensitive to the existence of a crack than A4B4. This can be explained by equation [4.6]. This can also be used to indicate that the damage is located in between rows A and B.

In Figure 4.32, the R-values of the pair B5C5 for every damage condition shows that the R-values starts to decrease for the 20mm crack and has significant reduction for the 30mm crack (i.e. when the crack passes the pair B5C5). Figure 4.33 presents R-value of the pair B6C6 that decreases with increasing damage conditions.

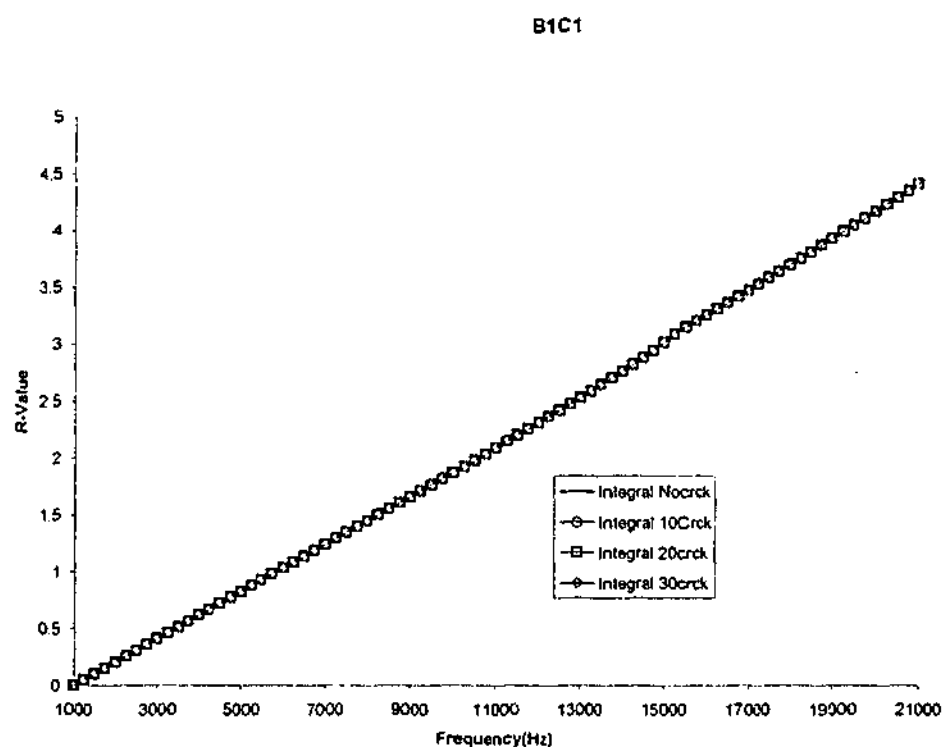


Figure 4.28. TF-data of the area under the frequency spectrum of the pair B1C1 for every damage condition

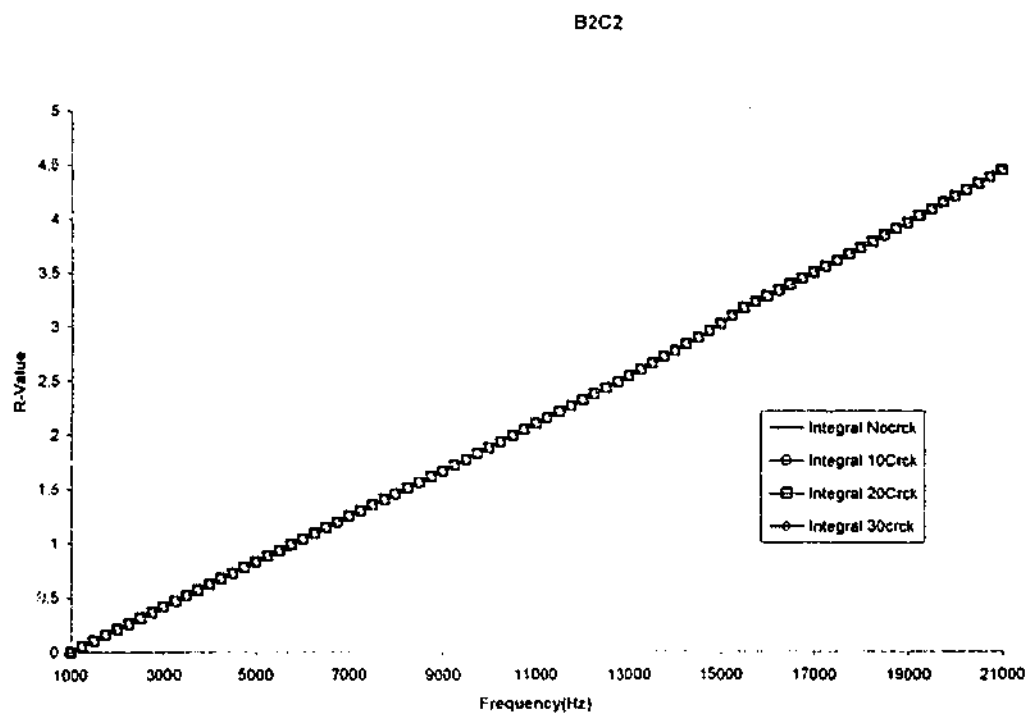


Figure 4.29. TF-data of the area under the frequency spectrum of the pair B2C2 for every damage condition

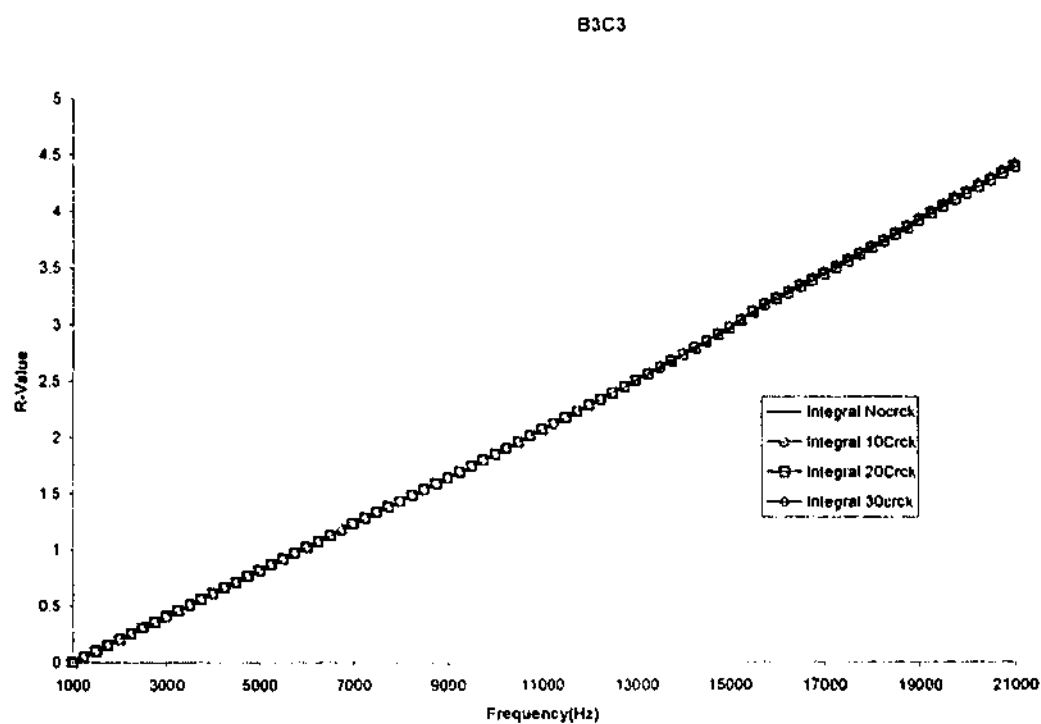


Figure 4.30. TF-data of the area under the frequency spectrum of the pair B3C3 for every damage condition

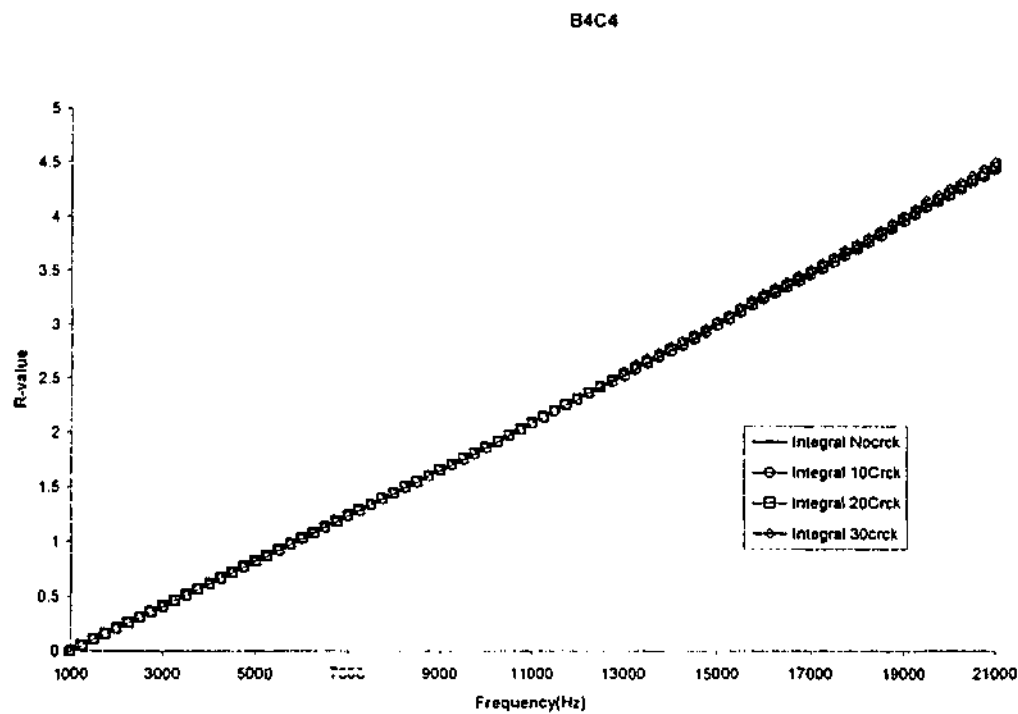


Figure 4.31. TF-data of the area under the frequency spectrum of the pair B4C4 for every damage condition

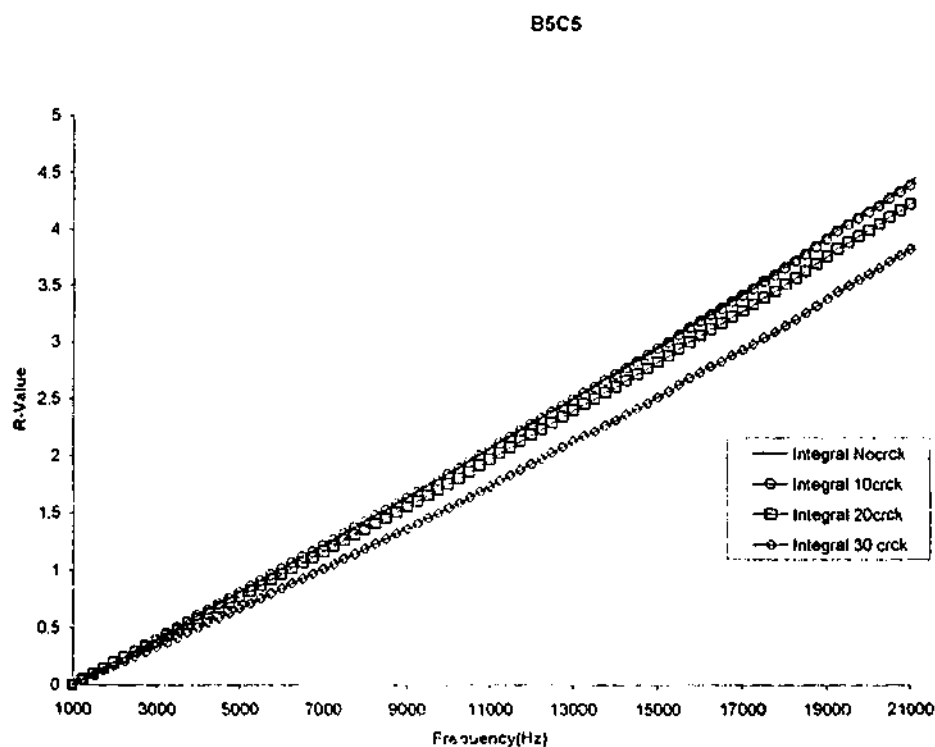


Figure 4.32. TF-data of the area under the frequency spectrum of the pair B5C5 for every damage condition

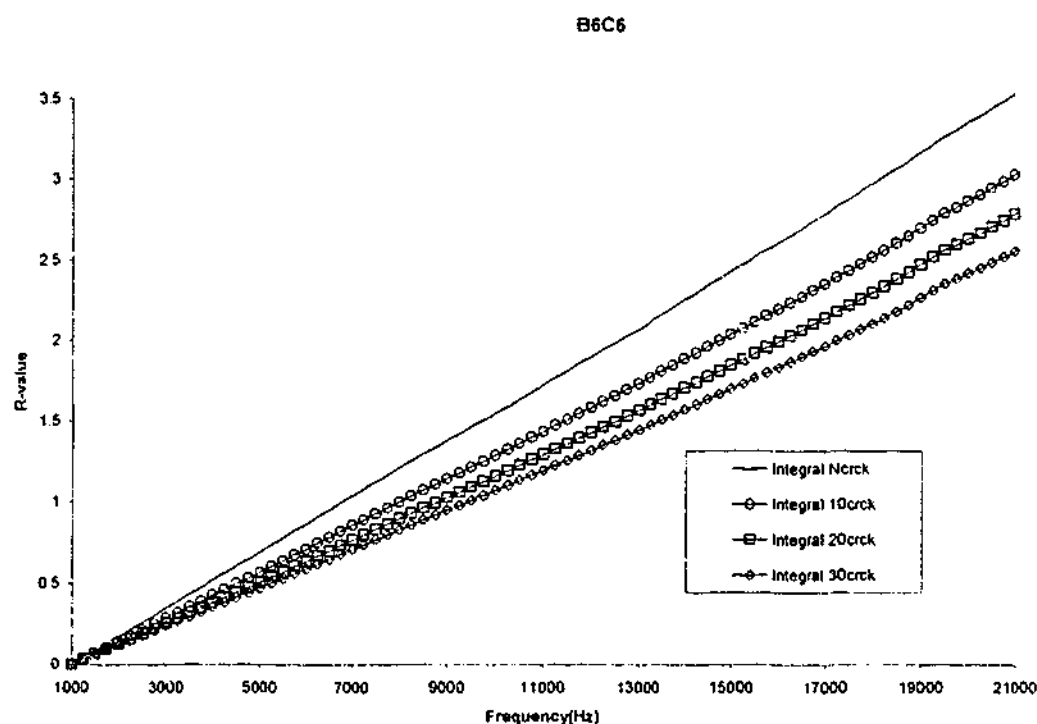


Figure 4.33. TF-data of the area under the frequency spectrum of the pair B6C6 for every damage condition

Sensitivity analysis for AnBn pairs combined with BnCn pairs

The sensitivity of the results from AnBn and BnCn to the various damage conditions is now analysed. The results of percentage reduction of R-value from the no-damage condition up to 20 kHz for these sensor-actuator combinations AnBn and BnCn are shown in Table 4.2. The results for A1B1, A2B2, B1C1 and B2C2 showed that the reduction of the R-value from the no-damage condition is insignificant (less than 1 percent).

Table 4.2. Percentage of reduction of R-value from no-damage condition using a direct-TF

Pairs	A1B1	B1C1	A2B2	B2C2	A3B3	B3C3	A4B4	B4C4	A5B5	B5C5	A6B6	B6C6
Cracks												
10mm	0.0515	0.0222	0.0825	0.0059	0.1231	-0.0113	0.94152	0.06356	1.0991	0.76145	17.2364	14.3943
20mm	0.1947	0.047	0.3798	0.0228	1.0312	-0.1376	6.15762	0.63497	3.31401	4.64259	0.55677	21.3966
30mm	0.5886	0.0234	1.0316	0.0096	3.5057	-0.7869	15.2957	1.62948	9.40373	13.9484	5.69977	27.793

Looking at the results in Table 4.2, the following can be observed:

- The reduction of R-value of the sensor-actuator pair A_nB_n has a low value except when the crack appeared in front of the pair. For the case of a 10mm crack, the reduction in R-value was observed at pair A6B6 and B6C6.
- For the case of 20mm crack, this crack is located in front of A5B5 (see Figure 4.1b). Looking at the results, a reduction in the R-value was observed for A4B4 and A5B5. Looking at the R-value for B_nC_n pairs, it was found that B5C5 and B6C6 experienced a reduction. Here it can be said that the crack spans from the 6th pair of sensor-actuator to the 5th pair of sensor-actuator. This inference is made due to the fact that a reduction in the R-value of A5B5, B5C5, A6B6 and B6C6 were observed. The small reduction in B5C5 and A5B5 infer that the crack has not completely crossed the 5th column of the sensor-actuator pair.
- For the 30mm crack case (see Figure 4.1b), the R-value for A4B4 and A3B3 was reduced. It is interesting to notice that the R-value for A4B4 reduced dramatically compared to the A3B3 with B3C3 and B4C4 are still relatively unchanged. The R-values for B5C5 and B6C6 has also reduced dramatically. These results imply that the crack now spans across the 5th and 6th pair of sensor-actuator and the crack tip is approaching the 4th pair. The large reduction in A4B4 implies that the crack is approaching the 4th column of sensor-actuator. However, the insignificant reduction in B4C4 implies that the crack has not developed pass the 4th column of sensor-actuator.

Based on the findings described above, it infers that:

- The pair of sensor-actuator, which encompasses the crack (i.e. A_nB_n), will show a reduction in the R-value prior to the B_nC_n pairs. This can

be used to indicate across which row of sensor-actuator the crack appears (i.e. between A and B or B and C).

- It is important also to note that the above results infer that the BnCn are also an important part of the monitoring procedure. The R-values of the BnCn pairs can be used to indicate the extent of the crack. This is because a large R-value reduction is obtained when the crack face spans across a BnCn pair.

Analysis of the R-Curve of A_nB_{n+1} cross-pairs

In this section of work, the cross-TF will be used to confirm the location of the crack inferred in the previous section. Figure 4.34 shows the R-values of the pair A1B2 for every damage condition. The R-value of the pair does not change for the five damage conditions. This is because the crack is far away from the pair. The relatively unchanged R-values continued for the pair A2B3 and A3B4 in Figure 4.35 and 4.36. This is because these A2B3 and A3B4 pairs are located relatively far from the damage location.

Figure 4.37 presents the R-values of the pair A4B5 for every damage condition. In general for all damage conditions, the R-value does not change except for the 30mm crack where the area is significantly decreased. Since the crack tip of this damage condition approximately lies between the pair A4B5 (see Figure 4.1b), this pair may be used to give an indication of the crack tip location. In Figure 4.38, for all damage conditions, the area under the frequency spectrum is significantly reduced compared to the no-damage condition. The crack tip of the 10mm crack can be detected by the pair A5B6 since the R-curve started to decrease significantly at that particular crack and the crack tip of this damage condition approximately lies between this pair (see Figure 4.1b).

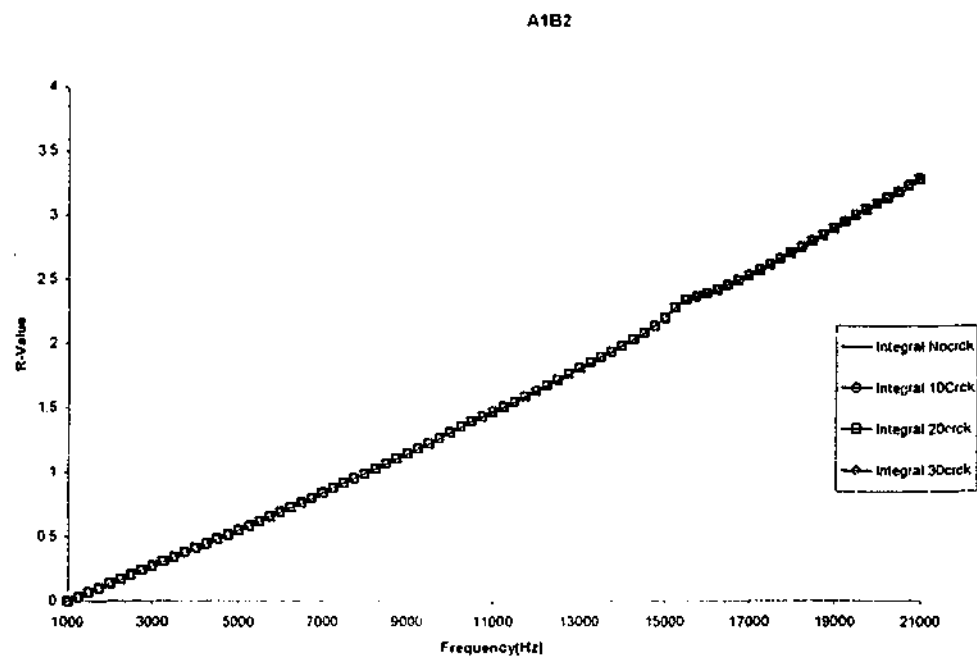


Figure 4.34. TF-data of the area under the frequency spectrum of the pair A1B2 for every damage condition

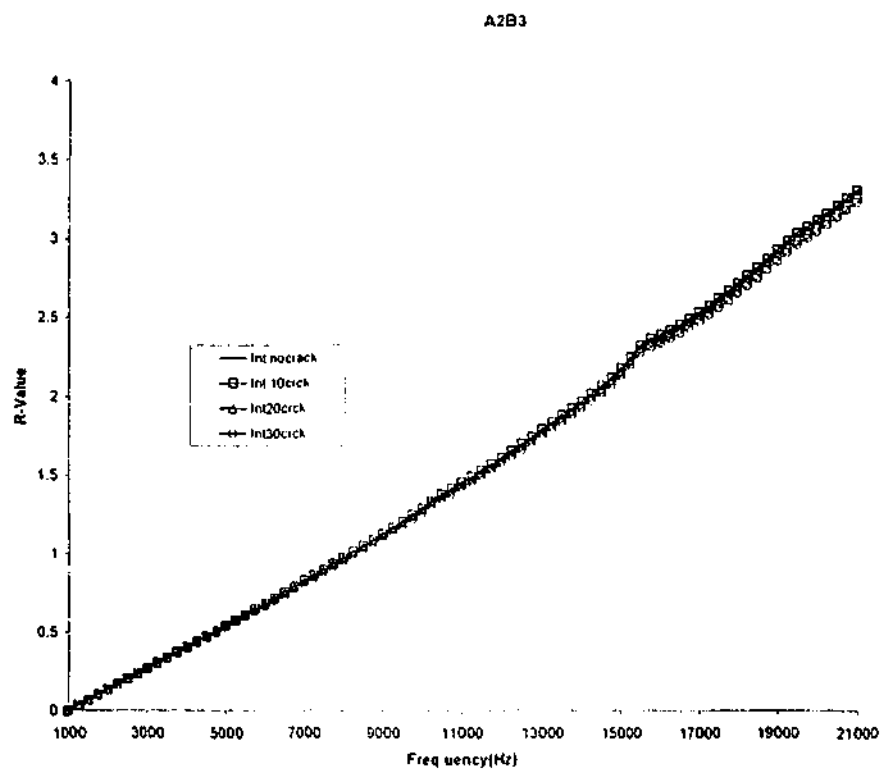


Figure 4.35. TF-data of the area under the frequency spectrum of the pair A2B3 for every damage condition

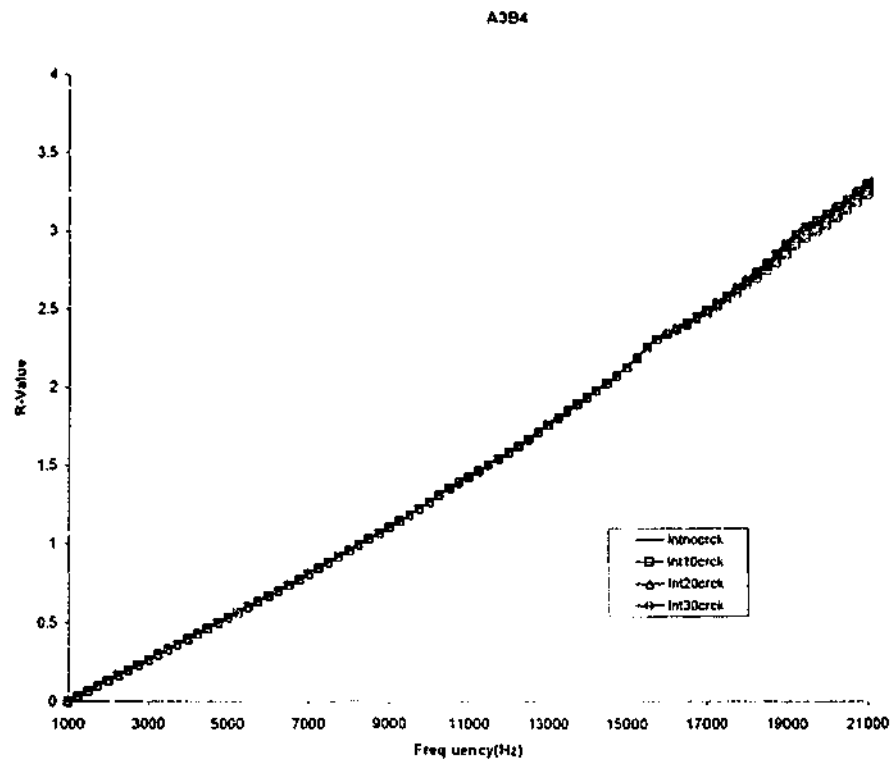


Figure 4.36. TF-data of the area under the frequency spectrum of the pair A3B4 for every damage condition

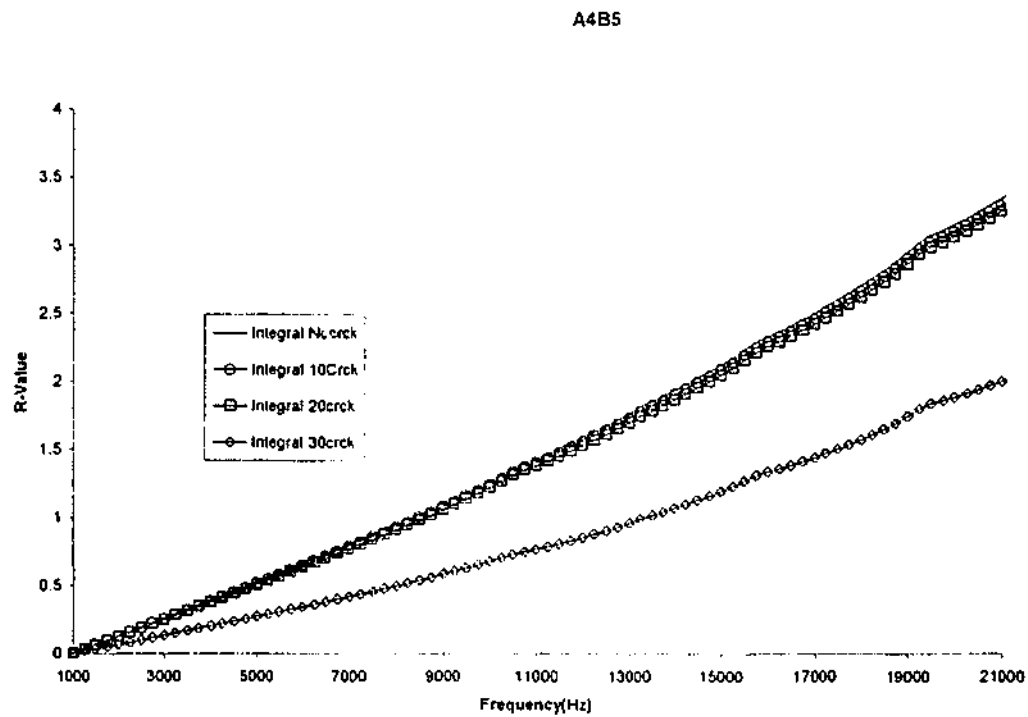


Figure 4.37. TF-data of the area under the frequency spectrum of the pair A4B5 for every damage condition

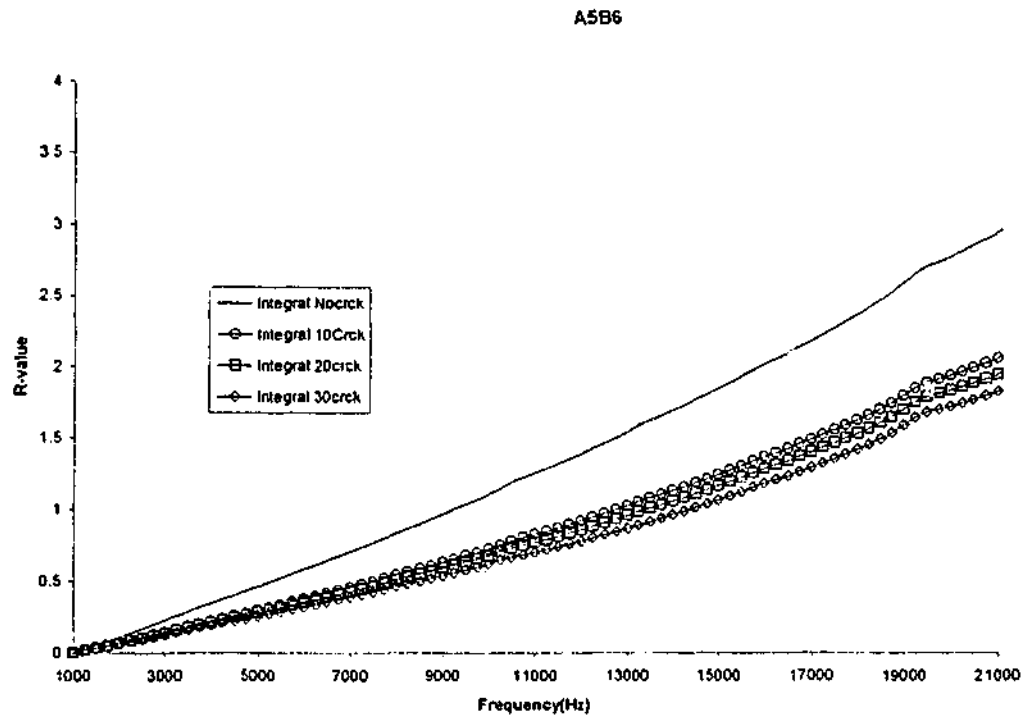


Figure 4.38. TF-data of the area under the frequency spectrum of the pair A5B6 for every damage condition

These sets of results show that a decrease in the R-value of the cross-TF was observed when the crack tip is located between the sensor-actuator pair. To help in the interpretation of these results the reduction in the R-value up to 20 kHz for the situation described above are tabulated in Table 4.3.

Table 4.3. Percentage of reduction of R-value from no-damage condition using a cross-TF

Pairs	A1B2	A2B3	A3B4	A4B5	A5B6
Cracks					
10mm	0.9122	0.1714	0.6479	1.4253	30.043
20mm	0.6465	0.8587	1.1490	2.7893	33.8128
30mm	0.5583	2.5136	2.7989	40.2807	37.931

The results from the cross-TF presented in Table 4.3 showed that:

- A significant reduction in the R-value occurs for the pairs A4B5 for the 30mm crack case. This shows that its crack tip is located between the sensor A4 and the actuator B5. (see Figure 4.1b)

- Another significant reduction also occurs for the pairs A5B6 that allows for the detection of a 10mm crack. This implies that its crack is located in the vicinity of sensor A5 and actuator B6.

Therefore, these cross-TF results in Table 4.3 together with the results from direct-TF shown in Table 4.2 can be used to predict the location of the crack.

4.4. Concluding Remarks

Findings from this numerical investigation can be summarised as follows:

- The application of the array sensor-actuator can be used satisfactorily to locate the damage and to monitor the growth of the damage.
- The modal response can be used to determine the presence of a crack by the shift of the modal frequency when the crack occurs between the sensor and the actuator.
- However, the investigation has to be conducted at a sufficiently high frequency domain (i.e. up to 100KHz) to allow for the tracking of the reduction of the frequency in the higher modes.
- To address the concern of "noisy " spectrum the concept of the R-curve was introduced. This R-curve is obtained by integrating the TF response in the lower range frequency. This analysis should be performed prior to the appearance of the first dominant mode of the frequency response of the structure.
- Based on the R-curve results an array sensor-actuator can be used to detect and locate the damage. This should be augmented or confirmed by another set of data generated from the sensor-actuator pairs located away from the damage (as in BnCn). The sensitivity

analysis of the rows of sensors-actuators can be used to estimate the location of the damage/crack.

- The location of the crack tip can be approximated using the method described above. The cross-TF of sensor-actuator is conducted between the rows where the crack is located. The approximate location of the crack tip can be confirmed by examining the reduction of R-Curve in a particular cross-pair and comparing it with the neighboring cross-pairs.

The above findings from the R-curve concept above need to be validated experimentally. The next chapter will present an experimental investigation to validate the results from this numerical work.

CHAPTER 5. EXPERIMENTAL INVESTIGATION OF THE DETECTION OF A FLAW IN THE SYSTEM

The numerical simulation results from Chapter 4 show how an array of sensors-actuators can be used to detect and to approximately localise damage in a metallic structure. These findings need to be validated. A series of experimental work is reported in this chapter to confirm the findings from the numerical investigation.

The first section of this chapter presents experimental results from a series of experiments conducted with a clamped plate with the artificial crack growth (i.e. saw cut). This is followed by a set of experiment with a clamped plate where a centre crack is grown by a fatigue.

5. 1. Experimental Investigation of the Clamped Plate with the Artificial Crack Growth

In this experimental work, the test equipment consisted of a signal generator (SG) Hewlett-Packard 33120A, a dual channel oscilloscope HAMEG HM 305, a frequency analyser AND AD-3525 and a plate specimen to which the PZT patches were attached. Three rows A, B, C of $5 \times 5 \text{ mm}^2$ of PZT patch were mounted on the plate (shown in Figure 4.1a). The distance between row A and B was 10 mm with the crack laid exactly in the middle of the rows. No crack was made between row B and C where the distance between them was 5 mm. Multiple switches were installed into the test plate to help the connections between sensors and actuators to the frequency analyser. The plate specimen is shown in Figure 5.1a.

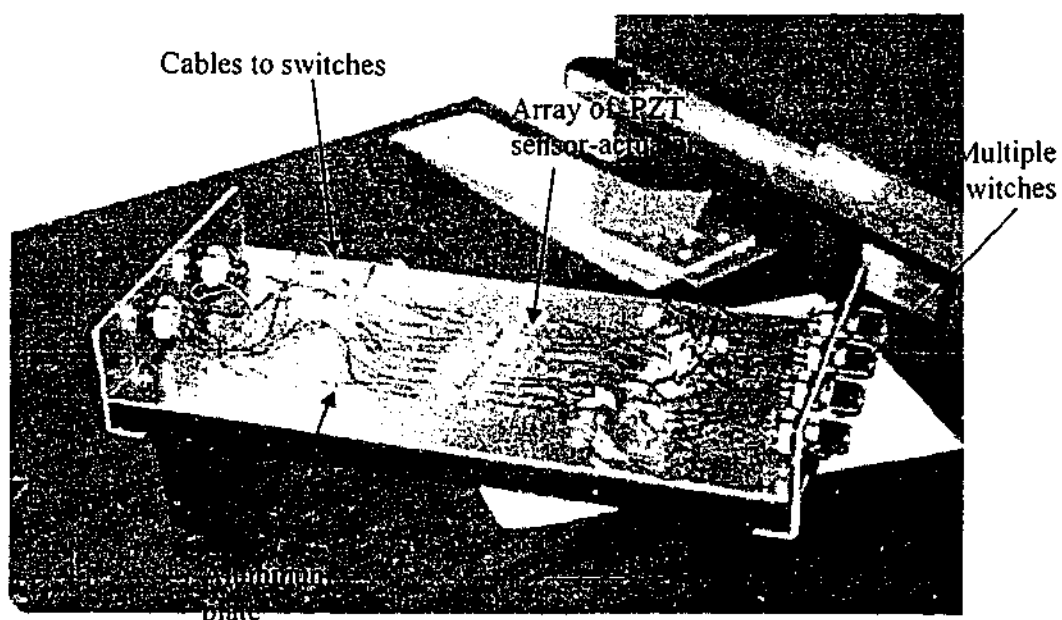


Figure 5.1a. The specimen for Transfer Function Investigation

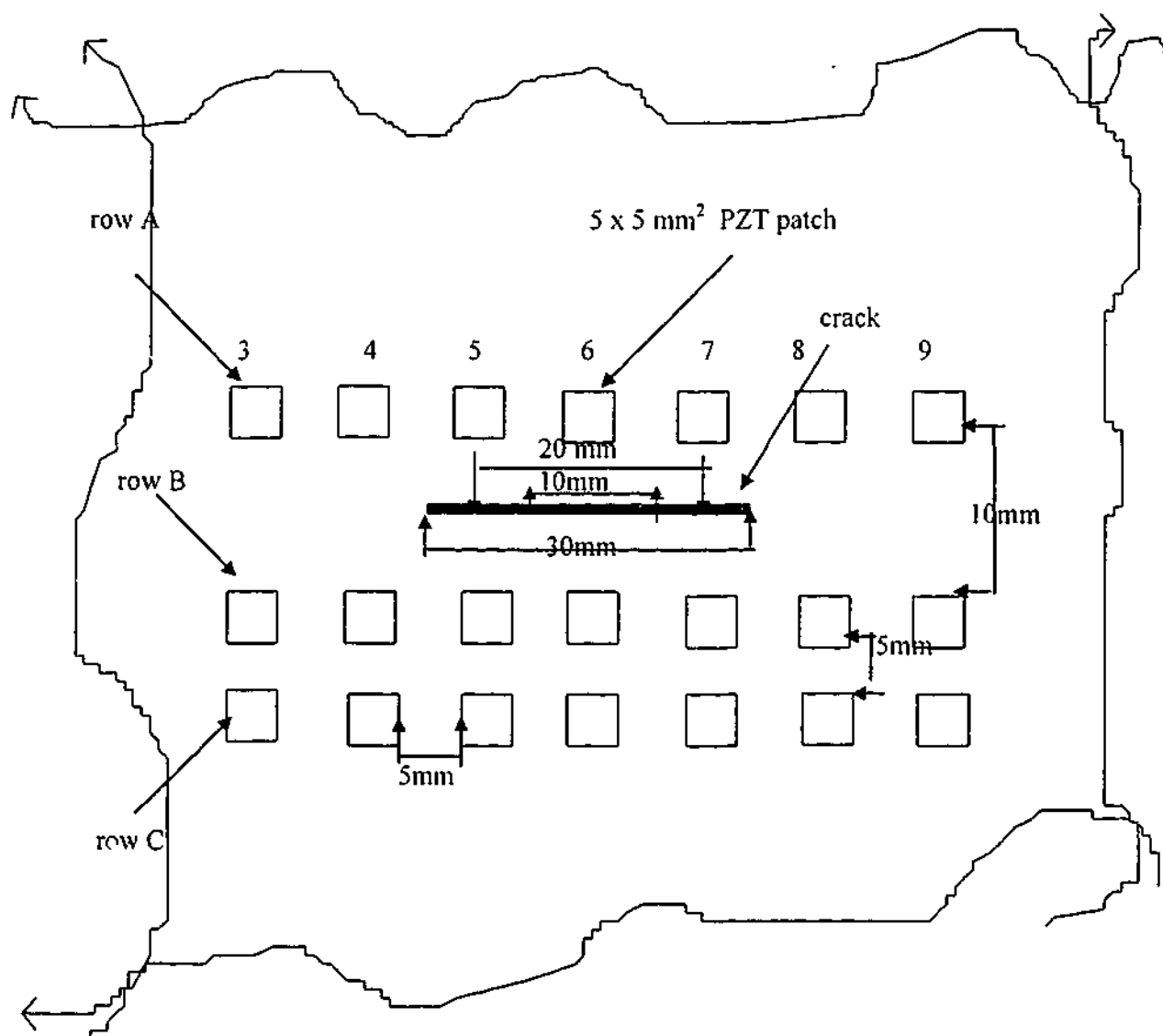


Figure 5.1b. Detailed Configuration of the Actuator-Sensor Pairs

Figure 5.1a shows a thin aluminium plate that is $200 \times 400 \times 2 \text{ mm}^3$, which is clamped on the shorter edges. The arrays of actuators and sensors are bonded on the surface of the plate. The detailed configuration of the actuator - sensor pairs is shown in Figure 5.1b.

The transfer function is measured from each actuator-sensor pair. As in the numerical investigation, the actuator-sensor pairs can be combined in two ways to produce the transfer function. The first is a direct-TF measurement i.e. $A_n B_n$, $B_n C_n$ ($n = 1 \dots 11$). The second is a cross-TF measurement i.e. $A_n B_{n+1}$ ($n = 1 \dots 10$). In the $A_n B_n$, $A_n B_{n+1}$ combinations, row A is an array of sensors where the responses were measured while row B is an array of actuators where the actuating signals were inputted. However, in $B_n C_n$ combinations, row B is an array of sensors while row C is an array of actuators. Three different damage conditions in the structure were made. First, the plate had only a small hole in the centre of the plate (diameter 0.5mm). This condition was classified as "no-damage". Then, a saw cut was made on either side of the hole to simulate crack of a specific length (see Figure 5.1b). The TF measurement was calculated for every condition of the plate i.e. no-damage, damage1 (10mm crack), damage2 (20mm crack), and damage3 (30mm crack) in order to verify the R-value concept presented in the previous chapter.

A 10V peak to peak broadband Gaussian³¹ white noise in a range of 250 to 100000Hz was supplied by the signal generator to excite the PZT actuator. Before the test was conducted all PZT actuators-sensors were tested by measuring their capacitances and their response to a given input voltage. The experimental set up is shown in Figure 5.2a and 5.2b.

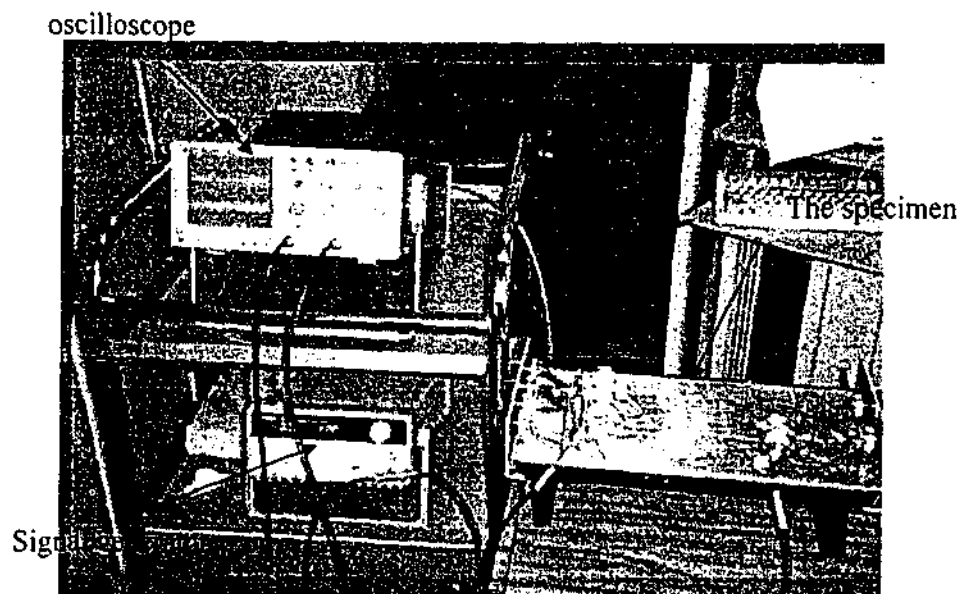


Figure 5.2a. The specimen - Oscilloscope - Signal generator set-up

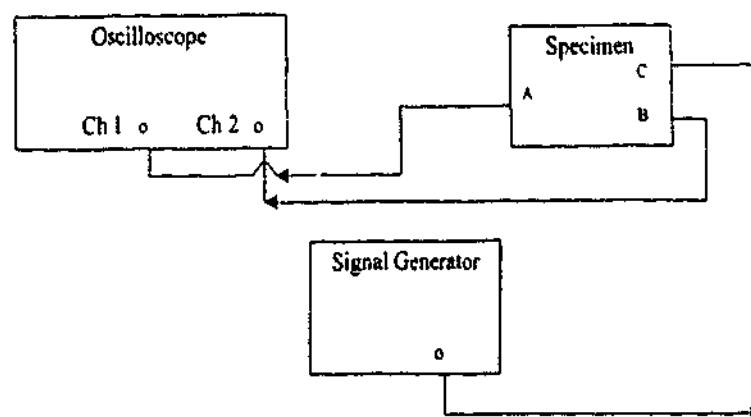


Figure 5.2b. A Schematic diagram of the Signal generator - oscilloscope - specimen set-up

The frequency analyser measured the transfer function of each actuator-sensor pair to which excitation from the signal generator and response from the sensor were channelled to the analyser. In this frequency analyser, the number of averaged spectrum ensembles was 30 and, the Hanning window was used to perform the TF measurement. The experimental set up is shown in Figure 5.3a and 5.3b.

5.2 Results and Discussions

The essential differences between this experimental study and that modelled numerically are:

- The waveforms that were used for the excitation of the actuator in the numerical and experimental work are different. In the experimental work we applied gaussian random noise, while in the numerical work a constant amplitude sinusoidal wave-sweep over a broad frequency range was applied.
- The choice of the amplitude of an excitation force for the two investigations was arbitrary. For the numerical work the force amplitude was 10N while on the experimental work A 10 V signal was used to actuate the PZT.

Despite these shortcomings, it will be shown in the subsequent section that, in a range below the first dominant mode the experimental results are similar to those obtained numerically. Since the results from the experimental tests will be used to confirm the results obtained numerically, the direct-pairs $A_n B_n$, $B_n C_n$ ($n = 1 \dots 6$) and the cross-pairs $A_n B_{n+1}$ ($n = 1 \dots 5$), under the three damage conditions no damage, and 10mm, 20mm, 30mm cracks are presented below.

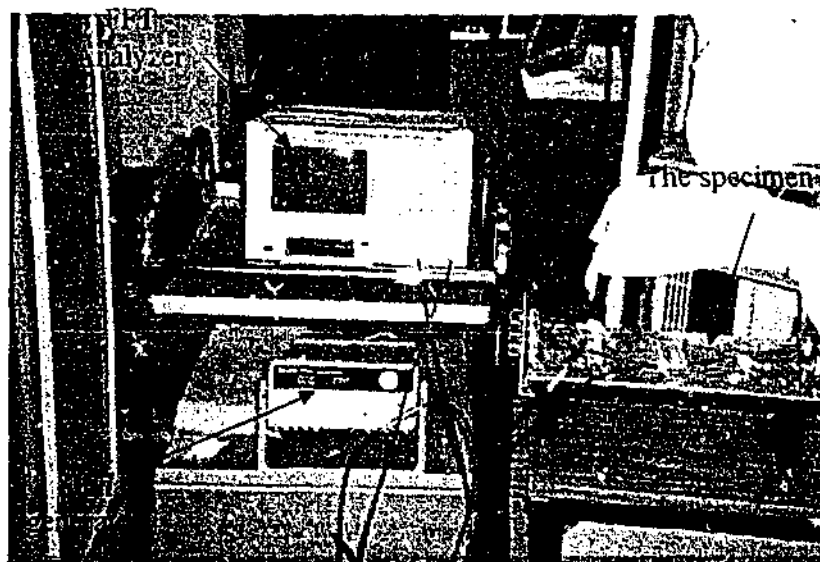


Figure 5.3a. The specimen - FFT analyzer - Signal generator set - up

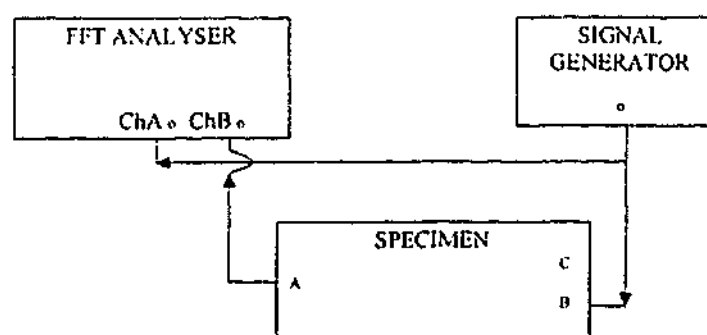


Figure 5.3b. A Schematic Diagram of the Signal generator - FFT analyser - specimen set-up

Analysis of the R-Curve of AnBn Pairs

Figure 5.4 and 5.5 show the R- value for the pair A1B1 and A2B2 for every damage condition. The results showed that there are no significant changes in the R-value for the various damage conditions. This is because the crack is located far away from these pairs. The R-values for every damage condition appeared unchanged for the pair A3B3 in Figure 5.6, except for 30mm crack case. Here, the A3B3 pair was able to sense the damage. This indicates that the 30mm crack is located relatively close to this A3B3 pair. A higher reduction of R-value for 30mm crack in this investigation than to those obtained numerically indicates the higher sensitivity of this pair to sense the presence of the crack compared to the numerical simulation. This may be due to the reduction of the local stiffness in this pair in the plate resulting by saw cut were greater than in the numerical modelling.

In Figure 5.7, the R-values for A4B4 pair of sensor-actuator for the 10mm, 20mm, and 30mm crack cases are lower than the no-damage case. This situation appears to differ to that predicted in the numerical work where only the 20mm and 30mm crack cases are lower than the no-damage case. It appears the A4B4 pair of sensor-actuator in this experiment is more sensitive than in the numerical work to sense the presence of 10mm crack. This confirms that the reduction of the local stiffness in the plate resulting by saw cut was greater than in the numerical modelling.

Figure 5.8 shows the R-value of the pair A5B5 for every damage condition. The R-curve for damaged cases is smaller than the no-damage condition. These results are similar to the numerical results presented in the preceding chapter. R-value was found to decrease as the crack approaches the pair A5B5 (i.e. 10mm and 20mm length). As in numerical investigation, the reduction in R- value for the pair A5B5 is more sensitive than pair A4B4 to the presence of the cracks.

In Figure 5.9, as in the numerical investigation, with the analysis up to 20khz region, shows that at 10mm crack the R-Value decrease significantly. It is also shown in this figure that as the crack passes the pair A6B6 in length of 20 and 30mm, the R-curve starts to behave differently. This situation indicates that the crack is large and has passed the particular sensor-actuator pair. This behaviour was also recorded in the numerical simulation (see Figure 4. 27).

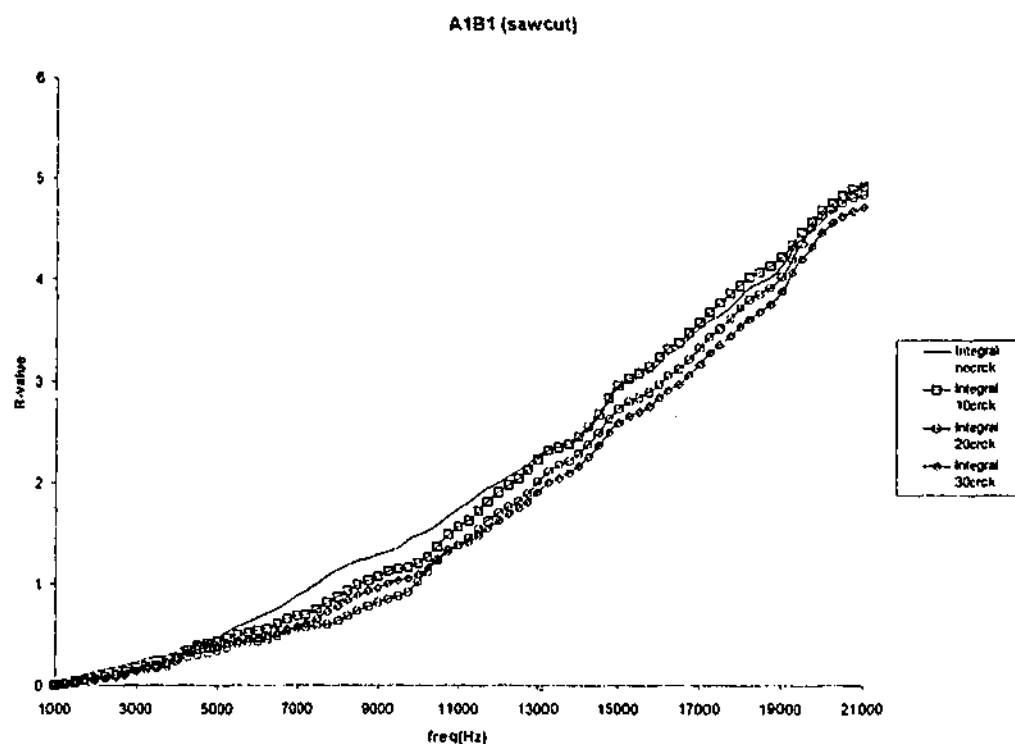


Figure 5.4. TF-data of the area under the frequency spectrum of the pair A1B1 for every damage condition

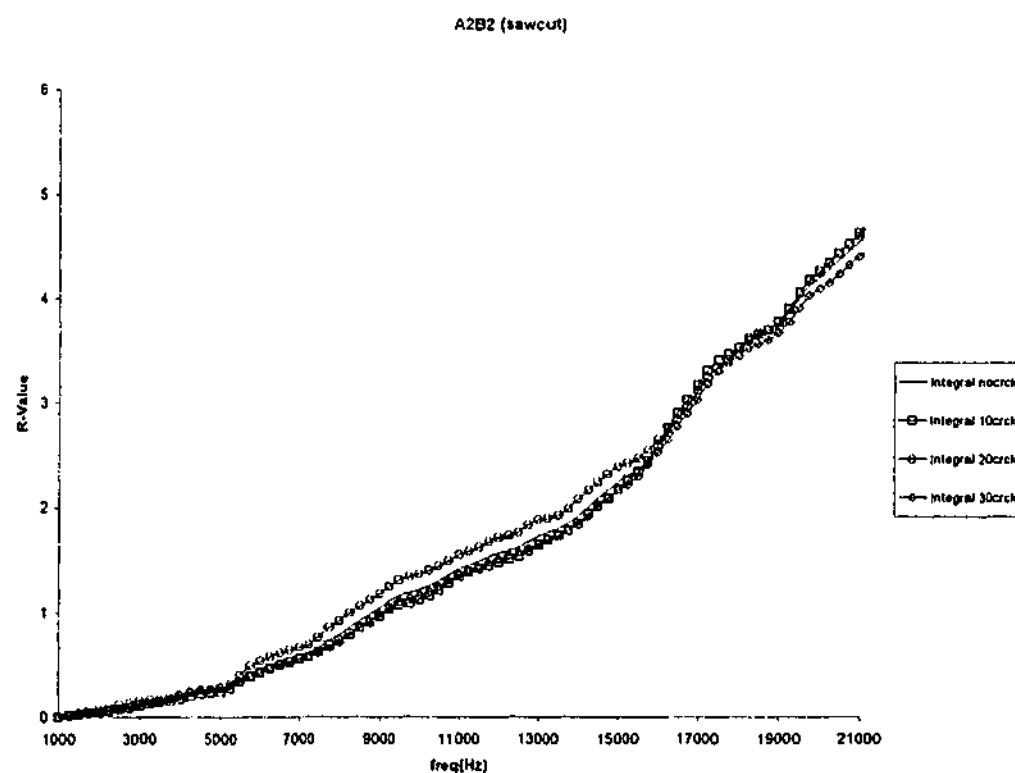


Figure 5.5. TF-data of the area under the frequency spectrum of the pair A2B2 for every damage condition

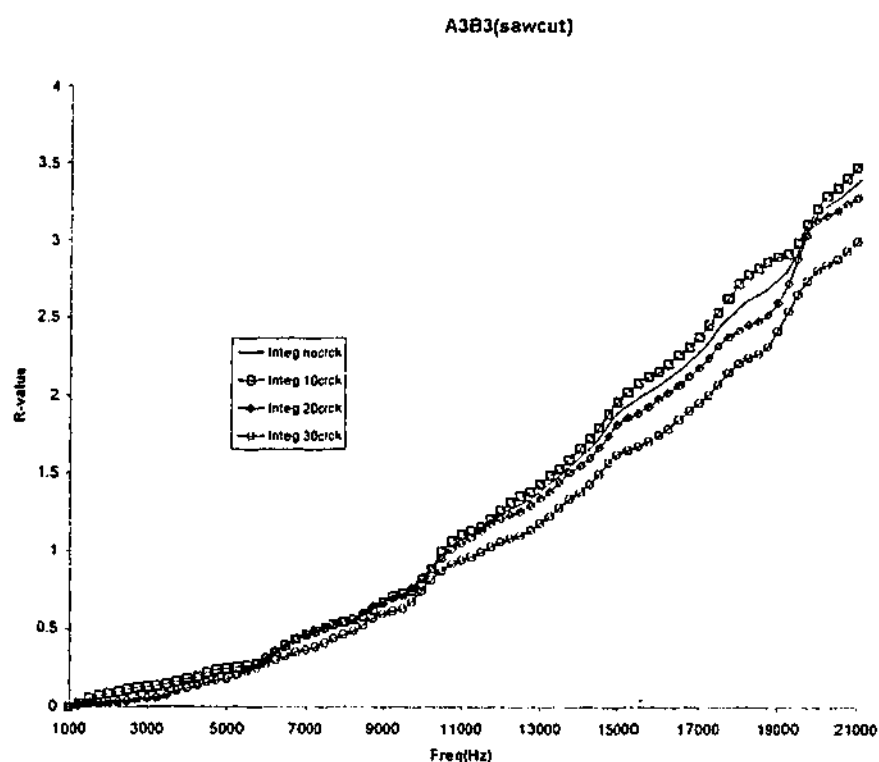


Figure 5.6. TF-data of the area under the frequency spectrum of the pair A3B3 for every damage condition

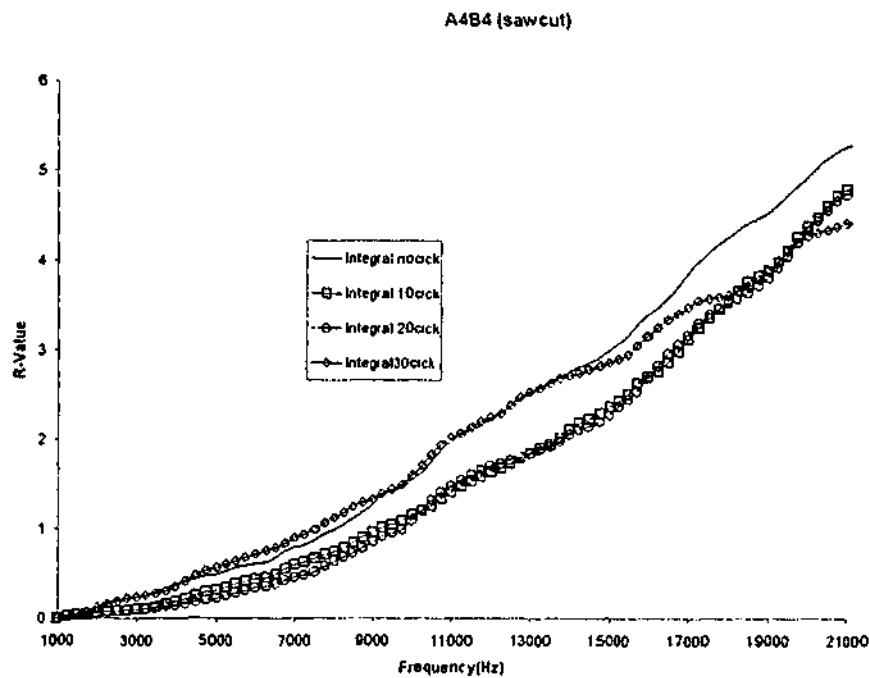


Figure 5.7. TF-data of the area under the frequency spectrum of the pair A4B4

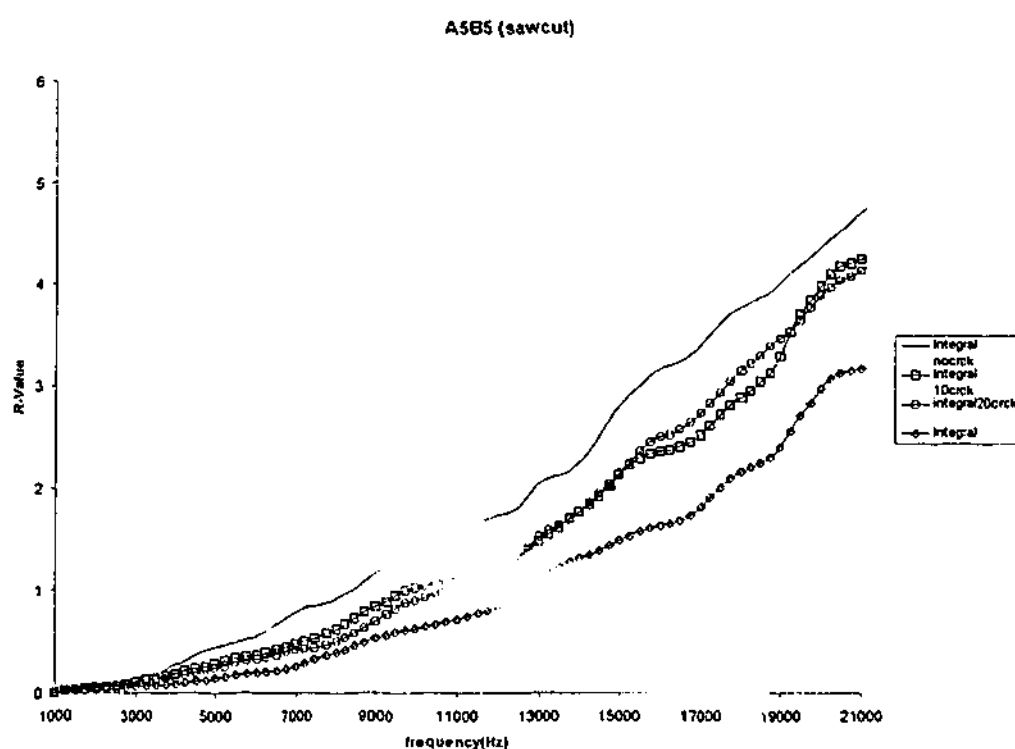


Figure 5.8. TF- data of the area under the frequency spectrum of the pair A5B5 for every damage condition

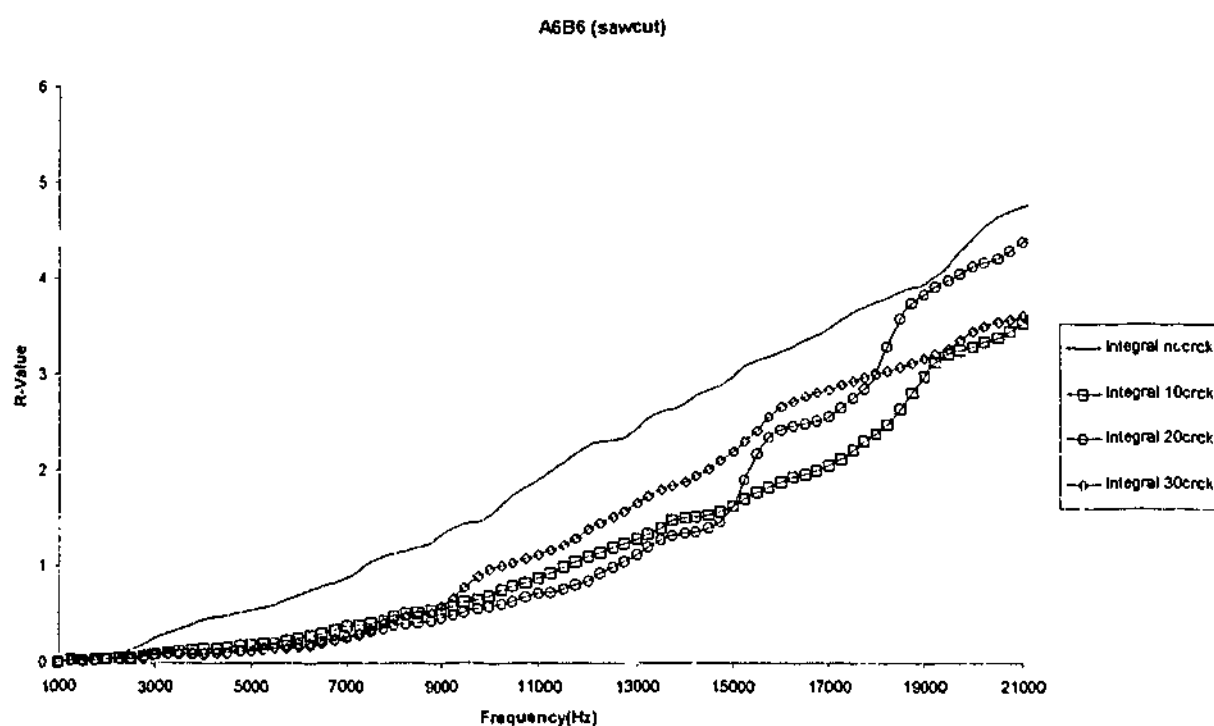


Figure 5.9. TF - data of the area under the frequency spectrum of the pair A6B6 for every damage condition

Analysis of the R-Curve of BnCn Pairs

Figure 5.10 shows the R-values of the pair B1C1 for every damage condition. The area of the pair does not change for all damage conditions. This is because the crack is located far away from the pair. The no-change of the R-values for every damage condition appears also on pairs B2C2 and B3C3 in Figure 5.11 and 5.12. These indicate that the crack is still located relatively far away from these B2C2 and B3C3 pairs. As in the numerical investigation, compared to the A4B4 pair (i.e. Figure 5.7), the R-values of the pair B4C4 in Figure 5.13 also does not change for every damage condition, in this case it appears that the pair B4C4 is less sensitive to the existence of a crack than A4B4. This situation can also be explained by equation [4.6] and can be used to indicate that the damage is located in between rows A and B.

There was an error in signal acquisition for 10-mm crack of the pair B5C5 because the sensor C5 was damaged. The damaged sensor was then replaced but the measurement for the 10-mm crack damage condition was not performed. Therefore, the R-value for the 10-mm crack condition is not shown in Figure 5.14. Looking at reduction of the R-value at 20mm crack this experimental result appears more sensitive than the numerical result (see Figure 4.32). As explained this may be due to the higher reduction of system stiffness in the experiment. The R-value of the pair B6C6 for every damage condition, which is shown in Figure 5.15, is similar to that obtained numerically (see Figure 4.33).

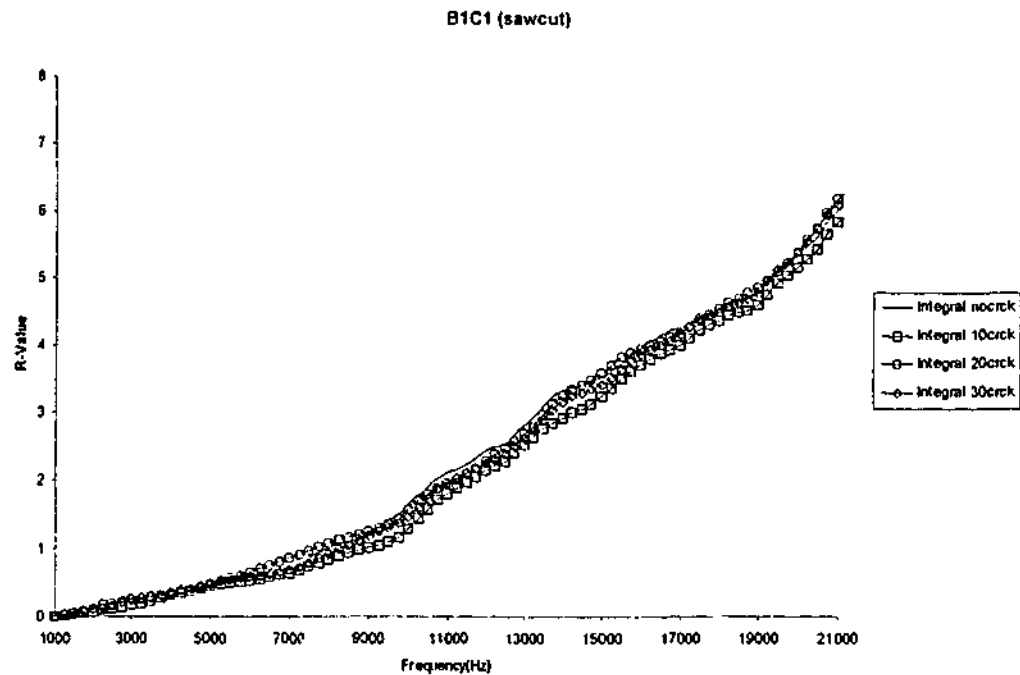


Figure 5.10. TF-data of the area under the frequency spectrum of the pair B1C1 for every damage condition

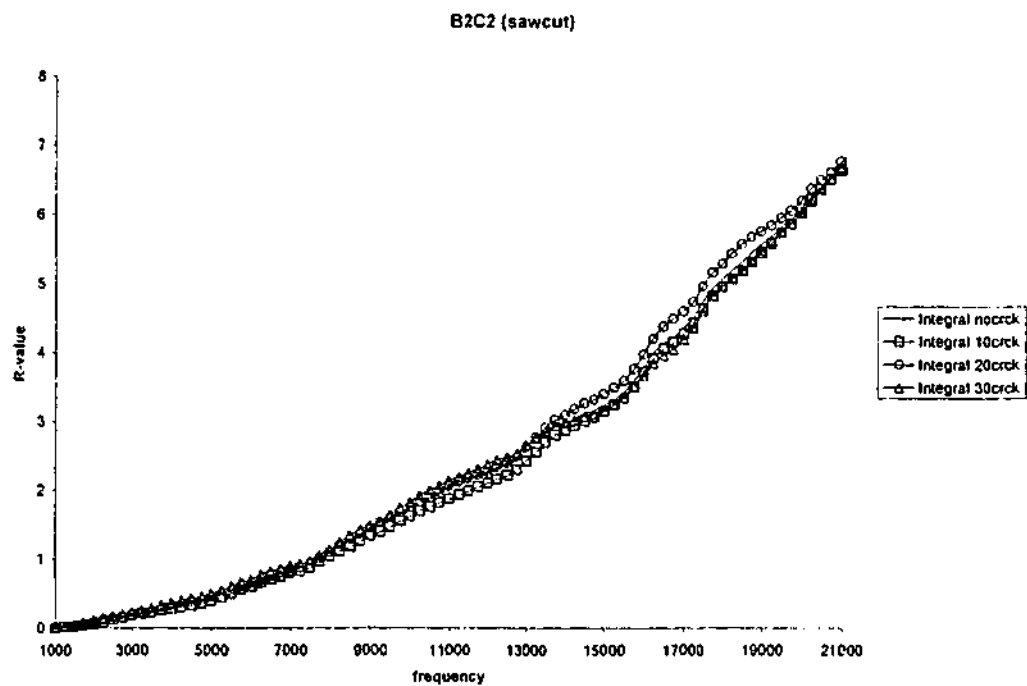


Figure 5.11. TF-data of the area under the frequency spectrum of the pair B2C2 for every damage condition

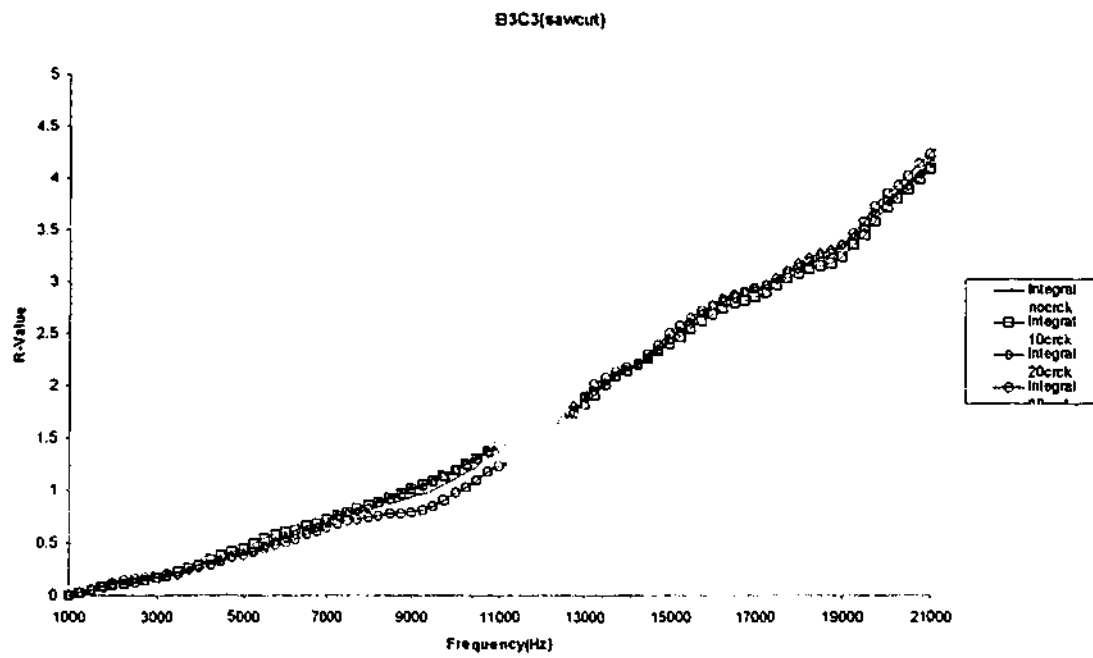


Figure 5.12. TF-data of the area under the frequency spectrum of the pair B3C3 for every damage condition

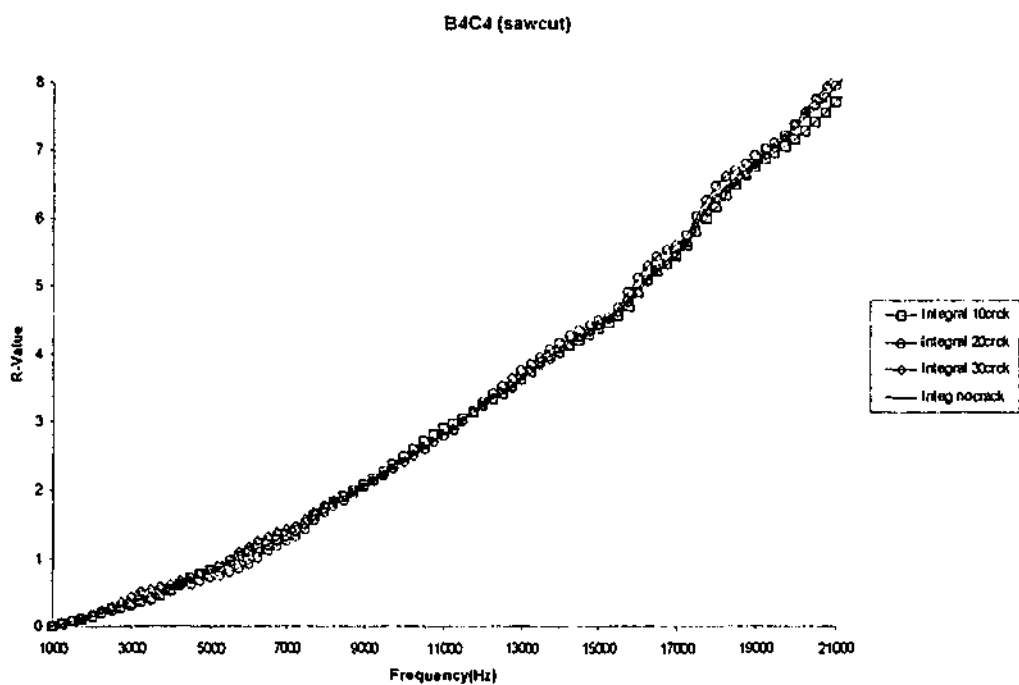


Figure 5.13. TF-data of the area under frequency spectrum of the pair B4C4 for every damage condition

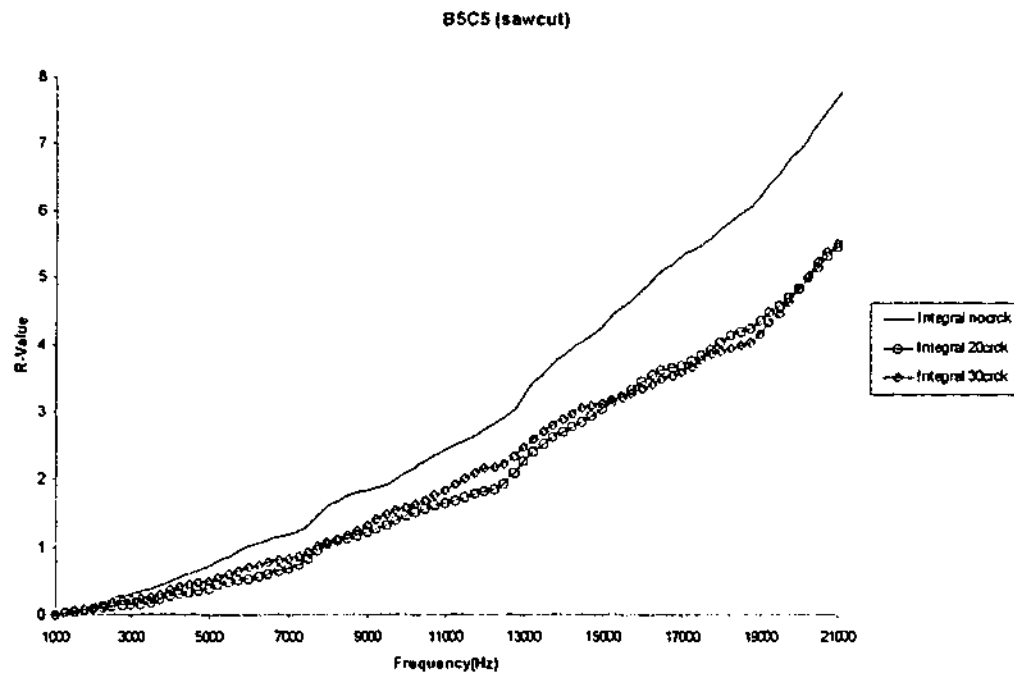


Figure 5.14. TF-data of the area under the frequency spectrum of the pair B5C5 for every damage condition

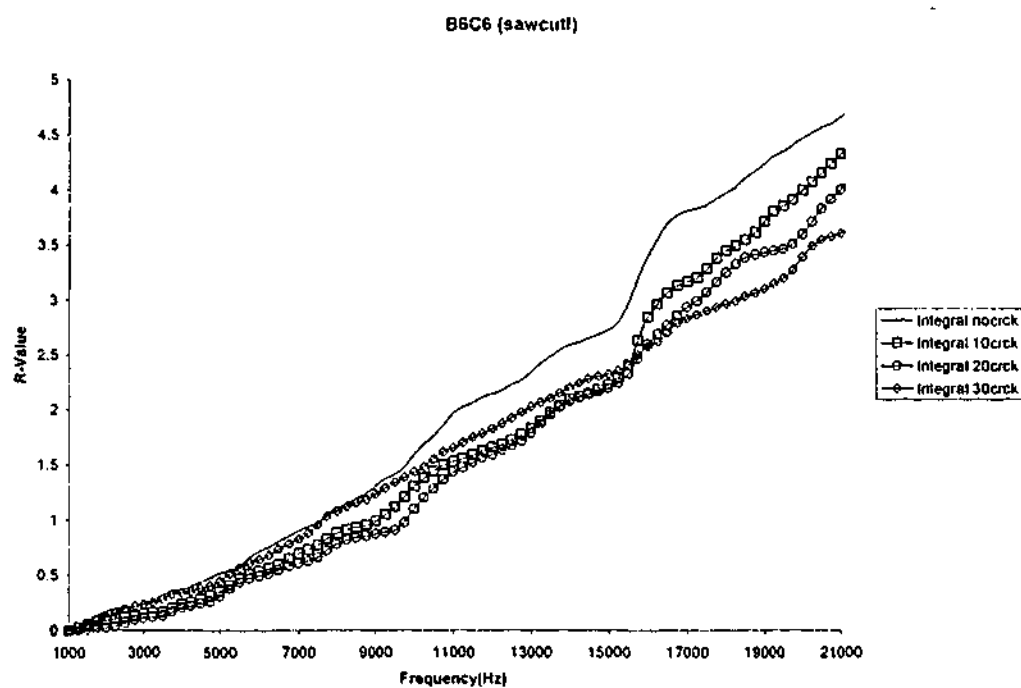


Figure 5.15. TF-data of the area under the frequency spectrum of the pair B6C6 for every damage condition

Table 5.1. Percentage of reduction of R-value from no-damage condition using a direct-TF (saw-cut)

Pairs	A1B1	B1C1	A2B2	B2C2	A3B3	B3C3	A4B4	B4C4	A5B5	B5C5	A6B6	B6C6
cracks												
10mm	-2.2403	3.4053	-1.4771	0.9255	-1.2171	1.6296	11.2556	1.95	9.0318	damage sensor	25.6105	10.4852
20mm	-1.1	-0.951	-1.0352	-2.0376	1.21714	0.2275	12.1129	-1.0065	11.171	29.8628	6.873	19.4273
30mm	2.702	-0.8064	2.51232	1.1122	11.4229	-1.8571	13.5126	-0.9434	32.215	30.1143	22.154	24.051

Sensitivity analysis for AnBn pairs combined with BnCn pairs

As in the numerical investigation, in order to explain the results presented, a sensitivity analysis is carried out on the results of AnBn and BnCn described in the preceding section. Here, it will be shown that the results can be used together to detect and localise the damage. The results of percentage reduction of R-value from the no-damage condition up to 20 kHz for these sensor-actuator combinations are shown in Table 5.1.

The following observation can be made from results shown in Table 5.1:

- The results that are shown in Table 5.1 are consistent with the numerical results that were presented in Table 4.1 in preceding chapter.
- In the numerical results, it was discussed that the reading from A1B1, A2B2, B1C1 and B2C2 should not change considerably at all damage sizes. The results shown in Table 5.1 for these sensor-actuator pair reveals that an experimental error of approximately (-2.5% to 3.5%) can be expected.
- The R-value of the sensor-actuator pair AnBn has a low value except when the crack appeared in front of the pair. For the case of a 10mm crack, the reduction in R-value was observed at pair A6B6 and B6C6.
- For the case of 20mm crack, this crack is located in front of A5B5 (see Figure 5.1b). Looking at the results, a reduction in the R-value was observed for A4B4 and A5B5. The relatively unchanged R-value for B4C4 shows the crack is still located in front of 4th pair of sensor-actuator. Due to the replacement of the damaged sensor for the pair B5C5, a difficulty is expected on this 20mm crack analysis.
- For the 30mm crack case (see Figure 5.1b), the R-value for A4B4 and A3B3 was reduced. It is interesting to notice that the R-value for A4B4 reduced dramatically compared to the A3B3 with B3C3 and B4C4 are still relatively unchanged. The R-values for B5C5 and B6C6

have also reduced dramatically. These results imply that the crack now spans across the 5th and 6th pair of sensor-actuator and the crack tip is approaching the 4th pair. The large reduction in A4B4 implies that the crack is approaching the 4th column of sensor-actuator. However, the insignificant reduction in B4C4 implies that the crack has not developed past the 4th column of sensor-actuator.

The main findings described above consolidates the following inferences drawn in the numerical investigation:

- The pair of sensor-actuator, which encompasses the crack (i.e. A_nB_n), will show a reduction in the R-value prior to the B_nC_n pairs. This can be used to indicate across which row of sensor-actuator the crack appears (i.e. between A and B or B and C).
- It is important also to note that the B_nC_n are also an important part of the monitoring procedure. The R-values of the B_nC_n pairs can be used to indicate the extent of the crack. This is because a large R-value reduction is obtained when the crack face spans across a B_nC_n pair.

Analysis of the R-Curve of A_nB_{n+1} Cross-Pairs

As in the numerical investigation, in this section of work, the cross-TF will be used to confirm the location of the crack implied in the previous section. Figure 5.16 shows the TF-data of the area under the frequency spectrum of the pair A1B2 for every damage condition. The area of the pair does not change for the all damage conditions. This is because the crack is far away from the pair. The relatively unchanged R-values continue for the pair A2B3 and A3B4 in Figure 5.17 and 5.18. This is because these A2B3 and A3B4 pairs still cannot sense the changes of the stiffness in the damage location.

In Figure 5.19, for all damage conditions, the area under the frequency spectrum of the pair A4B5 is smaller than the no-damage conditions. This situation is different with the numerical results where only 30mm-crack area is decreased. Since the crack tip for the 30mm lies between the pair A4B5 (see Figure 5.1b), this pair may be used to locate this crack tip. This conclusion was also reached in the numerical work.

Figure 5.20 shows R-value of the pair A5B6 for every damage condition. For all damage conditions, the area under the frequency spectrum is smaller than the no-damage condition. The area under the frequency spectrum is decreased proportionally to the damage conditions. These experimental results confirm the numerical ones.

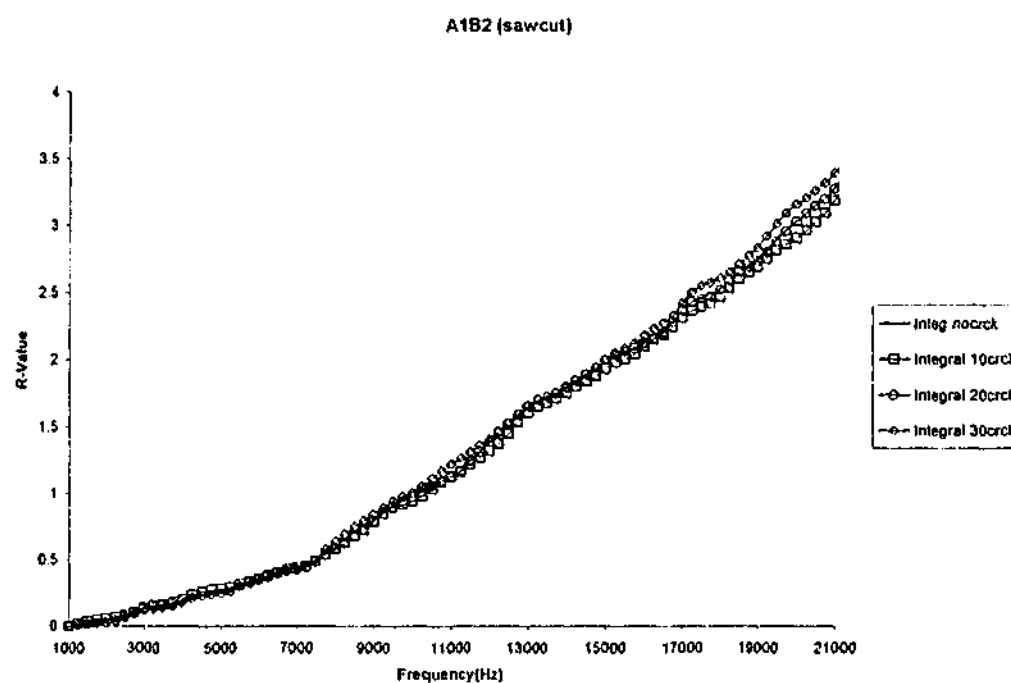


Figure 5.16. TF-data of the area under the frequency spectrum of the pair A1B2 for every damage condition

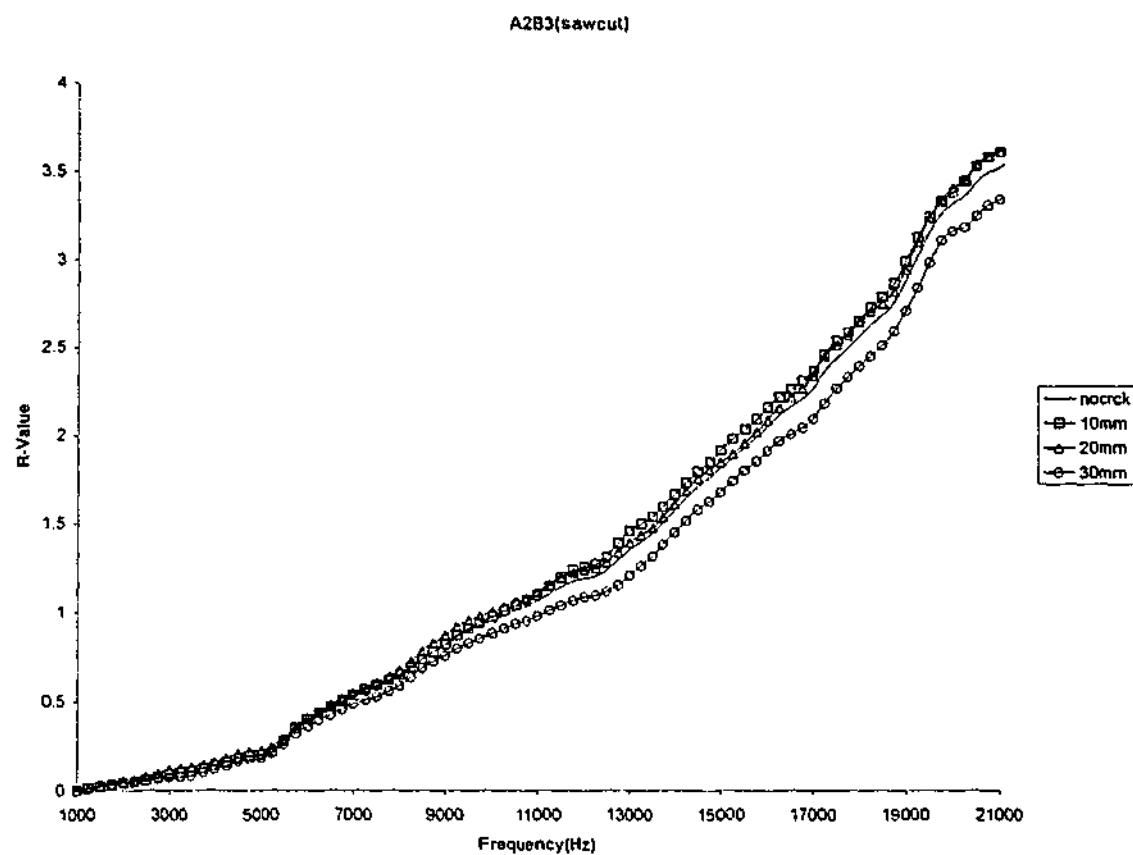


Figure 5.17. TF-data of the area under the frequency spectrum of the pair A2B3 for every damage condition

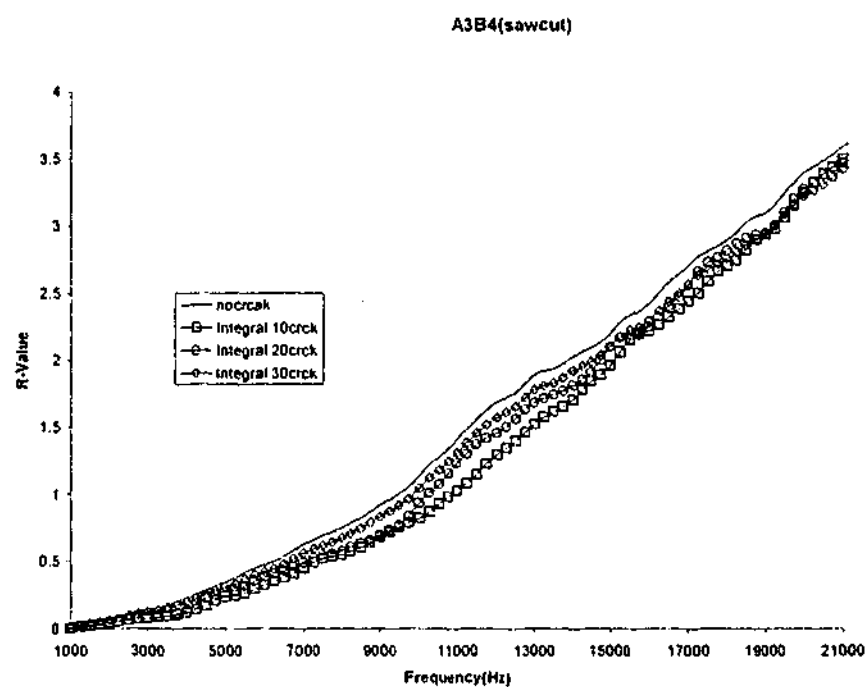


Figure 5.18. TF-data of the area under the frequency spectrum of the pair A3B4 for every damage condition

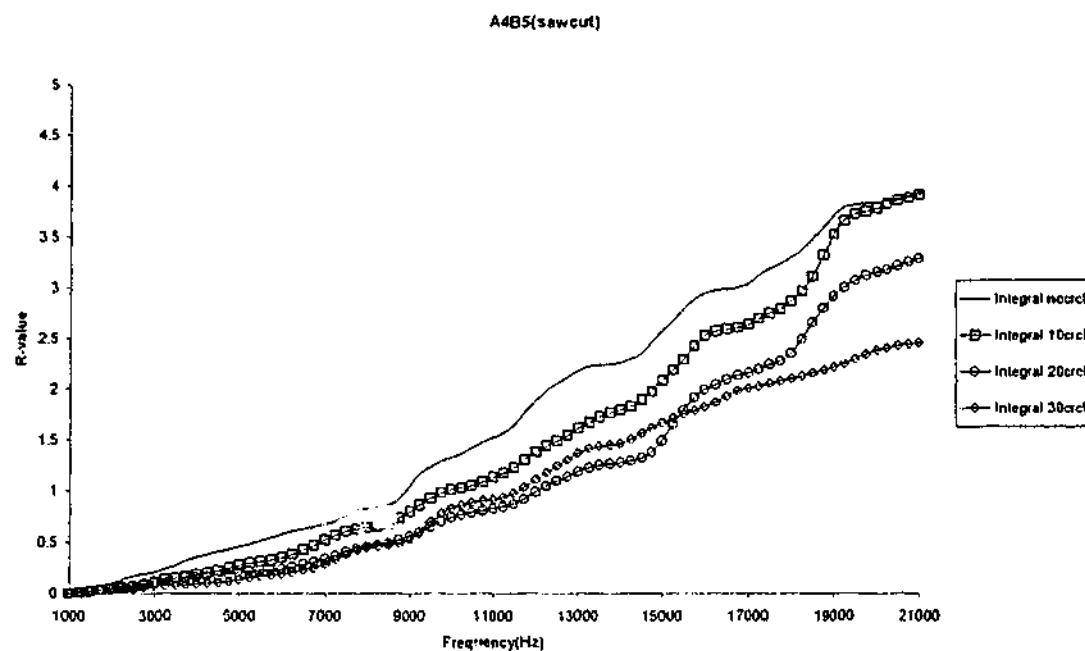


Figure 5.19. TF-data of the area under the frequency spectrum of the pair A4B5 for every damage condition

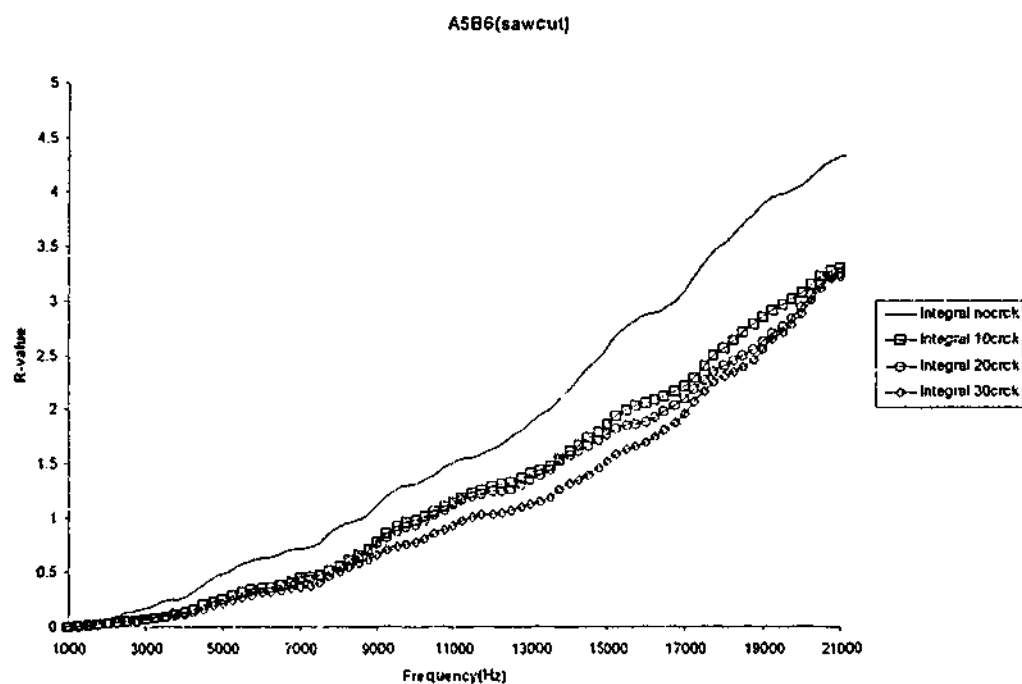


Figure 5.20. TF-data of the area under the frequency spectrum of the pair A5B6 for every damage condition

As in the numerical investigation, looking at the reduction of R-value the TF from cross-pair can be applied to locate approximately the crack tip. To help in the interpretation of these results the reduction in the R-value up to 20 kHz for the situation described above are tabulated in Table 5.2.

Table 5.2. Percentage of reduction of R-value from no-damage condition using a cross-TF (saw-cut)

Pairs	A1B2	A2B3	A3B4	A4B5	A5B6
Cracks					
10mm	4.1298	-1.9322	4.3949	1.6278	24.2575
20mm	0.0696	-2.7076	3.4623	17.8264	27.5614
30mm	-4.1994	4.63973	5.0833	37.9261	28.9774

Looking at the results in Table 5.2, the following can be observed:

- In the numerical results, it was shown that the R-value from A1B2, A2B3, and A3B4 should have a relatively insignificant change at all damage sizes. An experimental error for this case is approximately from -4.2% to 5.1%.
- The A4B5 sensor-actuator pair appears to have higher sensitivity than that in the numerical result. This pair can sense the 20mm crack case that did not occur at numerical investigation. This confirms the hypotheses that the crack induced here resulted in a lower stiffness than that obtained numerically. This result shows that the 30mm crack tip is located between the sensor A4 and the actuator B5 (See Figure 5.1b).
- As in the numerical investigation, a significant reduction that occurs for the pairs A5B6 allows for the detection of a 10mm crack. This implies that its crack tip is located in the vicinity of sensor A5 and actuator B6. (See Figure 5.1b)

These experimental results have shown that in general this R-curve concept can be applied to detect and locate the artificial crack resulted from the saw cut. In the next section, the applicability of this R-curve

concept will be extended to detect the fatigue crack growth resulting from the cyclic load in an MTS machine.

5.3. Experimental Investigation of the Clamped Plate with the Fatigue Crack Growth

An aluminum test plate was subjected to a constant amplitude cyclic loading from Material Test System (MTS) machine (See Figure 5.21). A loading cycle of $15 \pm 15\text{kN}$. This loading cycle was used to cause fatigue crack growth in the specimen. A fatigue crack of 10mm was obtained after 450,000 cycles. The loading was continued up to 730,000 cycles where a fatigue crack length of 16mm was obtained. The experiment was continued until a crack length of 28mm was obtained (i.e. up to 810,000 cycles). A Halec Eddy current crack detector was used (See Figure 5.22) to detect and monitor this crack growth. A schematic diagram of this experimental setup is shown in the Figure 5.23. At certain crack sizes; the transfer function was measured using a method described on the Section 5.1. The TF measurement was performed over these three different crack lengths.

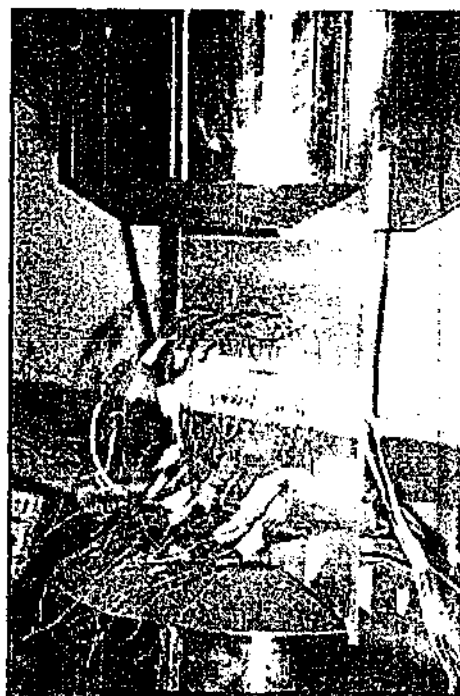


Figure 5.21. The plate specimen that is clamped on the MTS machine

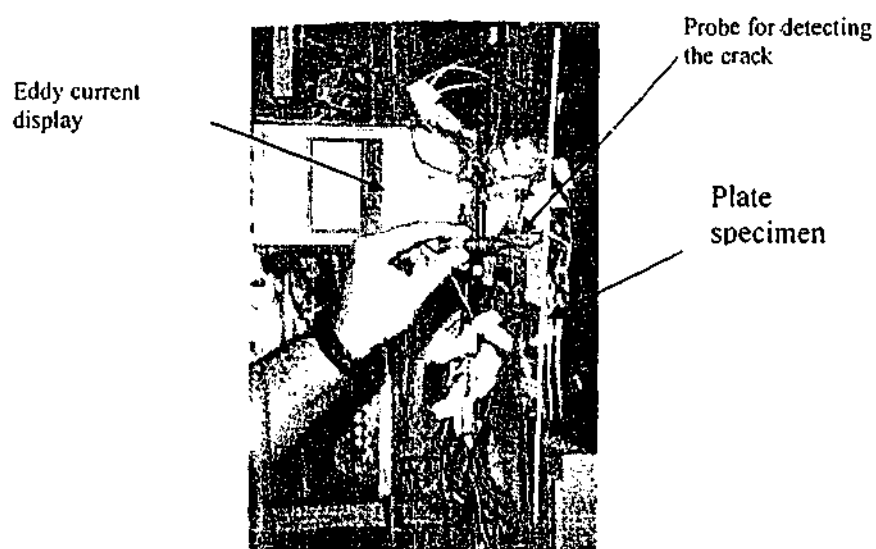


Figure 5.22. A Halec Eddy current crack detector

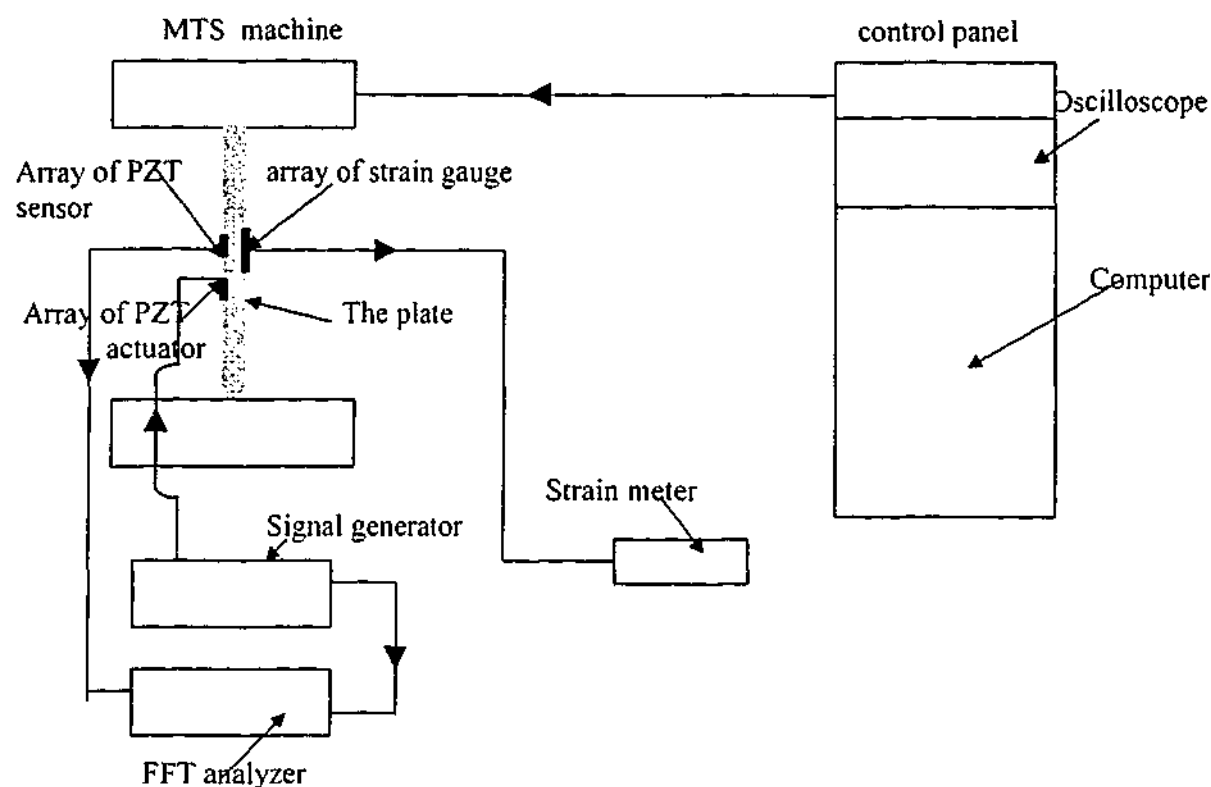


Figure 5.23. Schematic diagram of Transfer Function method for a detection of the fatigue crack

5. 4. Results and Discussions

In this experiment the 10-mm, 16-mm and 28-mm crack cases were evaluated using the TF technique described earlier. The position of the cracks relative to the sensor-actuator pair is shown in Figure 5.24. The R-curves from this experimental investigation for the direct-pairs $A_n B_n$, $B_n C_n$, where $n=1...6$, and the cross-pairs $A_n B_{n+1}$, where $n=1...5$ under the three damage conditions i.e. 10mm, 16mm, 28mm crack cases including the no-damage condition are presented.

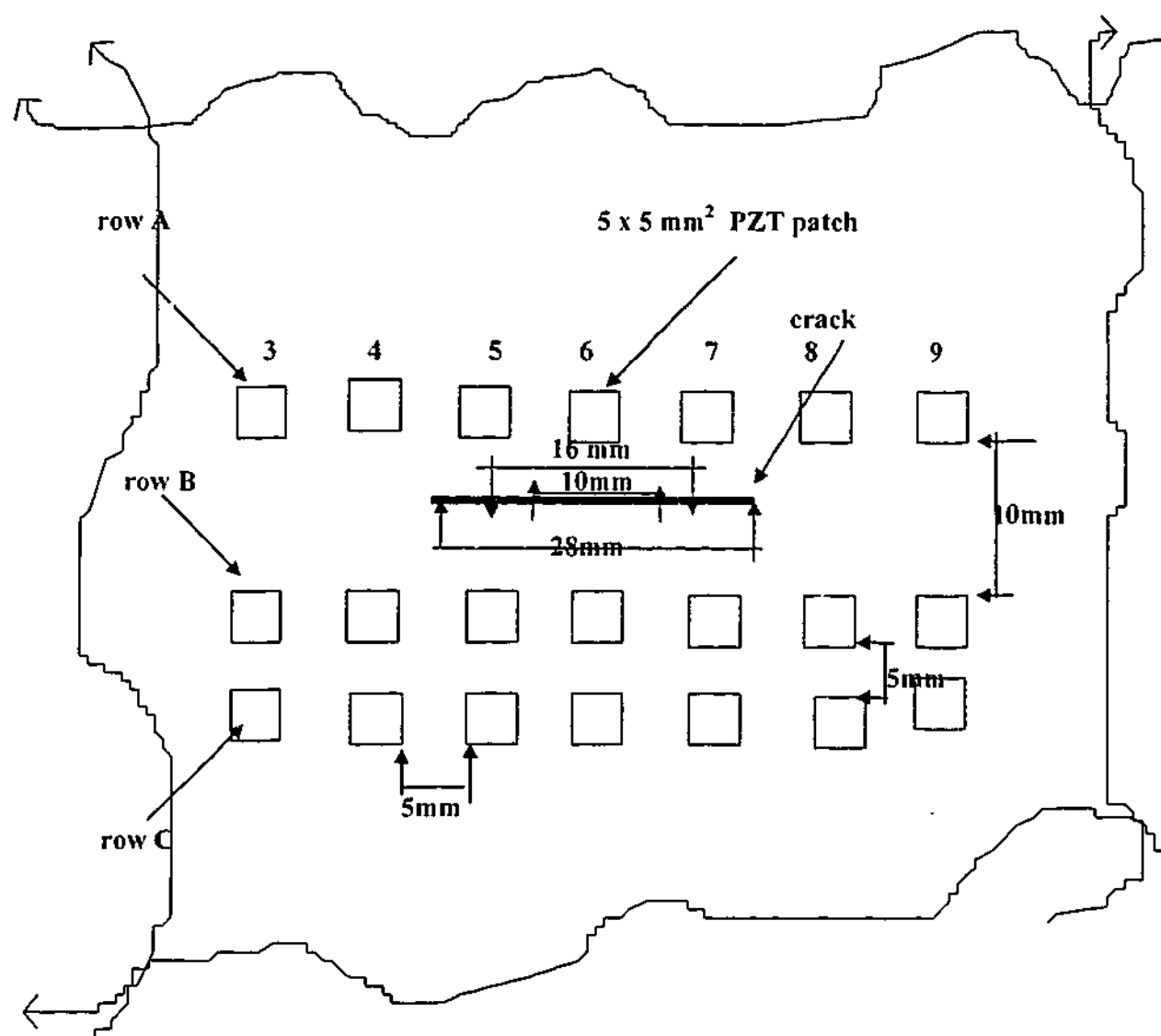


Figure 5.24. Detailed position of the occurred fatigue cracks in the test Plate

Analysis of the R-Curve of AnBn Pairs

Figure 5.25, 5.26, and 5.27 show the R-value for the sensor-actuator pairs A1B1, A2B2, and A3B3 for every damage condition. As expected from the numerical simulation, the R-value for these pairs remain relatively unchanged for all damage conditions. This is because the location of the crack is far away from these pairs. In Figure 5.28 for the 16, 28 -mm crack, the area under the frequency spectrum of the pair A4B4 is smaller than the no-damage condition and 10-mm crack. This situation is very similar to the numerical simulation. This pair cannot

sense the 10-mm crack because the 10mm is relatively still far away from this pair, but as the crack grows to 16 and 28 mm this pair are able to detect the cracks.

Figure 5.29 shows the R-value of the pair A5B5 for every damage condition. For all damage conditions, the area under the frequency spectrum is smaller than the no-damage condition. The detection of the damage by this pair starts at early phase (10mm crack) since the crack located relatively close to this pair. This situation confirms the numerical results. The results for the pair A6B6 can be obtained in Figure 5.25. As in the numerical results, the 10-mm crack has a more significant reduction of R-value than the 16mm and 28mm cracks. This indicates that all cracks are large and have extended across this actuator-sensor A6B6 pair. As discussed in the previous section, the change in boundary conditions at the crack face (16mm and 28mm crack length) led to a change in the TF response.

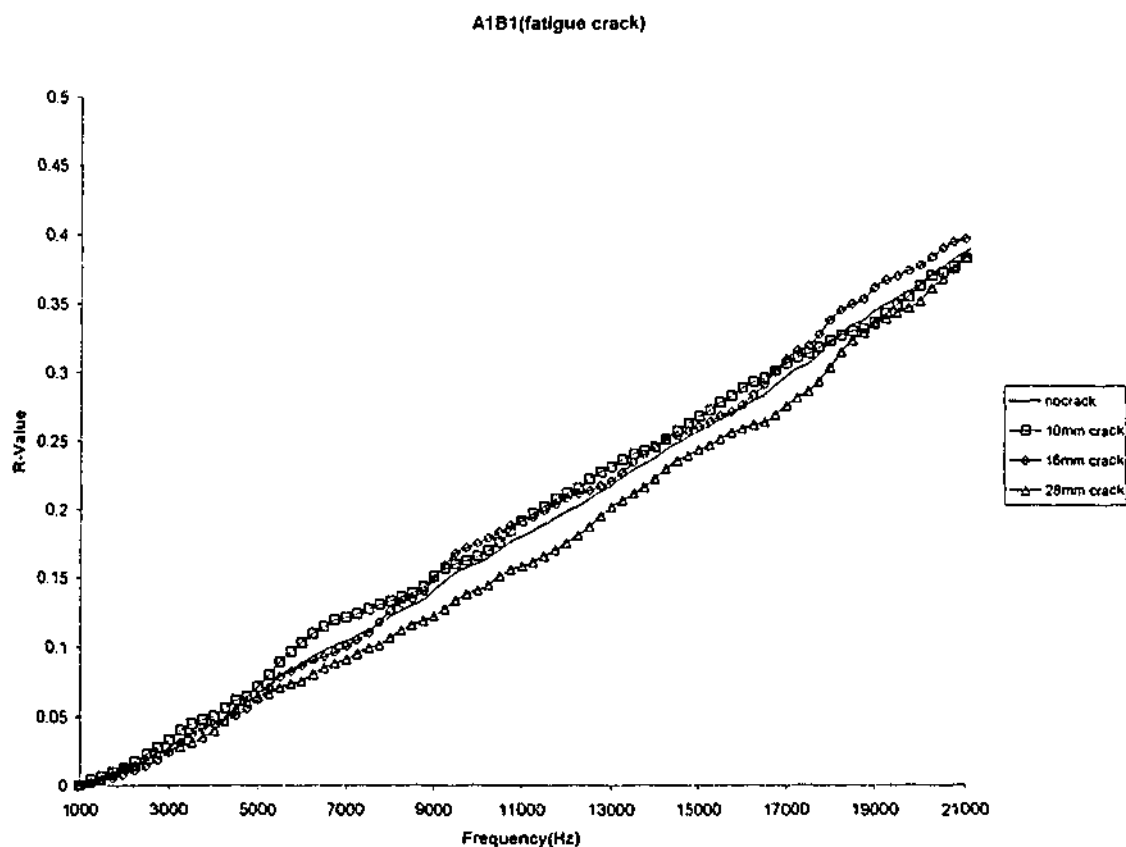


Figure 5.25. R-curve of pair A1B1

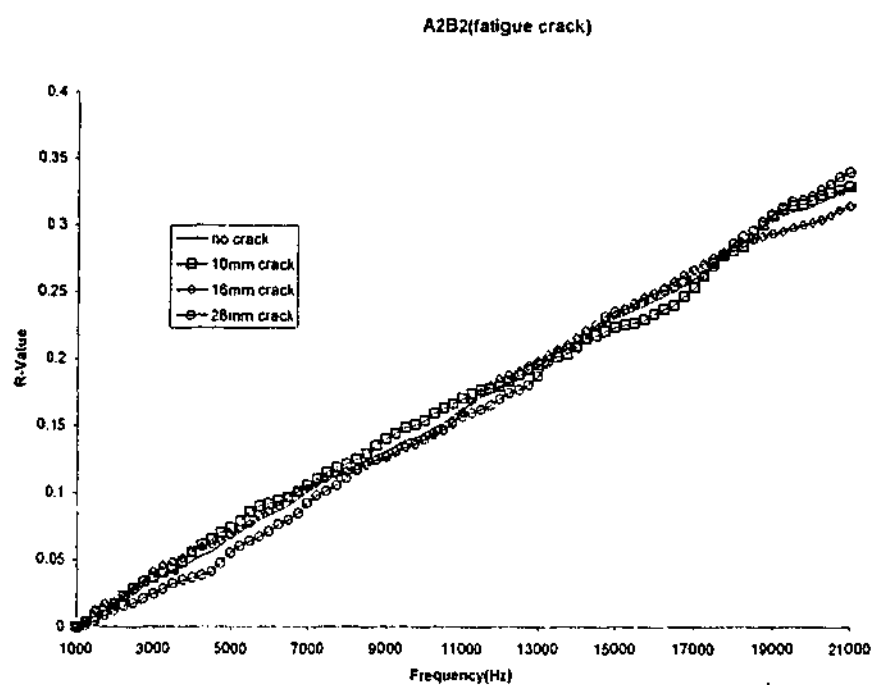


Figure 5.26. R-curve of pair A2B2

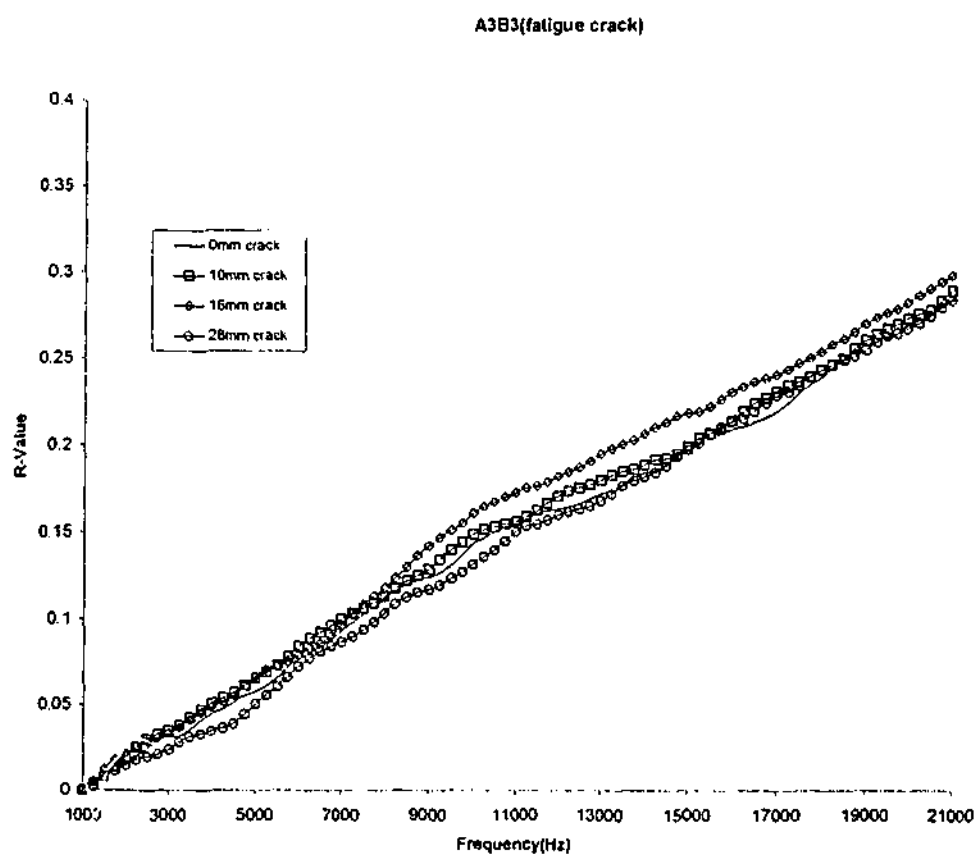


Figure 5.27. R-curve of pair A3B3

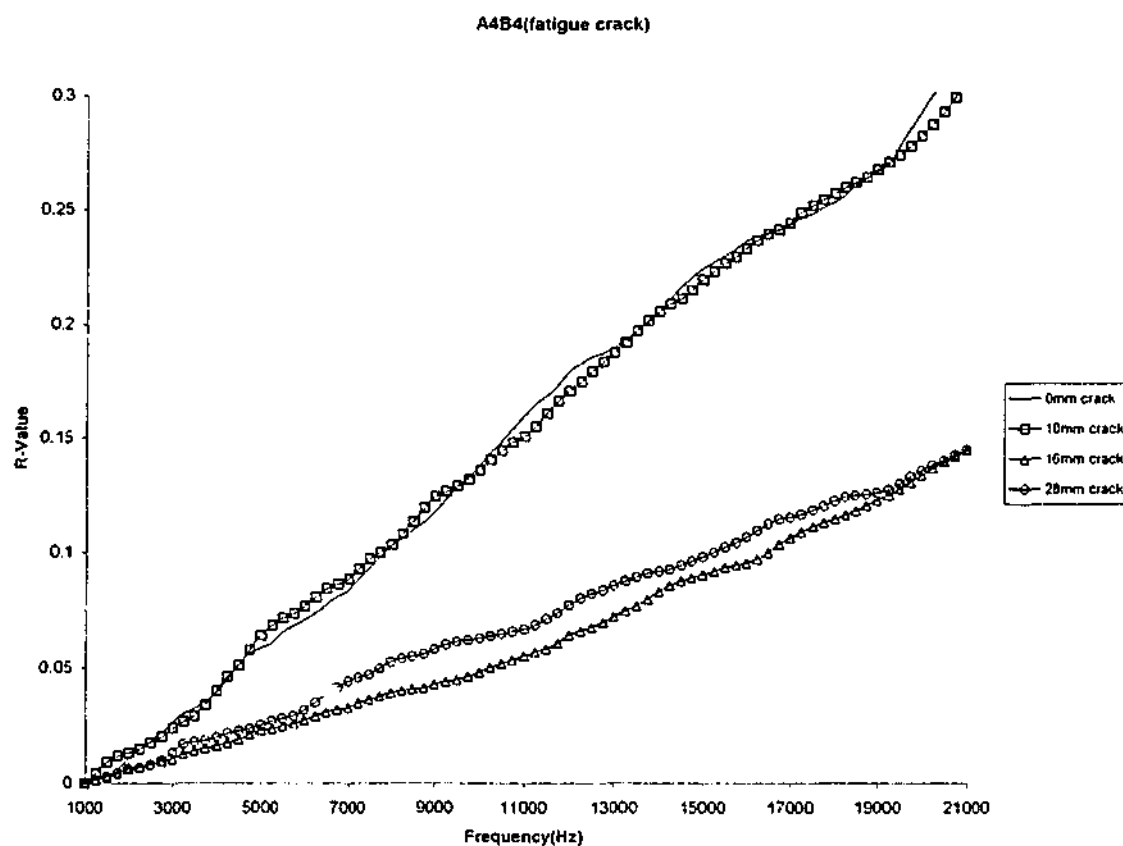


Figure 5.28 R-curve of pair A4B4

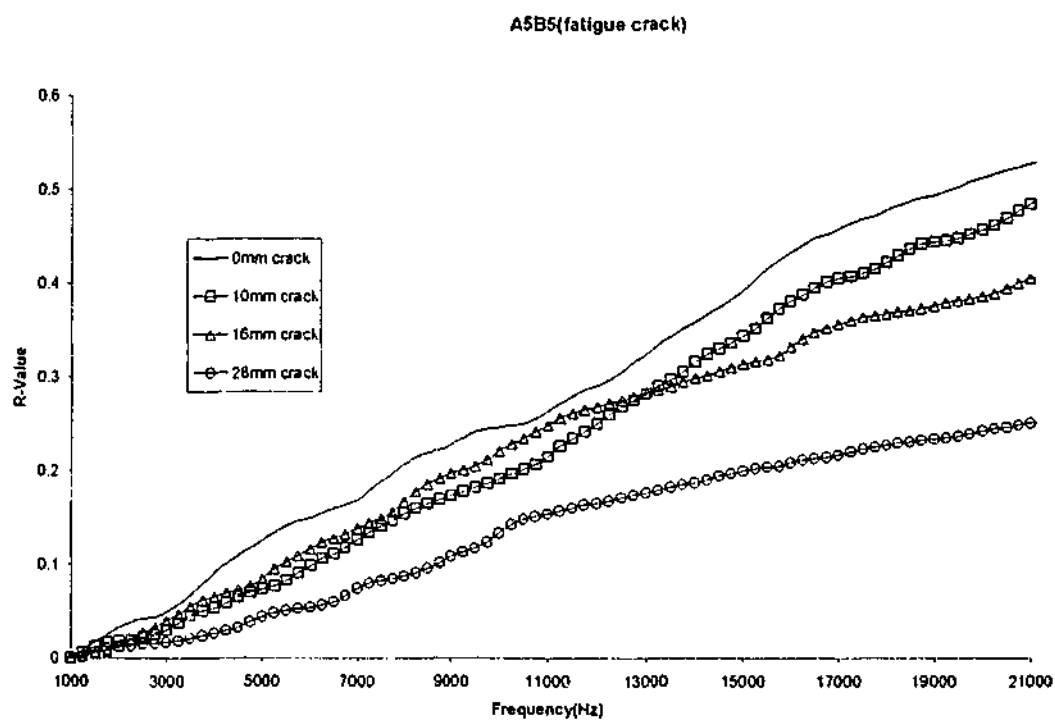


Figure 5.29. R-curve of pair A5B5

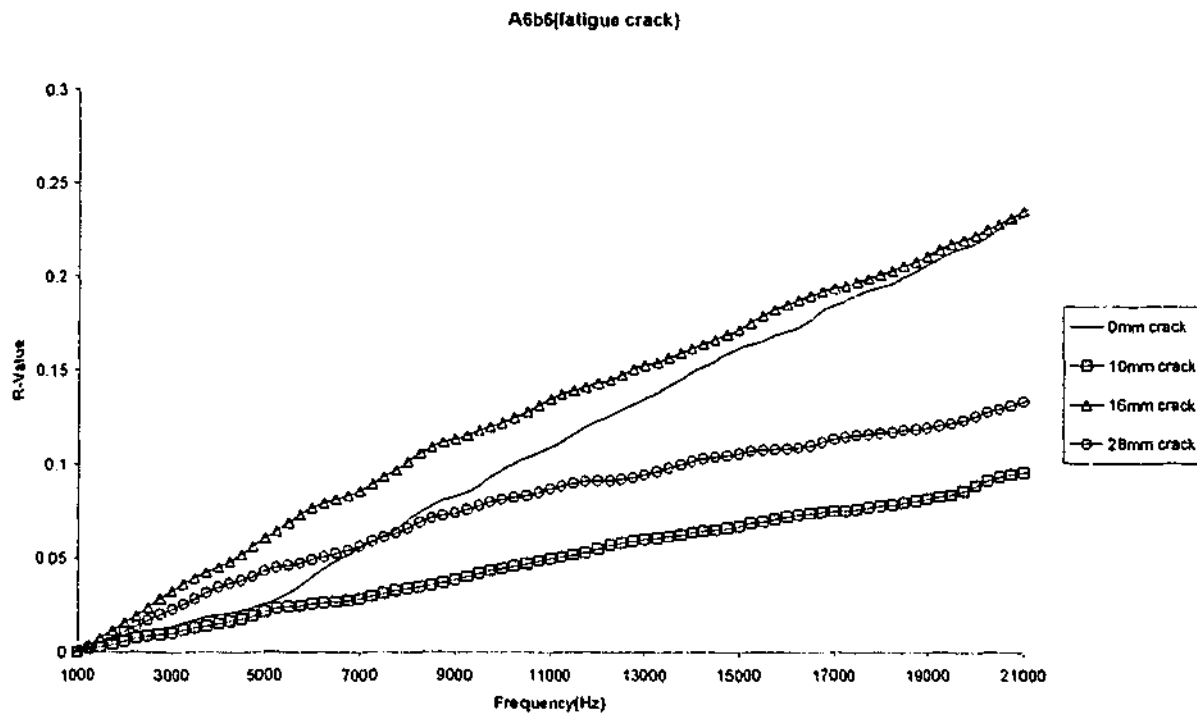


Figure 5.30. R-curve of pair A6B6

Analysis of the R-Curve of BnCn Pairs

Figure 5.31, 5.32, and 5.33 show the R-value for the pair B1C1, B2C2, and B3C3 for every damage condition. As shown in the numerical simulation, the R-value of the pair relatively does not show significant change for all damage conditions. This is because the crack is far away from these pairs. As in the numerical results in Figure 5.34 the R-value of the pair B4C4 for every damage condition relatively remain unchanged. As previously discussed, this indicates the insensitivity of this pair compared to A4B4. The changes of the R- Curve for the pair B5C5 is shown in Figure 5.35. Here, the R-values of all damage conditions are below the no damage, and decrease with increasing damage conditions. The R-value of the pair B6C6 for every damage condition, which is shown in Figure 5.36, again shows the R-curve decreasing proportionally to the damage conditions.

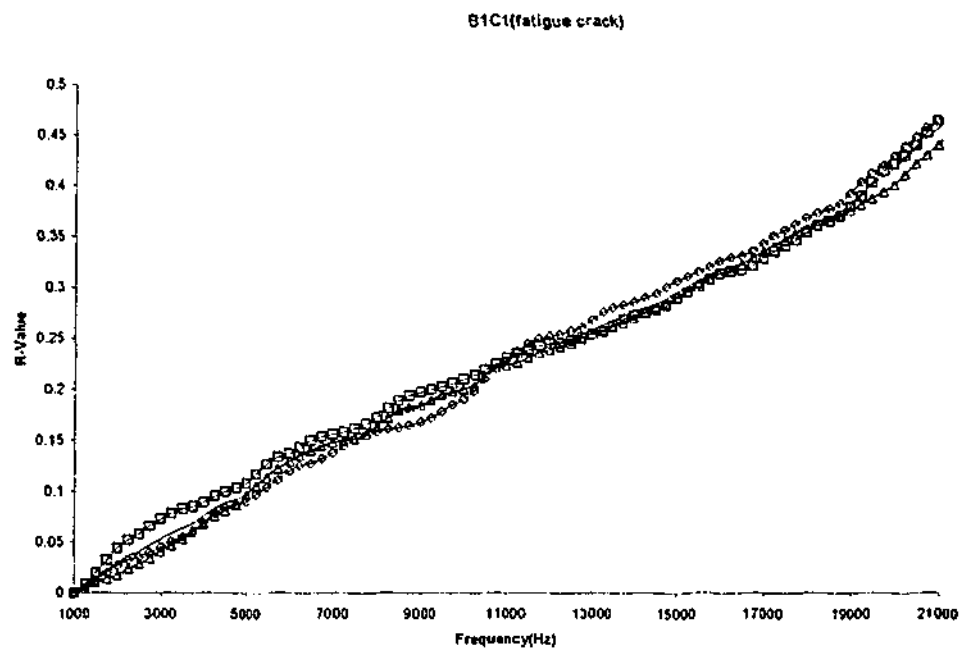


Figure 5.31. R-curve of pair B1C1

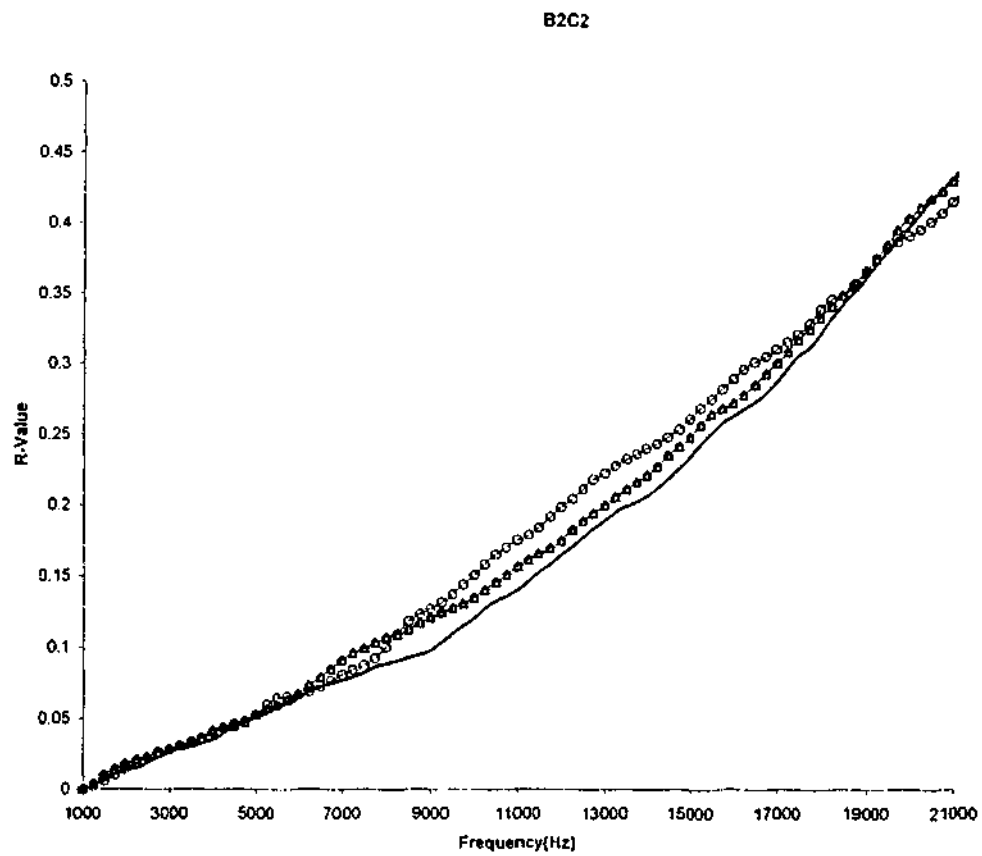


Figure 5.32. R-curve of pair B2C2

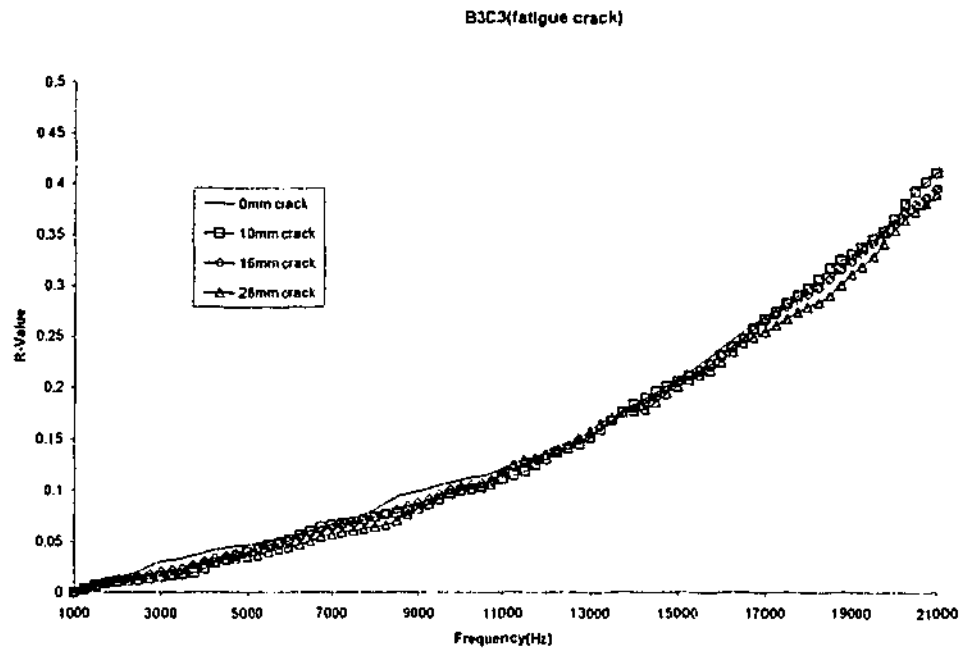


Figure 5.33. R-curve of pair B3C3

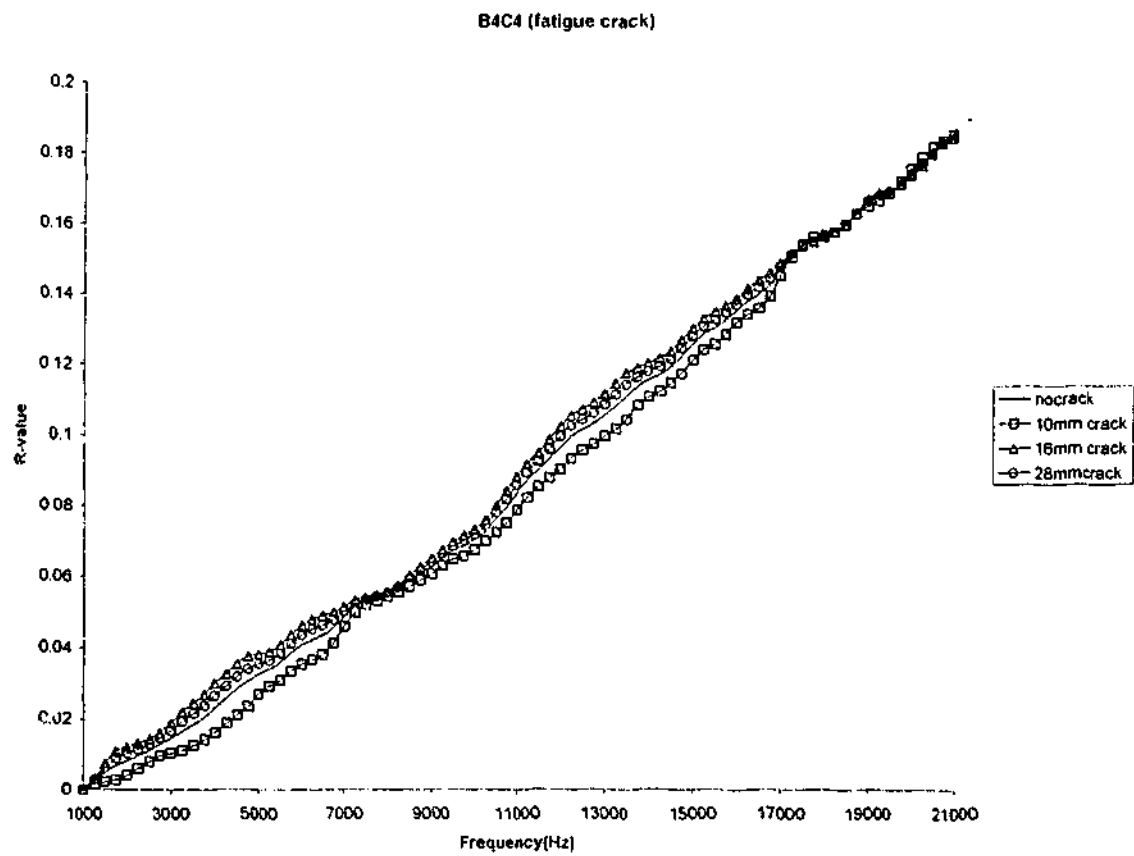


Figure 5.34. R-curve of pair B4C4

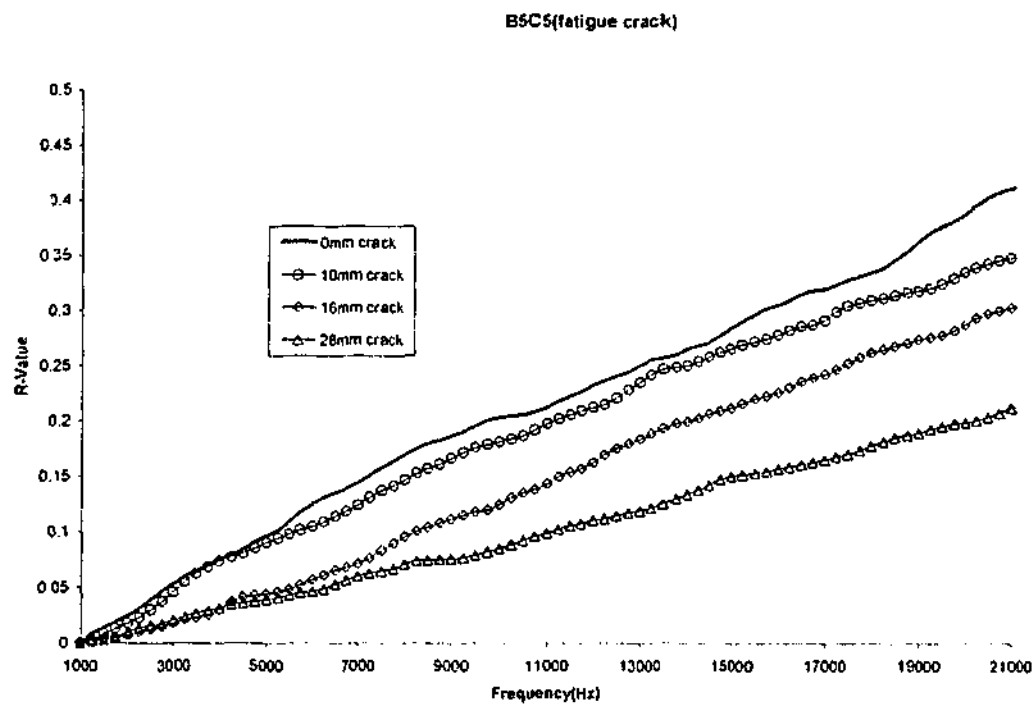


Figure 5.35. Curve of pair B5C5

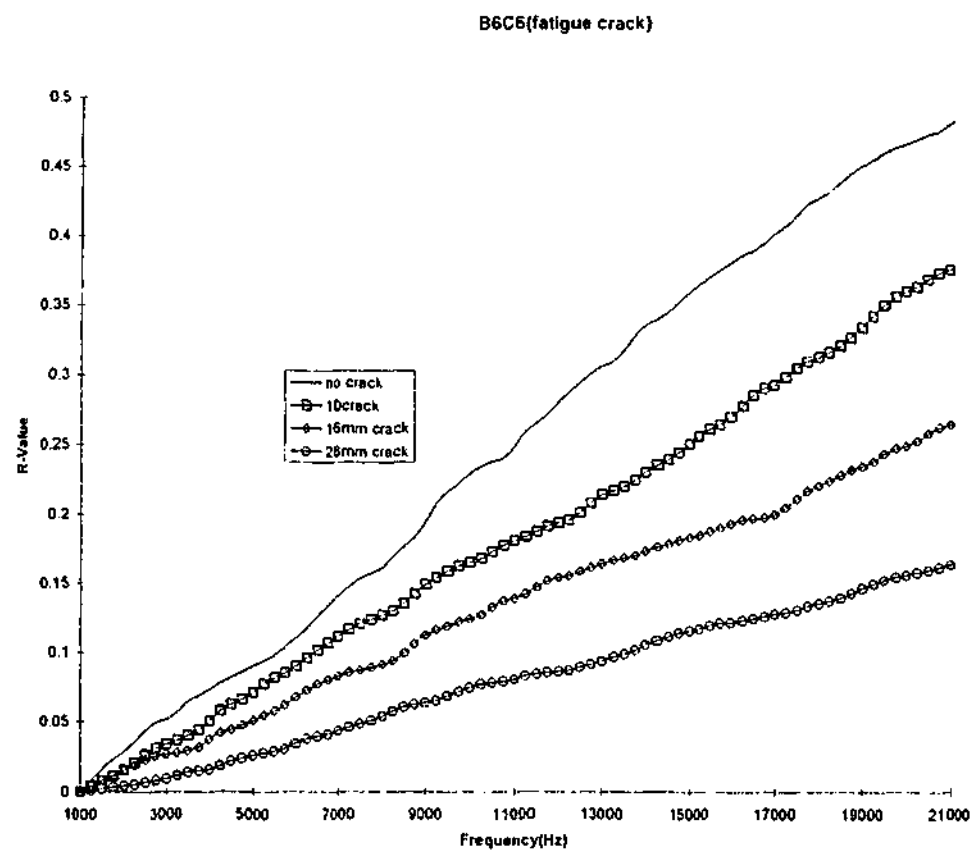


Figure 5.36. R-curve of pair B6C6

Sensitivity analysis for AnBn pairs combined with BnCn pairs

As in previous section, to explain the results presented above, a sensitivity analysis is carried out to the results of AnBn and BnCn described in the preceding section. The results of percentage reduction of R-value from the no-damage condition up to 20 kHz for these sensor-actuator combinations are tabulated in Table 5.3.

Following remarks can be inferred from the results presented on the table above:

- As expected from the numerical simulation, in Table 5.3 the pairs A1B1&B1C1, A2B2&B2C2, and A3B3&B3C3 show insignificant reduction of R-value because of the distant position of these pairs from the crack region. The experimental error limit does not exceed the error limit on the preceding section (-4.2% to 5.1%) i.e. Table 5.2.
- Looking at the reduction of R-value it can be said that the pair B4C4 is less sensitive than the pair A4B4. These results imply that the damage is located in rows A and B.
- For the sensor-actuator pairs A5B5 and B5C5 the results in Table 5.3 show the similarity reduction magnitude of R-value. Such a trend has been also shown in the numerical investigation. This situation can be used to indicate that at 10mm and 16mm the crack are still in front of the pairs. When the crack has extended cross the pairs i.e. 28mm crack case, a more significant reduction of R-value is expected.
- The significant reduction in pairs A6B6 for 10mm crack case and the significant reduction of the R-values accordingly to the increasing crack length in pair B6C6 indicate the cracks were large and has extended cross this sensor-actuator A6B6 pair.
- It is interesting to note that although the crack lengths (i.e. 16mm and 28mm) from the fatigue, were different from those in the numerical simulation (i.e. 20mm and 30mm) the trend of responses of sensor-actuator pairs show a similarity between them.

Table 5.3. Percentage of reduction of R-Value from no-damage condition using a direct-TF (Fatigue crack)

Pairs	A1B1	B1C1	A2B2	B2C2	A3B3	B3C3	A4B4	B4C4	A5B5	B5C5	A6B6	B6C6
cracks												
10mm	0.3963	-0.9607	-1.4745	-1.5642	0.3963	-0.4626	3.6557	-0.4942	10.9168	13.5003	59.1889	22.8331
16mm	-3.6965	-2.885	3.9551	2.6138	-3.6965	0.6647	54.3391	0.49423	24.7227	25.7015	-2.0866	46.5732
28mm	3.3002	3.8457	-2.4806	1.50803	3.3002	2.4567	53.5626	0.24711	52.7061	48.6924	42.0516	66.5057

Analysis of the R-Curve of A_nB_{n+1} Cross-Pairs

As discussed in the previous section, this cross-TF will be used to confirm the location of the crack implied in the previous section.

Figure 5.37 shows R-value for the pair A1B2 for every damage condition. The area of the pair does not change for the all damage conditions. This is because the crack is far away from the pair. The relatively unchanged R-values continued for the pair A2B3 and A3B4 in Figure 5.38 and 5.39. This is because these A2B3 and A3B4 pairs still can not sense the changes of the stiffness in the damage location. In Figure 5.40, for all damage conditions, the area under the frequency spectrum of the pair A4B5 is smaller than the no-damage conditions. This situation is similar to the saw cut results where only 30 mm-crack area is decreased. Here, in this experimental work, the 28mm crack, their areas are the lowest. Since the crack tip for the 28mm approximately lies between the pair A4B5 (see Figure 5.24), this pair may be used to locate this crack tip. This conclusion was also reached in the numerical and saw cut cases. Figure 5.41 above shows R-value of the pair A5B6 for every damage condition. For all damage conditions, the area under the frequency spectrum is smaller than the no-damage condition. The area under the frequency spectrum is decreased proportional to the damage conditions. These experimental results confirm the numerical simulations and the saw cut results.

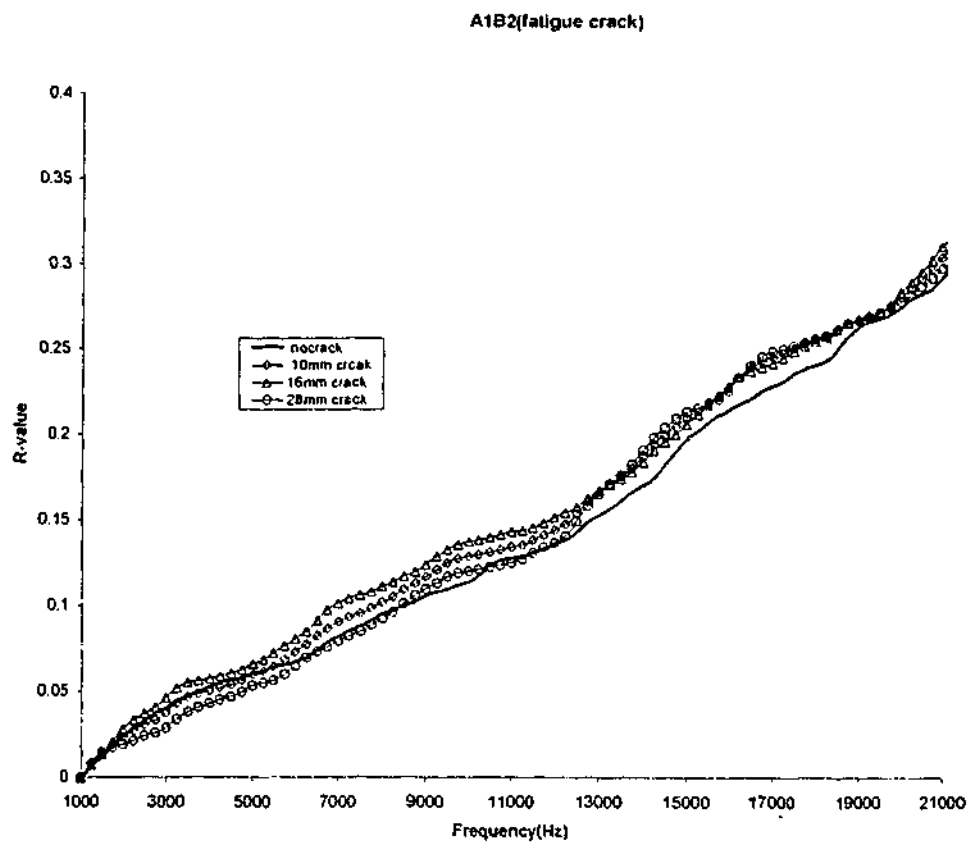


Figure 5.37. R-curve of pair A1B2

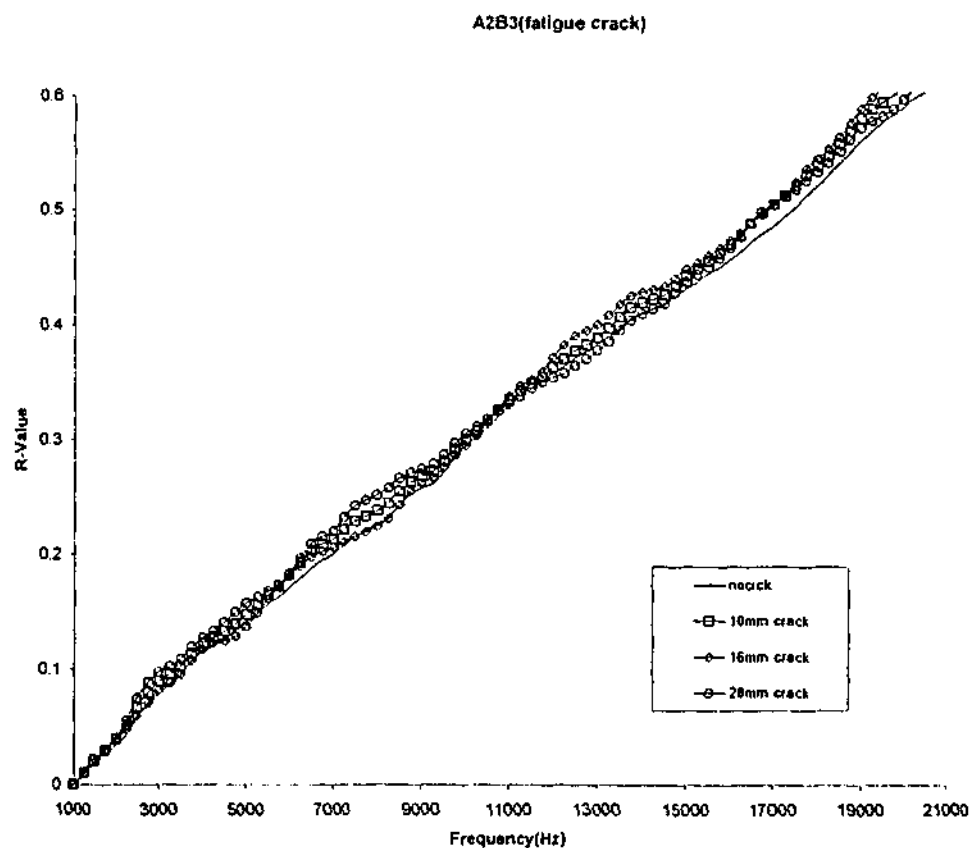


Figure 5.38. R-curve of pair A2B3

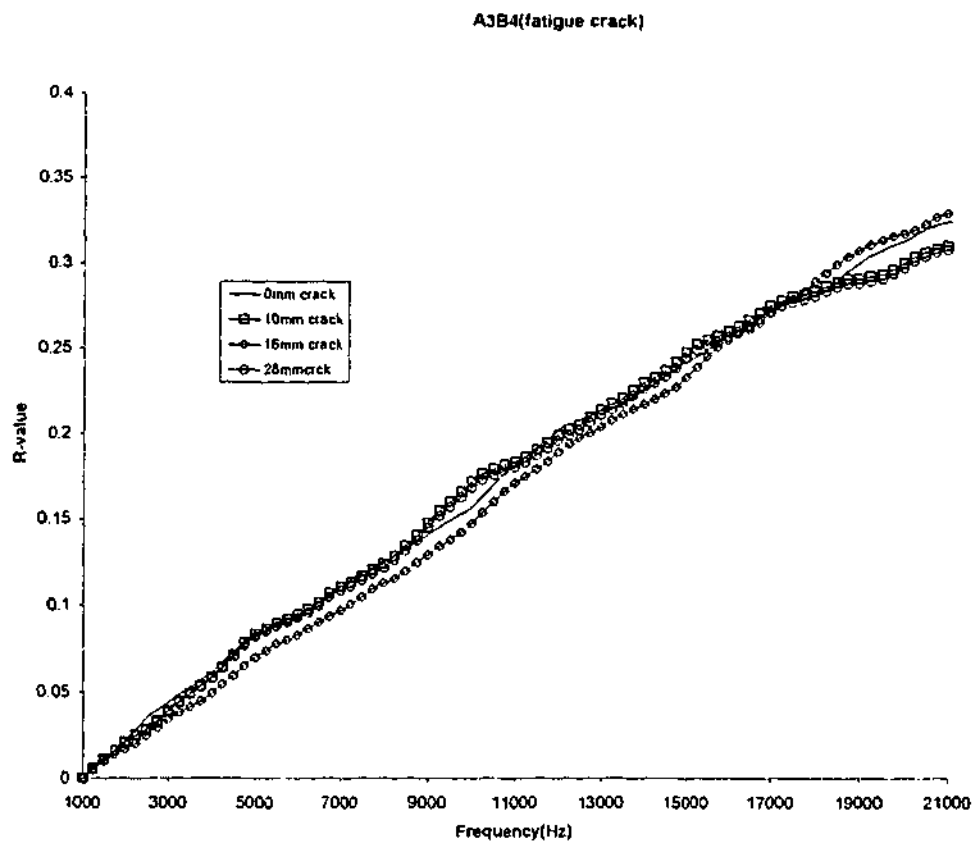


Figure 5.39. R-curve of pair A3B4

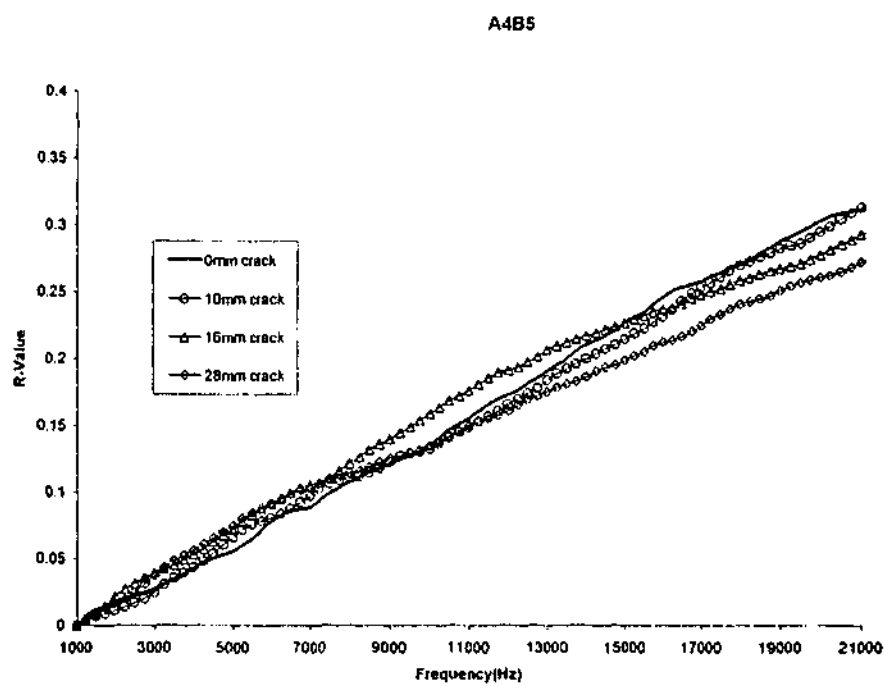


Figure 5.40. R-curve of pair A4B5

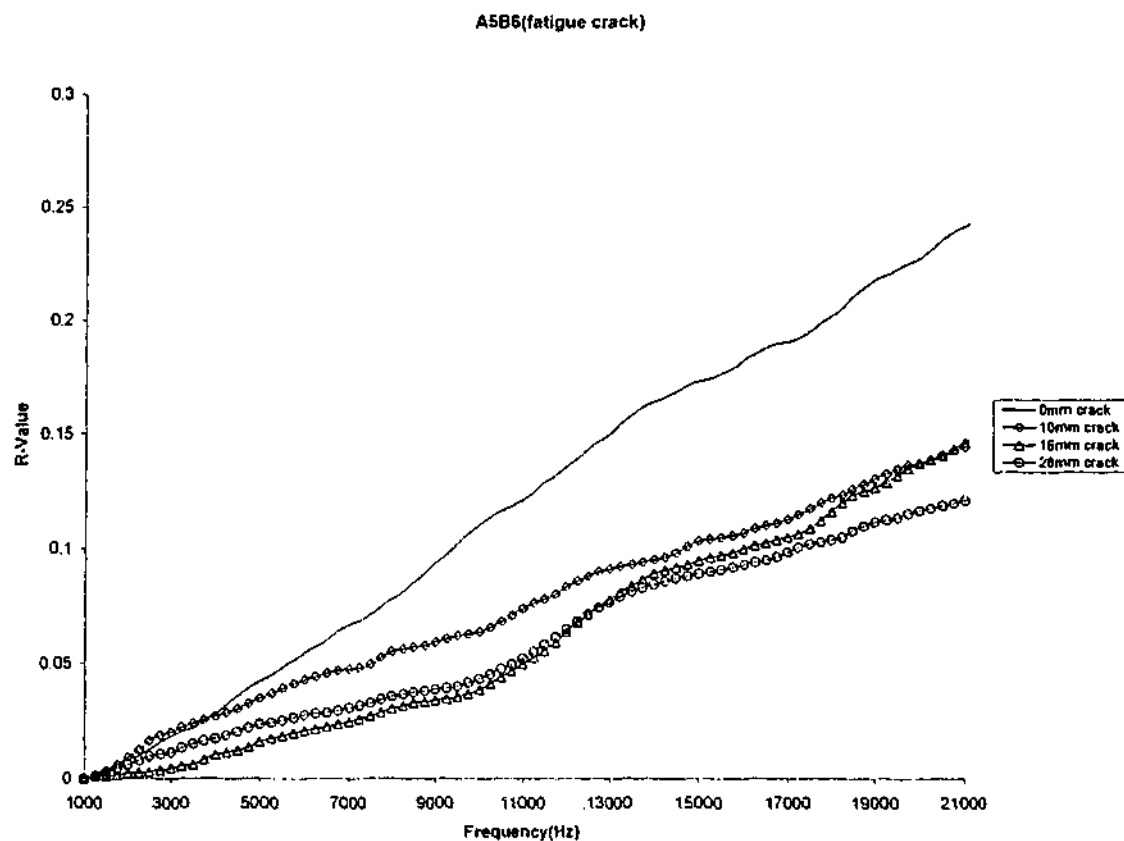


Figure 5.41. R-curve of pair A5B6

Table 5.4. Percentage of reduction of R-value from no-damage condition using a cross TF (fatigue crack)

pairs	A1B2	A2B3	A3B4	A4B5	A5B6
cracks					
10mm	-2.1499	-3.1556	4.2264	2.7477	39.5100
16mm	-3.2036	-5.1820	-1.3573	8.3727	39.5525
28mm	-1.0962	-1.1217	5.0401	13.9970	48.6561

As discussed in two preceding investigations, to help interpret the results above the R-value up to 20 kHz is tabulated in Table 5.4. Here, the cross-pairs showed a good trend agreement with the two previous investigations (numerical and saw cut crack).

Looking at Table 5.4 the following observation can be made:

- As discussed in the numerical investigation, the R-values of the sensors-actuators pairs of A1B2, A2B3, and A3B4 under all damage cases have to remain relatively unchanged. From the result for the pair A2B3 at 16mm crack case it appears that the lower limit of the experimental error is approximately -5.2%. Hence, a new upper and lower limit of these experimental investigations i.e. saw cut and fatigue cracks are approximately $\pm 5.2\%$.
- For the pair A4B5 and A5B6 show exactly the similar trend to the saw cut case. The A4B5 sensor-actuator pair appears to have higher sensitivity than in the numerical result. This pair can sense the 20mm crack case that did not occur at numerical investigation. This confirms the hypotheses that the crack induced here resulted in a lower stiffness than that obtained numerically. However, looking at the R-value for the pair A3B4 the results are consistent with the numerical investigations. This situation clearly shows that the 30mm crack tip is located between the sensor A4 and the actuator B5. (See Figure 5.24)
- As in the numerical investigation, a significant reduction that occurs for the pairs A5B6 allows for the detection of a 10mm crack. This implies that its crack tip is located in the vicinity of sensor A5 and actuator B6. (See Figure 5.24)
- Again, as in the direct-pair A_nB_n and B_nC_n , this cross-pair A_nB_{n+1} has also shown a similarity trend of responses of the sensor-actuator pair due to presence of crack between 16mm and 28mm crack lengths occurred from the fatigue crack and the one made in the numerical simulation (i.e. 20mm and 30mm). These consequently

- indicate the expected accuracy of the prediction of this method in this experiment are approximately $\pm 2\text{mm}$ for 20mm crack length and $\pm 1\text{mm}$ for 30mm crack length.

5.5. Concluding Remarks

The findings from the experimental investigation on this chapter can be summarized as follows:

- The R-curve method can be used to detect and localize the damage on a structural component. By taking the direct-TF of every pair on the mounted sensor-actuator rows (in this experiment is first used AnBn and the results is confirmed by BnCn) the location of the damage can be approximately determined. Based on the information from this direct-TF the position of the damage location can be confirmed by the cross-TF.

In general, this experimental investigation has shown a relatively good agreement with the numerical simulation. The information of the location of general damage area from the plate with the fatigue crack growth (in this case the area between A5B5 and A6B6 for 10mm crack, A4B4 and A6B6 for 16mm and 28mm cracks) can be inputted into the stress construction algorithm to find accurately the crack tip, described in the next chapter.

CHAPTER 6. THE USE OF AN ARRAY OF SENSORS FOR STRESS - FIELD CONSTRUCTION

Chapter 4 and 5 presented a technique that can be used to estimate the location of the damage in a structure. This chapter will describe a methodology to assess the integrity of the structure. In order to assess this structural integrity the stress field in the vicinity of the location of critical fatigue must be known. In the vicinity of the crack, the stress fields that are spatially changing can be constructed from point measurements from the array of sensors by using an algorithm that is based on the stress function. In this chapter, an algorithm for this purpose is presented and it is then applied to a single edged cracked plate and on a plate with an embedded semi-elliptical crack.

The structure of this chapter can be summarized as follows. In the first sections:

- A theoretical analysis of the stress field in a plate containing a crack is performed using the 2-D Airy's stress function
- This theoretical approach is then evaluated with an array of data obtained from a series of finite element (FE) analysis of a simple crack plate.
- This theoretical approach is subsequently validated experimentally

In the second section of this chapter:

- The derivation of the components of the 3D stress function to construct the stress field at the back surface of the plate that has a semi-elliptical crack embedded in it.
- These components of 3D stress function are subsequently used to reconstruct a stress field with an array of data obtained from a series of finite element (FE) analysis of a crack plate with an embedded semi-elliptical crack.

6.1. 2-D Stress Function for Stress Field Construction

The algorithm that is presented here is based on the 2D Airy stress function for the construction of a stress field. Chiu et al (1997)³² have demonstrated, that, inside a given array of sensors, this stress function can be used to construct accurately the stress field of a uniaxial loaded plate with a hole in it. Cheung (1997)³³ used the components of the 2D stress function for a cracked elastic sheet (see Figure 6.1) derived by Jones and Callinen (1977)³⁴ to construct the stress field inside an array of sensors in a given region of a cracked plate. In the work presented here, these stress components were used to predict the stress field outside an array of sensors in a cracked plate.

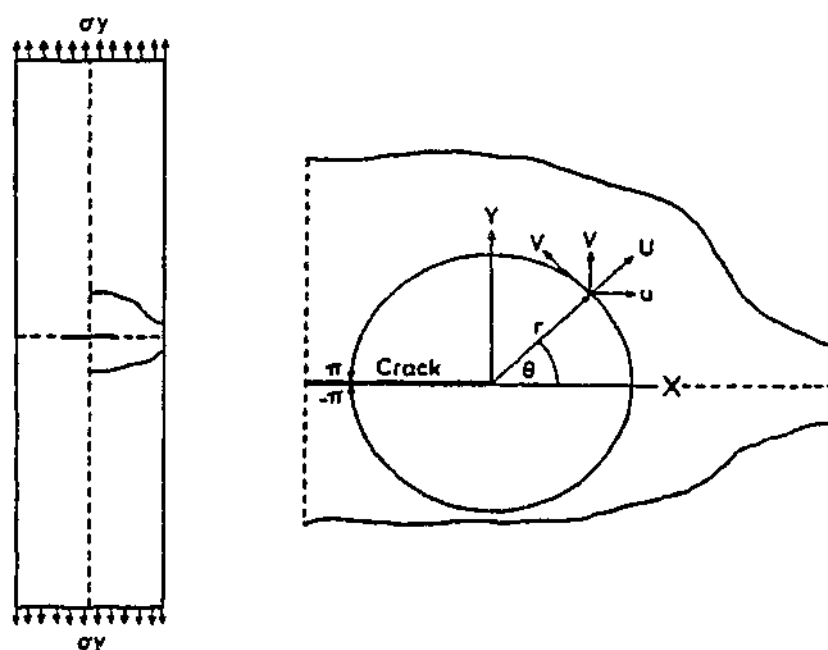


Figure 6.1. Geometry of the crack on an elastic sheet

The components of 2D stress function σ_{xx} , σ_{yy} and τ_{xy} are presented below :

$$\begin{aligned} \sigma_{xx} = \sum_n n(n+1) & \left(r_1^{n-1} \left(\left[(\alpha^2 - \beta^2) a_{4n-1} + 2\alpha\beta a_{4n} \right] \cos \xi_1 (n-1) \right. \right. \\ & + \left. \left[(\alpha^2 - \beta^2) a_{4n} - 2\alpha\beta a_{4n-1} \right] \sin(n-1) \xi_1 \right) + r_2^{n-1} \left(\left[(\alpha^2 - \beta^2) e_{4n-1} \right. \right. \\ & \left. \left. + 2\alpha\beta e_{4n} \right] \cos(n-1) \xi_2 + \left[(\alpha^2 - \beta^2) e_{4n} - 2\alpha\beta e_{4n-1} \right] \sin(n-1) \xi_2 \right) \end{aligned} \quad (6.1)$$

$$\begin{aligned} \sigma_{yy} = \sum_n n(n+1) & \left(r_1^{n-1} (a_{4n-1} \cos(n-1) \xi_1 + a_{4n} \sin(n-1) \xi_1) \right. \\ & \left. + r_2^{n-1} (e_{4n-1} \cos(n-1) \xi_2 + e_{4n} \sin(n-1) \xi_2) \right) \end{aligned} \quad (6.2)$$

and

$$\begin{aligned} \tau_{xy} = - \sum_n n(n-1) & \left(r_1^{n-1} \left(\cos(n-1) \xi_1 [\alpha a_{4n-1} + \beta a_{4n}] + \sin(n-1) \xi_1 [\alpha a_{4n} - \beta a_{4n-1}] \right) \right. \\ & \left. - r_2^{n-1} \left(\cos(n-1) \xi_2 [\alpha e_{4n-1} + \beta e_{4n}] + \sin(n-1) \xi_2 [\alpha e_{4n} - \beta e_{4n-1}] \right) \right) \end{aligned} \quad (6.3)$$

where $r_1 = \sqrt{(x + \alpha y)^2 + (\beta y)^2}$, $r_2 = \sqrt{(x - \alpha y)^2 + (\beta y)^2}$, $\xi_1 = \arctan \left[\frac{\beta y}{x + \alpha y} \right]$,

$$\xi_2 = \arctan \left[\frac{\beta y}{x - \alpha y} \right]$$

and σ_{xx} and σ_{yy} are the stress components in the X and Y direction respectively and τ_{xy} is the shear stress.

For the isotropic material used in this research, $\alpha = 0.5$, and $\beta = 1/2\sqrt{3}$. The summation point n in Equation 6.1, 6.2 and 6.3 is equal to $1/2, 1, 1(1/2), 2, \dots, n/2$ that can be explained by the derivation as follows:

If the origin of the system of Cartesian coordinates is placed at the crack tip (see Figure 6.2), then the stresses σ_y and τ_{xy} must vanish on $y = \pm 0$ to satisfy the requirement that the crack is stress free.

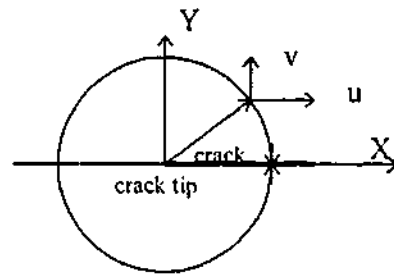


Figure 6.2. Geometry of the left hand crack tip

Hence, for $y = \pm 0$

$$r_1 = r_2 = x, \quad (6.4)$$

and

$$\xi_1 = 0, \quad \xi_2 = 2\pi, \quad (6.5)$$

or $\xi_1 = 2\pi, \xi_2 = 0$. The condition $\sigma_y = 0$ requires the following in Equation 6.2;

$$a_{4n-1} = -e_{4n-1} \cos(n-1)2\pi \quad (6.6)$$

and

$$\sin(n-1)2\pi = 0 \quad (6.7)$$

Thus the summation point n is equal to $n/2, 1, 1(1/2), 2, \dots, n/2$.

Acquiring stress/strain data from an array of sensors the constants a_{4n} , a_{4n-1} , e_{4n} , e_{4n-1} in Equation 6.1, 6.2 and 6.3 can be calculated using least square fit. These constants will then be used to re-construct the stress field in the vicinity of the region where the point measurements of the stress/strain data were obtained.

6.1.1. Determination Of Criticality

The criticality of the structure under the derived stress field can be assessed by calculating the mode I stress intensity factor (SIF), K_I . Dally and Sanford (1987)³⁵ have developed a method for placing the strain gauge in a region away from the crack tip to calculate the mode I stress intensity factor. The area near the crack tip is divided into three regions as shown in Figure 6.3.

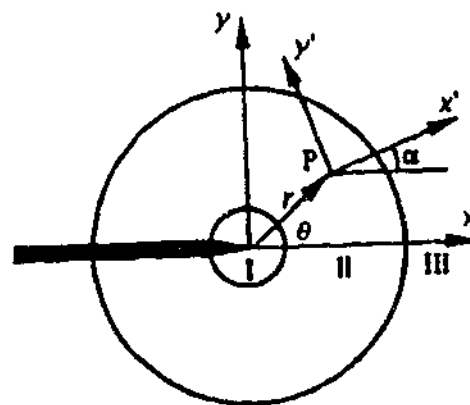


Figure 6.3. Crack tip region and geometry of the problem

Region I, is the innermost region, close to the crack tip and this region is difficult to quantify experimentally because of the rapidly changing stress field. Also, yielding can cause some ambiguities concerning whether the stress state is plane stress or plane strain. Region II, the intermediate region, is the region that can be used for data acquisition since it is sufficiently large to place strain gauges. The region III is the outermost region for the far fields stress where the strain field is not sufficiently accurate to determine the stress intensity factor.

The inner boundary of region II is determined by a circle of radius $r = h/2$, where h is the thickness of the plane body. This radius formula was derived experimentally by Rosakis and Ravi-Chandra (1984)³⁶. Hence, from a strain magnitude in this valid region the SIF Mode I, K_I of

the structure can be calculated. This strain is calculated using the following expression:

$$\begin{aligned}
 2G \varepsilon_{x'x'} = & A_0 r^{-\frac{1}{2}} \left[k \cos(\theta/2) - (1/2) \sin \theta \sin(3\theta/2) \cos 2\alpha + (1/2) \sin \theta \cos(3\theta/2) \sin 2\alpha \right] \\
 & + B_0 (k + \cos 2\alpha) + A_1 r^{-\frac{1}{2}} \cos(\theta/2) \left[k + \sin^2(\theta/2) \cos 2\alpha - (1/2) \sin \theta \sin 2\alpha \right] \\
 & + B_1 r \left[(k + \cos 2\alpha) \cos \theta - 2 \sin \theta \sin 2\alpha \right]
 \end{aligned} \quad (6.8)$$

where $k = (1 - \nu)/(1 + \nu)$ and $G = \frac{E}{2(1 + \nu)} \approx \frac{3}{8} E$, ν and E are the Poisson ratio and the modulus Young of the material.

This equation requires sensor readings at least four points since it has four unknown values, A_0 , A_1 , B_0 , B_1 . Parnas et al (1996)³⁷ successfully evaluated the method of three-parameter solution (A_0 , A_1 , B_0) for determining K_I by using only one strain gauge reading in the valid region (region II). Their experimental results and theoretical results were in good agreement. To evaluate Equation 6.8 by using only one point reading, firstly, B_0 term has to be eliminated by setting:

$$\cos 2\alpha = -k = -(1 - \nu)/(1 + \nu) \quad (6.9)$$

Then, the coefficient of the A_1 term is set to zero. Hence,

$$k + \sin^2(\theta/2) \cos 2\alpha - (1/2) \sin \theta \sin 2\alpha = 0$$

which can be satisfied if

$$\tan(\theta/2) = -\cot 2\alpha \quad (6.10)$$

As an example, for $\nu=1/3$, which is a typical Poisson's value for metals, then $\alpha=\theta=60^\circ$, Equation (6.8) can then be reduced to :

$$2G \varepsilon_{x'x'} = A_0 r^{-\frac{1}{2}} 3(\sqrt{3})/8 \quad (6.11)$$

Equation 6.11 can be used to calculate the mode I SIF, K_I from the equation below:

$$K_I = (\sqrt{2\pi}) A_0 \quad (6.12)$$

Thus :

$$\begin{aligned} K_I &= E \varepsilon_{x'x'} \left(\sqrt{(8/3)\pi r} \right) \\ \text{or } K_I &= \sigma_{x'x'} \left(\sqrt{(8/3)\pi r} \right) \end{aligned} \quad (6.13)$$

where $\sigma_{x'x'}$ is the stress in $x'x'$ direction (see Figure 6.3).

This stress component above can be found by the expressions below:

$$\sigma_{x'x'} = \sigma_{xx} \cos\alpha + \sigma_{yy} \sin\alpha \quad (6.14)$$

Using this method of calculating the K_I would require the knowledge of σ_{xx} and σ_{yy} . These values can be obtained from the stress function described by Equation 6.1, 6.2, and 6.3. Given an array of stress/strain data located in the vicinity of the crack tip, the constants in Equation 6.1, 6.2, and 6.3 can be evaluated using least square method. The values of σ_{xx} and σ_{yy} can then be substituted into Equation 6.14 and 6.13 to determine the K_I value.

In the next subsection this numerical methodology will be used to determine the mode I SIF, K_I for a single edge crack plate.

6.1.2 Numerical Investigations

In this numerical work, an aluminum plate with length of 100 mm, width of 50 mm and thickness of 8 mm with a single edged crack with length of 25 mm was modeled using 2D finite element method (FEM). The remote stress in Y direction was 48MPa. Figure 6.4 and 6.5 show a schematic representation of the case study examined.

An array of sensors was applied to a region close to the crack tip. In Figure 6.4, an array of sensor points (12 rows x 12 columns) was applied on the region at some distance from the crack while Figure 6.4a presents the detail of the position of the sensor points. Figure 6.5 shows two arrays of sensor points (each 6 rows x 12 columns) with a crack in between them. The detail of the sensor points for this arrangement is shown in Figure 6.5a.

To simulate readings from arrays of sensors, the stresses/strains of these FEM calculations in the vicinity of the crack were used as input into the stress field algorithm. The stress value at each of the sensors point was evaluated. These readings acted as the sensor output of the array. This was used to simulate an array of sensor readings from which the entire stress field inside the array was constructed by the algorithm described above. The constructed stress function was then used to predict the stress outside the array.

An algorithm was also developed to locate the crack tip for this crack plate. To determine the criticality of the plate in each of the stress fields described above, the location of the crack tip and the mode I stress intensity factor were calculated. The results obtained from finite element analysis, which was described the actual value were compared to those obtained from the stress prediction.

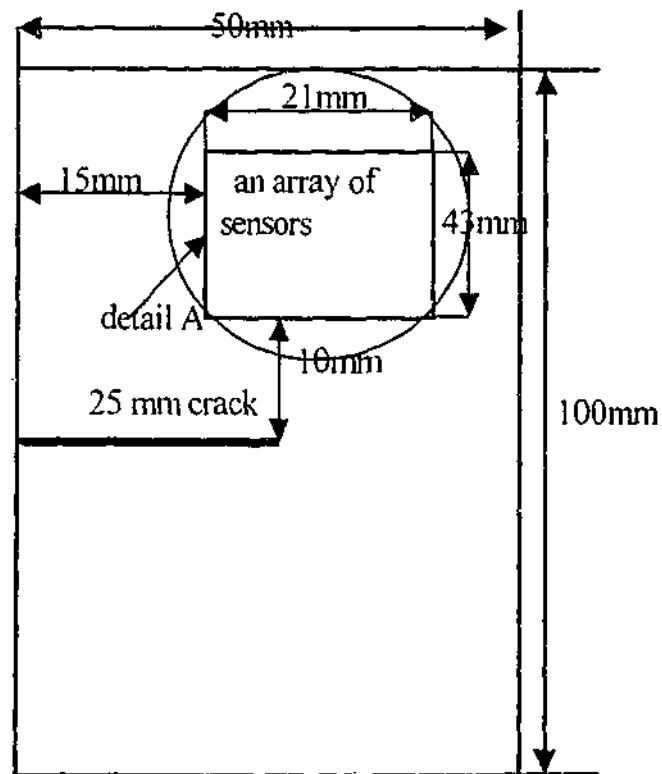


Figure 6.4. An array of sensors (12 rows x 12 columns), which applied on the region at some distance away from of the crack

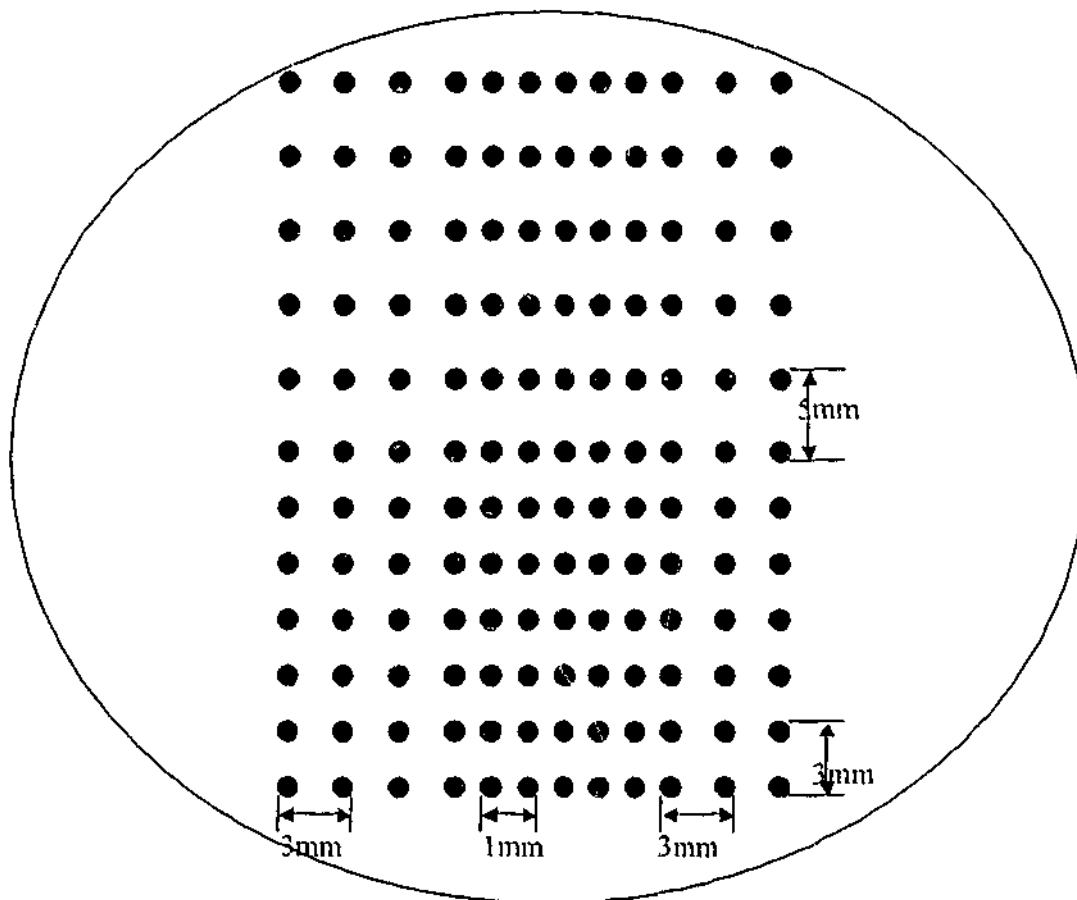


Figure 6.4a. Detail A, the position of the sensor point measurement on the plate in numerical investigation

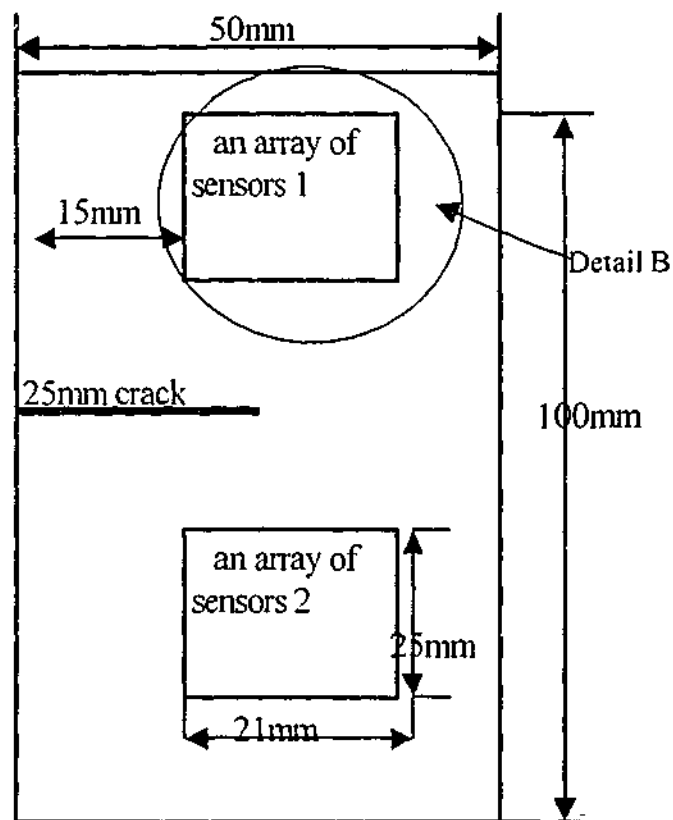


Figure 6.5. Two identical arrays of sensors (each is 6 rows x 12 columns) with a crack in between them

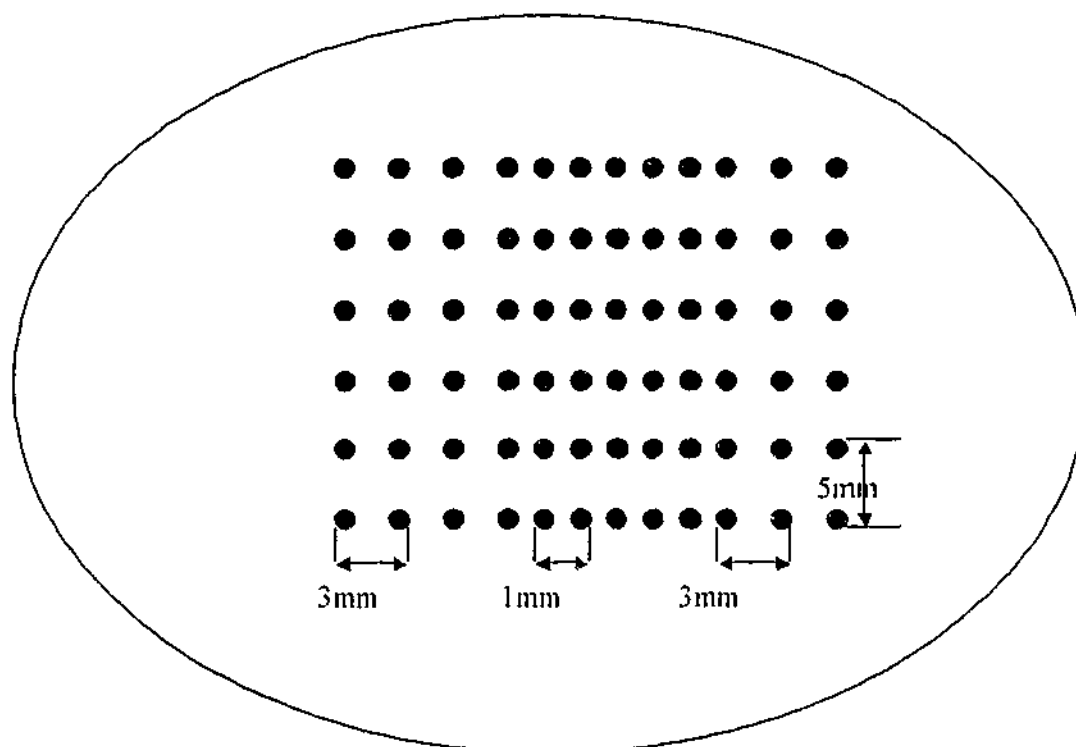
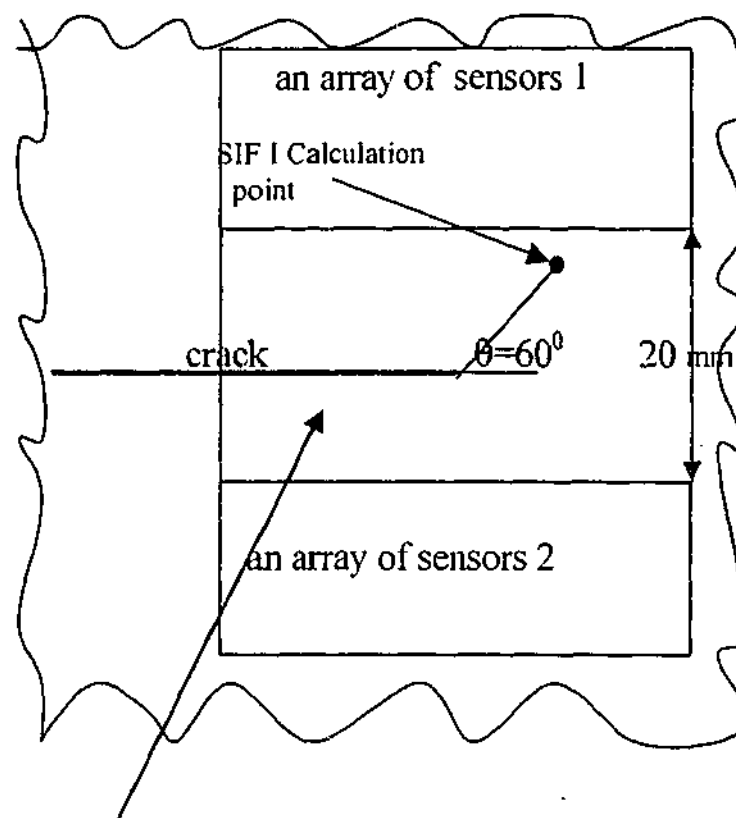


Figure 6.5a. Detail B, the position of the sensor point measurement on the plate in numerical investigation

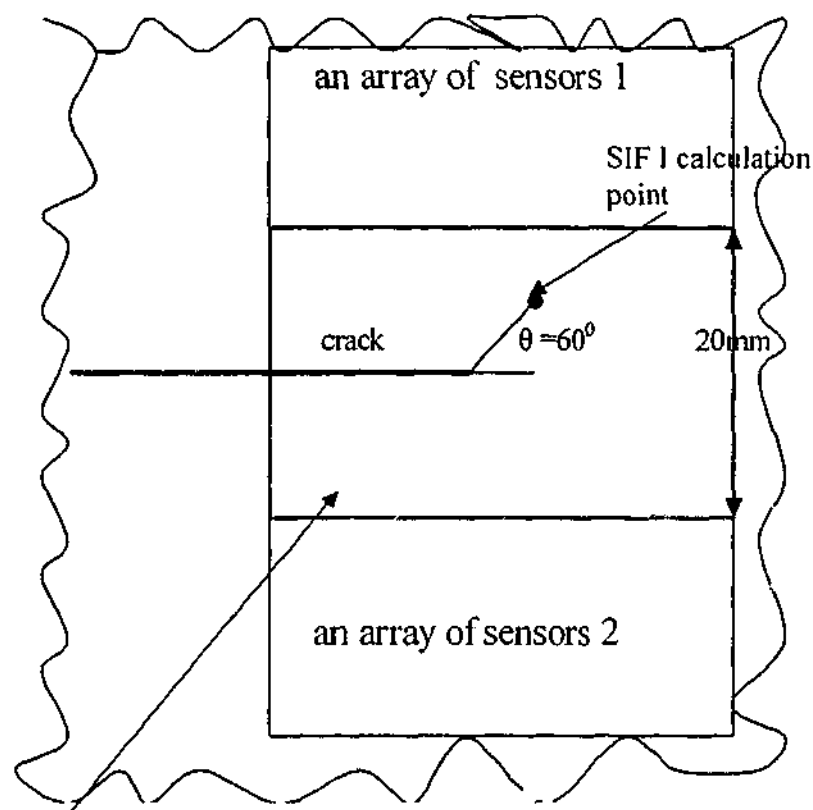
6.1.3. Results and Discussion

Some of the results reported in this section have been published by Wibowo et al (1998)³⁸. Figures 6.6 to 6.11 present the relative position of the sensor arrays to the crack and the mode I SIF, K_I calculation point. There are two positions of the mode I stress intensity factor calculation points to be evaluated, on the region I ($r < h/2$) and region II ($r \geq h/2$), where h is the thickness of the plate. Figure 6.7, 6.9 and 6.11 show the situation where K_I was calculated in region I. Figure 6.6, 6.8 and 6.10 shows the situation where K_I was calculated in region II. In the situation shown in Figure 6.10 and 6.11, only one array of sensor was used. In this study, the purpose is to predict the stress field exterior to the arrays of sensors. Therefore, the region of stress field prediction for two arrays of sensors is the area between them (see figures 6.6 to 6.9) and for one array of sensors is the area between the array and the crack (see Figure 6.10 and 6.11).



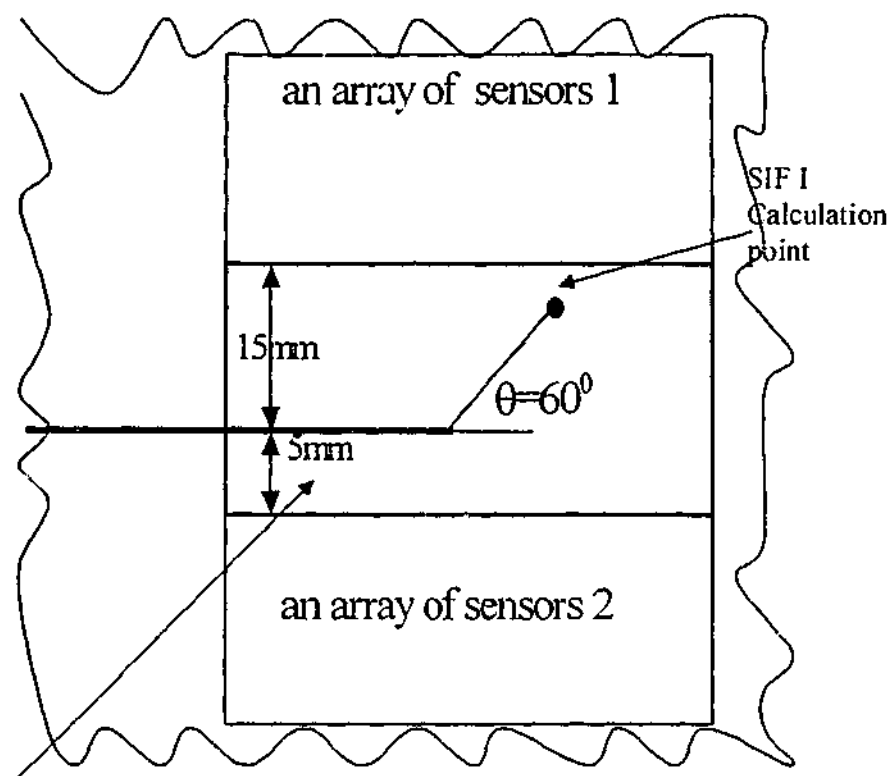
The region of Stress-field prediction

Figure 6.6. Sensors position with a crack is on equidistant line & The mode I SIF, K_I calculation point is in region II



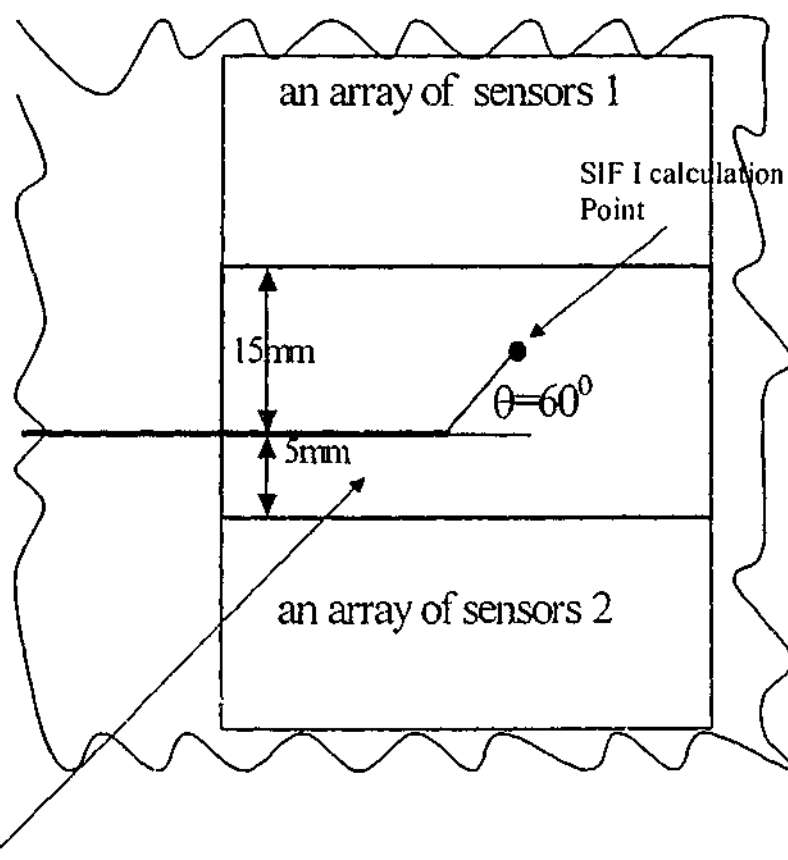
The region of stress-field prediction

Figure.6.7. Sensors position with a crack is on equidistant line & The mode I SIF, K_I calculation point is in region I



The region of stress-field prediction

Figure 6.8. Sensors position with a crack position is not on equidistant line & The mode I SIF, K_I calculation point is in region II



The region of stress-field prediction

Figure 6.9. Sensors position with a crack position is not on equidistant line & The mode I SIF, K_I calculation point is in region I

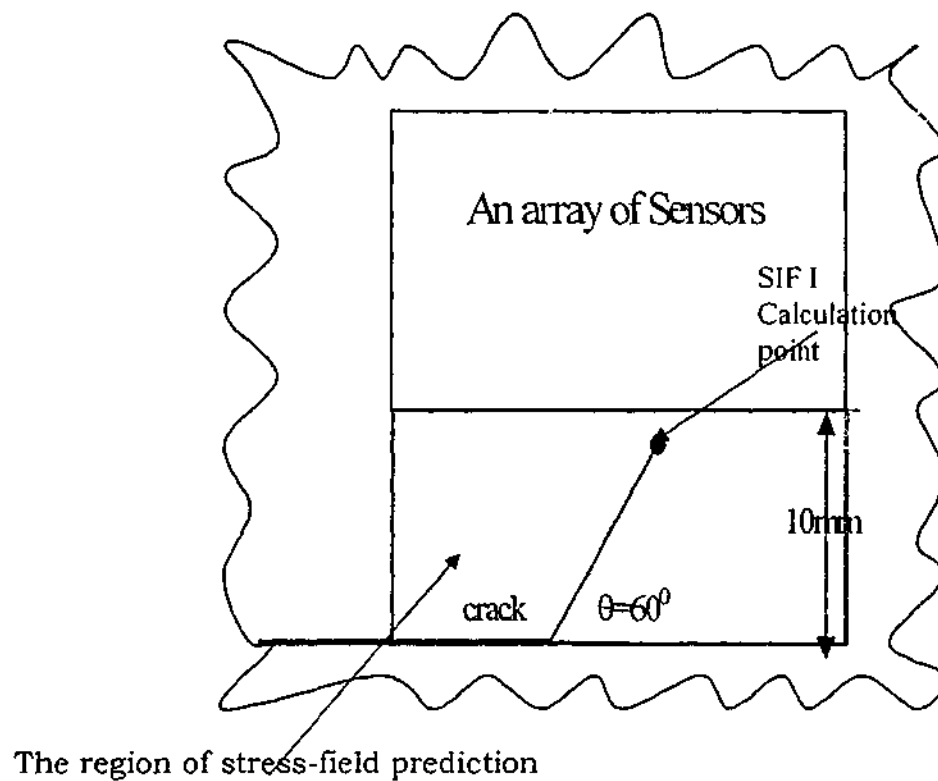


Figure 6.10. An array of sensors to predict the crack & The mode I SIF, K_I calculation point is in region II

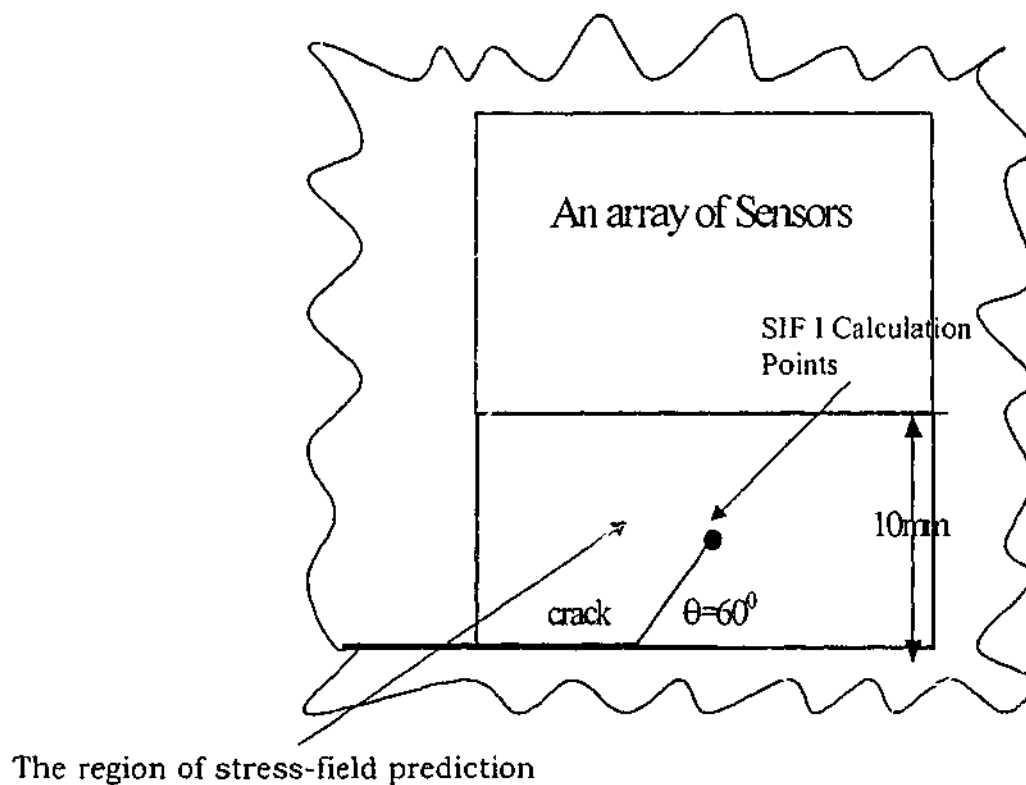


Figure 6.11. An array of sensors to predict the crack & The mode I SIF, K_I calculation point is in region close to crack tip (region I)

This study found that the stress field in the vicinity of the crack can be constructed by the stress function with the stress data provided from the array. The way in which the stress function i.e. Equation 6.1, 6.2 and 6.3 can be used to describe the stress field in the vicinity of the crack requires the coordinate of the axis used to be located at the crack tip. Therefore, if the location of the crack tip can be located approximately using the technique described in Chapter 5 and 6, the exact location of the crack tip can be determined by optimizing a statistical parameter, correlation coefficient in Y direction CorrYY . The error then is calculated by this following formula.

$$\text{Error} = (1 - \text{CorrYY}) \quad (6.15)$$

Where:

$$\text{CorrYY} = \frac{\sum_{i=0}^{N_p} \hat{y}_i y_i}{\sqrt{\sum_{i=0}^{N_p} y_i^2 \sum_{i=0}^{N_p} \hat{y}_i^2}} \quad \text{and,}$$

\hat{y}_i = Stress point value in Y-direction from the measurement of an array of sensors

y_i = Stress point value in Y-direction from the stress function interior of the array

N_p = Number of point sensors in the array

Figure 6.12 shows the error of the stress field calculated by the stress function when the origin of the function is moved in the vicinity of the crack tip. In this investigation, the crack size was 25 mm and it is evident from the figure that the minimum error occurs at the location of the crack tip i.e. 25mm. Therefore, once location of the minimum error is found the stress field can accurately be constructed. The constructions of the stress field exterior of the array using the stress function with the origin of (25 mm, 0) are shown in the following figures below.

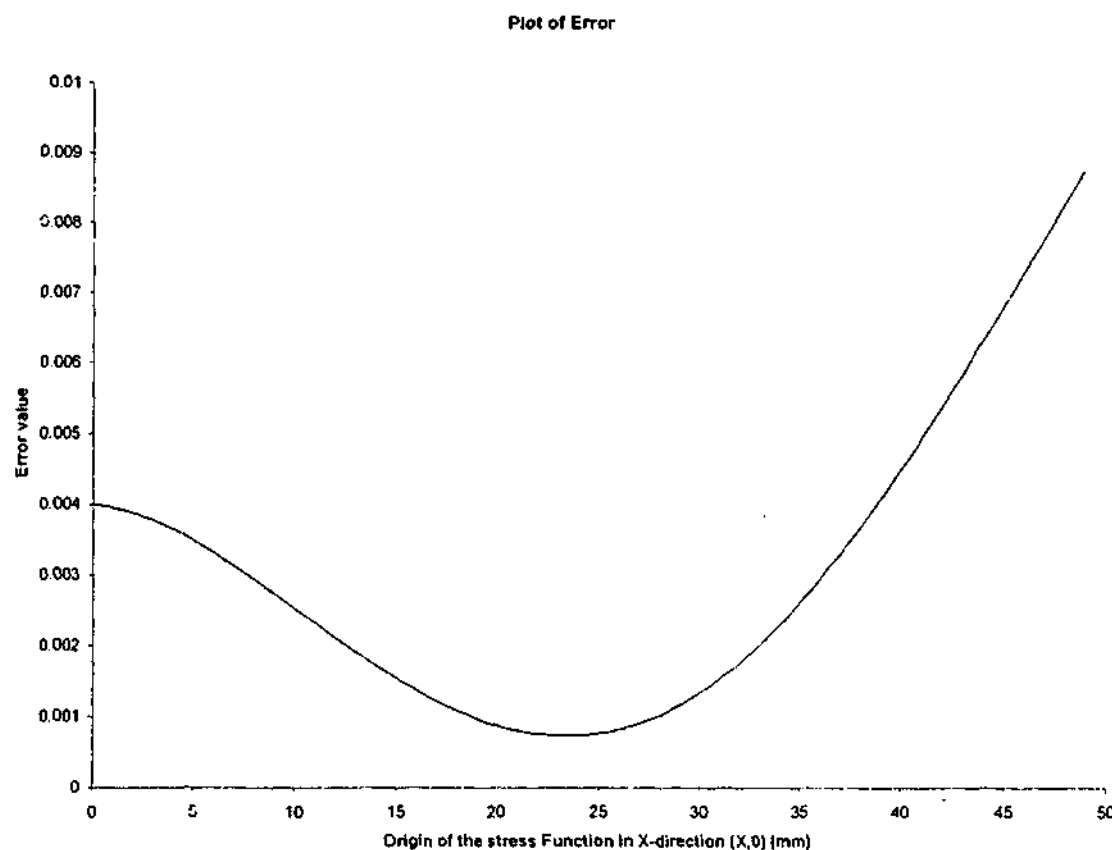


Figure 6.12. The error plot of the plate with a 25mm simple crack

Figure 6.13 and 6.14 show the Y-direction stress, σ_{yy} in the region between the array of sensor (as shown in Figure 6.6 and 6.7). It is evident that there is a good agreement between the stress field predicted and that calculated from finite element analysis.

Figure 6.15 shows the stress field, σ_{yy} predicted by the stress function technique. Here, the agreement with that finite element results (Figure 6.16) is good. The crack location in this case is shown in Figure 6.8 and 6.9.

When only an array of sensors is used (Figure 6.10 and 6.11) the stress field, σ_{yy} predicted exterior to the array is shown in Figure 6.17. This agreed well with the results obtained from finite element analysis (Figure 6.18).

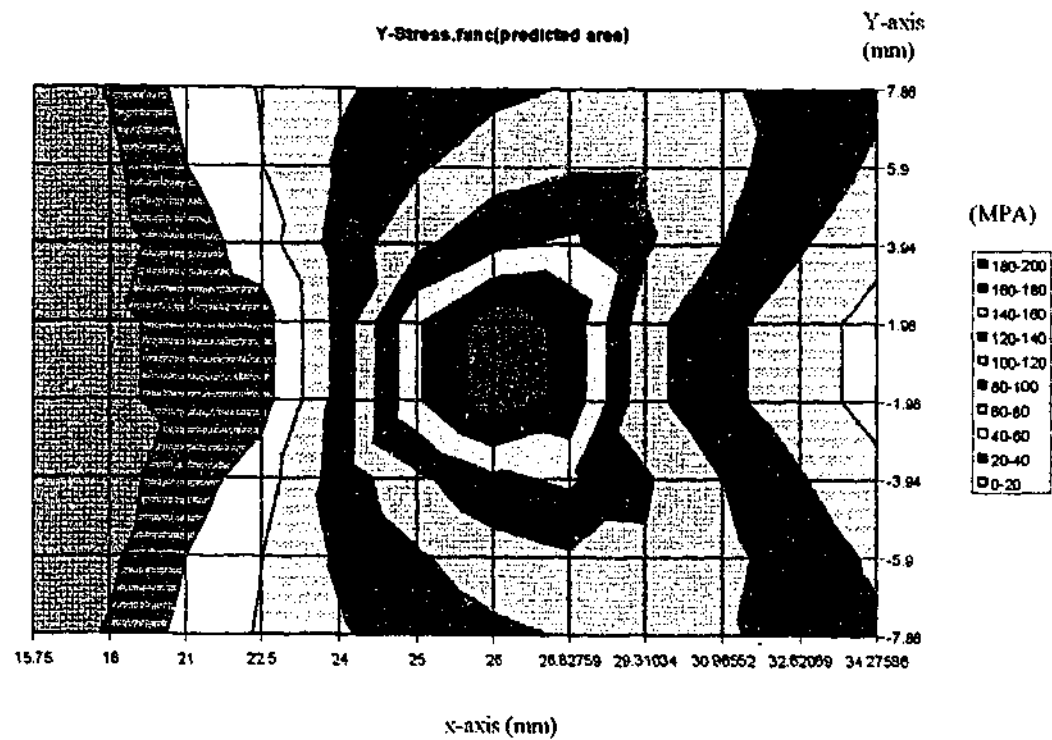


Figure 6.13. The stress field in y-direction σ_{yy} constructed by the Stress Function (equidistant)

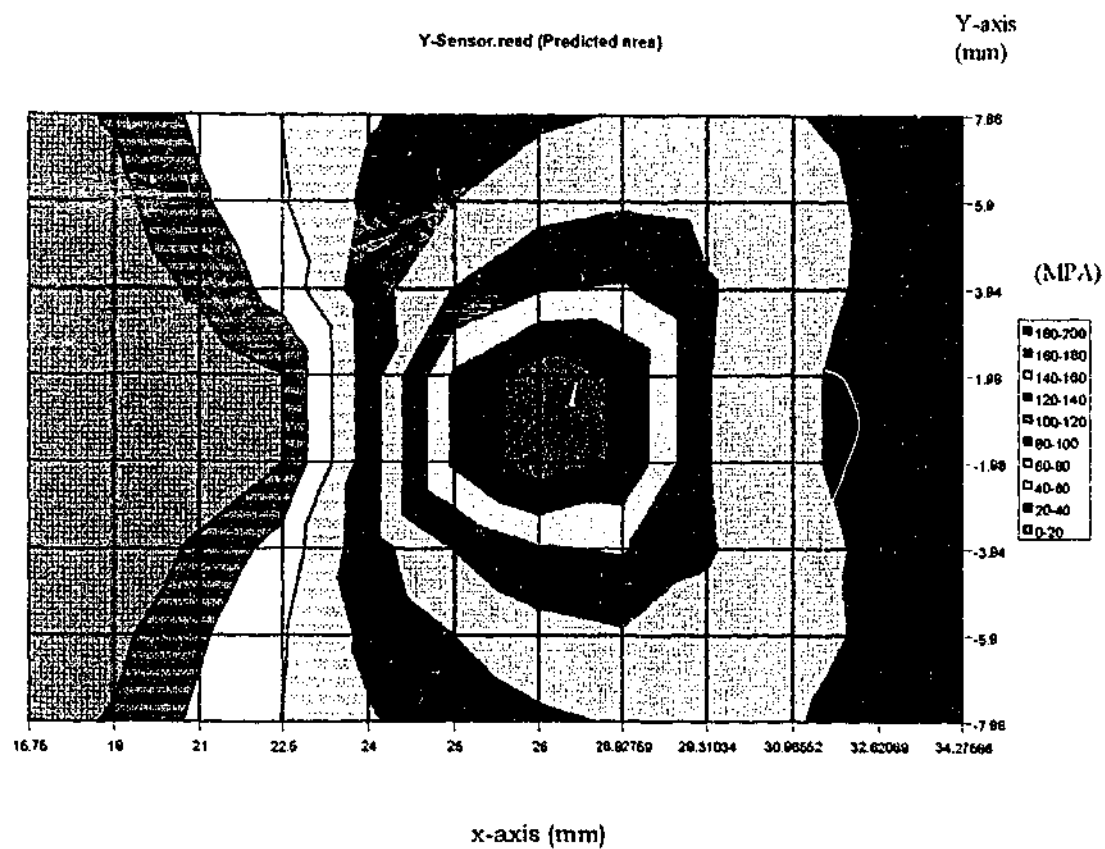


Figure 6. 14. The stress field in y-direction σ_{yy} calculated by FEM (equidistant)

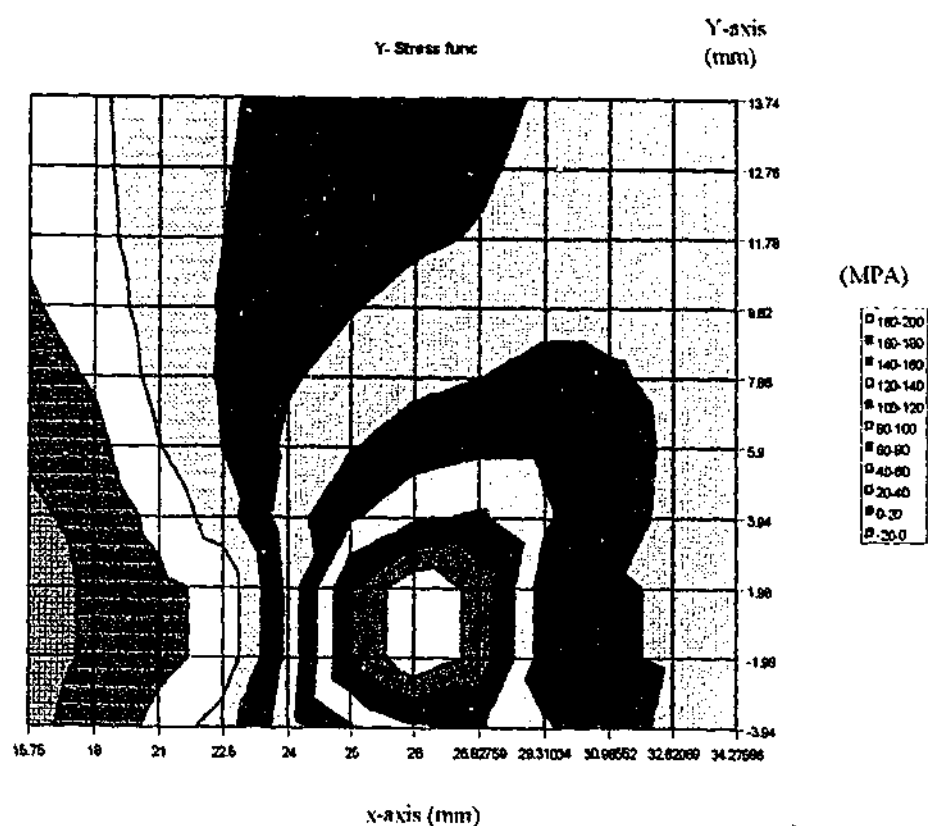


Figure 6.15. The stress field in y-direction σ_{yy} constructed by The Stress Function (not equidistant)

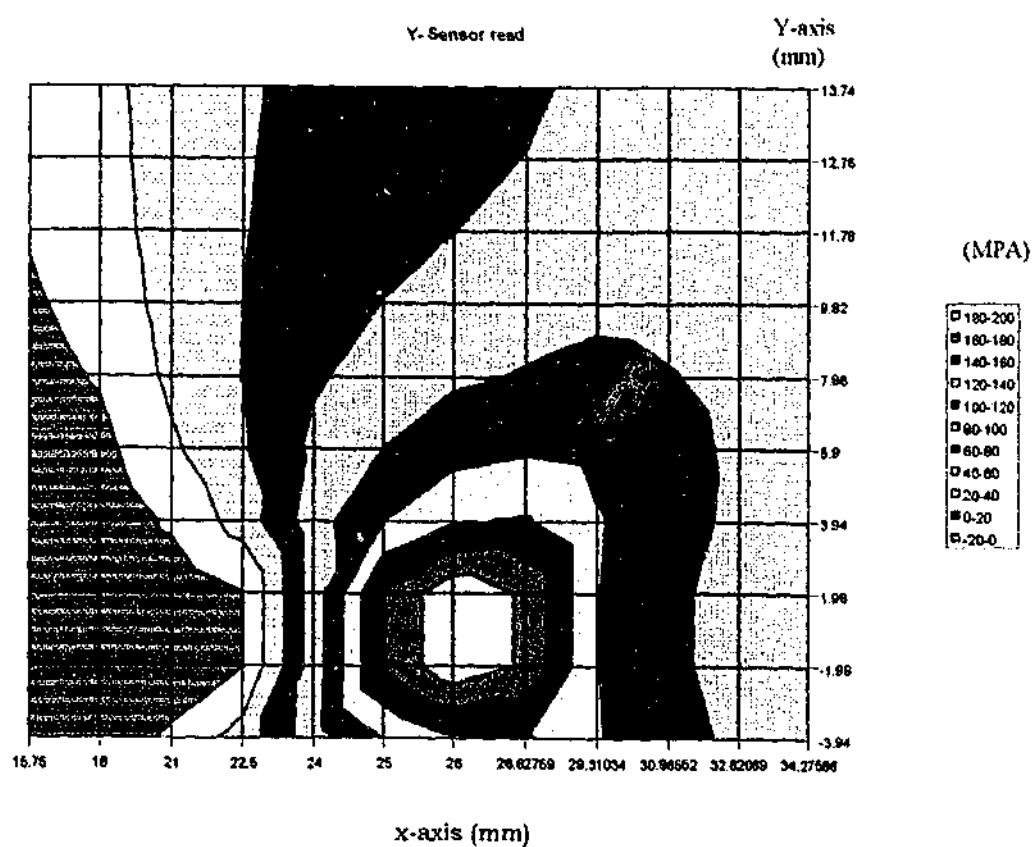


Figure 6.16. The stress field in y-direction σ_{yy} calculated by FEM (not equidistant)

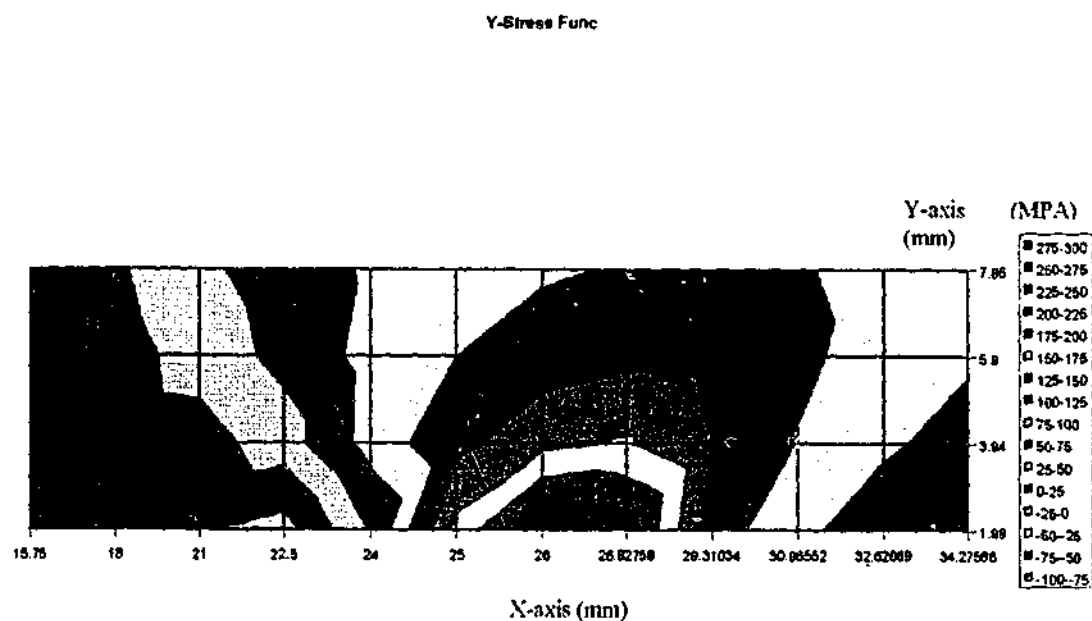


Figure 6.17. The stress field in y-direction σ_{yy} constructed from
The Stress Function (one array)

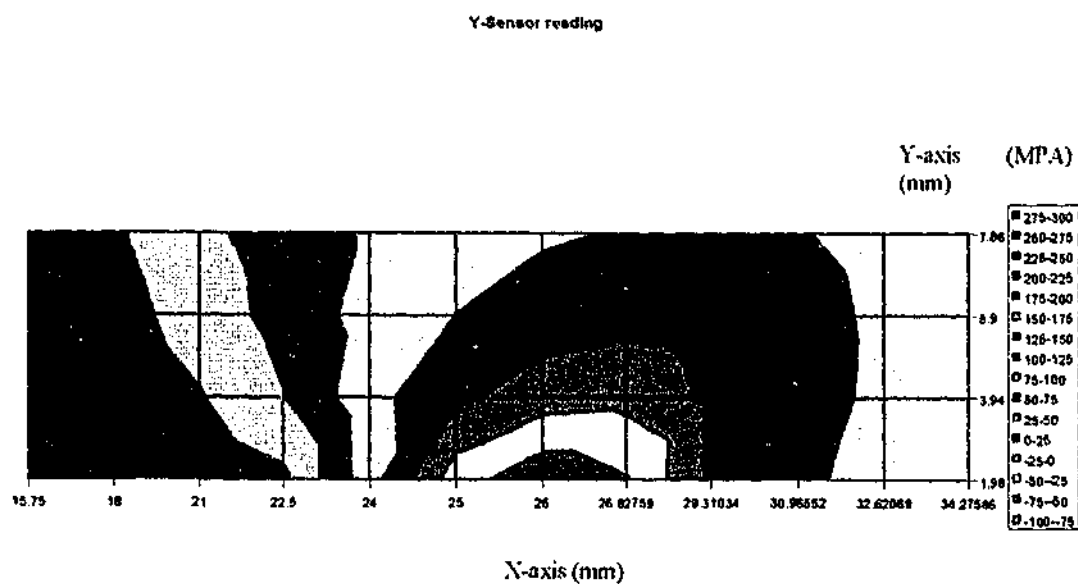


Figure 6.18. The stress field in y-direction σ_{yy} calculated from
FEM (one array)

In each of the stress fields described above, the mode I stress intensity factor, K_I was calculated using Equation 6.13. The results are shown in Table 6.1. Here it is seen that there is a good agreement on region II between the results obtained from finite element analysis and that obtained from the methodology described in this research. This is because region I is close to the singularity point, where the term $r^{(-1/2)}$ in Equation 6.1, 6.2 and 6.3, is dominant and contributes higher numerical error to the stress field calculation than in region II. With the knowledge of the crack tip location and stress field around it the SIF mode I, K_I can be determined to within 15%. Hence, the severity of the structural component can be assessed.

Table 6.1. Mode I Stress Intensity Factor from the numerical investigation

Sensors Positions	SIF from FE Calculation (MPa \sqrt{m})	SIF from Stress Function (MPa \sqrt{m})	% Differences
Figure 6.7(region I)	20.904	25.808	27.335
Figure 6.9(region I)	20.904	24.874	18.992
Figure 6.11(region I)	20.904	27.783	32.91
Figure 6.6(region II)	20.115	23.185	15.262
Figure 6.8(region II)	20.115	20.794	3.376
Figure 6.10(region II)	20.115	22.444	11.578

The results from this numerical study can be summarized as follows:

- The location of the crack tip can be predicted by minimizing Equation 6.15. This information can be used to calculate the stress field in the vicinity of the crack exterior to the array.
- The reconstructed stress field can, then, be used to predict the mode I stress intensity factor, K_I . As shown in this analysis the stress

component in region II can be used to determine the K_I value for integrity assessment.

These findings above will be validated experimentally in the next section.

6.1.4. Experimental Investigation

In this experimental investigation the numerical methodology presented above will be used to construct the stress/strain field of the test plate of the various different crack lengths. As the crack on the test plate develops, the stress/strain field will be re-constructed for every crack condition. The mode I SIF, K_I then will be calculated in every crack condition that can be used to determine the residual strength of the test plate.

A plate with a centered crack was used. An array of strain gauges was mounted in the vicinity of the crack in region II. The schematic arrangement of the sensors can be seen in Figure 6.19. The detail of the strain gauges position is shown in Figure 6.19a. This plate was also used for experiment described in Chapter 5 in Section 5.3 (see Figure 6.20). At same pre-determined crack development the MTS machine was stopped and a 15KN static load was applied to the plate. The static strain field was measured using the array of strain gauges. This measurement was performed for the cases where the crack length was at 10mm, 16mm and 28mm. With the data provided by the gauges the strain fields were re-constructed using methodology presented in the earlier section.

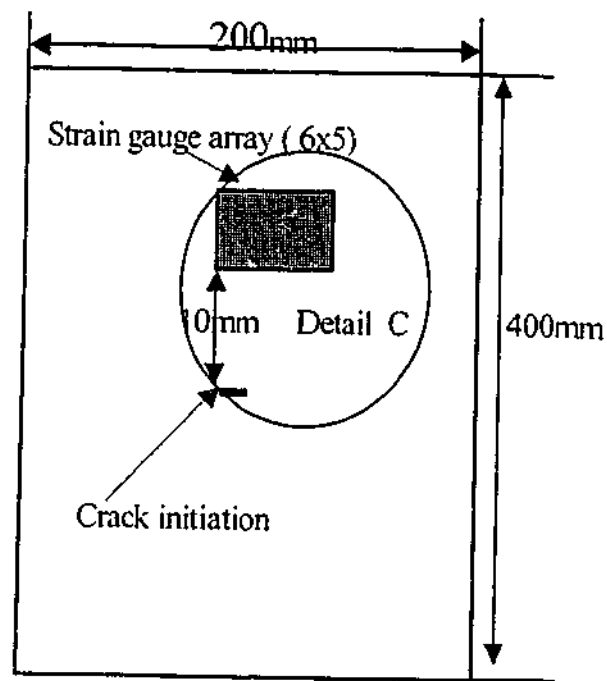


Figure 6.19. Schematic diagram of the experimental investigation of the $(200 \times 400 \times 2) \text{ mm}^3$ plate with an initial center crack

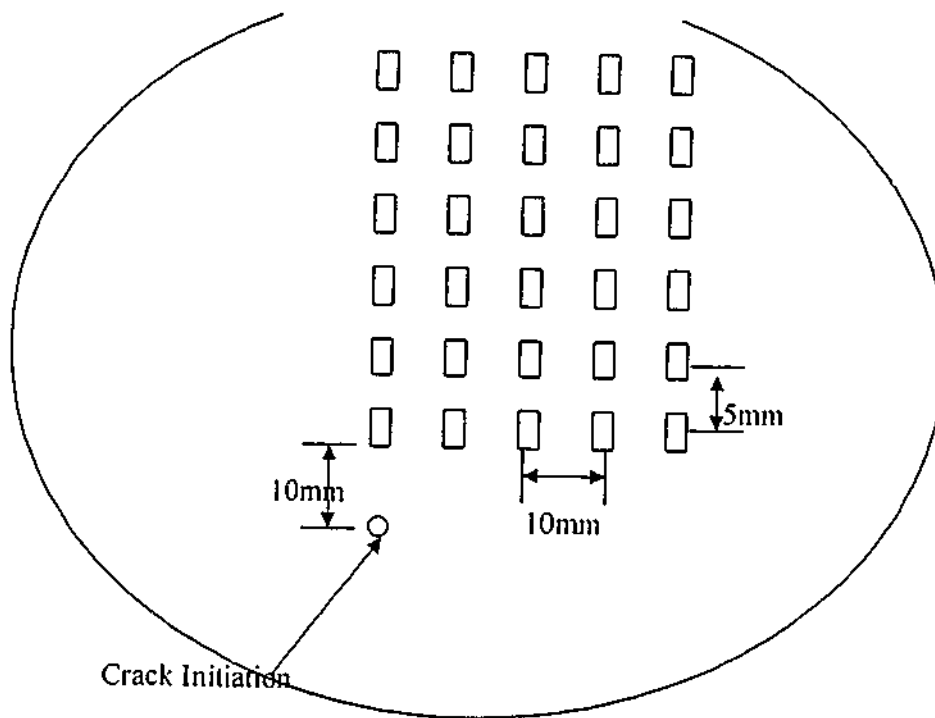


Figure 6.19a. Detail C, the position of the array of strain gauges mounted on the plate in the experimental investigation

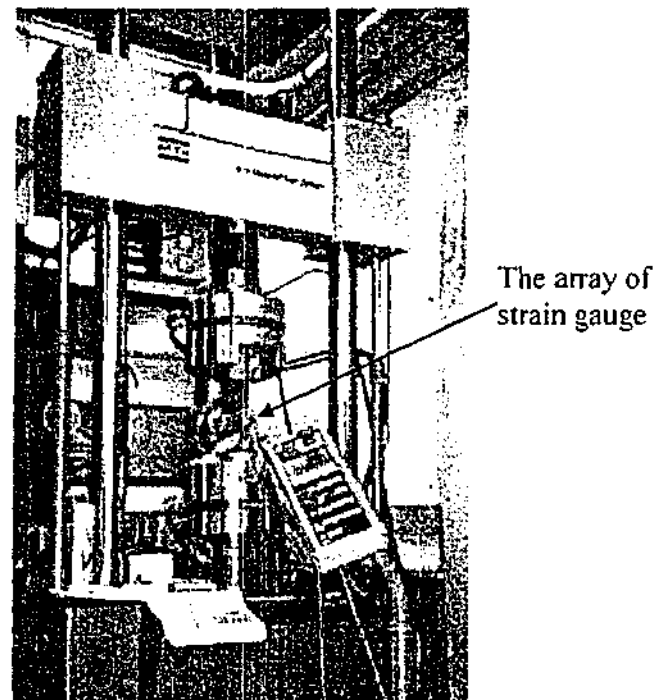


Figure 6.20. The plate specimen of this experimental investigation

6.1.5. Results and Discussions

The strain field from the data from the array of strain gauges is reconstructed using the stress function. As described in the numerical methodology in the section 6.1.3, in order to reconstruct the stress/strain field we need firstly to locate the crack tip by minimizing Equation 6.15 by moving the origin $(X,0)$ of the stress function. To correctly located the crack tip in this investigation, the results from Section 5.4 are incorporated to this methodology to determine the region for searching the crack tip.

The results in Section 5.4 have provided the general location of the damage. For the 10mm crack case the length of interest is 2.5mm to 10mm. By minimizing Equation 6.15 it was found that the minimum error was found at $X=5.75\text{mm}$ (see Figure 6.21). For the second crack (16mm) the search region was determined in Section 5.4 to be between 6mm to 20mm. By minimizing Equation 6.15 the minimum error was found to be at $X = 11.5\text{mm}$ (see Figure 6.22). In the last crack (28-mm), the region of interest is between 11.75mm and 24mm. From the error analysis of this particular length a minimum error was found in 19.25 mm (see Figure 6.23).

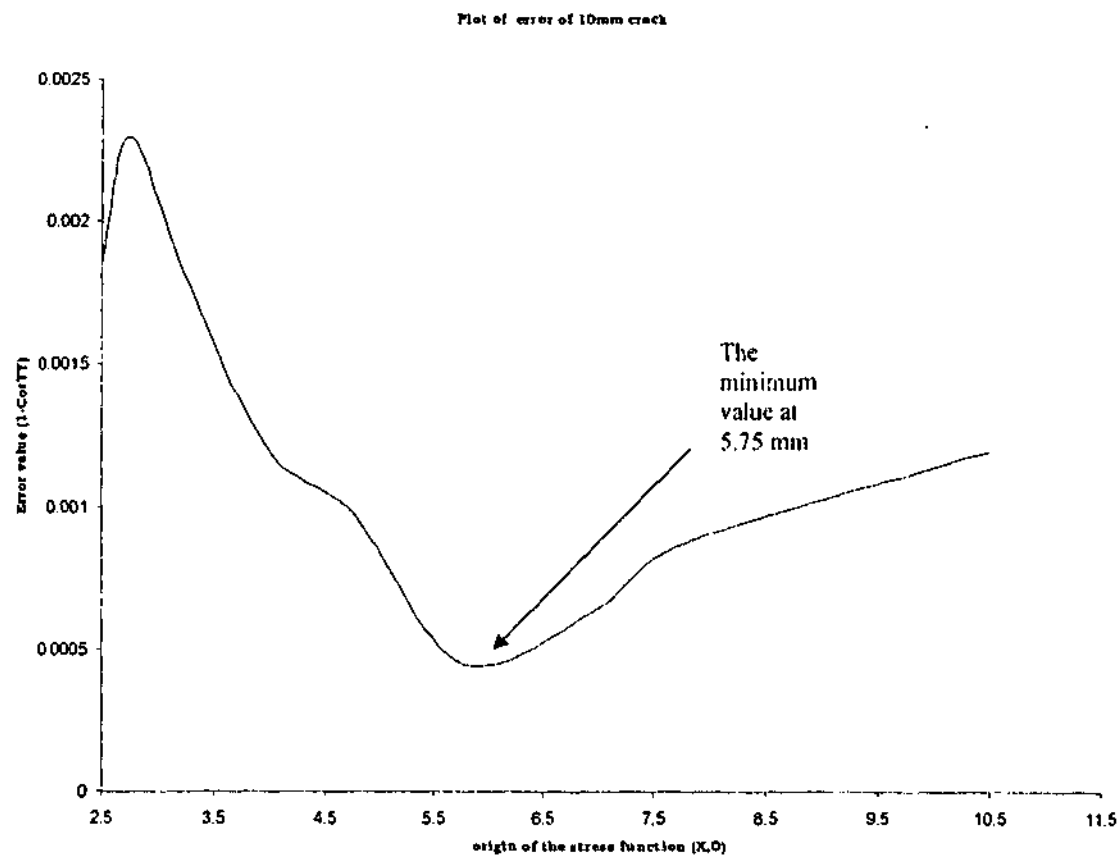


Figure 6.21. The plot of error of 10mm crack

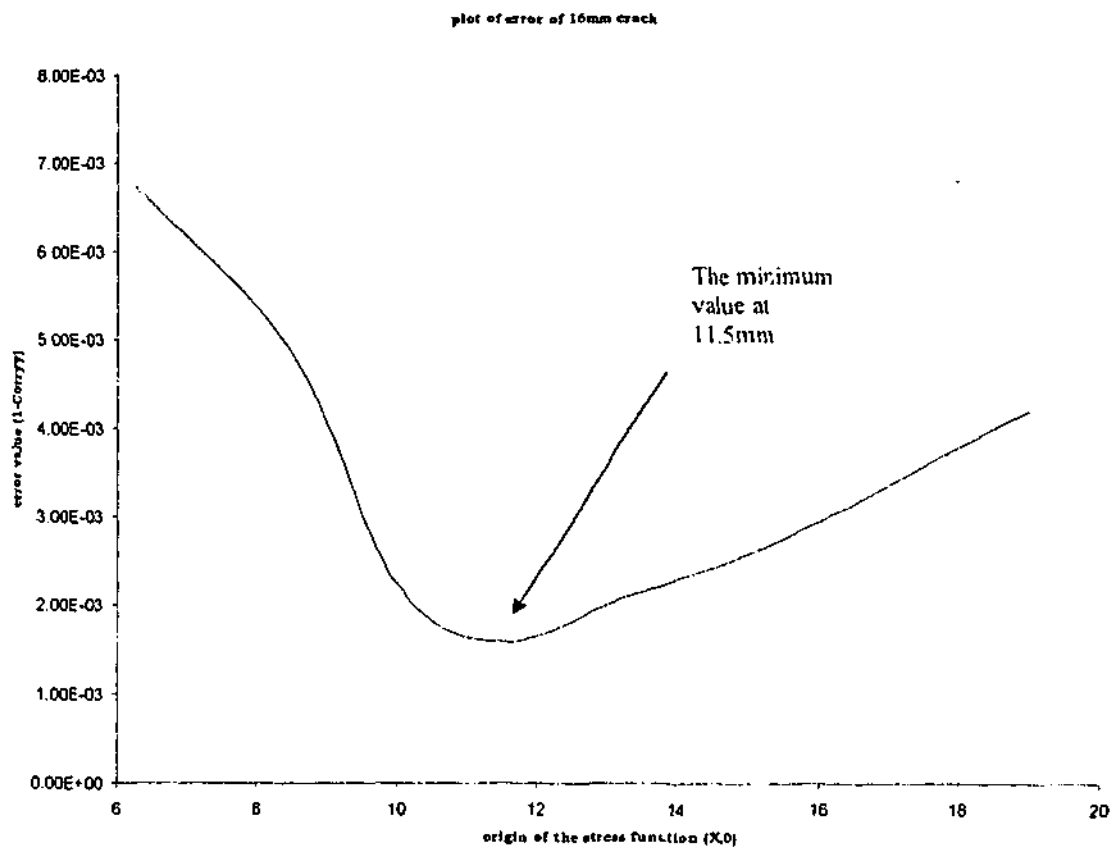


Figure 6.22. Plot of error of 16mm crack

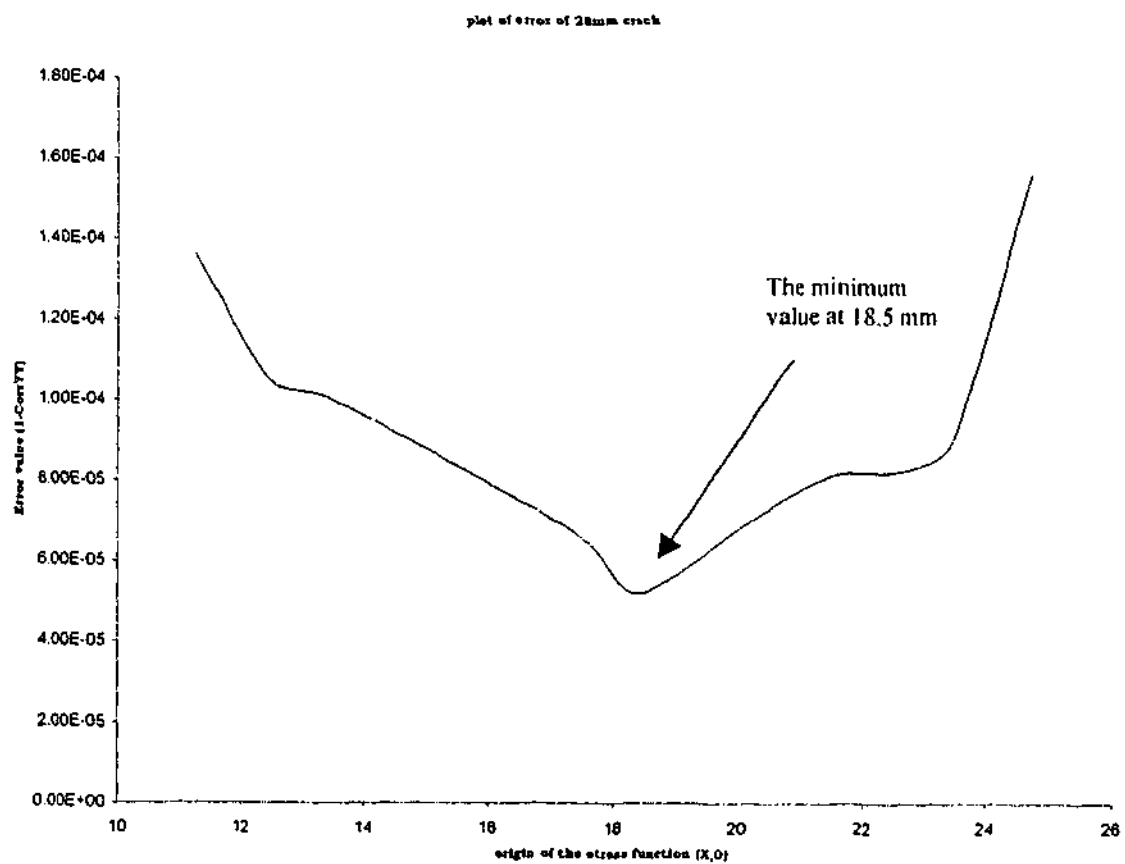


Figure 6.23. Plot of error of 28-mm crack

The results obtained for the location of the crack tip by minimizing Equation 6.15 is shown in Table 6.2. In this table, the theoretical crack length due to plasticity is also presented. The apparent crack extension due to plasticity zone size r_p is obtained from Broek(1986)³⁹ using this following formula:

$$r_p = \frac{a}{2} \left(\frac{\sigma}{\sigma_{ys}} \right)^2 \quad (6.16)$$

where σ , is the remote stress, σ_{ys} is the yield stress that was equal to 41 Mpa for this aluminum plate, and a is the half of crack length.

Table 6.2. The Crack Tip Location

Actual half crack size a (mm)	Calculated from Theory $(a+r_p)$ (mm)	Predicted Experiment $(a+r_p)$ (mm)
5	7.3173	5.75
8	11.954	11.5
14	22.3	18.5

The deviation in the predicted crack length from the actual crack length can be attributed to the plasticity in the crack tip region. The strain fields inside the array of strain gauges from this experiment are shown on the Appendix C. The mode I stress intensity factor, K_I was calculated using Equation 6.13 with the strain value from the reconstructed strain field inside the array. The position of the mode I stress intensity factor, K_I calculation point is schematically shown in Figure 6.24. This position was considered in region II, so the mode I stress intensity factor, K_I calculation was valid. Using stress-strain relationship Equation 6.14 can be written as follow:

$$\varepsilon_{x'x'} = \varepsilon_{xx} \cos\alpha + \varepsilon_{yy} \sin\alpha \quad (6.17)$$

where $\alpha=\theta$ was selected to be 60° , as discussed in the numerical methodology

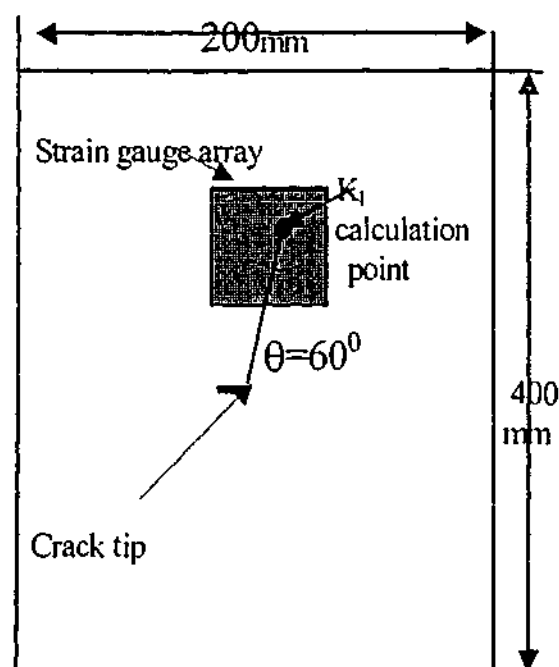


Figure 6.24. Schematic diagram of the experimental mode I SIF, K_I calculation point

The results from this experimental investigation were compared with the theoretical calculation. The SIF mode I, K_I can be calculated theoretically by this following equation;

$$K_I = \sigma \sqrt{\pi a} \quad (6.18)$$

where σ is the remote stress

The calculation of the SIF mode I, K_I is then presented in the Table 6.3. In general, Table 6.3 shows a relatively good agreement between the results of mode I SIF, K_I calculation obtained from theory and the experiment that based on the methodology described in the numerical investigation.

Table 6.3. Mode I Stress Intensity Factor from the experimental investigation

Crack length 2a (mm)	Measured crack size a(mm)	Stress Intensity Factor K_I $\text{Pa}\sqrt{\text{m}}$	Measured Crack size with plasticity zone Correction (mm)	Stress Intensity Factor K_I $\text{Pa}\sqrt{\text{m}}$	Predicted Crack size from experiment (mm)	Stress Intensity Factor K_I from Strain gauge measurement $\text{Pa}\sqrt{\text{m}}$	Stress Intensity Factor K_I from Stress Function $\text{Pa}\sqrt{\text{m}}$
10	5	4.95E+06	7.3173	5.98E+06	5.75	8.87E+06	8.98E+06
16	8	6.46E+06	11.954	7.90E+06	11.45	9.18E+06	9.51E+06
28	14	9.36E+06	22.3	1.18E+07	18.5	1.15E+07	1.14E+07

Since the length of the crack $2a$ in the plate can be determined, the fracture stress (residual strength) of the plate can also be calculated. The fracture stress can be determined by the formula below³⁹:

$$\sigma_c = \frac{K_{IC}}{\sqrt{\pi a}} \quad (6.19)$$

where K_{IC} is the fracture toughness and a is the half of the crack length

Since the plasticity zone size r_p occurred on this experiment the Equation 6.19 becomes

$$\sigma_c = \frac{K_{IC}}{\sqrt{\pi(a + r_p)}} \quad (6.20)$$

In this experimental investigation the fracture toughness of the Aluminum plate was assumed to be $32\text{MPa}\sqrt{\text{m}}$. The crack lengths $2a$ were 10mm, 16mm, and 28mm while the $2(a + r_p)$ were found to be 11.5mm, 23mm, and 37mm. The relationship between the residual strength and the crack length calculating from the theory and experiment are shown in Figure 6.25. In this figure the residual stress is similar to that proposed by Broek(1986)³⁹. The result showed that the methodology presented here can be used to predict the residual strength of the crack plate.

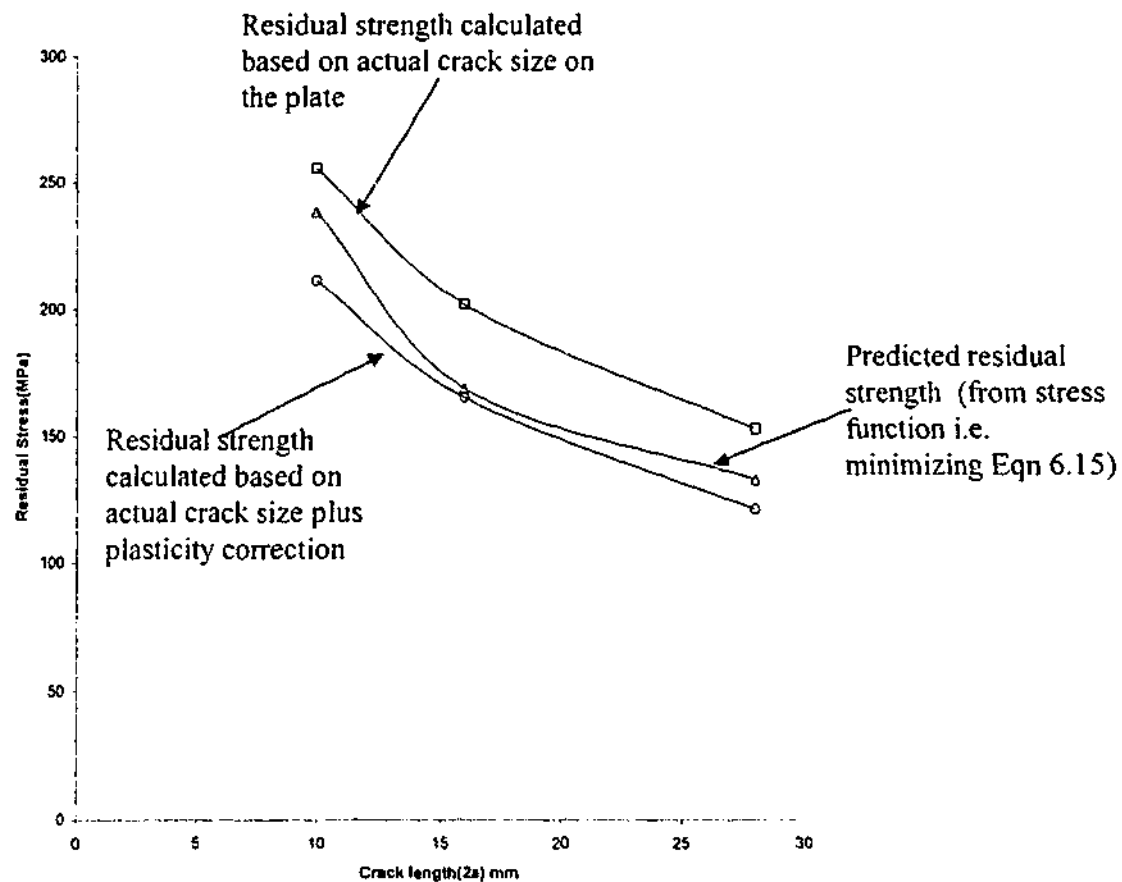


Figure 6.25. Relationship between the residual strength σ_c and the crack length $2a$

The finding from this experimental investigation can be summarized as follows;

- The stress/strain field inside the array can be reconstructed by searching for the minimum error (Equation 6.15). This minimum error occurs on the location further than the actual crack tip position. It appears the plasticity zone size r_p is included.
- Based on the information of the crack tip position and the crack length the mode I SIF, K_I and residual strength (fracture stress) of the structural component can be predicted.

6.2. 3-D Stress Function for Stress Field Construction

In this section, this stress field construction from the array of sensor will be extended to construct the stress field at the back surface of plate with the embedded semi-elliptical crack.

The numerical methodology is now extended so that it can be applied to a thicker structure. A thick plate with an internal surface crack i.e. an embedded semi-elliptical crack will be modeled. The 2D Airy stress function would not be used to construct the stress field at the back of the plate since this problem is a 3D. Hence, a suitable stress function that satisfied the embedded surface crack condition needed to be found. The components of the 3D-stress function are derived in the next section. By replacing the 2D with the 3D-stress function, the numerical methodology could be modified and then applied to a plate with an embedded semi-elliptical crack.

6.2.1. Derivation of the Components of the 3-D Stress Function

In this section the components of the 3D-stress function to be used for constructing an embedded semi-elliptical crack are derived. The derivation results in elliptic integral equations that can then, be solved by analytical formulas. The solutions are in terms of Legendre the 1st and the 2nd kind elliptic integral and Jacobian elliptic function. The values of the terms are then calculated numerically. The completed derivation is shown in Appendix D. The elliptical integral equations obtained from the derivation and the method for solving them are presented below.

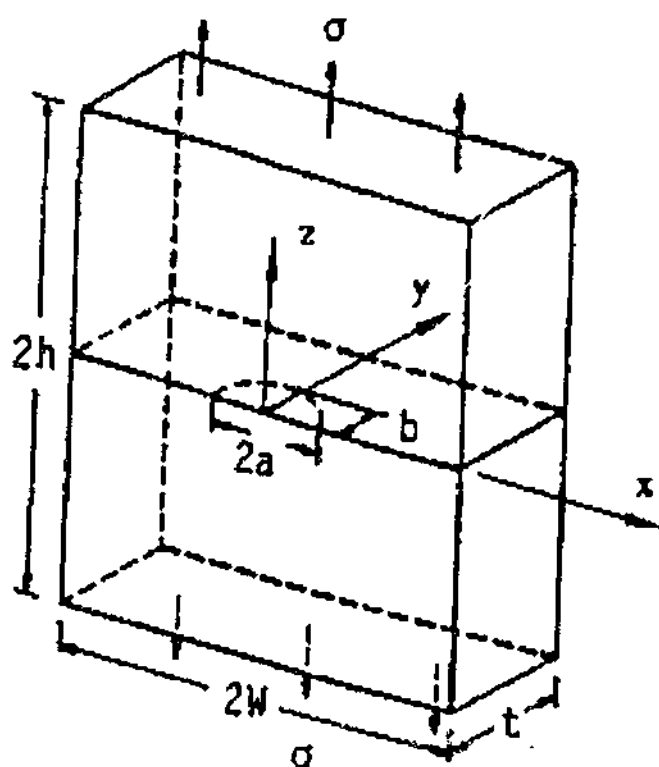


Figure 6.26. A plate with a semi-elliptical crack under tension

Consider a plate with a thickness t that has an embedded semi-elliptical crack as shown in Figure 6.26. The boundary of the semi-elliptical crack is described by:

$$\frac{x^2}{a^2} + \frac{y^2}{b^2} = 1, \quad z = 0, \quad y \geq 0 \quad (6.21)$$

where a is the semi-major axis and b is the semi-minor axis of the ellipse.

The components of the 3D-stress function σ_{xx} , σ_{zz} and τ_{xz} at the back surface of the plate are presented below :

$$\sigma_{xx} = 2G \left[z \frac{\partial^3 \phi}{\partial x^2 \partial z} + \frac{\partial^2 \phi}{\partial x^2} + 2\eta \frac{\partial^2 \phi}{\partial y^2} \right] \quad (6.22)$$

$$\sigma_{zz} = 2G \left[z \frac{\partial^3 \phi}{\partial z^3} - \frac{\partial^2 \phi}{\partial z^2} \right] \quad (6.23)$$

$$\tau_{xz} = 2G \left[z \frac{\partial^3 \phi}{\partial z^2 \partial x} \right] \quad (6.24)$$

where G is the shear modulus.

From Shah and Kobayashi (1971)⁴⁰ the harmonic stress function ϕ can be represented as:

$$\phi = \sum_{i=0}^p \sum_{j=0}^q C_{ij} \frac{\partial^{i+j}}{\partial x^i \partial y^j} \nu^{(i+j+1)} \quad , \quad i+j \leq 4 \quad (6.25)$$

$$\text{where } \nu^{(n)} = \int_{\lambda}^{\infty} \frac{\omega^n(s) ds}{\sqrt{Q(s)}}, \quad \omega(s) = 1 - \frac{x^2}{(a^2 + s)} - \frac{y^2}{(b^2 + s)} - \frac{z^2}{s}, \quad Q(s) = s(a^2 + s)(b^2 + s)$$

By substituting Equation 6.25 into Equation 6.22 the following equation is obtained:

$$\begin{aligned} \sigma_{xx} = 2G \left[z(-8x^2z) \sum_{i=0}^p \sum_{j=0}^q C_{ij} \frac{\partial^{i+j}}{\partial x^i \partial y^j} \int_{\lambda}^{\infty} \frac{1}{(a^2 + s)^2 \sqrt{Q(s)}} \omega^{(i+j)-2}(s) ds (i+j+1)(i+j)(i+j-1) + \right. \\ \left. (4z^2)(i+j+1)(i+j) \sum_{i=0}^p \sum_{j=0}^q C_{ij} \frac{\partial^{i+j}}{\partial x^i \partial y^j} \int_{\lambda}^{\infty} \frac{1}{(a^2 + s) \sqrt{Q(s)}} \omega^{(i+j)-1}(s) ds + \right. \\ \left. (-2)(i+j+1) \sum_{i=0}^p \sum_{j=0}^q C_{ij} \frac{\partial^{i+j}}{\partial x^i \partial y^j} \int_{\lambda}^{\infty} \frac{1}{(a^2 + s) \sqrt{Q(s)}} \omega^{(i+j)}(s) ds + \right. \end{aligned}$$

$$\begin{aligned}
 & (4x^2)(i+j+1)(i+j) \sum_{i=0}^p \sum_{j=0}^q C_{ij} \frac{\partial^{i+j}}{\partial x^i \partial y^j} \int_{\lambda}^{\infty} \frac{1}{(a^2+s)^2 \sqrt{Q(s)}} \omega^{(i+j)-1}(s) ds + \\
 & (-4\eta)(i+j+1) \sum_{i=0}^p \sum_{j=0}^q C_{ij} \frac{\partial^{i+j}}{\partial x^i \partial y^j} \int_{\lambda}^{\infty} \frac{1}{(b^2+s) \sqrt{Q(s)}} \omega^{(i+j)}(s) ds + \\
 & (8\eta^2)(i+j+1)(i+j) \sum_{i=0}^p \sum_{j=0}^q C_{ij} \frac{\partial^{i+j}}{\partial x^i \partial y^j} \int_{\lambda}^{\infty} \frac{1}{(b^2+s)^2 \sqrt{Q(s)}} \omega^{(i+j)-1}(s) ds \Big] \quad (6.26)
 \end{aligned}$$

By substituting Equation 6.25 into Equation 6.23 the following equation is obtained

$$\begin{aligned}
 \sigma_{zz} = 2G \Bigg[& -8z^4 \sum_{i=0}^p \sum_{j=0}^q C_{ij} \frac{\partial^{i+j}}{\partial x^i \partial y^j} \int_{\lambda}^{\infty} \frac{1}{s^3 \sqrt{Q(s)}} \omega^{(i+j)-2}(s) ds (i+j+1)(i+j)(i+j-1) \\
 & + 2(i+j+1) \sum_{i=0}^p \sum_{j=0}^q C_{ij} \frac{\partial^{i+j}}{\partial x^i \partial y^j} \int_{\lambda}^{\infty} \frac{1}{s \sqrt{Q(s)}} \omega^{(i+j)}(s) ds \\
 & + (8z^2)(i+j+1)(i+j) \sum_{i=0}^p \sum_{j=0}^q C_{ij} \frac{\partial^{i+j}}{\partial x^i \partial y^j} \int_{\lambda}^{\infty} \frac{1}{s^2 \sqrt{Q(s)}} \omega^{(i+j)-1}(s) ds \Big] \quad (6.27)
 \end{aligned}$$

By substituting Equation 6.25 into Equation 6.24 the following equation is obtained

$$\begin{aligned}
 \tau_{xz} = 2G \Bigg[& -8xz^3 \sum_{i=0}^p \sum_{j=0}^q C_{ij} \frac{\partial^{i+j}}{\partial x^i \partial y^j} \int_{\lambda}^{\infty} \frac{1}{(a^2+s)^2 \sqrt{Q(s)}} \omega^{(i+j)-2}(s) ds (i+j+1)(i+j)(i+j-1) + \\
 & (4xz)(i+j+1)(i+j) \sum_{i=0}^p \sum_{j=0}^q C_{ij} \frac{\partial^{i+j}}{\partial x^i \partial y^j} \int_{\lambda}^{\infty} \frac{1}{(a^2+s) \sqrt{Q(s)}} \omega^{(i+j)-1}(s) ds \Big] \quad (6.28)
 \end{aligned}$$

To solve these integral equations, the transformation formula from Byrd and Friedman (1954)⁴¹ is used. This formula is used to transform the integral equation into the elliptic function integral,

$$\int_y^{\infty} \frac{R(t)dt}{\sqrt{(t-a)(t-b)(t-c)}} = g \int_0^{u_1} R[c + (a-c)ns^2u] du \quad (6.29)$$

where $R(t)$ is any rational function of t , and

$$sn^2u = \frac{a-c}{t-c}, \quad k^2 = \frac{b-c}{a-c}, \quad g = \frac{2}{\sqrt{a-c}}, \quad k'^2 = 1 - k^2, \quad \varphi = am u_1 = \sin^{-1} \sqrt{\frac{a-c}{y-c}}, \quad sn u_1 = \sin \varphi$$

In case for the integral equations above the following conditions must be satisfied;

$$a = 0, \quad b = -b^2, \quad c = -a^2, \quad t = s, \quad y = \lambda$$

After the transformation, the following recursive formula (also from Byrd and Friedman (1954)) for the Jacobian function are used:

$$\begin{aligned} \int \frac{sn^n u du}{cn^p u dn^{2m} u} &= \int sn^n unc^p und^{2m} u du \\ &= \frac{1}{(p-1)k'^2} \left\{ sn^{n+1} unc^{p-1} und^{2m-1} u + [p-n-2 + (n-2p+4-2m)k^2] \right. \\ &\quad \left. \int sn^n unc^{p-2} und^{2m} u du + k^2(p-n+2m-3) \int sn^n unc^{p-4} und^{2m} u du \right\} \quad (6.30) \\ p &\neq 1 \end{aligned}$$

and

$$\int sn^{2m} u cn^{2n} und^{2p} u du = \frac{1}{k^{2(m+n)}} \sum_{j=0}^m \sum_{\gamma=0}^n \frac{(-1)^{j+\gamma+n} k^{2(n-\gamma)} m! n!}{(m-j)! j! (n-\gamma)! \gamma!} I_{2(p-j-\gamma)} \quad (6.31)$$

The analytical calculations from the integrals are presented at Appendix D. The calculations of the Legendre elliptic integral of the 1st kind, $F(\varphi, k) = u_1$ and the 2nd kind, $E(u_1)$ and the Jacobian elliptic functions $sn u_1$, $cn u_1$,

and are done numerically using recipe (see Appendix D) from Press, W.H et al(1992)⁴². The analytical calculations of the integrals combined with the numerical program of the elliptic integral and functions that are incorporated into the Equation 6.26, 6.27 and 6.28 are the core of this new algorithm.

6.2.2. Numerical Investigations

To evaluate this algorithm the following numerical work was conducted. As test cases 12 mild steel plate of length 120 mm, width 120 mm and thickness 20 mm were modeled using 3D FE models. Each of the plate had an embedded semi-elliptical crack with $b/t = 0.1, 0.2, 0.4, 0.5$ and $b/a = 0.2, 0.4, 0.6$, where a , b , and t are the semi-minor, semi-major axis of the ellipse and the thickness of the plate respectively. The remote stress in the Z direction was 69600 MPa. The mesh design of the FE model on the crack surface was based on Raju-Newmans(1980)⁴³ work. An example of the 3D FE model of the plate can be seen in Figure 6.27 and the detailed surface crack element is shown in Figure 6.27a. Two arrays of sensor points (each is 6 rows x 12 columns) are at the back surface of the plate where the embedded semi-elliptical crack between them. Figure 6.28 shows a schematic representation of this case study while the detail of position of the sensor points is shown in Figure 6.28a.

To simulate readings from arrays of sensors, the stresses/strains of these FEM calculations at the back surface of the plates were used as input into the stress field algorithm. The stress value at each sensors point was evaluated. These sensor readings acted as the sensor output of the array from which the entire stress field inside the array was constructed by the new algorithm. The stress field predicted by the algorithm with the model input was then compared with the FEM results.

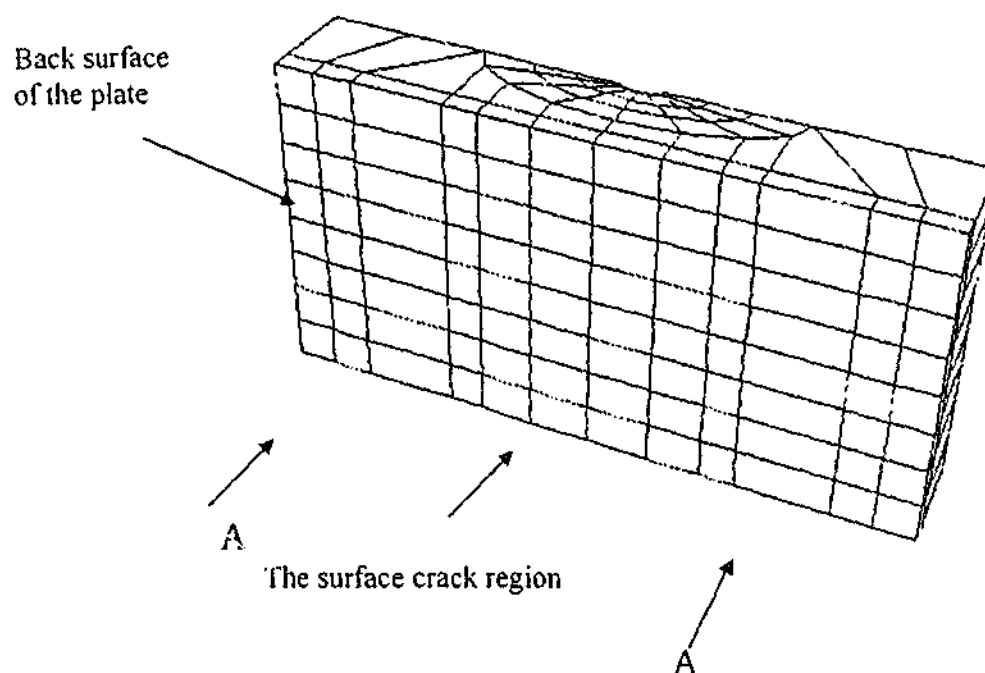


Figure 6.27. Half plate 3D FE model of the investigation

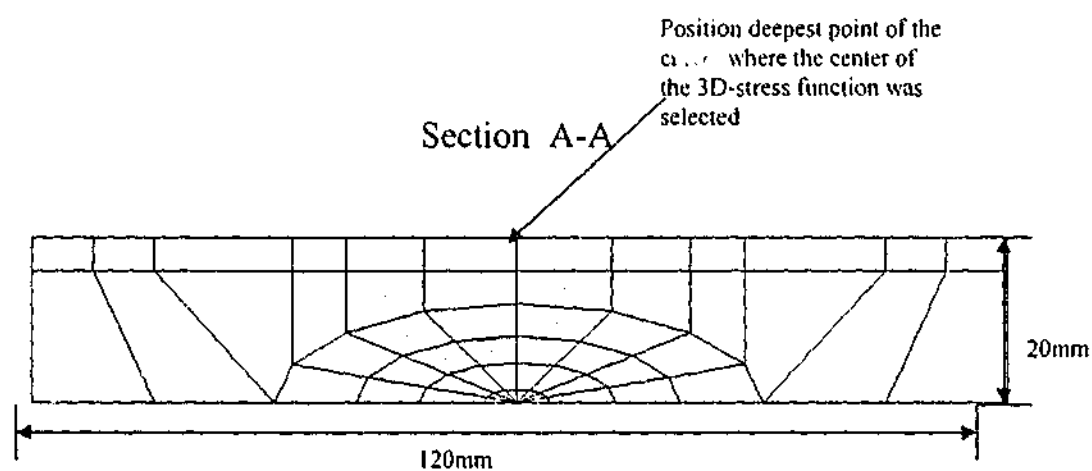


Figure 6.27a. Detailed element of the surface crack

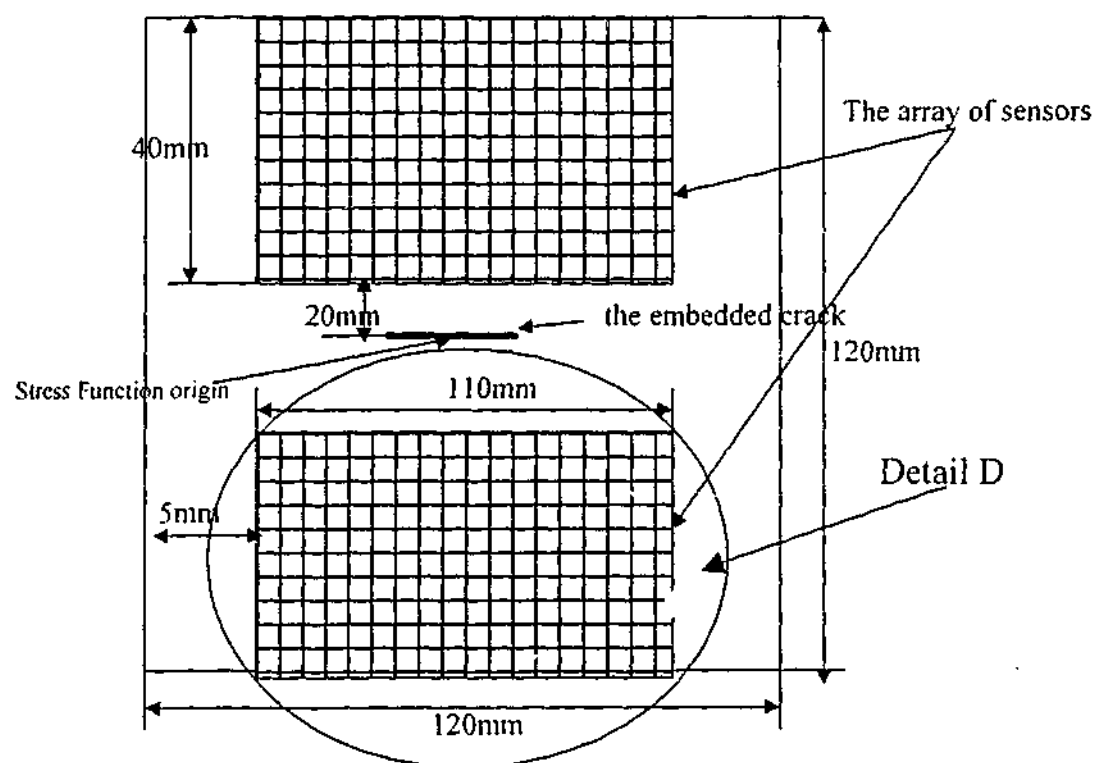


Figure 6.28. Two identical arrays of sensors (each is 6 rows x 12 columns) at the back surface of the plate with an embedded semi-elliptical crack in between them

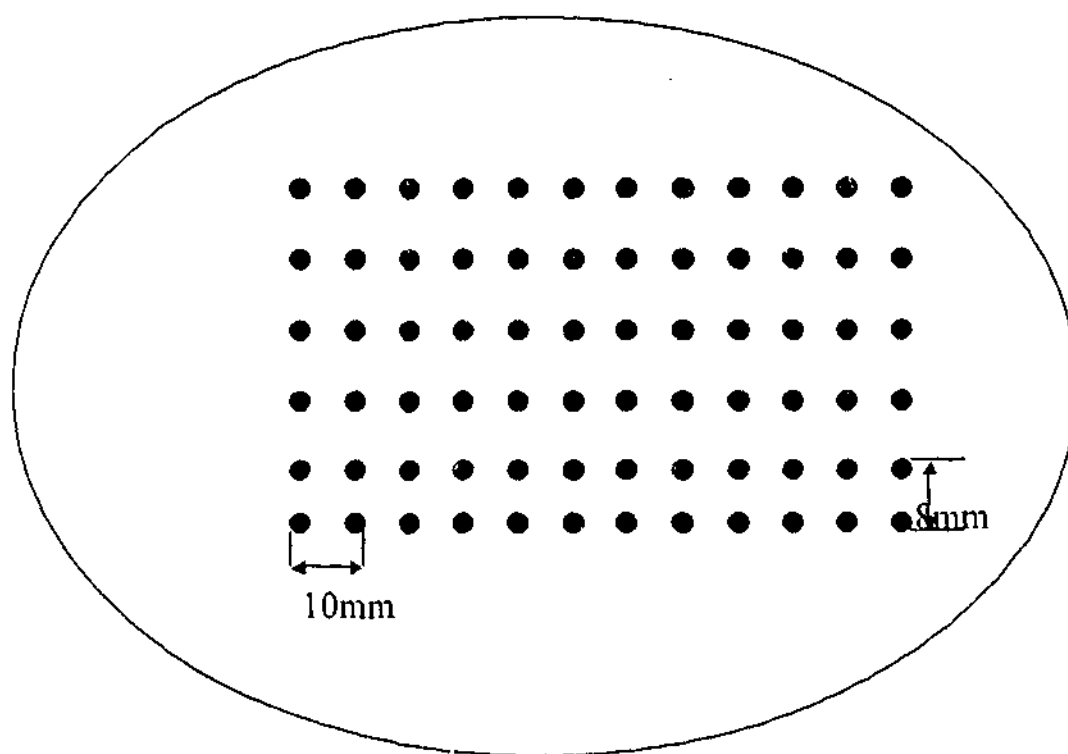


Figure 6.28a. Detail D, the position of the sensor point measurement on the plate in numerical investigation

6.2.3 Results and Discussion

The results from this numerical investigation are presented in this section. All the stress fields inside the array of this numerical investigation were constructed using the (derived) 3D-stress function in the previous section. The origin of the stress function $(X,0,Z)$ was selected in the position of the deepest point of the crack i.e. $(60,0,20)$. This is shown schematically in Figure 6.27a and 6.28.

For the plate that has an embedded semi-elliptical of $b/a=0.2$ with $b/t=0.1, 0.2, 0.4$ and 0.5 , the stress field in Z-direction obtained from a set of finite element results are shown in Figure 6.29, 6.31, 6.33 and 6.35, while the stress fields that are constructed with the 3D stress function are presented in Figure 6.30, 6.32, 6.34 and 6.36. It can be seen from those figures that the derived 3D-stress function is able to construct the stress field inside the array of the sensors in relatively accurately with the stress field from the finite element calculation.

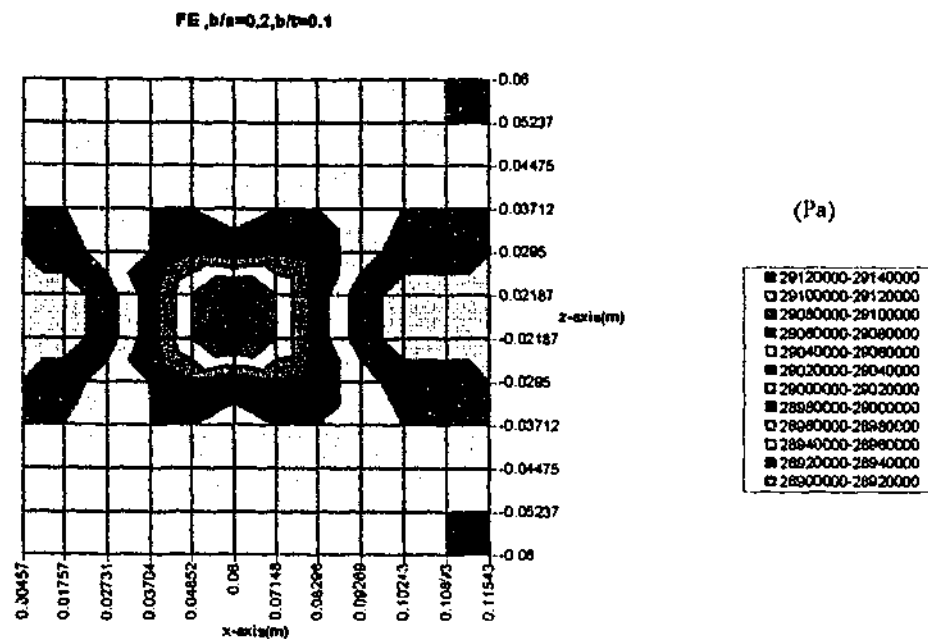


Figure 6.29. Stress field in Z-direction σ_{zz} for $b/a=0.2, b/t=0.1$, calculated from FEM

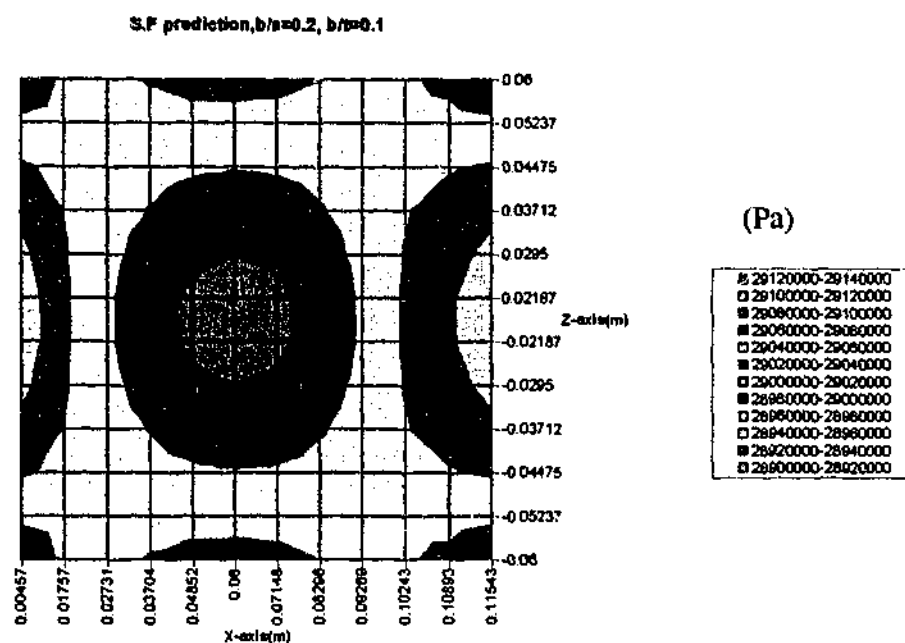


Figure 6.30. Stress field in Z-direction σ_{zz} for $b/a=0.2, b/t=0.1$, constructed from The Stress Function

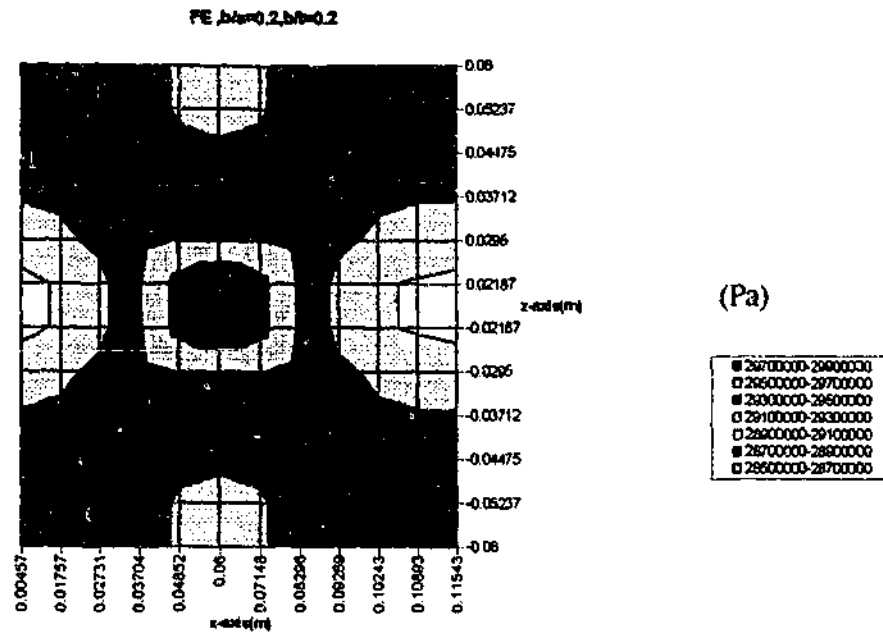


Figure 6.31. Stress field in Z-direction σ_{zz} for $b/a=0.2$, $b/t=0.2$, calculated from FEM

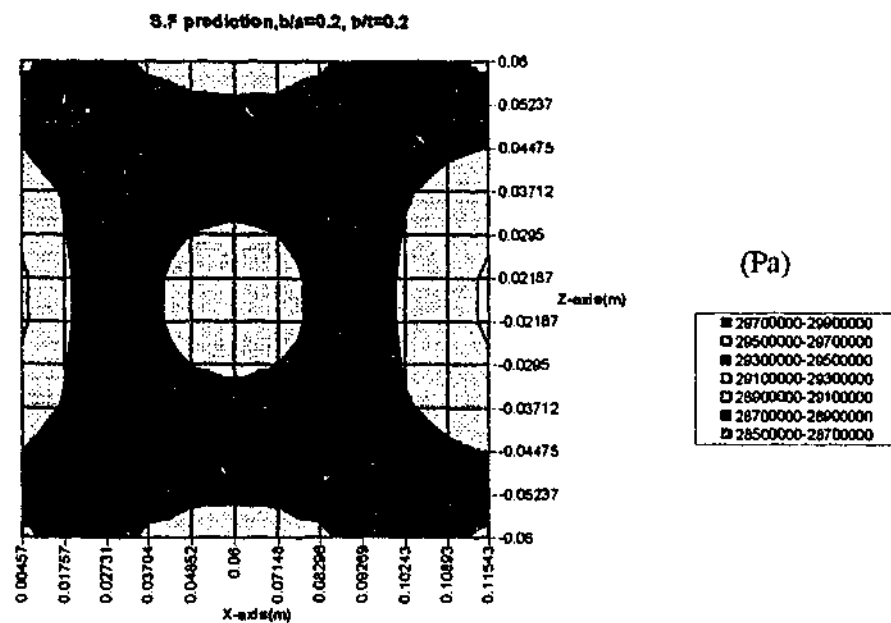


Figure 6.32. Stress field in Z-direction σ_{zz} for $b/a=0.2$, $b/t=0.2$, constructed from The Stress Function

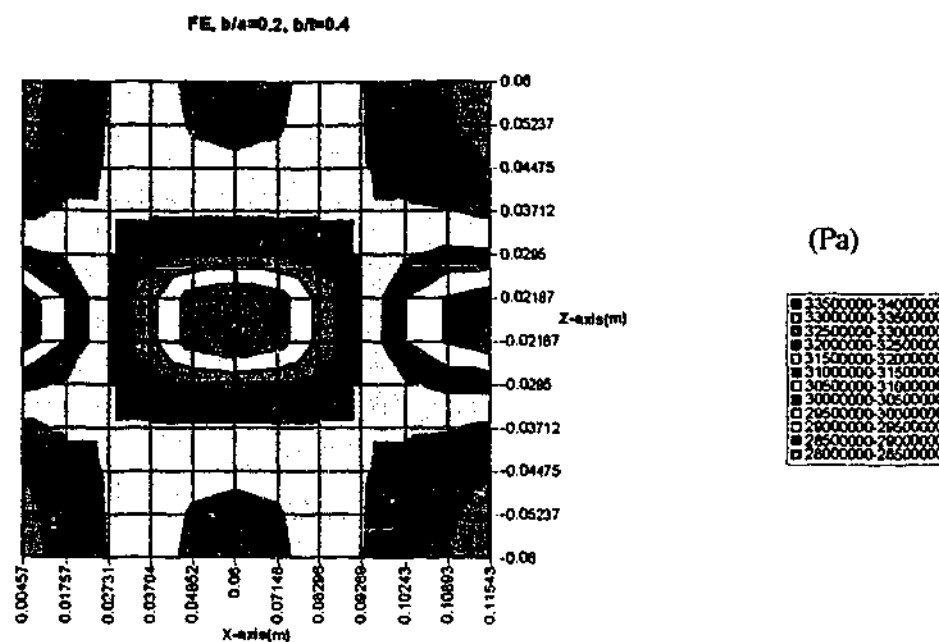


Figure 6.33. Stress field in Z-direction σ_{zz} for $b/a=0.2$, $b/t=0.4$, calculated from FEM

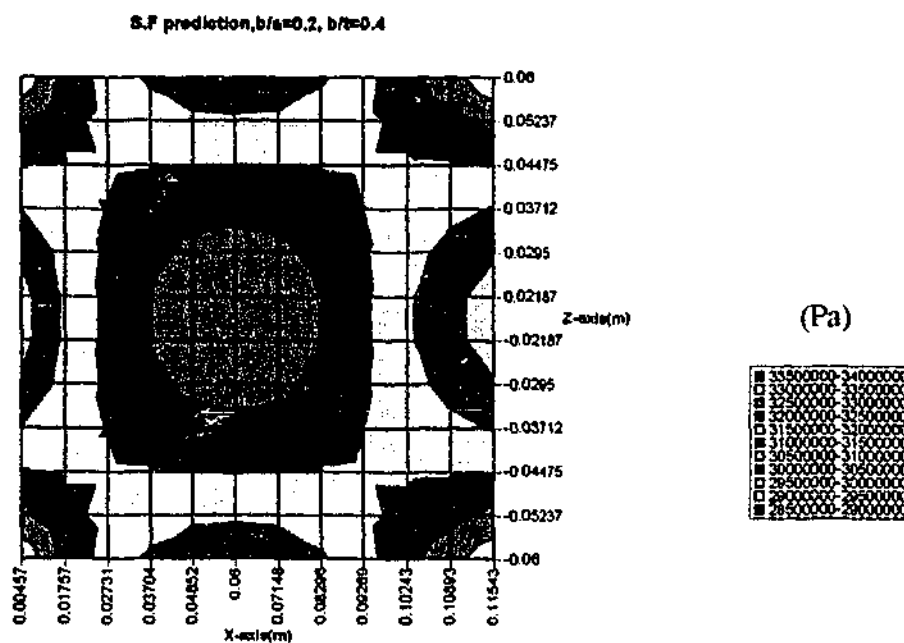


Figure 6.34. Stress field in Z-direction σ_{zz} for $b/a=0.2$, $b/t=0.4$, constructed from The Stress Function

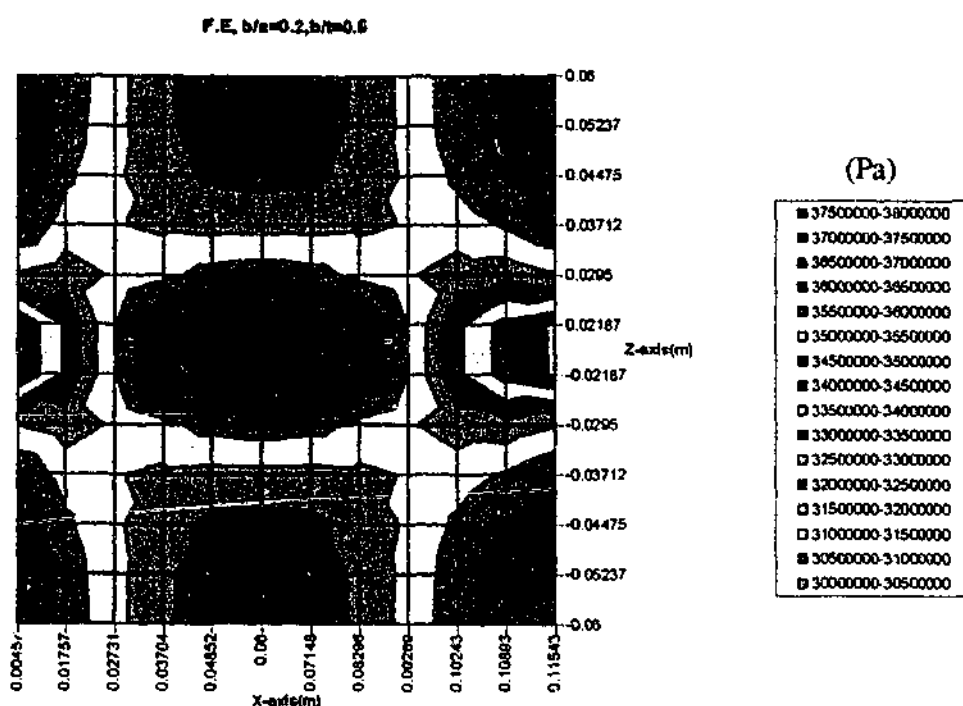


Figure 6.35. Stress field in Z-direction σ_{zz} for $b/a=0.2$, $b/t=0.5$, calculated from FEM

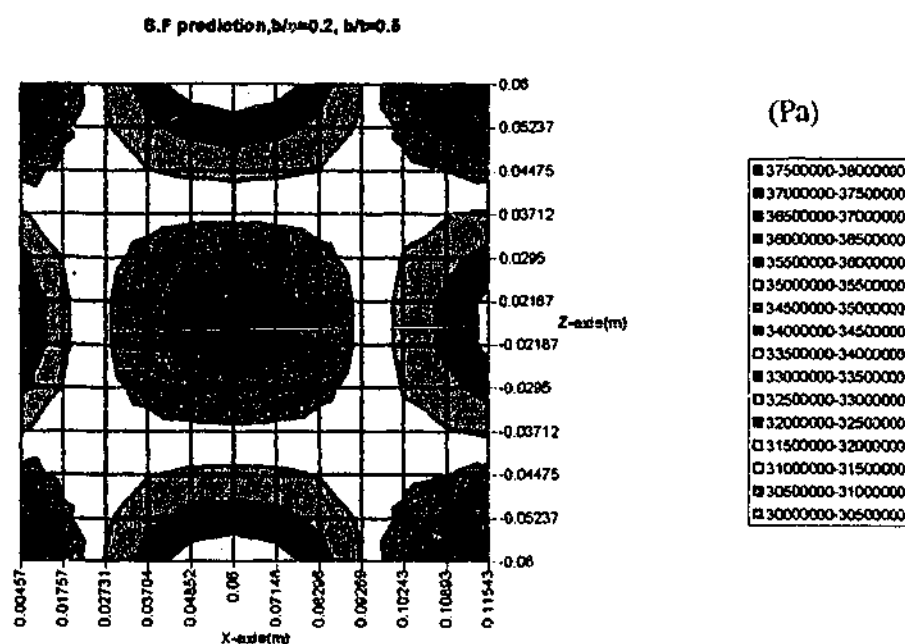


Figure 6.36. Stress field in Z-direction σ_{zz} for $b/a=0.2$, $b/t=0.5$, constructed from The Stress Function

For the plate that has an embedded semi-elliptical of $b/a=0.4$ with $b/t=0.1, 0.2, 0.4$ and 0.5 , the stress fields in Z-direction obtained from a set of finite element results are shown in Figure 6.37, 6.39, 6.41 and 6.43, while the stress fields that are constructed with the 3D stress function are presented in Figure 6.38, 6.40, 6.42 and 6.44. In Figure 6.37 and 6.38 the constructed stress field of the stress function is slight different from the finite element calculation. However, when the thickness ratio b/t increase to $0.2, 0.4$ and 0.5 the constructed stress field inside the array of the sensors are in a good agreement with the stress field from the finite element calculation (see Figure 6.39 to 6.44).

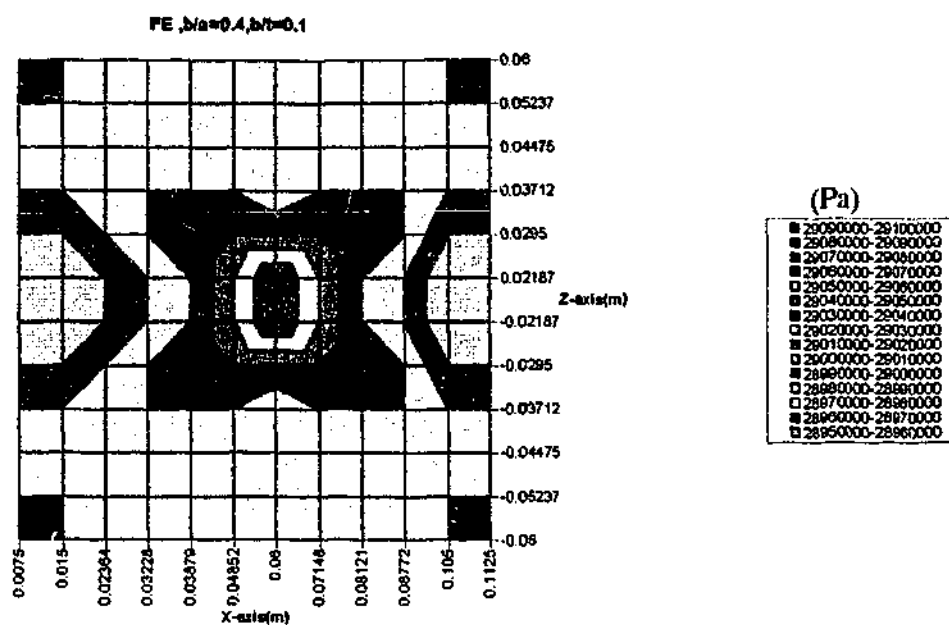


Figure 6.37. Stress field in Z-direction σ_{zz} for $b/a=0.4$, $b/t=0.1$, calculated from FEM

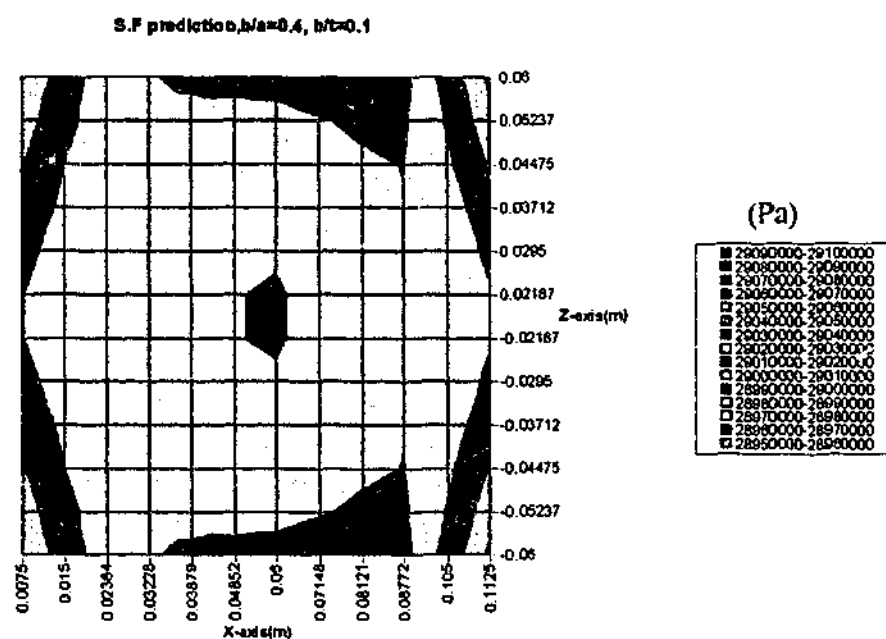


Figure 6.38. Stress field in Z-direction σ_{zz} for $b/a=0.4$, $b/t=0.1$, constructed from The Stress Function

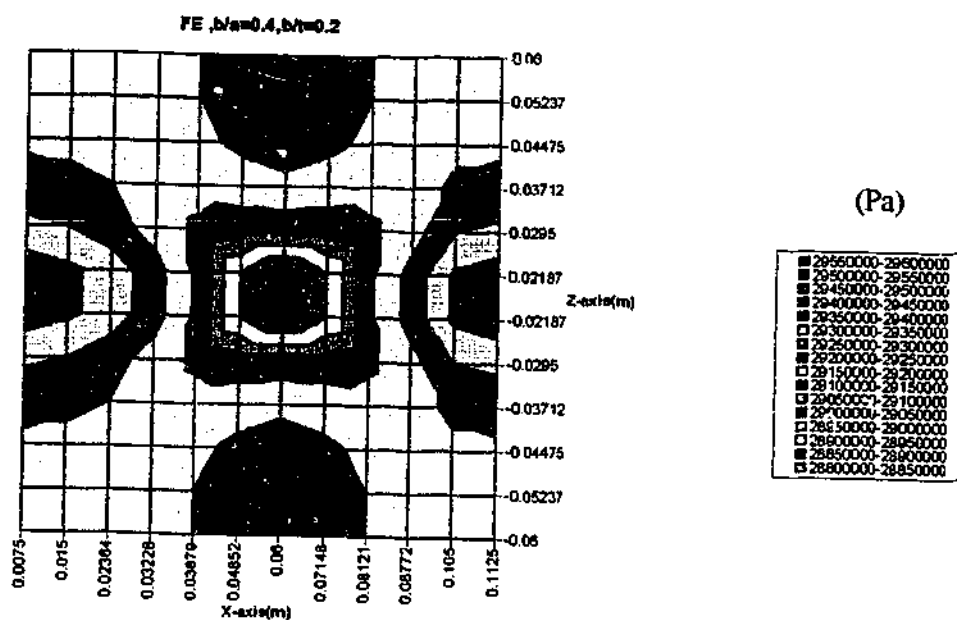


Figure 6.39. Stress field in Z-direction σ_{zz} for $b/a=0.4, b/t=0.2$, calculated from FEM

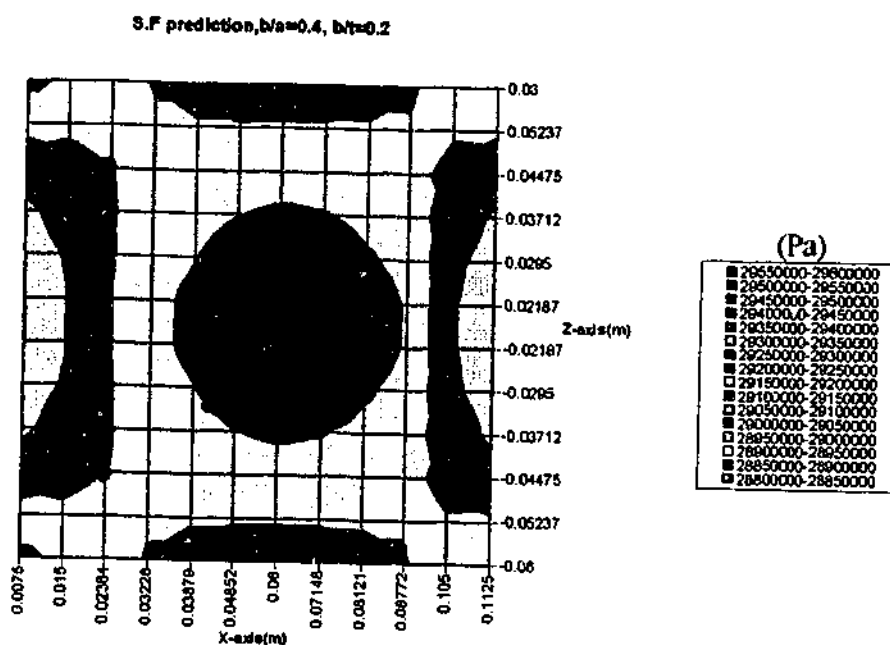


Figure 6.40. Stress field in Z-direction σ_{zz} for $b/a=0.4, b/t=0.2$, constructed from The Stress Function

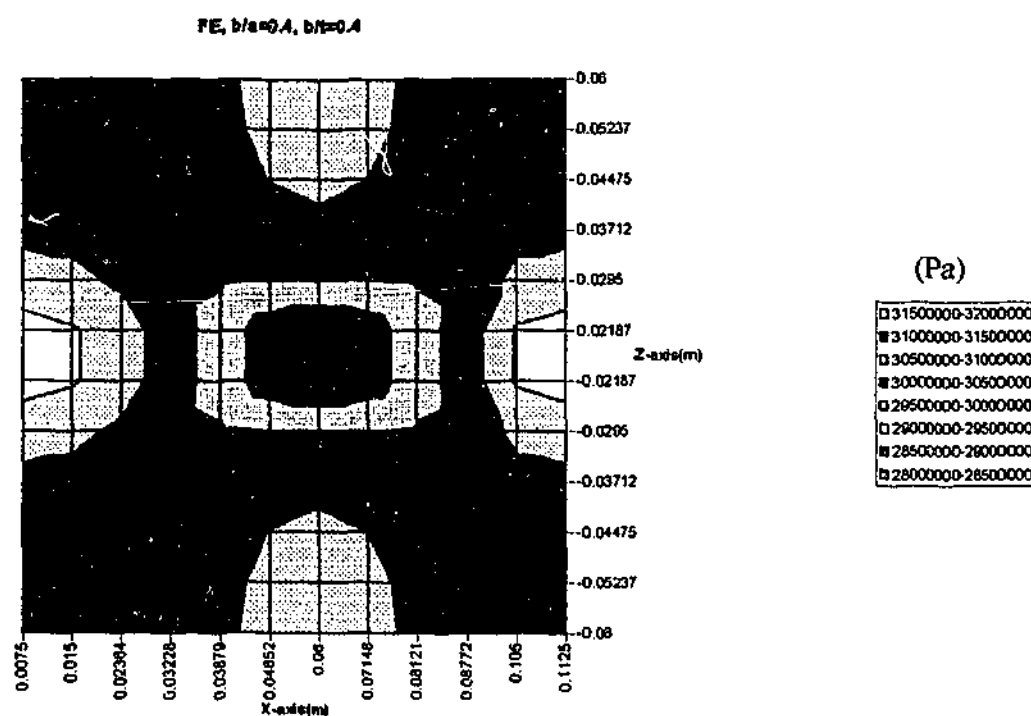


Figure 6.41. Stress field in Z-direction σ_{zz} for $b/a=0.4$, $b/t=0.4$, calculated from FEM

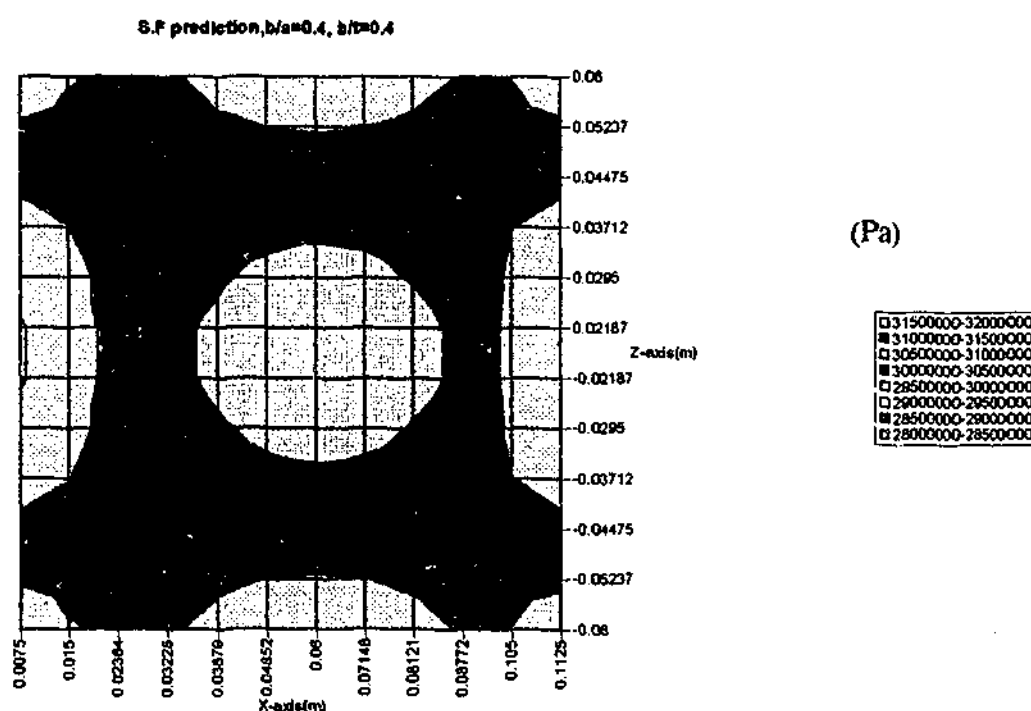


Figure 6.42. Stress field in Z-direction σ_{zz} for $b/a=0.4$, $b/t=0.4$, constructed from The Stress Function

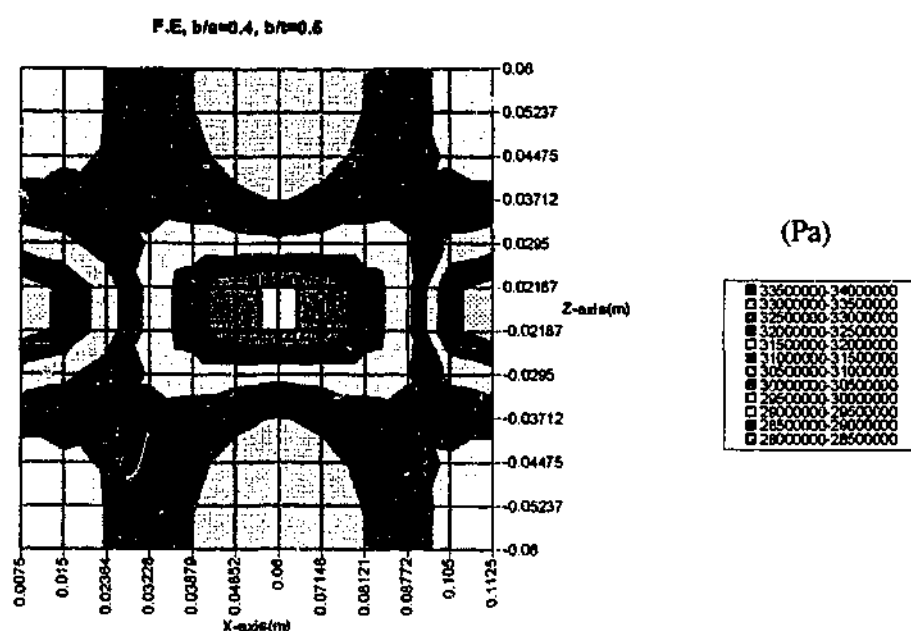


Figure 6.43. Stress field in Z-direction σ_{zz} for $b/a=0.4$, $b/t=0.5$, calculated from FEM

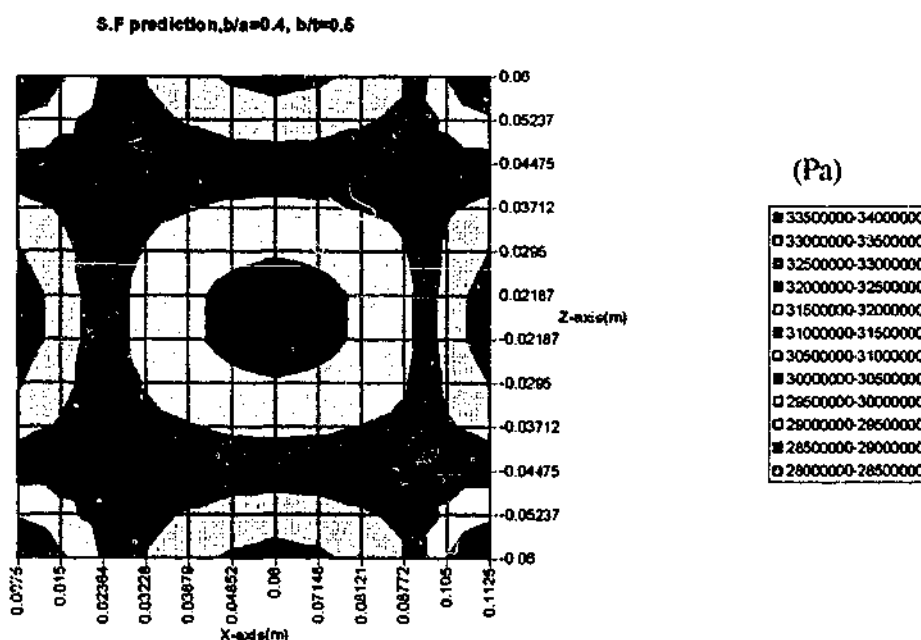


Figure 6.44. Stress field in Z-direction σ_{zz} for $b/a=0.4$, $b/t=0.5$, constructed from The Stress Function

For the plate that has an embedded semi-elliptical of $b/a=0.6$ with $b/t=0.1, 0.2, 0.4$ and 0.5 , the stress field in Z-direction obtained from a set of finite element results are shown in Figure 6.45, 6.47, 6.49 and 6.51, while the stress fields that are constructed with the 3D stress function are presented in Figure 6.46, 6.48, 6.50 and 6.52. It can be seen from those figures the derived 3D-stress function is also be able to construct the stress field inside the array of the sensors in a relatively good agreement with the stress field from the finite element calculation.

The stress field results from the numerical investigation above have shown the ability of the 3D stress function that was derived in Section 6.2.1 to construct the stress field. However, for the case of $b/t=0.1$ with $b/a=0.4$ and 0.6 the stress function construction appears to be different with the calculation from FEM. This is because the crack is relatively small. This may be a limitation of this technique to construct the stress field.

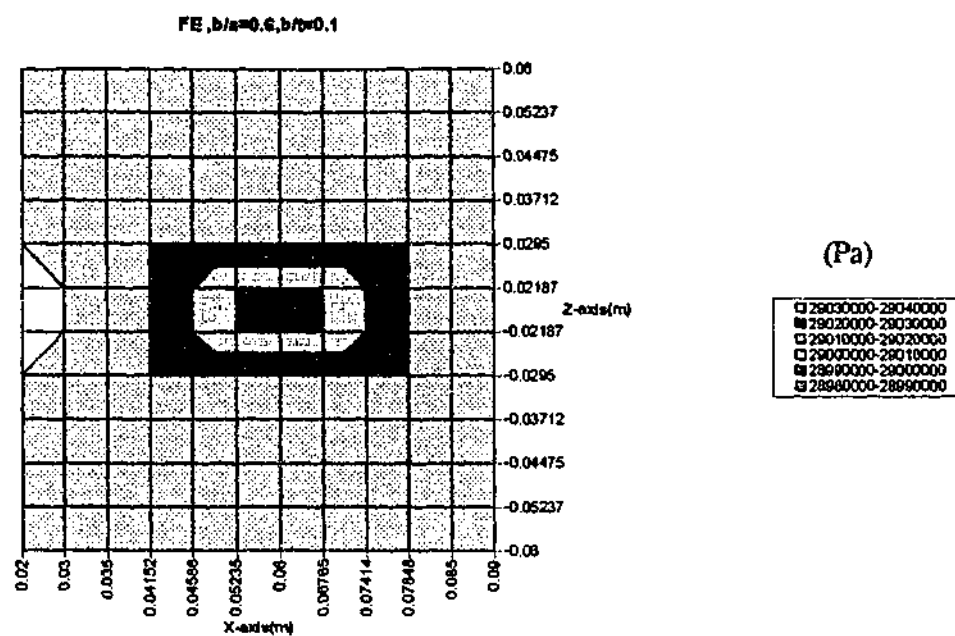


Figure 6.45. Stress field in Z-direction σ_{zz} for $b/a=0.6$, $b/t=0.1$, calculated from FEM

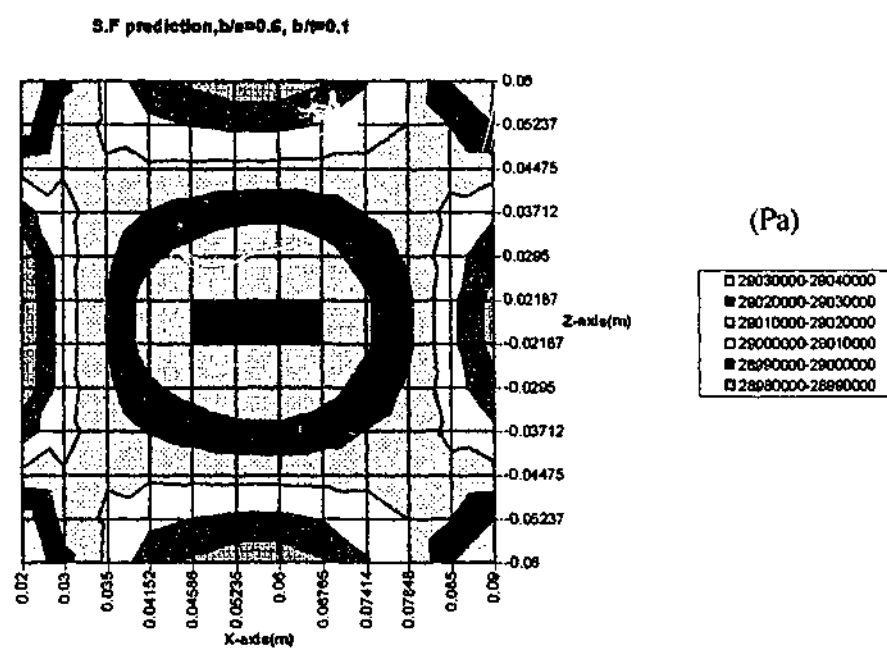


Figure 6.46. Stress field in Z-direction σ_{zz} for $b/a=0.6$, $b/t=0.1$, constructed from The Stress Function

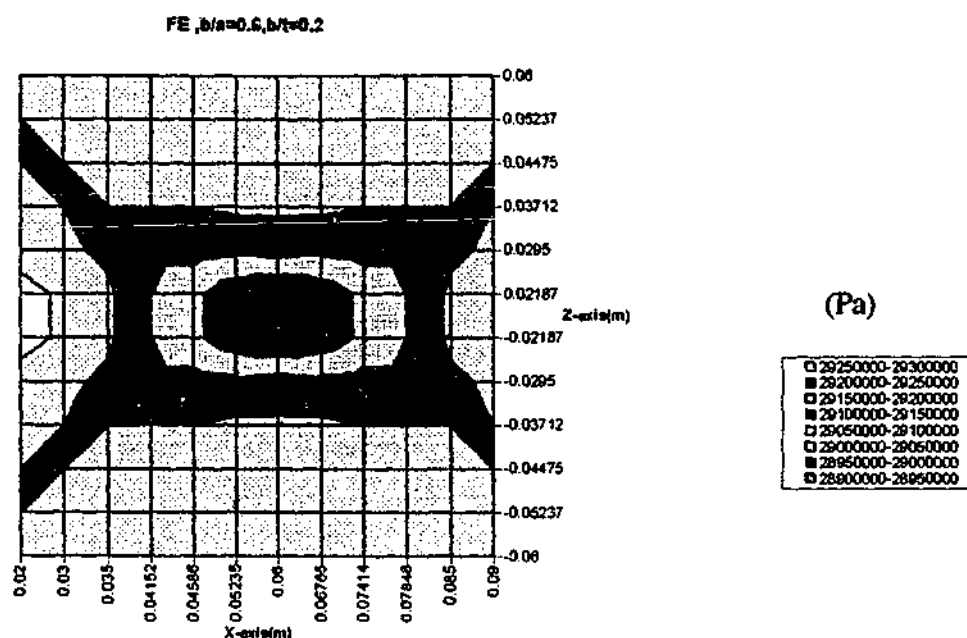


Figure 6.47. Stress field in Z-direction σ_{zz} for $b/a=0.6$, $b/t=0.2$, calculated from FEM

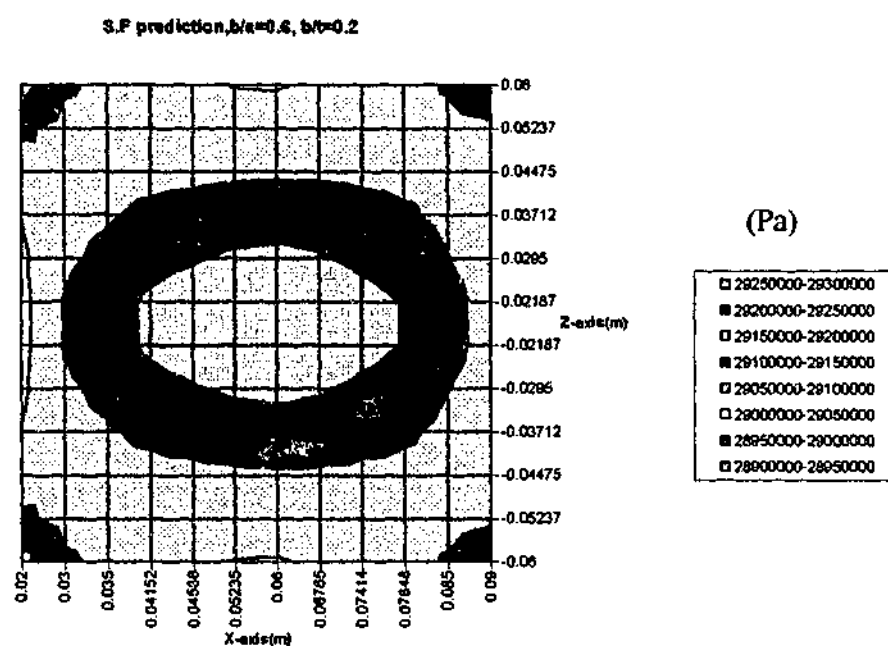


Figure 6.48. Stress field in Z-direction σ_{zz} for $b/a=0.6$, $b/t=0.2$, constructed from The Stress Function

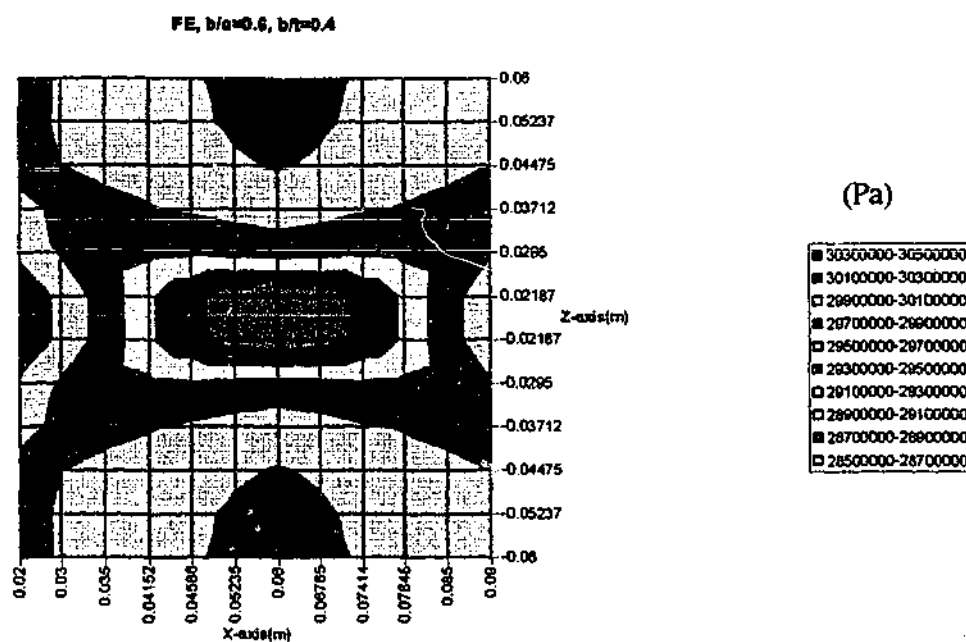


Figure 6.49. Stress field in Z-direction σ_{zz} for $b/a=0.6$, $b/t=0.4$, calculated from FEM

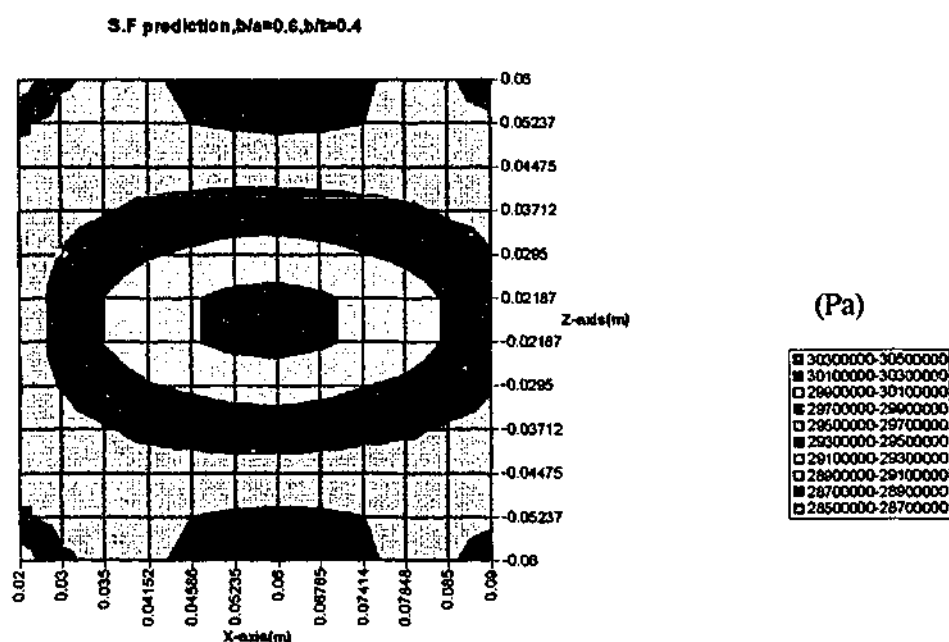


Figure 6.50. Stress field in Z-direction σ_{zz} for $b/a=0.6$, $b/t=0.4$, constructed from The Stress Function

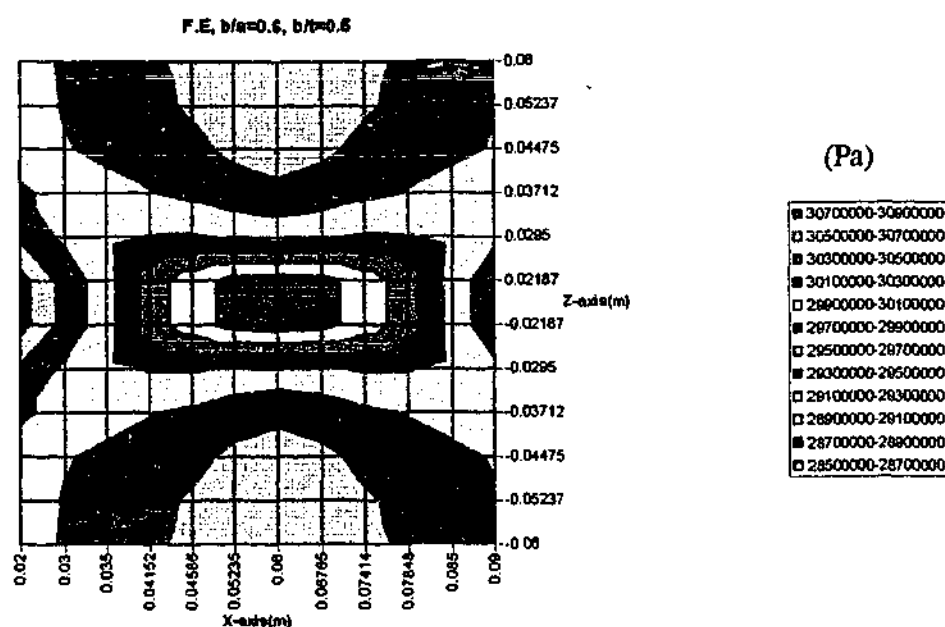


Figure 6.51. Stress field in Z-direction σ_{zz} for $b/a=0.6$, $b/t=0.5$, calculated from FEM

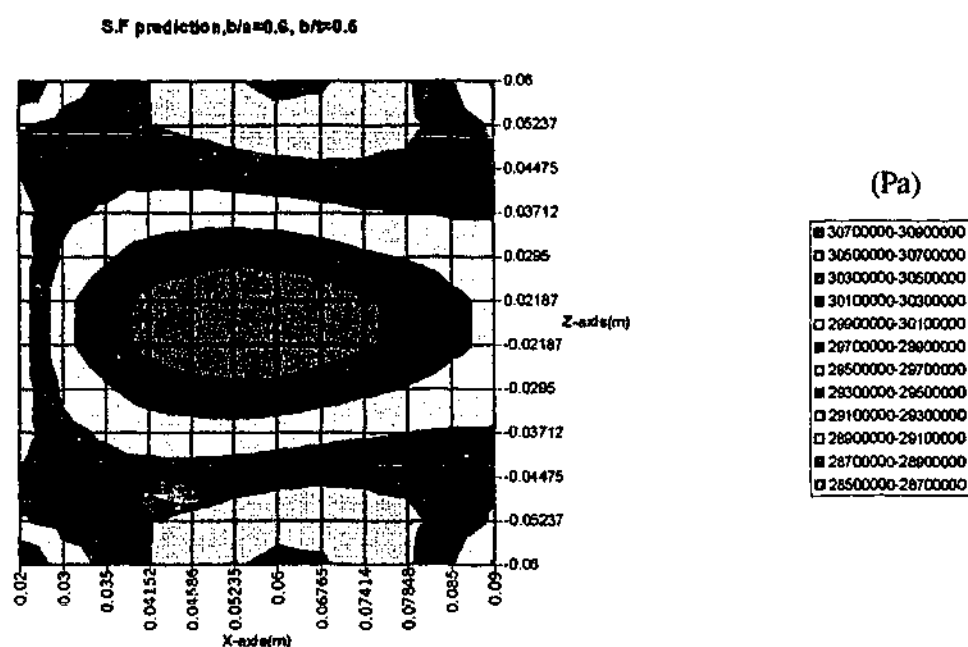


Figure 6.52. Stress field in Z-direction σ_{zz} for $b/a=0.6$, $b/t=0.5$, constructed from The Stress Function

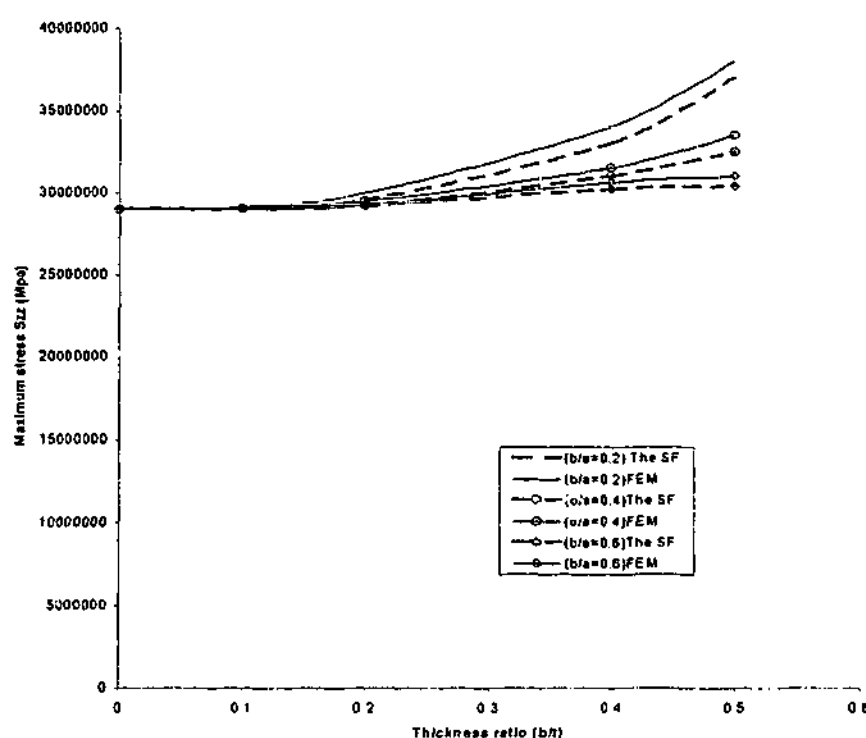


Figure 6.53. Comparison between the calculation from FEM and constructed from The Stress Function in thickness ratio versus maximum stress in Z-direction σ_{zz} for $b/a=0.2$, 0.4, 0.6

The maximum stress in Z-direction σ_{zz} is found to be in the middle region of the sensor (see Figure 6.27a and 6.28). This is the closest region to the embedded semi-elliptical crack. The graphs of the maximum stresses in Z-direction σ_{zz} s are presented in Figure 6.53. It can be seen from this figure the graphs are in a good agreement. The highest gradient of the maximum stress plot occurs at $b/a=0.2$. The gradient of the plot is inversely proportional to the b/a (semi-minor/major-axis) ratio. The highest maximum stress is found to be at the plate with the b/a ratio equals to 0.2 and the thickness ratio b/t equal to 0.5. This is particularly true because at that condition the structural component has the largest embedded semi-elliptical crack. The percentages of differences between the maximum stresses σ_{zz} s calculated from FEM and reconstructed from the stress function are shown in Table 6.4. The results from the table show a good agreement between them with a maximum error 3%.

Table 6.4. Percentage differences of the maximum stresses σ_{zz} s calculated from FEM and reconstructed from the stress function

b/t	(b/a=0.2) From Stress Function Prediction	(b/a=0.2) From FEM	% difference	(b/a=0.4) From Stress Function Prediction	(b/a=0.4) From FEM	% difference	(b/a=0.6) From Stress Function Prediction	(b/a=0.6) From FEM	% difference
0	-	29000000	-	-	29000000	-	-	29000000	-
0.1	29100000	29150000	0.171526587	29020000	29080000	0.206327373	29060000	29040000	0.06887052
0.2	29600000	30000000	1.333333333	29250000	29500000	0.847457627	29200000	29250000	0.17094017
0.4	33000000	34000000	2.941176471	31000000	31500000	1.587301587	30200000	30600000	1.30718954
0.5	37000000	38000000	2.631578947	32500000	33500000	2.985074627	30400000	31000000	1.93548387

To detect the development of the embedded semi-elliptical crack in a structural component it is recommended to mount an array of sensors on the region where the semi-elliptical crack is most likely to occur on the structural component. The maximum stress is, then, calculated by the 3D-stress function based on the results from the sensor reading. The changes in the value of this maximum stress σ_{zz} represent changes of the b/t and b/a ratios.

6.3. Concluding Remarks

This chapter has shown the ability of the stress function to construct the stress field by making use of the array of sensors. The findings from the first section of this chapter can be summarized as follow.

- The location of the crack tip can be predicted by minimizing Equation 6.15. This information can be used to calculate the stress field in the vicinity of the crack exterior to the array.
- The reconstructed stress field can be used to predict the mode I stress intensity factor, K_I . As shown in this analysis the stress component in region II can also be used to determine the K_I value for integrity assessment.
- The result in this section can be used to refine the location of the crack tip results from Section 5.4.
- The stress/strain field inside the array can be reconstructed by searching of the minimum error (Equation 6.15). This minimum error occurs on the location further than the actual crack tip position. It appears the plasticity zone size r_p is included.

- Based on the information of the crack tip position and the crack length the mode I SIF, K_I and residual strength (fracture stress) of the structural component can be predicted.

For the second section of this chapter the major findings are:

- A derivation of a suitable 3D-stress function, which satisfied the embedded semi-elliptical crack condition. This derived stress function has been proved to be appropriate since it can be used to reconstruct the stress field interior to the array of sensors.
- In case of $b/t = 0.1$ with $b/a = 0.4$ and 0.6 the stress function construction appears to be different with the calculation from FEM. This is because the crack is relatively small. This may be a limitation of this technique to construct the stress field.
- The maximum stress in Z-direction σ_{zz} appears to be in the middle region of the sensor, which is the closest region to the embedded semi-elliptical crack. The maximum percentage of difference between the maximum stresses σ_{zz} s calculated from FEM and reconstructed from the stress function is found to be 3%.

CHAPTER 7. CONCLUSIONS AND RECOMMENDATIONS FOR FUTURE WORK

The main findings of this work can be divided into two parts. In the first part of the work, a methodology was described whereby the approximate location of a crack can be estimated using an array of PZT sensors-actuators. The main conclusions of the part of the work are:

(i) The findings from the numerical investigation can be summarised as follows:

- The application of the array sensor-actuator can be used satisfactorily to locate the damage, and to monitor the growth of the damage.
- The modal response can be used to determine the presence of a crack by the shift of the modal frequency when the crack occurs between the sensor and the actuator.
- However, the investigation has to be conducted at a sufficiently high frequency domain (i.e. up to 100KHz) to allow for the tracking of the reduction of the frequency in the higher modes.
- To address the concern of "noisy " spectrum the concept of the R-curve was introduced. This R-curve is obtained by integrating the TF response in a lower range frequency. This analysis was conducted prior to the appearance of the first dominant mode of the frequency response of the structure.
- Based on the R-curve results it was shown that an array sensor-actuator can be used to detect and locate the damage. This can be augmented or confirmed by another set of data generated from the sensor-actuator pairs located away from the damage (as in BnCn). The sensitivity analysis of the rows of sensors-actuators can be used to estimate the location the damage/crack.

- The approximate location of the crack tip can be confirmed by examining the reduction of R-Curve in a particular cross-pair and comparing it with the neighboring cross-pairs.

(ii) The findings from the experimental investigation can be summarized as follows:

- The R-curve method is able to detect and localize the damage on a structural component. By taking the direct-TF of every pair on the mounted sensor-actuator rows (in this experiment is first used AnBn and the results is confirmed by BnCn) the approximate location of the damage can be determined. Based on the information from this direct-TF the position of the damage location can then be confirmed by the cross-TF to approximately locate the crack tip.

In the second part of this work, a numerical algorithm was presented to refine the prediction of the location of the crack tip estimated in the previous section. From the knowledge of the location of the crack tip, the mode I stress intensity factor, K_I can then be calculated using a fracture mechanics methodology.

The main findings of the part of the work are:

- The location of the crack tip can be predicted by minimizing Equation 6.15. This information can be used to calculate the stress field in the vicinity of the crack exterior to the array.

- The reconstructed stress field can be used to predict the mode I stress intensity factor, K_I . As shown in this analysis the stress component in region II can also be used to determine the K_I value for integrity assessment.
- In the experimental investigation, to refine the location of the crack tip the results from Section 5.5 are incorporated to the numerical methodology.
- The stress/strain field inside the array can be reconstructed by searching of the minimum error (Equation 6.15). This minimum error occurs on the location further than the actual crack tip position. It appears the plasticity zone size r_p is included.
- Based on the information of the crack tip position and the crack length the mode I SIF, K_I and residual strength (fracture stress) of the structural component can be predicted.

The numerical methodology can be also extended in a thick structure, which has the finding as follows:

- A derivation of a suitable 3D-stress function, which satisfied the embedded semi-elliptical crack condition. This derived stress function has been proved to be appropriate since it can be used to re-construct the stress field interior to the array of sensors.
- In case of $b/t = 0.1$ with $b/a = 0.4$ and 0.6 the stress function construction appears to be different with the results from FEM. This is because the crack is relatively small and may be a limitation of this technique to construct the stress field.
- The maximum stress in Z-direction σ_{zz} appears to be in the middle region of the sensor, which is the closest region to the embedded semi-elliptical crack. The maximum percentage of difference

between the maximum stresses σ_{zz} s calculated from FEM and reconstructed from the stress function is found to be 3%.

Based on all findings above this research has demonstrated a potential technique of pipeline monitoring which combines:

- An active system for in-situ monitoring, using an active element PZT as a sensor/actuator, in conjunction with a passive sensor such as a strain gauge.
- A suitable stress function based algorithm that detects and assesses the damage levels present in the structure by evaluating structural response data acquired from bonded sensors such as PZT patches and strain gauges.

Recommendations of the future research work to continue this field of structural monitoring are as follows:

- Numerical and experimental investigation of the accuracy of the R-curve method to locate various types of crack (through crack, surface crack) and their positions relative to the pair of PZT sensors-actuators.
- Numerical and experimental investigation of the effect of external disturbance such as temperature irregularity, mechanical disturbance to the result from the PZT sensor-actuator pair.
- The R-curve method should be evaluated for detecting cracks in a thick structure. This then, can be incorporated to the stress field reconstruction algorithm for semi-elliptical crack, which are quite common in a thick structure.
- Study of the support tool to incorporate this R-Curve method and the numerical methodology for the integrity assessment into the remotely structural monitoring system (data acquisition and transmission by computer system).

REFERENCES:

1. Irving, P.E., " **Smart structure- a new strategy for health and usage monitoring**," IMechE 1996, pp 31-38.
2. Venzi S., Demofonti G., and Kanninen," **Analysis of Ductile Fracture Propagation in High - Pressure Pipelines: A Review of Present -Day Prediction Theories**", SNAM S.p.a (1993).
3. Emery A.F., Chao Y.H., Kobayashi A.S., Love W.J.," **Numerical Modelling of Full-Scale Pipe Rupture Tests**", Journal of Pressure Vessel Technology (1992), August, Vol.114, pp 265-270.
4. Kanninen M.F., Morrow T.B, Grant T.S., and Demofonti G.," **The Development and Validation of A Ductile Fracture Analysis Model**", Pipeline Research Committee, American Gas Association Arlington, Virginia (May 1994).
5. Setz W., and Grüter L.," **Tolerable Flaws for the Leak - Before - Break Criterion**", Int.Journal. Pressure Vessel & Piping 43 (1990), pp 193-202.
6. Sharples J.K., and Clayton A.M.,"**A Leak - Before - Break Assessment Method for Pressure Vessels and Some Current Unresolved Issues**", Int.Journal. Pressure Vessel & Piping 43 (1990), pp 317-327.
7. Lee K.Y., and Liebowitz H.," **An Expert System in Fracture Mechanics**", Engineering Fracture Mechanics (1995), Vol 50, No. 5/6.pp 609-629.
8. Celant, M., Re, G. and Venzi, S.," **Fatigue Analysis for Submarine Pipelines**,"Offshore Tech Conf paper nu 4233(1982), pp 37-40.
9. Ronsky, D.N. and Trefanenko, B.," **Managing Pipeline Integrity: A Look at Costs and Benefits**," 1992 OMAE-Volume V-B, Pipeline Technology ASME 1992.
10. Spillman Jr, W.B., Sirkis, J.S., and Gardiners, P.T.," **Smart materials and structures: what are they?**" Smart Material , Structure (vol 5, 1996), pp 247-254.

11. Culshaw, B., " **Smart Structure and Materials**," ARTECH HOUSE, INC. (1996), pp 40-41 and 121-122.
12. Shannon, R.W.E., " **Crack Growth Monitoring by Strain Sensing**," Journal of Pressure vessel & piping (vol 1, 1973), pp 61-73.
13. Report of the Research Council on Pipeline Crossings of Railroads and Highways of the Pipeline Division, " **Strain - Gage Analysis for Uncased Pipeline Crossings**", Journal of the Pipeline Division, Proceedings of the American Society of Civil Engineers (1964) January, pp 49-87.
14. Thrall, D.E. and Pokladnik, R.L., " **Garden Banks 388 Deep Water Production Riser Structural and Environmental Monitoring System**," Offshore Technical Conf paper no 7751(1995), pp 517-521.
15. Rogers, L.M., " **Pipeline Blockage Location by Strain Measurement Using an ROV**," Offshore Tech Conf paper no 7862(1995), pp 521-528.
16. Khan, A.S. and Chen, J.C., " **On the Measurement of Strain in the Hostile Environment of High-pressure Water (80 Mpa)**," EXPERIMENTAL MECHANICS, October (1982), pp 401-406.
17. Marshall P.W., Larrabee R.D., Burk J.D., and Egan G.R., " **The Cognac Fatigue Experiment**," Offshore Tech Conf paper no 4522(1983), pp 83-87.
18. Swanson R.C., Baxter G.D., " **The Bullwinkle Platform Instrumentation**," Offshore Tech Conf paper no 6052, pp 93-96.
19. Hertanto. M., " **Offshore Natuna a Major Marine Gasfield Development**", Regional Maritime Conference Indonesia 1995.
20. Wibowo-Baskoro, " **Private Communication (e-mail)**", March 1997.
21. Demofonti. G., Buzzichelli. G., Venzi. S., and Kanninen. M., " **Step by step procedure for the two specimen CTOA test** ", Pipeline Technology, Volume II (1995) pp 502-513.

22. Avalone E.A., Baumeister III T., " **STANDARD HANDBOOK for MECHANICAL ENGINEERS**", Ninth Edition, McGraw-Hill Book Company, pp 5-49, 5-58 and 5-59
23. Lichtenwalner P.F., Dunne J.P., Becker R.S., and Baumann E.W., " **Active Damage Interrogation System for Structural Health Monitoring**", SPIE Vol.3044 (1997), pp 186-194.
24. Crawley E.F., and Lazarus K.B., " **Induced Strain Actuation of Isotropic and Anisotropic Plates**", AIAA Journal, Vol. 29, No.6, 1991, pp. 944-951
25. Crawley E.F., and de Luis J., " **Use of Piezoelectric Actuator as Elements of Intelligent Structures** ", AIAA Journal, Vol. 25, No.10, 1987, pp. 1373-1385
26. Ha S.K., Keilers C., Chang F.K., " **Finite Element Analysis of Composite Structures Containing Distributed Piezoceramic Sensors and Actuators** ", AIAA Journal, Vol. 30, No. 3, March 1992
27. Mc.Connell K.G., " **Vibration Testing, Theory and Practice**", John Wiley & Son, Inc(1995), pp 114-119.
28. **PAFEC: Data Preparation , user manual 6.1** (1984)
29. <http://www.piezo.com/5a.html>
30. Shackelford J.F., Alexander W., Park J.S., " **CRC Practical Handbook of Materials Selection**", Boca Raton, CRC Press(1995), pp 398-399
31. **HP33120A Function Generator/Arbitrary Waveform Generator, User's Guide** pp298
32. Chiu, W.K., and Jones, R., " **Sensor Development for Determination of A Complex Rapidly Varying Stress Field: A Numerical Study**," AEROSPACE TECHNOLOGY SEMINAR (1997) pp ST3-1 to ST3-13.
33. Cheung, Y.H., " **Determination of Stress components from an Array of Piezoelectric Sensors**," Final Year Project Thesis (1997), Department of Mechanical Engineering, Monash University, pp 21-26.

34. Jones, R., and Callinan, R.J., " **On the use of special crack tip elements in cracked elastic sheets,**" International Journal of Fracture (vol.13, 1977), pp 51-64.
35. Dally, J.W., and Sanford, R.J., " **Strain - Gage Methods for Measuring the Opening - Mode Stress-Intensity Factor, K_I ,**" Experimental Mechanics (1987), No 27, pp 381-388.
36. Rosakis, A.J. and Ravi Chandra, K., " **On Crack Tip Stress States and Experimental Evaluation of three-dimensional Effects,**" Cal.Inst. Of Tech.Rep., FM.84-2 (March 1984).
37. Parnas, L., Bilir, Ö. G., and Tezcan, " **Strain Gage Methods for Measurement of Opening Mode Stress Intensity Factor,**" Engineering Fracture Mechanics (1996), Vol.55.No3, pp.485-492
38. Wibowo, H.N., and Chiu, W.K, , " **Monitoring of the severity of a cracked structure using discrete point measurements: A Numerical Study** ", COMADEM Proceedings, 1998, pp. 905-917
39. Broek, D, " **Elementary engineering fracture mechanics,**" Martinus Nijhoff Publisher"(fourth ed 1986), pp 19-21, and 194-198
40. Shah, R.C and Kobayashi, A.S, " **Stress Intensity Factor for an Elliptical Crack under arbitrary normal loading,** " Eng.Frac Mechanics, 1971 vol3, pp71-96
41. Byrd, P.F and Friedman, M.D, " **Handbook of elliptical Integral for Engineers and Scientist,**" Springer-Verlag(1954), pp.85,190-195,209-210
42. Press, W.H et al, " **Numerical recipes in FORTRAN,** ", 2nd edition (1992), pp255-263
43. Raju, I.S and Newman Jr, J.C, " **Stress Intensity Factor for a Wide Range of Semi-Elliptical Surface Cracks in Finite-Thickness Plates,** " Eng.Frac Mechanics(1979), vol 11, pp817-829

APPENDICES

APPENDIX A. Specifications of Piezoelectric single sheet-5A T107-A4E-602²⁹

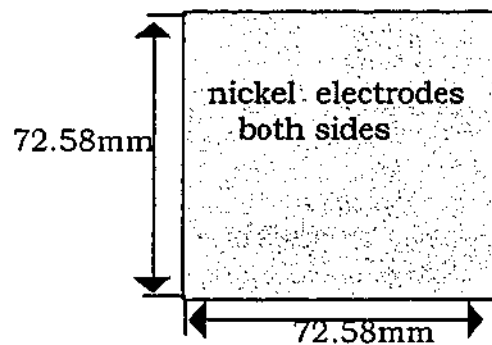


Figure A.1. A single sheet of PZT T107-A4E-602

In this research a single sheet of PZT that is shown in Figure A.1 was cut into several pieces of the required dimensions. Then, they were mounted to the Al bar specimen and test plate to be used in Chapter 3 and Chapter 5. The general specifications of this T107-A4E-602 are shown below:

- | | |
|-------------------------------------|---|
| • Thickness | 0.0075mm |
| • Capacitance | 430nF ($\pm 10\%$) |
| • Composition | Lead Zirconate Titanate |
| • Relative Dielectric Constant | $K^T_3 = 1800$ (@1kHz) |
| • Piezoelectric Strain Coefficient | $d_{33} = 390 \times 10^{-12}$ Meters/Volt |
| • | $d_{31} = -190 \times 10^{-12}$ Meters/Volt |
| • Piezoelectric Voltage Coefficient | $g_{33} = 24.0 \times 10^{-3}$ Volt Meters/Volt |
| • | $g_{31} = -11.60 \times 10^{-3}$ Volt Meters/Volt |
| • Coupling Coefficient | $k_{33} = 0.72$ |
| • | $k_{31} = 0.32$ |
| • Polarisation Field | $E_p = 2.0 \times 10^6$ Volts/ Meters |

- Initial depolarisation Field $E_c = 5.0 \times 10^5$ Volts/ Meters
- Density 7800 kg/Meter³
- Mechanical Q 80
- Elastic Modulus $\dot{g}^E_3 = 5.2 \times 10^{10}$ Newtons/Meter²
- $\dot{g}^E_1 = 6.6 \times 10^{10}$ Newtons/Meter²
- Thermal Expansion Coefficient $\sim 4 \times 10^{-6}$ Meters/Meter⁰C
- Curie Temperature 350 °C

APPENDIX B. Pipeline data design:

This line will be located in the seabed with depth of 145m.

The wave magnitude for design purpose is 13m.¹⁹

The materials will be used for this pipeline are²⁰:

a) API L X-65 outer diameter 965.2 mm and wall thickness 31.75 mm

b) API L X-80 outer diameter 762 mm and wall thickness 19.05 mm

The mechanical properties of the pipe-steel²¹:

Grade of steel	σ_y (MPa) Yield Strength	σ_u (MPa) Ultimate Tensile Stress	Charpy Energy (J/mm ²)	DWTT Energy (J/mm ²)	Modulus E (GPa)	CTOA _c (critical Crack Tip Opening Angle)
X-65	447	596	0.96	3.55	200	8.68
X-80	541	658	2.01	7.06	200	11.13

The maximum pressure (P_{max}) that allowed to prevent ductile fracture is calculated with this following formula⁴:

$$P_{\max} = (2h/D)(CTOA_c / C)^{\alpha} (E^{\beta} \sigma_o^{\delta}) / (D/h)^{\epsilon}$$

P_{max} is the same unit as the modulus, E, other constants provided in table below:

Parameter	Lower Bound (Methane)	Upper Bound (Rich Gas)
C	106	670
α	0.653	0.551
β	0.492	0.649
δ	0.508	0.351
ϵ	0.425	0.535

The results of the calculations are presented below:

	C(Pr)	alp(Pr)	bet(Pr)	del(pr)	ep(Pr)	
pure gas	106	0.653	0.492	0.508	0.425	
rich gas	670	0.551	0.649	0.351	0.535	
material	h(mm)thkns	D(mm)dmtr	CTOAc(deg)	E(GPa)mdls	yld str(MPa)	UTS(MPa)
x-65	31.75	965.2	8.68	200	447	597
x-80	19.05	762	11.13	200	541	658
Fw strs(GPa)	Pmax(MPa)	material	material	R/t	note:	
0.6786	33.48346437	x-65(pure)	x-65	15.2	thin cylinder	
0.6786	26.24467068	x-65(rich)	x-80	20	thin cylinder	
0.77935	28.57840644	x-80(pure)				
0.77935	20.73414431	x-80(rich)				
Hydrostatic pressure	material	total Press (Mpa)	Hoop Stress(Mpa)	strain	microstrain	
(rho*g*depth)(MPa)	x-65(pure)	32.02595101	486.7944553	0.00243397	2433.97228	
1.457513356	x-65(rich)	24.78715732	376.7647913	0.00188382	1883.82396	
	x-80(pure)	27.12089308	542.4178616	0.00271209	2712.08931	
	x-80(rich)	19.27663095	385.532619	0.00192766	1927.6631	

APPENDIX C: The Comparisons of the Strain Fields Inside the Array of Sensors between Strain Gauge Reading and the 2-D Stress Function

Figure C.1 and C.2 show the Y-direction strain, ϵ_{yy} for 10mm crack using data provided from the array of strain gauges. It is evident that there is a good agreement between the strain field measured from the strain gauges and that reconstructed by the stress function. This re-constructed strain field is based on the minimum error value in Figure 6.21.

Figure C.4 shows the strain field, ϵ_{yy} reconstructed by the stress function technique for 16mm crack. This reconstructed strain field is based on the minimum error value in Figure 6.22. Here, the agreement with that strain gauge results (Figure C.3) is relatively good.

The reconstructed strain field, ϵ_{yy} for 28mm crack using data provided from the array of strain gauges is shown in Figure C.6. This reconstructed strain field is based on the minimum error value in Figure 6.23. The results agreed well with the ones obtained from the sensor measurements (Figure C.5).

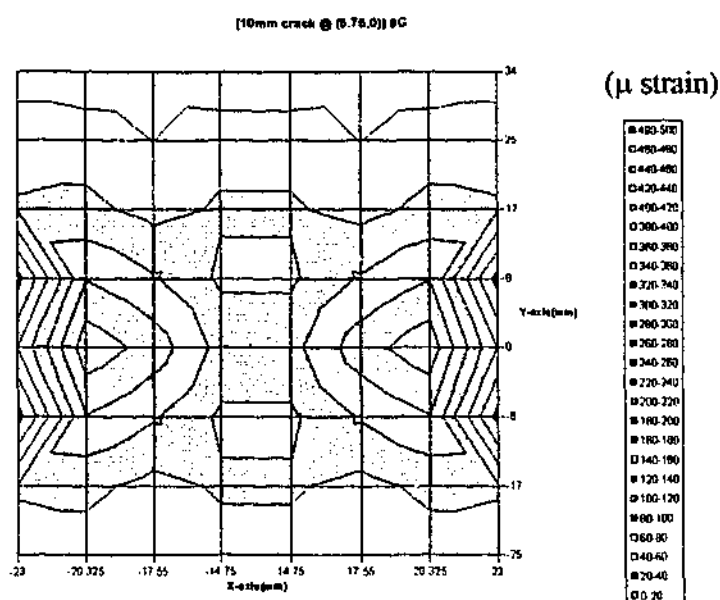


Figure C.1. Strain field in Y-direction ε_{yy} from strain gauge measurement
(10mm crack length)

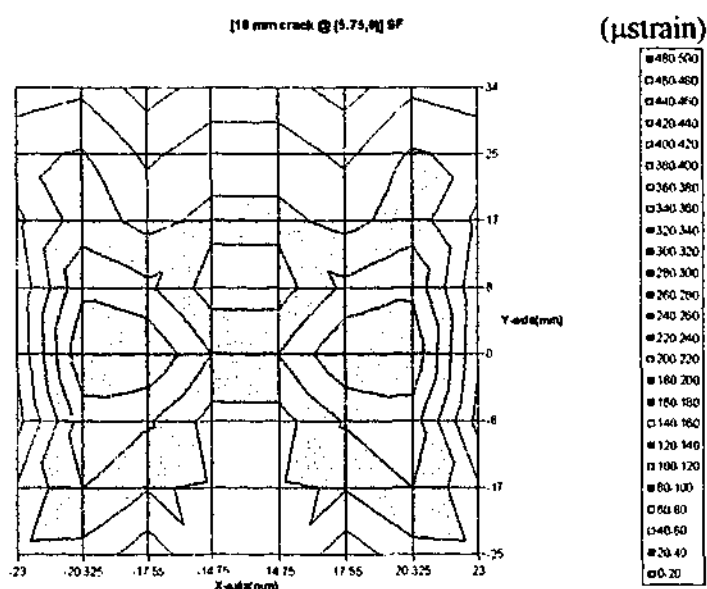


Figure C.2. Constructed Strain field in Y-direction ε_{yy} from stress function
with origin of (5.75mm,0)

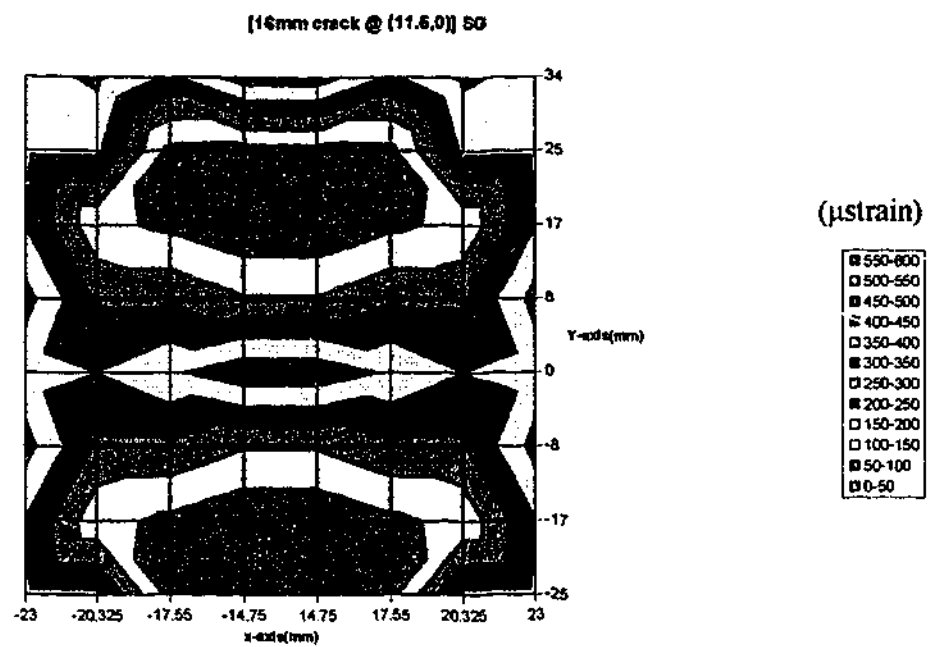


Figure C.3. Strain field in Y-direction ϵ_{yy} from strain gauge measurement (16mm crack length)

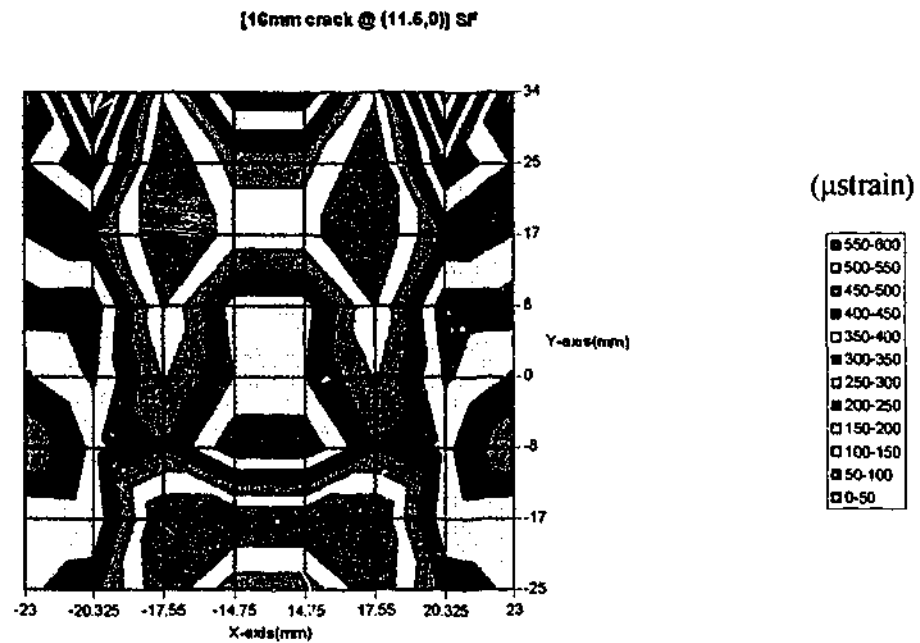


Figure C.4. Strain field in Y-direction ϵ_{yy} constructed from the Stress Function with origin of (11.5,0)

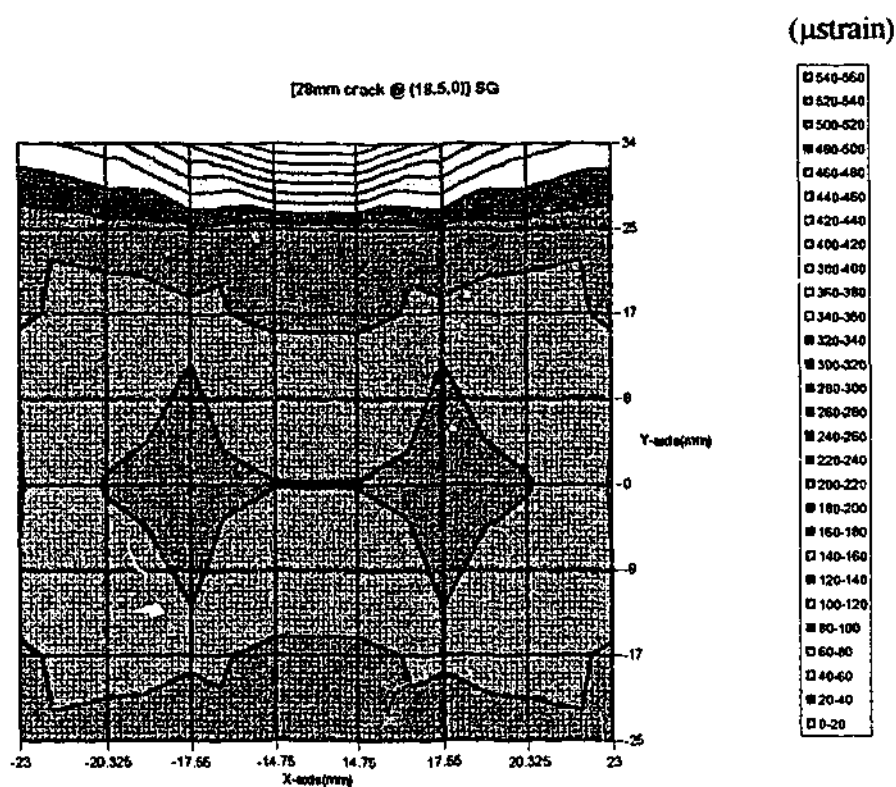


Figure C.5. Strain field in Y-direction ϵ_{yy} from strain gauge measurement (28mm crack length)

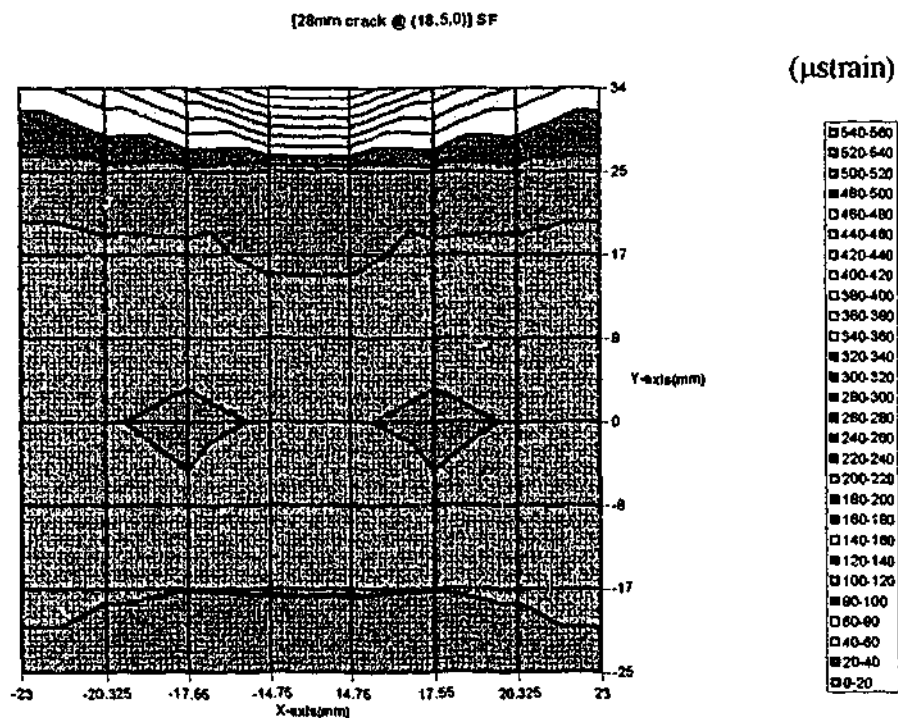


Figure C.6. Strain field in Y-direction ϵ_{yy} constructed from the Stress Function with origin of (18.5mm,0)

APPENDIX D: ON THE USE OF THE 3D-STRESS FUNCTION TO MONITOR AN EMBEDDED SEMI-ELLIPTICAL CRACK IN A THICKPLATE

The components of 3-D stress function to be used on monitoring an embedded semi-elliptical crack will be derived. The derivation will lead to solving elliptic integral equations by analytical formulas. The solutions will then in terms of Legendre 1st and 2nd kind elliptic integral ($F(\phi, k)=u1$ and $E(u1)$) and Jacobian elliptic function ($sn u1$, $cn u1$ and $dn u1$). The values of the terms will be calculated numerically. These derived components of stress function will be acted as a fitting curve of a point reading of an array of sensors at the back surface of a thick plate that has an internal semi-embedded crack. This study is the continuation of the previous numerical work³⁸.

The suitable 3D harmonic potential function⁴⁰ ϕ is represented in:

$$\phi = \sum_{i=0}^p \sum_{j=0}^q C_{ij} \frac{\partial^{i+j}}{\partial x^i \partial y^j} V^{(i+j+1)}, \quad i+j \leq 4 \quad (1)$$

where :

$$V^{(n)} = \int_{\lambda}^{\infty} \frac{\omega''(s) ds}{\sqrt{Q(s)}}$$

$$\omega(s) = 1 - \frac{x^2}{(a^2 + s)} - \frac{y^2}{(b^2 + s)} - \frac{z^2}{s}$$

$$Q(s) = s(a^2 + s)(b^2 + s)$$

Only 2 of the normal stresses σ_{xx} , σ_{zz} , and 1 shear stress τ_{xz} are on interest. The stresses are³;

$$\sigma_{xx} = 2G \left[z \frac{\partial^3 \phi}{\partial x^2 \partial z} + \frac{\partial^2 \phi}{\partial x^2} + 2\eta \frac{\partial^2 \phi}{\partial y^2} \right] \quad (2)$$

$$\sigma_{zz} = 2G \left[z \frac{\partial^3 \phi}{\partial z^3} - \frac{\partial^2 \phi}{\partial z^2} \right] \quad (3)$$

$$\tau_{xz} = 2G \left[z \frac{\partial^3 \phi}{\partial z^2 \partial x} \right] \quad (4)$$

Where G is the shear modulus

Rewrite (2) by using (1)

$$\begin{aligned} \sigma_{xx} = 2G & \left[z(-8x^2z) \sum_{i=0}^p \sum_{j=0}^q C_{ij} \frac{\partial^{i+j}}{\partial x^i \partial y^j} \int_{\lambda}^{\infty} \frac{1}{(a^2+s)^{\frac{3}{2}} s \sqrt{Q(s)}} \omega^{(i+j)-2}(s) ds (i+j+1)(i+j)(i+j-1) + \right. \\ & (4z^2)(i+j+1)(i+j) \sum_{i=0}^p \sum_{j=0}^q C_{ij} \frac{\partial^{i+j}}{\partial x^i \partial y^j} \int_{\lambda}^{\infty} \frac{1}{(a^2+s)^{\frac{3}{2}} \sqrt{Q(s)}} \omega^{(i+j)-1}(s) ds + \\ & (-2)(i+j+1) \sum_{i=0}^p \sum_{j=0}^q C_{ij} \frac{\partial^{i+j}}{\partial x^i \partial y^j} \int_{\lambda}^{\infty} \frac{1}{(a^2+s)^{\frac{3}{2}} \sqrt{Q(s)}} \omega^{(i+j)}(s) ds + \\ & (4x^2)(i+j+1)(i+j) \sum_{i=0}^p \sum_{j=0}^q C_{ij} \frac{\partial^{i+j}}{\partial x^i \partial y^j} \int_{\lambda}^{\infty} \frac{1}{(a^2+s)^{\frac{3}{2}} \sqrt{Q(s)}} \omega^{(i+j)-1}(s) ds + \\ & (-4\eta)(i+j+1) \sum_{i=0}^p \sum_{j=0}^q C_{ij} \frac{\partial^{i+j}}{\partial x^i \partial y^j} \int_{\lambda}^{\infty} \frac{1}{(b^2+s)^{\frac{3}{2}} \sqrt{Q(s)}} \omega^{(i+j)}(s) ds + \\ & \left. (8\eta y^2)(i+j+1)(i+j) \sum_{i=0}^p \sum_{j=0}^q C_{ij} \frac{\partial^{i+j}}{\partial x^i \partial y^j} \int_{\lambda}^{\infty} \frac{1}{(b^2+s)^{\frac{3}{2}} \sqrt{Q(s)}} \omega^{(i+j)-1}(s) ds \right] \quad (5) \end{aligned}$$

After expanding with $i+j \leq 4$, and replacing the integral terms with A, H, J, B, K, D the equation above becomes;

$$\begin{aligned}
 \sigma_{xy} = & 2G \left[-8x^2z^2 \left(60C04 \frac{\partial^4 \omega^2(s)}{\partial y^4} A + 60C22 \frac{\partial^4 \omega^2(s)}{\partial y^2 \partial y^2} A + 60C40 \frac{\partial^4 \omega^2(s)}{\partial x^4} A \right) + \right. \\
 & 4z^2 \left(6C02 \frac{\partial^2 \omega(s)}{\partial y^2} H + 12C03 \frac{\partial^3 \omega^2(s)}{\partial y^3} H + 20C04 \frac{\partial^4 \omega^3(s)}{\partial y^4} H + \right. \\
 & 12C12 \frac{\partial^3 \omega^2(s)}{\partial x \partial y^2} H + 20C13 \frac{\partial^4 \omega^3(s)}{\partial x \partial y^3} H + 6C20 \frac{\partial^2 \omega(s)}{\partial x^2} H + 12C21 \frac{\partial^3 \omega^2(s)}{\partial x^2 \partial y} H \\
 & \left. + 20C22 \frac{\partial^4 \omega^3(s)}{\partial x^2 \partial y^2} H + 12C30 \frac{\partial^3 \omega^2(s)}{\partial x^3} H + 20C31 \frac{\partial^4 \omega^3(s)}{\partial x^3 \partial y} H + 20C40 \frac{\partial^4 \omega^3(s)}{\partial x^4} H \right) + \\
 & -2 \left(C00J + 2C01 \frac{\partial \omega(s)}{\partial y} J + 3C02 \frac{\partial^2 \omega^2(s)}{\partial y^2} J + 4C03 \frac{\partial^3 \omega^3(s)}{\partial y^3} J + 5C04 \frac{\partial^4 \omega^4(s)}{\partial y^4} J + \right. \\
 & 2C10 \frac{\partial \omega(s)}{\partial x} J + 3C11 \frac{\partial^2 \omega^2(s)}{\partial x \partial y} J + 4C12 \frac{\partial^3 \omega^3(s)}{\partial x \partial y^2} J + 5C13 \frac{\partial^4 \omega^4(s)}{\partial x \partial y^3} J + 3C20 \frac{\partial^2 \omega^2(s)}{\partial x^2} J + 4C21 \frac{\partial^3 \omega^3(s)}{\partial x^2 \partial y} J \\
 & \left. + 5C22 \frac{\partial^4 \omega^4(s)}{\partial x^2 \partial y^2} J + 4C30 \frac{\partial^3 \omega^3(s)}{\partial x^3} J + 5C31 \frac{\partial^4 \omega^4(s)}{\partial x^3 \partial y} J + 5C40 \frac{\partial^4 \omega^4(s)}{\partial x^4} J \right) + \\
 & 4x^2 \left(6C02 \frac{\partial^2 \omega(s)}{\partial y^2} B + 12C03 \frac{\partial^3 \omega^2(s)}{\partial y^3} B + 20C04 \frac{\partial^4 \omega^3(s)}{\partial y^4} B + \right. \\
 & 12C12 \frac{\partial^3 \omega^2(s)}{\partial x \partial y^2} B + 20C13 \frac{\partial^4 \omega^3(s)}{\partial x \partial y^3} B + 6C20 \frac{\partial^2 \omega(s)}{\partial x^2} B + 12C21 \frac{\partial^3 \omega^2(s)}{\partial x^2 \partial y} B \\
 & \left. + 20C22 \frac{\partial^4 \omega^3(s)}{\partial x^2 \partial y^2} B + 12C30 \frac{\partial^3 \omega^2(s)}{\partial x^3} B + 20C31 \frac{\partial^4 \omega^3(s)}{\partial x^3 \partial y} B + 20C40 \frac{\partial^4 \omega^3(s)}{\partial x^4} B \right) +
 \end{aligned}$$

$$\begin{aligned}
& -4\eta \left(C00K + 2C01 \frac{\partial \omega(s)}{\partial y} K + 3C02 \frac{\partial^2 \omega^2(s)}{\partial y^2} K + 4C03 \frac{\partial^3 \omega^3(s)}{\partial y^3} K + 5C04 \frac{\partial^4 \omega^4(s)}{\partial y^4} K + \right. \\
& 2C10 \frac{\partial \omega(s)}{\partial x} K + 3C11 \frac{\partial^2 \omega^2(s)}{\partial x \partial y} K + 4C12 \frac{\partial^3 \omega^3(s)}{\partial x \partial y^2} K + 5C13 \frac{\partial^4 \omega^4(s)}{\partial x \partial y^3} K + 3C20 \frac{\partial^2 \omega^2(s)}{\partial x^2} K + 4C21 \frac{\partial^3 \omega^3(s)}{\partial x^2 \partial y} K \\
& \left. + 5C22 \frac{\partial^4 \omega^4(s)}{\partial x^2 \partial y^2} K + 4C30 \frac{\partial^3 \omega^3(s)}{\partial x^3} K + 5C31 \frac{\partial^4 \omega^4(s)}{\partial x^3 \partial y} K + 5C40 \frac{\partial^4 \omega^4(s)}{\partial x^4} K \right) + \\
& 8\eta y^2 \left(6C02 \frac{\partial^2 \omega(s)}{\partial y^2} D + 12C03 \frac{\partial^3 \omega^2(s)}{\partial y^3} D + 20C04 \frac{\partial^4 \omega^3(s)}{\partial y^4} D + \right. \\
& 12C12 \frac{\partial^3 \omega^2(s)}{\partial x \partial y^2} D + 20C13 \frac{\partial^4 \omega^3(s)}{\partial x \partial y^3} D + 6C20 \frac{\partial^2 \omega(s)}{\partial x^2} D + 12C21 \frac{\partial^3 \omega^2(s)}{\partial x^2 \partial y} D \\
& \left. + 20C22 \frac{\partial^4 \omega^3(s)}{\partial x^2 \partial y^2} D + 12C30 \frac{\partial^3 \omega^2(s)}{\partial x^3} D + 20C31 \frac{\partial^4 \omega^3(s)}{\partial x^3 \partial y} D + 20C40 \frac{\partial^4 \omega^3(s)}{\partial x^4} D \right) \Bigg] \quad (6)
\end{aligned}$$

Then , deriving the ω'' this equation becomes :

$$\begin{aligned}
\sigma_{xx} = & 2G \left[-x^2 z^2 \left(10520C04 \frac{A}{(a^2 + s)^2} + 3840C22 \frac{A}{(a^2 + s)(b^2 + s)} + 10520C40 \frac{A}{(b^2 + s)^2} \right) + \right. \\
& 4z^2 \left(-12C02 \frac{H}{(b^2 + s)} + 288yC03 \frac{H}{(b^2 + s)^2} + 1440C04 \frac{H\omega(s)}{(b^2 + s)^2} - 5760y^2C04 \frac{H}{(b^2 + s)^3} + \right. \\
& 96xC12 \frac{H}{(b^2 + s)(a^2 + s)} - 2880xyC13 \frac{H}{(a^2 + s)(b^2 + s)^2} - 12C20 \frac{H}{(a^2 + s)} + 96yC21 \frac{H}{(b^2 + s)(a^2 + s)} \\
& - 960x^2C22 \frac{H}{(b^2 + s)(a^2 + s)^2} - 960y^2C22 \frac{H}{(a^2 + s)(b^2 + s)^2} + 288xC30 \frac{H}{(a^2 + s)^2} - 2880xyC31 \frac{H}{(b^2 + s)(a^2 + s)^2} + \\
& \left. \left. 1440C40 \frac{H\omega(s)}{(b^2 + s)(a^2 + s)^2} - 5760x^2C40 \frac{H}{(a^2 + s)^3} \right) \right] +
\end{aligned}$$

$$\begin{aligned}
& -2 \left(C00J + 2 \left(\frac{-2y}{b^2+s} \right) J + 3C02 \left(\frac{8y^2}{(b^2+s)^2} - \frac{4\omega(s)}{(b^2+s)} \right) J + 4C03 \left(\frac{72y}{(b^2+s)^2} \omega(s) - \frac{48y^3}{(b^2+s)^3} \right) J + \right. \\
& 5C04 \left(\frac{128\omega^2(s)}{(b^2+s)^2} - \frac{1088y^2\omega(s)}{(b^2+s)^3} + \frac{384y^4}{(b^2+s)^4} \right) J + 2C10 \left(\frac{-2x}{(a^2+s)} \right) J + 3C11 \left(\frac{8xy}{(b^2+s)(a^2+s)} \right) J + 4C12 \left(\frac{24x\omega(s)}{(b^2+s)(a^2+s)} - \frac{48xy^2}{(b^2+s)^2(a^2+s)} \right) J + \\
& 5C13 \left(\frac{384xy^3}{(a^2+s)(b^2+s)^3} - \frac{512xy\omega(s)}{(a^2+s)(b^2+s)^2} \right) J + 3C20 \left(\frac{8x^2}{(a^2+s)^2} - \frac{4\omega(s)}{(a^2+s)} \right) J + 4C21 \left(\frac{24y\omega(s)}{(a^2+s)(b^2+s)} - \frac{48x^2y}{(a^2+s)^2(b^2+s)} \right) J \\
& 5C22 \left(\frac{48\omega^2(s)}{(b^2+s)(a^2+s)} - \frac{192x^2\omega(s)}{(b^2+s)(a^2+s)^2} - \frac{192y^2\omega(s)}{(a^2+s)(b^2+s)^2} + \frac{384x^2y^2}{(a^2+s)^2(b^2+s)^2} \right) J + \\
& + 4C30 \left(\frac{72x\omega(s)}{(a^2+s)^2} - \frac{48x^3}{(a^2+s)^3} \right) J + 5C31 \left(\frac{512xy\omega(s)}{(b^2+s)(a^2+s)^2} - \frac{384x^3y}{(b^2+s)(a^2+s)^3} \right) J + \\
& \left. 5C40 \left(\frac{128\omega^2(s)}{(a^2+s)^2} - \frac{1088x^2\omega(s)}{(a^2+s)^3} + \frac{384x^4}{(a^2+s)^4} \right) J \right) + \\
& 4x^2 \left(-12C02 \frac{B}{(b^2+s)} + 288yC03 \frac{B}{(b^2+s)^2} + 1440C04 \frac{B\omega(s)}{(b^2+s)^2} - 5760y^2C04 \frac{B}{(b^2+s)^3} + \right. \\
& 96xC12 \frac{B}{(b^2+s)(a^2+s)} - 2880xyC13 \frac{B}{(a^2+s)(b^2+s)^2} - 12C20 \frac{B}{(a^2+s)} + 96yC21 \frac{B}{(b^2+s)(a^2+s)} \\
& - 960x^2C22 \frac{B}{(b^2+s)(a^2+s)^2} - 960y^2C22 \frac{B}{(a^2+s)(b^2+s)^2} + 288C30x \frac{B}{(a^2+s)^2} - 2880xyC31 \frac{B}{(b^2+s)(a^2+s)^2} + \\
& \left. 1440C40 \frac{B\omega(s)}{(b^2+s)(a^2+s)^2} - 5760x^2C40 \frac{B}{(a^2+s)^3} \right) + \\
& -4\eta \left(C00K + 2 \left(\frac{-2y}{b^2+s} \right) K + 3C02 \left(\frac{8y^2}{(b^2+s)^2} - \frac{4\omega(s)}{(b^2+s)} \right) K + 4C03 \left(\frac{72y}{(b^2+s)^2} \omega(s) - \frac{48y^3}{(b^2+s)^3} \right) K + \right.
\end{aligned}$$

$$\begin{aligned}
& 5C04 \left(\frac{128\omega^2(s)}{(b^2+s)^2} - \frac{1088y^2\omega(s)}{(b^2+s)^3} + \frac{384y^4}{(b^2+s)^4} \right) K + 2C10 \left(\frac{-2x}{(a^2+s)} \right) K + 3C11 \left(\frac{8xy}{(b^2+s)(a^2+s)} \right) K + 4C12 \left(\frac{24x\omega(s)}{(b^2+s)(a^2+s)} - \frac{48xy^2}{(b^2+s)^2(a^2+s)} \right) K + \\
& 5C13 \left(\frac{384xy^3}{(a^2+s)(b^2+s)^3} - \frac{512xy\omega(s)}{(a^2+s)(b^2+s)^2} \right) K + 3C20 \left(\frac{8x^2}{(a^2+s)^2} - \frac{4\omega(s)}{(a^2+s)} \right) K + 4C21 \left(\frac{24y\omega(s)}{(a^2+s)(b^2+s)} - \frac{48x^2y}{(a^2+s)^2(b^2+s)} \right) K \\
& 5C22 \left(\frac{48\omega^2(s)}{(b^2+s)(a^2+s)} - \frac{192x^2\omega(s)}{(b^2+s)(a^2+s)^2} - \frac{192y^2\omega(s)}{(a^2+s)(b^2+s)^2} + \frac{384x^2y^2}{(a^2+s)^2(b^2+s)^2} \right) K + \\
& + 4C30 \left(\frac{72x\omega(s)}{(a^2+s)^2} - \frac{48x^3}{(a^2+s)^3} \right) K + 5C31 \left(\frac{512xy\omega(s)}{(b^2+s)(a^2+s)^2} - \frac{384x^3y}{(b^2+s)(a^2+s)^3} \right) K + \\
& 5C40 \left(\frac{128\omega^2(s)}{(a^2+s)^2} - \frac{1088x^2\omega(s)}{(a^2+s)^3} + \frac{384x^4}{(a^2+s)^4} \right) K + \\
& 8\eta y^2 \left(-12C02 \frac{D}{(b^2+s)} + 288yC03 \frac{D}{(b^2+s)^2} + 1440C04 \frac{B\omega(s)}{(b^2+s)^2} - 5760y^2C04 \frac{D}{(b^2+s)^3} + \right. \\
& 96xC12 \frac{D}{(b^2+s)(a^2+s)} - 2880xyC13 \frac{D}{(a^2+s)(b^2+s)^2} - 12C20 \frac{D}{(a^2+s)} + 96yC21 \frac{D}{(b^2+s)(a^2+s)} \\
& - 960x^2C22 \frac{D}{(b^2+s)(a^2+s)^2} - 960y^2C22 \frac{D}{(a^2+s)(b^2+s)^2} + 288xC30 \frac{D}{(a^2+s)^2} - 2880xyC31 \frac{D}{(b^2+s)(a^2+s)^2} + \\
& \left. 1440C40 \frac{D\omega(s)}{(b^2+s)(a^2+s)^2} - 5760x^2C40 \frac{D}{(a^2+s)^3} \right) \quad (7)
\end{aligned}$$

By replacing all the completed integral terms with IntN , where N is the integral number.

The Equation 7 can be written as:

$$\begin{aligned}
\sigma_{xx} = & 2G \left[-x^2z^2(10520C04\text{Int15} + 3840C22\text{Int16} + 10520C40\text{Int17}) + \right. \\
& \left. 4z^2(-12C02\text{Int43} + 288yC03\text{Int44} + 1440C04(\text{Int44} - x^2\text{Int17} - y^2\text{Int46} - z^2\text{Int8}) - 5760y^2C04\text{Int46} + \right.
\end{aligned}$$

$$\begin{aligned}
& 96xC_{12}Int_{48} - 2880xyC_{13}Int_{21} - 12C_{20}Int_{49} + 96yC_{21}Int_{48} \\
& - 960x^2C_{22}Int_{16} - 960y^2C_{22}Int_{58} + 288C_{30}Int_{51} - 2880xyC_{31}Int_{16} + \\
& 1440C_{40}(Int_{51} - x^2Int_{15} - y^2Int_{16} - z^2Int_{11}) - 5760x^2C_{40}Int_{15} + \\
& - 2(C_{00}Int_{52} - 4yC_{01}Int_{53} + 24y^2C_{02}Int_{36} - 12C_{02}(Int_{53} - x^2Int_{54} - y^2Int_{36} - z^2Int_{43}) \\
& + 288yC_{03}(Int_{36} - x^2Int_{18} - y^2Int_{35} - z^2Int_{14}) - 192y^3C_{03}Int_{35} \\
& + 640C_{04}(Int_{36} - 2x^2Int_{18} + x^4Int_{19} - 2y^2Int_{35} - 2z^2Int_{44} + 2x^2y^2Int_{54} + 2x^2z^2Int_{21} + y^4Int_{46} + 2y^2z^2Int_{44} + x^4Int_{8}) \\
& + 5440y^2C_{04}(Int_{35} - x^2Int_{20} - y^2Int_{32} - z^2Int_{46}) + 1920y^4C_{04}Int_{32} - 4xC_{10}Int_{55} + 24xyC_{11}Int_{54} \\
& 96xC_{12}(Int_{54} - x^2Int_{24} - y^2Int_{18} - z^2Int_{48}) - 192xy^2C_{12}Int_{18} + 1920xy^3C_{13}Int_{37} \\
& - 2560xyC_{13}(Int_{18} - x^2Int_{19} - y^2Int_{37} - z^2Int_{21}) + 24x^2C_{20}Int_{23} - \\
& 12C_{20}(Int_{55} - x^2Int_{23} - y^2Int_{54} - z^2Int_{49}) + 96yC_{21}(Int_{54} - x^2Int_{24} - y^2Int_{18} - z^2Int_{48}) - 192x^2yC_{21}Int_{24} \\
& + 240C_{22}(Int_{54} - 2x^2Int_{24} + x^4Int_{25} - 2y^2Int_{18} - 2z^2Int_{48} + 2x^2y^2Int_{19} + 2x^2z^2Int_{16} + y^4Int_{20} + 2y^2z^2Int_{18} + x^4Int_{9}) \\
& - 960x^2C_{22}(Int_{24} - x^2Int_{25} - y^2Int_{19} - z^2Int_{16}) - 960y^2C_{22}(Int_{18} - x^2Int_{19} - y^2Int_{20} - z^2Int_{21}) \\
& 1920x^2y^2C_{22}Int_{19} + 288xC_{30}(Int_{23} - x^2Int_{27} - y^2Int_{24} - z^2Int_{51}) - 192x^3C_{30}Int_{27} \\
& + 2560xyC_{31}(Int_{24} - x^2Int_{25} - y^2Int_{19} - z^2Int_{16}) + 1920x^3yC_{31}Int_{25} \\
& + 640C_{40}(Int_{23} - 2x^2Int_{27} + x^4Int_{28} - 2y^2Int_{24} - 2z^2Int_{51} + 2x^2y^2Int_{25} + 2x^2z^2Int_{15} + y^4Int_{19} + 2y^2z^2Int_{16} + x^4Int_{11}) \\
& - 5440x^2C_{40}(Int_{27} - x^2Int_{28} - y^2Int_{25} - z^2Int_{15}) + 1920x^4C_{40}Int_{28} \\
& 4x^2(-12C_{02}Int_{39} + 288yC_{03}Int_{18} + 1440C_{04}(Int_{18} - x^2Int_{19} - y^2Int_{20} - z^2Int_{21}) - 5760y^2C_{04}Int_{20} + \\
& 96xC_{12}Int_{24} - 2880xyC_{13}Int_{26} - 12C_{20}Int_{23} + 96yC_{21}Int_{24} \\
& - 960x^2C_{22}Int_{25} - 960y^2C_{22}Int_{26} + 288C_{30}Int_{27} - 2880xyC_{31}Int_{25} + \\
& 1440C_{40}(Int_{27} - x^2Int_{28} - y^2Int_{25} - z^2Int_{29}) - 5760x^2C_{40}Int_{28}) +
\end{aligned}$$

$$\begin{aligned}
& -4\eta \left(C00 \ln 56 - 4yC01 \ln 57 + 24y^2C02 \ln 30 - 12C02 \left(\ln 57 - x^2 \ln 36 - y^2 \ln 30 - z^2 \ln 42 \right) \right. \\
& \quad \left. + 288yC03 \left(\ln 30 - x^2 \ln 35 - y^2 \ln 31 - z^2 \ln 45 \right) - 192y^3C03 \ln 31 \right. \\
& \quad \left. + 640C04 \left(\ln 30 - 2x^2 \ln 35 + x^4 \ln 20 - 2y^2 \ln 31 - 2z^2 \ln 45 + 2x^2y^2 \ln 36 + 2x^2z^2 \ln 46 + y^4 \ln 33 + 2y^2z^2 \ln 34 + z^4 \ln 7 \right) \right. \\
& \quad \left. + 5440y^2C04 \left(\ln 31 - x^2 \ln 32 - y^2 \ln 33 - z^2 \ln 34 \right) - 1920y^4C04 \ln 33 \right. \\
& \quad \left. - 4xC10 \ln 53 + 24xyC11 \ln 36 + 96xC12 \left(\ln 36 - x^2 \ln 18 - y^2 \ln 35 - z^2 \ln 44 \right) \right. \\
& \quad \left. - 192xy^2C12 \ln 35 + 1920xy^3C13 \ln 32 + 2560xyC13 \left(\ln 35 - x^2 \ln 20 - y^2 \ln 32 - z^2 \ln 46 \right) \right. \\
& \quad \left. + 24x^2C20 \ln 39 - 12C20 \left(\ln 53 - x^2 \ln 39 - y^2 \ln 36 - z^2 \ln 43 \right) \right. \\
& \quad \left. + 96yC21 \left(\ln 36 - x^2 \ln 18 - y^2 \ln 35 - z^2 \ln 44 \right) - 192x^2yC21 \ln 18 \right. \\
& \quad \left. 240C22 \left(\ln 36 - 2x^2 \ln 18 + x^4 \ln 19 - 2y^2 \ln 35 - 2z^2 \ln 44 + 2x^2y^2 \ln 20 + 2x^2z^2 \ln 21 + y^4 \ln 32 \right. \right. \\
& \quad \left. \left. + 2y^2z^2 \ln 35 + z^4 \ln 8 \right) - 960x^2C22 \left(\ln 18 - x^2 \ln 19 - y^2 \ln 20 - z^2 \ln 21 \right) \right. \\
& \quad \left. - 96y^2C22 \left(\ln 35 - x^2 \ln 20 - y^2 \ln 32 - z^2 \ln 46 \right) + 1920x^2y^2C22 \ln 20 \right. \\
& \quad \left. + 288xC30 \left(\ln 39 - x^2 \ln 24 - y^2 \ln 18 - z^2 \ln 48 \right) - 192x^3C30 \ln 24 \right. \\
& \quad \left. + 2560xyC31 \left(\ln 18 - x^2 \ln 19 - y^2 \ln 20 - z^2 \ln 21 \right) + 1920x^3yC31 \ln 19 \right. \\
& \quad \left. 640C40 \left(\ln 39 - 2x^2 \ln 24 + x^4 \ln 28 - 2y^2 \ln 18 - 2z^2 \ln 48 + 2x^2y^2 \ln 19 + 2x^2z^2 \ln 16 + y^4 \ln 20 \right. \right. \\
& \quad \left. \left. + 2y^2z^2 \ln 21 + z^4 \ln 9 \right) - 5440x^2C40 \left(\ln 24 - x^2 \ln 25 - y^2 \ln 19 - z^2 \ln 16 \right) + 1920x^4C40 \ln 25 \right) \\
& + 8\eta y^2 \left(-12C02 \ln 30 + 288yC03 \ln 31 + 1440C04 \left(\ln 31 - x^2 \ln 32 - y^2 \ln 33 - z^2 \ln 34 \right) - 5760y^2C04 \ln 33 + \right. \\
& \quad 96xC12 \ln 35 - 2880xyC13 \ln 32 - 12C20 \ln 36 + 96yC21 \ln 35 \\
& \quad - 960x^2C22 \ln 37 - 960y^2C22 \ln 32 + 288C30 \ln 38 - 2880xyC31 \ln 20 + \\
& \quad \left. 1440C40 \left(\ln 38 - x^2 \ln 26 - y^2 \ln 20 - z^2 \ln 21 \right) - 5760x^2C40 \ln 26 \right) \Bigg] \tag{8}
\end{aligned}$$

Rewrite Equation 3 by substituting Equation 1 in it,

$$\begin{aligned}
\sigma_{zz} = 2G \left[-8z^4 \sum_{i=0}^p \sum_{j=0}^q C_{ij} \frac{\partial^{i+j}}{\partial x^i \partial y^j} \int_{\lambda}^{\infty} \frac{1}{s^3 \sqrt{Q(s)}} \omega^{(i+j)-2}(s) ds (i+j+1)(i+j)(i+j-1) \right. \\
+ 2(i+j+1) \sum_{i=0}^p \sum_{j=0}^q C_{ij} \frac{\partial^{i+j}}{\partial x^i \partial y^j} \int_{\lambda}^{\infty} \frac{1}{s \sqrt{Q(s)}} \omega^{(i+j)}(s) ds \\
\left. + (8z^2)(i+j+1)(i+j) \sum_{i=0}^p \sum_{j=0}^q C_{ij} \frac{\partial^{i+j}}{\partial x^i \partial y^j} \int_{\lambda}^{\infty} \frac{1}{s^2 \sqrt{Q(s)}} \omega^{(i+j)-1}(s) ds \right] \quad (9)
\end{aligned}$$

After expanding with $i+j \leq 4$, and replacing the integral terms with F, M, G the Equation 9 above becomes;

$$\begin{aligned}
\sigma_{zz} = 2G \left[-8z^4 \left(60C04 \frac{\partial^4 \omega^2(s)}{\partial y^4} F + 60C22 \frac{\partial^4 \omega^2(s)}{\partial x^2 \partial y^2} F + 60C40 \frac{\partial^4 \omega^2(s)}{\partial x^4} F \right) \right. \\
+ 2 \left(C00M + 2C01 \frac{\partial \omega(s)}{\partial y} M + 3C02 \frac{\partial^2 \omega^2(s)}{\partial y^2} M + 4C03 \frac{\partial^3 \omega^3(s)}{\partial y^3} M + 5C04 \frac{\partial^4 \omega^4(s)}{\partial y^4} M + \right. \\
2C10 \frac{\partial \omega(s)}{\partial x} M + 3C11 \frac{\partial^2 \omega^2(s)}{\partial x \partial y} M + 4C12 \frac{\partial^3 \omega^3(s)}{\partial x \partial y^2} M + 5C13 \frac{\partial^4 \omega^4(s)}{\partial x \partial y^3} M + 3C20 \frac{\partial^2 \omega^2(s)}{\partial x^2} M + 4C21 \frac{\partial^3 \omega^3(s)}{\partial x^2 \partial y} M \\
+ 5C22 \frac{\partial^4 \omega^4(s)}{\partial x^2 \partial y^2} M + 4C30 \frac{\partial^3 \omega^3(s)}{\partial x^3} M + 5C31 \frac{\partial^4 \omega^4(s)}{\partial x^3 \partial y} M + 5C40 \frac{\partial^4 \omega^4(s)}{\partial x^4} M \left. \right) + \\
8z^2 \left(6C02 \frac{\partial \omega(s)}{\partial y^2} G + 12C03 \frac{\partial^3 \omega^2(s)}{\partial y^3} G + 12C12 \frac{\partial^3 \omega^2(s)}{\partial x \partial y^2} G + \right. \\
6C20 \frac{\partial^2 \omega(s)}{\partial x^2} G + 12C21 \frac{\partial^3 \omega^2(s)}{\partial x^2 \partial y} G + 12C30 \frac{\partial^3 \omega^2(s)}{\partial x^3} G + 20C04 \frac{\partial^4 \omega^3(s)}{\partial y^4} G + \\
\left. 20C13 \frac{\partial^4 \omega^3(s)}{\partial x \partial y^3} G + 20C22 \frac{\partial^4 \omega^3(s)}{\partial x^2 \partial y^2} G + 20C31 \frac{\partial^4 \omega^3(s)}{\partial x^3 \partial y} G + 20C40 \frac{\partial^4 \omega^3(s)}{\partial x^4} G \right) \left. \right] \quad (10)
\end{aligned}$$

Then, deriving the ω'' this equation becomes :

$$\begin{aligned}
\sigma_{zz} = & 2G \left[-8z^4 \left(1440C04 \frac{F}{(b^2+s)^2} + 480C22 \frac{F}{(a^2+s)(b^2+s)} + 1440C40 \frac{F}{(a^2+s)^2} \right) \right. \\
& + 2 \left(C00M + 2 \left(\frac{-2y}{b^2+s} \right) M + 3C02 \left(\frac{8y^2}{(b^2+s)^2} - \frac{4\omega(s)}{(b^2+s)} \right) M + 4C03 \left(\frac{72y}{(b^2+s)^2} \omega(s) - \frac{48y^3}{(b^2+s)^3} \right) M + \right. \\
& 5C04 \left(\frac{128\omega^2(s)}{(b^2+s)^2} - \frac{1088y^2\omega(s)}{(b^2+s)^3} + \frac{384y^4}{(b^2+s)^4} \right) M + 2C10 \left(\frac{-2x}{(a^2+s)} \right) M + 3C11 \frac{8xy}{(b^2+s)(a^2+s)} M + 4C12 \left(\frac{24x\omega(s)}{(b^2+s)(a^2+s)} - \frac{48xy^2}{(b^2+s)^2(a^2+s)} \right) M + \\
& 5C13 \left(\frac{384xy^3}{(a^2+s)(b^2+s)^3} - \frac{512xy\omega(s)}{(a^2+s)(b^2+s)^2} \right) M + 3C20 \left(\frac{8x^2}{(a^2+s)^2} - \frac{4\omega(s)}{(a^2+s)} \right) M + 4C21 \left(\frac{24y\omega(s)}{(a^2+s)(b^2+s)} - \frac{48x^2y}{(a^2+s)^2(b^2+s)} \right) M \\
& 5C22 \left(\frac{48\omega^2(s)}{(b^2+s)(a^2+s)} - \frac{192x^2\omega(s)}{(b^2+s)(a^2+s)^2} - \frac{192y^2\omega(s)}{(a^2+s)(b^2+s)^2} + \frac{384x^2y^2}{(a^2+s)^2(b^2+s)^2} \right) M + \\
& + 4C30 \left(\frac{72x\omega(s)}{(a^2+s)^2} - \frac{48x^3}{(a^2+s)^3} \right) M + 5C31 \left(\frac{512xy\omega(s)}{(b^2+s)(a^2+s)^2} - \frac{384x^3y}{(b^2+s)(a^2+s)^3} \right) M + \\
& \left. 5C40 \left(\frac{128\omega^2(s)}{(a^2+s)^2} - \frac{1088x^2\omega(s)}{(a^2+s)^3} + \frac{384x^4}{(a^2+s)^4} \right) M \right] + \\
& + 8z^2 \left(-12C02 \frac{G}{(b^2+s)} + 288yC03 \frac{G}{(b^2+s)^2} + 96xC12 \frac{G}{(a^2+s)(b^2+s)} - 12C20 \frac{G}{(a^2+s)} + \right. \\
& 96yC21 \frac{G}{(b^2+s)(a^2+s)} + 288xC30 \frac{G}{(a^2+s)^2} + 1440C04 \frac{G\omega(s)}{(b^2+s)^2} - 5760y^2C04 \frac{G}{(b^2+s)^3} \\
& - 2880C13xy \frac{G}{(a^2+s)(b^2+s)^2} - 960x^2C22 \frac{G}{(b^2+s)(a^2+s)^2} - 960y^2C22 \frac{G}{(a^2+s)(b^2+s)^2} - 2880xyC31 \frac{G}{(b^2+s)(a^2+s)^2} +
\end{aligned}$$

$$\left. 1440C40 \frac{G\omega(s)}{(a^2+s)^2} - 5760x^2C40 \frac{G}{(a^2+s)^3} \right] \quad (11)$$

By replacing all the completed integral terms with $\text{Int}N$ where N is integral number, the Equation 11 can be written as:

$$\begin{aligned} \sigma_{\infty} = & 2G \left[-8z^4 (1440C04 \text{Int}12 + 480C22 \text{Int}13 + 1440C40 \text{Int}14) \right. \\ & + 2(C00 \text{Int}40 - 4yC01 \text{Int}41 + 24y^2C02 \text{Int}42 - 12C02(\text{Int}41 - x^2 \text{Int}43 - y^2 \text{Int}42 - z^2 \text{Int}1)) \\ & + 288yC03(\text{Int}42 - x^2 \text{Int}44 - y^2 \text{Int}45 - z^2 \text{Int}2) - 192y^3C03 \text{Int}45 \\ & + 640C04(\text{Int}42 - 2x^2 \text{Int}44 + x^4 \text{Int}17 - 2y^2 \text{Int}45 - 2z^2 \text{Int}2 + 2x^2y^2 \text{Int}46 + 2x^2z^2 \text{Int}8 + y^4 \text{Int}34 + 2y^2z^2 \text{Int}7 + z^4 \text{Int}12) \\ & + 5440y^2C04(\text{Int}45 - x^2 \text{Int}46 - y^2 \text{Int}39 - z^2 \text{Int}7) - 1920y^4C04 \text{Int}39 \\ & - 4xC10 \text{Int}47 + 24xyC11 \text{Int}43 + 96xC12(\text{Int}43 - x^2 \text{Int}48 - y^2 \text{Int}44 - z^2 \text{Int}5) \\ & - 192xy^2C12 \text{Int}44 + 1920xy^3C13 \text{Int}46 + 2560xyC13(\text{Int}44 - x^2 \text{Int}21 - y^2 \text{Int}46 - z^2 \text{Int}8) \\ & + 24x^2C20 \text{Int}49 - 12C20(\text{Int}47 - x^2 \text{Int}49 - y^2 \text{Int}43 - z^2 \text{Int}4) \\ & + 96yC21(\text{Int}43 - x^2 \text{Int}48 - y^2 \text{Int}44 - z^2 \text{Int}5) - 192x^2yC21 \text{Int}48 \\ & 240C22(\text{Int}43 - 2x^2 \text{Int}48 + x^4 \text{Int}22 - 2y^2 \text{Int}44 - 2z^2 \text{Int}5 + 2x^2y^2 \text{Int}21 + 2x^2z^2 \text{Int}9 + y^4 \text{Int}46 \\ & + 2y^2z^2 \text{Int}44 + z^4 \text{Int}50) - 960x^2C22(\text{Int}48 - x^2 \text{Int}22 - y^2 \text{Int}21 - z^2 \text{Int}9) \\ & - 96y^2C22(\text{Int}44 - x^2 \text{Int}21 - y^2 \text{Int}46 - z^2 \text{Int}8) + 1920x^2y^2C22 \text{Int}21 \\ & + 288xC30(\text{Int}49 - x^2 \text{Int}51 - y^2 \text{Int}48 - z^2 \text{Int}6) - 192x^3C30 \text{Int}51 \\ & + 2560xyC31(\text{Int}48 - x^2 \text{Int}16 - y^2 \text{Int}21 - z^2 \text{Int}9) + 1920x^3yC31 \text{Int}16 \\ & 640C40(\text{Int}49 - 2x^2 \text{Int}51 + x^4 \text{Int}15 - 2y^2 \text{Int}48 - 2z^2 \text{Int}6 + 2x^2y^2 \text{Int}16 + 2x^2z^2 \text{Int}11 + y^4 \text{Int}21 \\ & + 2y^2z^2 \text{Int}9 + z^4 \text{Int}14) - 5440x^2C40(\text{Int}51 - x^2 \text{Int}15 - y^2 \text{Int}16 - z^2 \text{Int}11) + 1920x^4C40 \text{Int}15) \\ & \left. + 8z^2(-12C02 \text{Int}1 + 288yC03 \text{Int}2 + 96xC12 \text{Int}3 - 12C20 \text{Int}4 + \right. \end{aligned}$$

$$\begin{aligned}
& 96yC21Int5 + 288xC30Int6 + 1440C04(Int2 - x^2Int8 - y^2Int7 - z^2Int12) - 5760y^2C04Int7 \\
& - 2880C13xyInt8 - 960x^2C22Int9 - 960y^2C22Int8 - 2880xyC31Int9 + \\
& 1440C40(Int6 - x^2Int11 - y^2Int9 - z^2Int14) - 5760x^2C40Int11 \Big\} \quad (12)
\end{aligned}$$

Rewrite equation 4 by substituting equation 1 in it,

$$\begin{aligned}
\tau_{xz} = 2G \Bigg[& -8xz^3 \sum_{i=0}^p \sum_{j=0}^q C_{ij} \frac{\partial^{i+j}}{\partial x^i \partial y^j} \int_{\lambda}^{\infty} \frac{1}{(a^2 + s)^2 \sqrt{Q(s)}} \omega^{(i+j)-2}(s) ds (i+j+1)(i+j)(i+j-1) + \\
& (4xz)(i+j+1)(i+j) \sum_{i=0}^p \sum_{j=0}^q C_{ij} \frac{\partial^{i+j}}{\partial x^i \partial y^j} \int_{\lambda}^{\infty} \frac{1}{(a^2 + s)^2 \sqrt{Q(s)}} \omega^{(i+j)-1}(s) ds \Bigg] \quad (13)
\end{aligned}$$

After expanding with $i+j \leq 4$, and replacing the integral terms with E, H the Equation 13 above becomes;

$$\begin{aligned}
\tau_{xz} = 2G \Bigg[& -8xz^3 \left(60C04 \frac{\partial^4 \omega^2(s)}{\partial y^4} E + 60C22 \frac{\partial^4 \omega^2(s)}{\partial x^2 \partial y^2} E \right) + 60C40 \frac{\partial^4 \omega^2(s)}{\partial x^4} E + \\
& 4xz \left(6C02 \frac{\partial^2 \omega(s)}{\partial y^2} H + 12C03 \frac{\partial^3 \omega^2(s)}{\partial y^3} H + 20C04 \frac{\partial^4 \omega^3(s)}{\partial y^4} H + \right. \\
& 12C12 \frac{\partial^3 \omega^2(s)}{\partial x \partial y^2} H + 20C13 \frac{\partial^4 \omega^3(s)}{\partial x \partial y^3} H + 6C20 \frac{\partial^2 \omega(s)}{\partial x^2} H + 12C21 \frac{\partial^3 \omega^2(s)}{\partial x^2 \partial y} H \\
& \left. + 20C22 \frac{\partial^4 \omega^3(s)}{\partial x^2 \partial y^2} H + 12C30 \frac{\partial^3 \omega^2(s)}{\partial x^3} H + 20C31 \frac{\partial^4 \omega^3(s)}{\partial x^3 \partial y} H + 20C40 \frac{\partial^4 \omega^3(s)}{\partial x^4} H \right) \Bigg] \quad (14)
\end{aligned}$$

Then, deriving the ω'' Equation 14 becomes:

$$\begin{aligned} \tau_{xz} = 2G \left[-8xz^3 \left(60C04 \frac{24}{(b^2+s)^2} E + 60C22 \frac{8}{(a^2+s)(b^2+s)} E + 60C40 \frac{24}{(a^2+s)^2} E \right) + \right. \\ 4xz \left(-12C02 \frac{H}{(b^2+s)} + 288yC03 \frac{H}{(b^2+s)^2} + 1440C04 \frac{H\omega(s)}{(b^2+s)^2} - 5760y^2C04 \frac{H}{(b^2+s)^3} + \right. \\ 96xC12 \frac{H}{(b^2+s)(a^2+s)} - 2880xyC13 \frac{H}{(a^2+s)(b^2+s)^2} - 12C20 \frac{H}{(a^2+s)} + 96yC21 \frac{H}{(b^2+s)(a^2+s)} \\ - 960x^2C22 \frac{H}{(b^2+s)(a^2+s)^2} - 960y^2C22 \frac{H}{(a^2+s)(b^2+s)^2} + 288xC30 \frac{H}{(a^2+s)^2} - 2880xyC31 \frac{H}{(b^2+s)(a^2+s)^2} + \\ \left. \left. 1440C40 \frac{H\omega(s)}{(b^2+s)(a^2+s)^2} - 5760x^2C40 \frac{H}{(a^2+s)^3} \right) \right] \quad (15) \end{aligned}$$

By replacing all the completed integral terms with $\text{Int}N$, where N is the integral number, Equation 15 can be written as:

$$\begin{aligned} \tau_{xz} = 2G \left[-xz^3 (480C04 \text{Int}8 + 480C22 \text{Int}9 + 480C40 \text{Int}11) \right. \\ + 4xz \left(-12C02 \text{Int}43 + 288yC03 \text{Int}44 + 1440C04 (\text{Int}44 - x^2 \text{Int}17 - y^2 \text{Int}46 - z^2 \text{Int}8) - 5760y^2C04 \text{Int}46 + \right. \\ 96xC12 \text{Int}48 - 2880xyC13 \text{Int}21 - 12C20 \text{Int}49 + 96yC21 \text{Int}48 \\ - 960x^2C22 \text{Int}16 - 960y^2C22 \text{Int}58 + 288C30 \text{Int}51 - 2880xyC31 \text{Int}16 + \\ \left. \left. 1440C40 (\text{Int}51 - x^2 \text{Int}15 - y^2 \text{Int}16 - z^2 \text{Int}11) - 5760x^2C40 \text{Int}15 \right) \right] \quad (16) \end{aligned}$$

All completed integral terms will be evaluated below:

It is known that $Q(s) = s(a^2+s)(b^2+s)$, then

$$\text{Int}1 = \int_{-\infty}^{\infty} \frac{ds}{s^2(b^2+s)[Q(s)]^{\frac{1}{2}}}$$

$$\text{Int}2 = \int_{-\infty}^{\infty} \frac{ds}{s^2(b^2+s)^2[Q(s)]^{\frac{1}{2}}}$$

$$\text{Int3} = \int_{\lambda}^{\infty} \frac{ds}{s^2(a^2+s)(b^2+s)[Q(s)]^{\frac{1}{2}}}$$

$$\text{Int4} = \int_{\lambda}^{\infty} \frac{ds}{s^2(a^2+s)[Q(s)]^{\frac{1}{2}}}$$

$$\text{Int5} = \text{Int3}$$

$$\text{Int6} = \int_{\lambda}^{\infty} \frac{ds}{s^2(a^2+s)^2[Q(s)]^{\frac{1}{2}}}$$

$$\text{Int7} = \int_{\lambda}^{\infty} \frac{ds}{s^2(b^2+s)^3[Q(s)]^{\frac{1}{2}}}$$

$$\text{Int8} = \int_{\lambda}^{\infty} \frac{ds}{s^2(a^2+s)(b^2+s)^2[Q(s)]^{\frac{1}{2}}}$$

$$\text{Int9} = \int_{\lambda}^{\infty} \frac{ds}{s^2(a^2+s)^2(b^2+s)[Q(s)]^{\frac{1}{2}}}$$

$$\text{Int10} = \int_{\lambda}^{\infty} \frac{ds}{s^2(a^2+s)^2(b^2+s)^2[Q(s)]^{\frac{1}{2}}}$$

$$\text{Int11} = \int_{\lambda}^{\infty} \frac{ds}{s^2(a^2+s)^3[Q(s)]^{\frac{1}{2}}}$$

$$\text{Int12} = \int_{\lambda}^{\infty} \frac{ds}{s^3(b^2+s)^2[Q(s)]^{\frac{1}{2}}}$$

$$\text{Int13} = \int_{\lambda}^{\infty} \frac{ds}{s^3(a^2+s)[Q(s)]^{\frac{1}{2}}}$$

$$\text{Int14} = \int_{\lambda}^{\infty} \frac{ds}{s^3(a^2+s)^2[Q(s)]^{\frac{1}{2}}}$$

$$\text{Int15} = \int_{\lambda}^{\infty} \frac{ds}{s(a^2+s)^4[Q(s)]^{\frac{1}{2}}}$$

$$\text{Int16} = \int_{\lambda}^{\infty} \frac{ds}{s(a^2+s)^3(b^2+s)[Q(s)]^{\frac{1}{2}}}$$

$$\text{Int17} = \int_{\lambda}^{\infty} \frac{ds}{s(a^2+s)^2(b^2+s)^2[Q(s)]^{\frac{1}{2}}}$$

$$\text{Int18} = \int_{\lambda}^{\infty} \frac{ds}{(a^2+s)^2(b^2+s)^2[Q(s)]^{\frac{1}{2}}}$$

$$\text{Int19} = \int_{\lambda}^{\infty} \frac{ds}{(a^2+s)^3(b^2+s)^2[Q(s)]^{\frac{1}{2}}}$$

$$\text{Int20} = \int_{\lambda}^{\infty} \frac{ds}{(a^2+s)^2(b^2+s)^3[Q(s)]^{\frac{1}{2}}}$$

$$\text{Int21} = \text{Int17}$$

$$\text{Int23} = \int_{\lambda}^{\infty} \frac{ds}{(a^2 + s)^3 [\mathcal{Q}(s)]^{\frac{1}{2}}}$$

$$\text{Int25} = \int_{\lambda}^{\infty} \frac{ds}{(a^2 + s)^4 (b^2 + s) [\mathcal{Q}(s)]^{\frac{1}{2}}}$$

$$\text{Int27} = \int_{\lambda}^{\infty} \frac{ds}{(a^2 + s)^4 [\mathcal{Q}(s)]^{\frac{1}{2}}}$$

$$\text{Int29} = \text{Int15}$$

$$\text{Int31} = \int_{\lambda}^{\infty} \frac{ds}{(b^2 + s)^4 [\mathcal{Q}(s)]^{\frac{1}{2}}}$$

$$\text{Int33} = \int_{\lambda}^{\infty} \frac{ds}{(b^2 + s)^5 [\mathcal{Q}(s)]^{\frac{1}{2}}}$$

$$\text{Int35} = \int_{\lambda}^{\infty} \frac{ds}{(a^2 + s)(b^2 + s)^3 [\mathcal{Q}(s)]^{\frac{1}{2}}}$$

$$\text{Int37} = \text{Int20}$$

$$\text{Int39} = \int_{\lambda}^{\infty} \frac{ds}{(a^2 + s)^2 (b^2 + s) [\mathcal{Q}(s)]^{\frac{1}{2}}}$$

$$\text{Int22} = \text{Int16}$$

$$\text{Int24} = \int_{\lambda}^{\infty} \frac{ds}{(a^2 + s)^3 (b^2 + s) [\mathcal{Q}(s)]^{\frac{1}{2}}}$$

$$\text{Int26} = \text{Int19}$$

$$\text{Int28} = \int_{\lambda}^{\infty} \frac{ds}{(a^2 + s)^5 [\mathcal{Q}(s)]^{\frac{1}{2}}}$$

$$\text{Int30} = \int_{\lambda}^{\infty} \frac{ds}{(b^2 + s)^3 [\mathcal{Q}(s)]^{\frac{1}{2}}}$$

$$\text{Int32} = \int_{\lambda}^{\infty} \frac{ds}{(a^2 + s)(b^2 + s)^4 [\mathcal{Q}(s)]^{\frac{1}{2}}}$$

$$\text{Int34} = \int_{\lambda}^{\infty} \frac{ds}{(b^2 + s)^4 s [\mathcal{Q}(s)]^{\frac{1}{2}}}$$

$$\text{Int36} = \int_{\lambda}^{\infty} \frac{ds}{(a^2 + s)(b^2 + s)^2 [\mathcal{Q}(s)]^{\frac{1}{2}}}$$

$$\text{Int38} = \text{Int18}$$

$$\text{Int40} = \int_{\lambda}^{\infty} \frac{ds}{s [\mathcal{Q}(s)]^{\frac{1}{2}}}$$

$$\text{Int41} = \int_{\lambda}^{\infty} \frac{ds}{s(b^2 + s)[Q(s)]^{\frac{1}{2}}}$$

$$\text{Int42} = \int_{\lambda}^{\infty} \frac{ds}{s(b^2 + s)^2[Q(s)]^{\frac{1}{2}}}$$

$$\text{Int43} = \int_{\lambda}^{\infty} \frac{ds}{(a^2 + s)(b^2 + s)s[Q(s)]^{\frac{1}{2}}}$$

$$\text{Int44} = \int_{\lambda}^{\infty} \frac{ds}{(a^2 + s)(b^2 + s)^2s[Q(s)]^{\frac{1}{2}}}$$

$$\text{Int45} = \int_{\lambda}^{\infty} \frac{ds}{(b^2 + s)^3s[Q(s)]^{\frac{1}{2}}}$$

$$\text{Int46} = \int_{\lambda}^{\infty} \frac{ds}{(a^2 + s)(b^2 + s)^3s[Q(s)]^{\frac{1}{2}}}$$

$$\text{Int47} = \int_{\lambda}^{\infty} \frac{ds}{(a^2 + s)s[Q(s)]^{\frac{1}{2}}}$$

$$\text{Int48} = \int_{\lambda}^{\infty} \frac{ds}{(a^2 + s)^2(b^2 + s)s[Q(s)]^{\frac{1}{2}}}$$

$$\text{Int49} = \int_{\lambda}^{\infty} \frac{ds}{(a^2 + s)^2s[Q(s)]^{\frac{1}{2}}}$$

$$\text{Int50} = \int_{\lambda}^{\infty} \frac{ds}{(a^2 + s)(b^2 + s)s^3[Q(s)]^{\frac{1}{2}}}$$

$$\text{Int51} = \int_{\lambda}^{\infty} \frac{ds}{(a^2 + s)^3s[Q(s)]^{\frac{1}{2}}}$$

$$\text{Int52} = \int_{\lambda}^{\infty} \frac{ds}{(a^2 + s)[Q(s)]^{\frac{1}{2}}}$$

$$\text{Int53} = \int_{\lambda}^{\infty} \frac{ds}{(a^2 + s)(b^2 + s)[Q(s)]^{\frac{1}{2}}}$$

$$\text{Int54} = \text{Int39}$$

$$\text{Int55} = \int_{\lambda}^{\infty} \frac{ds}{(a^2 + s)^2[Q(s)]^{\frac{1}{2}}}$$

$$\text{Int56} = \int_{\lambda}^{\infty} \frac{ds}{(b^2 + s)[Q(s)]^{\frac{1}{2}}}$$

$$\text{Int57} = \int_{\lambda}^{\infty} \frac{ds}{(b^2 + s)^2[Q(s)]^{\frac{1}{2}}}$$

$$\text{Int58} = \int_{\lambda}^{\infty} \frac{ds}{(a^2 + s)^3(b^2 + s)^2s[Q(s)]^{\frac{1}{2}}}$$

To solve these integral equations using :

Transformation formula⁴¹:

This formula is to transform the integral equation into the elliptic function integral

$$\int_y^{\infty} \frac{R(t)dt}{\sqrt{(t-a)(t-b)(t-c)}} = g \int_0^{u_1} R[c + (a-c)ns^2u] du$$

Where $R(t)$ is any rational function of t

$$sn^2u = \frac{a-c}{t-c}, \quad k^2 = \frac{b-c}{a-c}, \quad g = \frac{2}{\sqrt{a-c}}, \quad k'^2 = 1 - k^2$$

$$\varphi = am u_1 = \sin^{-1} \sqrt{\frac{a-c}{y-c}}, \quad sn u_1 = \sin \varphi$$

In case of the integral equations above these condition must be satisfied;

$$a=0, \quad b=-b^2, \quad c=-a^2, \quad t=s, \quad y=\lambda$$

After the transformation the recursive formula⁴¹ for Jacobian function below are used:

$$\begin{aligned} \int \frac{sn^n u du}{cn^p u dn^{2m} u} &= \int sn^n unc^p und^{2m} u du \\ &= \frac{1}{(p-1)k'^2} \left\{ sn^{n+1} unc^{p-1} und^{2m-1} u + [p-n-2 + (n-2p+4-2m)k^2] \right. \\ &\quad \left. \int sn^n unc^{p-2} und^{2m} u du + k^2(p-n+2m-3) \int sn^n unc^{p-4} und^{2m} u du \right\} \\ p &\neq 1 \end{aligned}$$

and

$$\int sn^{2m} u cn^{2n} u dn^{2p} u du = \frac{1}{k^{2(m+n)}} \sum_{j=0}^m \sum_{\gamma=0}^n \frac{(-1)^{j+\gamma+n} k^{2(n-\gamma)} m! n!}{(m-j)! j! (n-\gamma)! \gamma!} I_{2(p-j-\gamma)}$$

other formulas⁴¹ that are very useful

$$nsu = \frac{1}{snu}, \quad ncu = \frac{1}{cnu}, \quad cdu = \frac{cnu}{dnu}$$

$$ndu = \frac{1}{dnu}, \quad tnu = \frac{snu}{cnu}, \quad sn^2 u + cn^2 u = 1, \quad k^2 sn^2 u + dn^2 u = 1$$

$$A_m = \int sn^m u du$$

$$A_0 = \int du = u = F(\varphi, k)$$

$$A_1 = \int snu du = \frac{1}{k} \ln(dnu - kcnu)$$

$$A_2 = \int sn^2 u du = \frac{1}{k^2} [u - E(u)]$$

$$A_{2m+2} = \frac{sn^{2m-1} u cnu dnu + 2m(1+k^2)A_{2m} + (1-2m)A_{2m-2}}{(2m+1)k^2}$$

$$A_{2m+3} = \frac{sn^{2m} u cnu dnu + (2m+1)(1+k^2)A_{2m+1} - 2mA_{2m-1}}{2(m+1)k^2}$$

$$B_m = \int ns^m u du$$

$$B_{2m+2} = \frac{2m(1+k^2)B_{2m} + (1-2m)k^2 B_{2m-2} - cnu dnuns^{2m+1} u}{2m+1}$$

$$B_{2m+3} = \frac{(2m+1)(1+k^2)B_{2m+1} - 2mk^2 B_{2m-1} - cnu dnuns^{2m+2} u}{2(m+1)}$$

$$G_m = \int dn^m u du$$

$$G_1 = \int dnu du = amu = \sin^{-1}(snu)$$

$$G_2 = \int dn^2 u du = E(u)$$

$$G_{2m+2} = \frac{k^2 dn^{2m-1} u smucnu + (1-2m)k^2 G_{2m-2} + 2m(2-k^2)G_{2m}}{2m+1}$$

$$G_{2m+3} = \frac{k^2 dn^{2m} usnucnu - 2mk^2 G_{2m-1} + (2m+1)(2-k^2)G_{2m+1}}{2(m+1)}$$

$$I_m = \int nd^m u du$$

$$I_1 = \int ndu du = \frac{1}{k'} \tan^{-1} \left[\frac{k' snu - cnu}{k' snu + cnu} \right]$$

$$I_{2m+2} = \frac{2m(2-k^2)I_{2m} + (1-2m)I_{2m-2} - k^2 snucnund^{2m+1}u}{(2m+1)k'^2}$$

$$I_{2m+3} = \frac{(2m+1)(2-k^2)I_{2m+1} - 2mI_{2m-1} - k^2 snucnund^{2m+2}u}{2(m+1)k'^2}$$

The results of the analytical evaluation are presented below:

$$k^2 = (a^2 - b^2) / (a^2)$$

$$k'^2 = 1 - k^2$$

$$cdul = cnu1 / dnu1$$

$$ndu1 = 1 / dnu1$$

$$ncu1 = 1 / cnu1$$

$$tnu1 = snu1 / cnu1$$

$$I_0 = u1$$

$$I_2 = (1/k'^2)(Eu1 - k^2 snu1 cdul)$$

$$I_4 = (1/(3k'^2k^2))(2(2-k^2)Eu1 - k'^2 u1 - k^2 snu1 cnu1 (k'^2 ndu1 ndu1 + 4 - 2k^2))$$

$$I_6 = (1/(5k'^2))(4(2-k^2)I_4 - 3I_2 - k^2 snu1 cnu1 ndu1^5)$$

$$I_8 = (1/(7k'^2))(6(2-k^2)I_6 - 5I_4 - k^2 snu1 cnu1 ndu1^7)$$

$$I_{10} = (1/(9k'^2))(8(2-k^2)I_8 - 7I_6 - k^2 snu1 cnu1 ndu1^9)$$

$$G_2 = Eu1$$

$$G_4 = (1/3)(k^2 snu1 cnu1 dnu1 - k'^2 u1 + 2(1+k'^2)Eu1)$$

$$G_6 = (1/5)(k^2 snu1 cnu1 dnu1^3 - 3k'^2 G_2 + 4(2-k^2)G_4)$$

$$G_8 = (1/7)(k^2 snu1 cnu1 dnu1^5 - 5k'^2 G_4 + 6(2-k^2)G_6)$$

$$G_{10} = (1/9)(k^2 snu1 cnu1 dnu1^7 - 7k'^2 G_6 + 8(2-k^2)G_8)$$

$$G_{12} = (1/11)(k^2 \text{snulcnu} \text{ldnu}^9 - 9k'^2 G_8 + 10(2-k^2)G_{10})$$

$$A_0 = u_1$$

$$A_2 = (1/k^2)(u_1 - Eu_1)$$

$$A_4 = (1/(3k^2 k^2))((2+k^2)u_1 - 2(1-k^2)Eu_1 + k^2 \text{snulcnu} \text{ldnu})$$

$$A_6 = (1/(5k^2))(\text{cnu} \text{ldnu} \text{lsnu}^3 + 4(1+k^2)A_4 - 3A_2)$$

$$A_8 = (1/(7k^2))(\text{cnu} \text{ldnu} \text{lsnu}^5 + 6(1+k^2)A_6 - 5A_4)$$

$$A_{10} = (1/(9k^2))(\text{cnu} \text{ldnu} \text{lsnu}^7 + 8(1+k^2)A_8 - 7A_6)$$

$$S_1 = (1/(k^{24}))(\text{I}2 - 4\text{I}0 + 6G_2 - 4G_4 + G_6)$$

$$S_2 = (1/(k^{25}))(-k'^2 \text{I}2 + 4k'^2 \text{I}0 - 6k'^2 G_2 + 4k'^2 G_4 - k'^2 G_6 + \text{I}0 - 4G_2 + 6G_4 - 4G_6 + G_8)$$

$$S_3 = (1/(k^{25}))(\text{I}6 - 5\text{I}4 + 10\text{I}2 - 10\text{I}0 + 5G_2 - G_4)$$

$$S_4 = (1/(k^{26}))(-k'^2 \text{I}6 + 5k'^2 \text{I}4 - 10k'^2 \text{I}2 + 10k'^2 \text{I}0 - 5k'^2 G_2 + k'^2 G_4 + \text{I}4 - 5\text{I}2 + 10\text{I}0 - 10G_2 + 5G_4 - G_6)$$

$$S_5 = (1/(k^{25}))(\text{I}4 - 5\text{I}2 + 10\text{I}0 - 10G_2 + 5G_4 - G_6)$$

$$S_6 = (1/(k^{26}))(-k'^2 \text{I}4 + 5k'^2 \text{I}2 - 10k'^2 \text{I}0 + 10k'^2 G_2 - 5k'^2 G_4 + k'^2 G_6 + \text{I}2 - 5\text{I}0 + 10G_2 - 10G_4 + 5G_6 - G_8)$$

$$S_7 = (1/(k^{25}))(\text{I}2 - 5\text{I}0 + 10G_2 - 10G_4 + 5G_6 - G_8)$$

$$S_8 = (1/(k^{26}))(-k'^2 \text{I}2 + 5k'^2 \text{I}0 - 10k'^2 G_2 + 10k'^2 G_4 - 5k'^2 G_6 + k'^2 G_8 + \text{I}0 - 5G_2 + 10G_4 - 10G_6 + 5G_8 - G_{10})$$

$$S_9 = (1/(k^{26}))(\text{I}4 - 6\text{I}2 + 15\text{I}0 - 20G_2 + 15G_4 - 6G_6 + G_8)$$

$$S_{10} = (1/(k^{27}))(-k'^2 \text{I}4 + 6k'^2 \text{I}2 - 15k'^2 \text{I}0 + 20k'^2 G_2 - 15k'^2 G_4 + 6k'^2 G_6 - k'^2 G_8 + \text{I}2 - 6\text{I}0 + 15G_2 - 20G_4 + 15G_6 - 6G_8 + G_{10})$$

$$S_{11} = (1/(k^{25}))(-k'^2 \text{I}0 + 4k'^2 G_2 - 6k'^2 G_4 + 4k'^2 G_6 - k'^2 G_8 + G_2 - 4G_4 + 6G_6 - 4G_8 + G_{10})$$

$$S_{12} = (1/(k^{26}))(-k'^2 \text{I}0 + 5k'^2 G_2 - 10k'^2 G_4 + 10k'^2 G_6 - 5k'^2 G_8 + k'^2 G_{10} + G_2 - 5G_4 + 10G_6 - 10G_8 + 5G_{10} - G_{12})$$

$$S_{13} = (1/(k^{24}))(\text{I}4 - 4\text{I}2 + 6\text{I}0 - 4G_2 + G_4)$$

$$S_{14} = (1/(k^{25}))(\text{I}4 - 5\text{I}2 + 10\text{I}0 - 10G_2 + 5G_4 - G_6)$$

$$S_{15} = (1/(k^{24}))(\text{I}8 - 4\text{I}6 + 6\text{I}4 - 4\text{I}2 + \text{I}0)$$

$$S_{16} = (1/(k^{23}))(\text{I}6 - 3\text{I}4 + 3\text{I}2 - \text{I}0)$$

$$S_{17} = (1/(k^{25}))(\text{I}8 - 5\text{I}6 + 10\text{I}4 - 10\text{I}2 + 5\text{I}0 - G_2)$$

$$S_{18} = (1/(k^{25}))(\text{I}10 - 5\text{I}8 + 10\text{I}6 - 10\text{I}4 + 5\text{I}2 - \text{I}0)$$

$$S19 = (1 / (k^{26})) (-k'^2 I_8 + 5k'^2 I_6 - 10k'^2 I_4 + 10k'^2 I_2 - 5k'^2 I_0 + k'^2 G_2 + I_6 - 5I_4 + 10I_2 - 10I_0 + 5G_2 - G_4)$$

$$S20 = (1 / (k^{24})) (I_6 - 4I_4 + 6I_2 - 4I_0 + G_2)$$

$$S21 = (1 / (k^{23})) (I_4 - 3I_2 + 3I_0 - G_2)$$

$$S22 = (1 / (k^{23})) (I_2 - 3I_0 + 3G_2 - G_4)$$

$$S23 = (1 / (k^{24})) (-k'^2 I_2 + 3k'^2 I_0 - 3k'^2 G_2 + k'^2 G_4 + I_0 - 3G_2 + 3G_4 - G_6)$$

$$S24 = (1 / (k^{25})) (-k'^2 I_4 + 4k'^2 I_2 - 6k'^2 I_0 + 4k'^2 G_2 - k'^2 G_4 + I_2 - 4I_0 + 6G_2 - 4G_4 + G_6)$$

$$S25 = (1 / (k^{24})) (-k'^2 I_0 + 3k'^2 G_2 - 3k'^2 G_4 + k'^2 G_6 + G_2 - 3G_4 + 3G_6 - G_8)$$

$$S26 = (1 / (k^{22})) (I_2 - 2I_0 + G_2)$$

$$S27 = (1 / (k^{23})) (-k'^2 I_2 + 2k'^2 I_0 - k'^2 G_2 + I_0 - 2G_2 + G_4)$$

$$S28 = S21$$

$$S29 = (1 / (k^{24})) (-k'^2 I_4 + 3k'^2 I_2 - 3k'^2 I_0 + k'^2 G_2 + I_2 - 3I_0 + 3G_2 - G_4)$$

$$S30 = S22$$

$$S31 = S23$$

$$S32 = S13$$

$$S33 = S24$$

$$S34 = S20$$

$$S35 = (1 / (k^{25})) (-k'^2 I_6 + 4k'^2 I_4 - 6k'^2 I_2 + 4k'^2 I_0 - k'^2 G_2 + I_4 - 4I_2 + 6I_0 - 4G_2 + G_4)$$

$$S36 = (1 / (k^{23})) (-k'^2 I_0 + 2k'^2 G_2 - k'^2 G_4 + G_2 - 2G_4 + G_6)$$

$$Int1 = (2 / (3k'^2 a^7)) (ndu1(ncu1^3)snu1^7 - 4((1/k'^2)(ncu1ndu1snu1^7 + (4k^2 - 6)S22 - 5k^2 S23)) - 3k^2 S22)$$

$$Int2 = (2 / (3k'^2 a^9)) ((ndu1^3)(ncu1^3)snu1^9 - 6((1/k'^2)(ncu1(ndu1^3)snu1^9 + (4k^2 - 8)S13 - 13k^2 S24)) - 11k^2 S13)$$

$$Int3 = (2 / (3k'^2 a^9)) (ndu1(ncu1^3)snu1^9 + (2k^2 - 6)((1/k'^2)(ncu1ndu1snu1^9 + (6k^2 - 8)S1 - 7k^2 S2)) - 11k^2 S1)$$

$$Int4 = (2 / (3k'^2 a^7)) (dnul(ncu1^3)snu1^7 + (2k^2 - 4)((1/k'^2)(ncu1dnul1snu1^7 + (6k^2 - 6)A6 - 7k^2 S25)) - 5k^2 A6)$$

$$Int5 = Int3$$

$$Int6 = (2 / (3k'^2 a^9)) (dnul(ncu1^3)snu1^9 + (4k^2 - 6)((1/k'^2)(ncu1dnul1snu1^9 + (8k^2 - 8)A8 - 9k^2 S11)) - 7k^2 A8)$$

$$\text{Int7} = (2/(3k'^2a^{11}))((\text{ndu}1^5)(\text{ncu}1^3)\text{snu}1^{11} - 8((1/k'^2)(\text{ncu}1(\text{ndu}1^5)\text{snu}1^{11} + (4k^2 - 10)S3 - 5k^2S4)) - 3k^2S3)$$

$$\text{Int8} = (2/(3k'^2a^{11}))((\text{ndu}1^3)(\text{ncu}1^3)\text{snu}1^{11} + (2k^2 - 8)((1/k'^2)(\text{ncu}1(\text{ndu}1^3)\text{snu}1^{11} + (6k^2 - 10)S5 - 7k^2S6)) - 5k^2S5)$$

$$\text{Int9} = (2/(3k'^2a^{11}))(\text{ndu}1(\text{ncu}1^3)\text{snu}1^{11} + (4k^2 - 8)((1/k'^2)(\text{ncu}1\text{ndu}1\text{snu}1^{11} + (8k^2 - 10)S7 - 9k^2S8)) - 7k^2S7)$$

$$\text{Int10} = (2/(3k'^2a^{13}))((\text{ndu}1^3)(\text{ncu}1^3)\text{snu}1^{13} + (4k^2 - 10)((1/k'^2)(\text{ncu}1(\text{ndu}1^3)\text{snu}1^{13} + (8k^2 - 12)S9 - 9k^2S10)) - 7k^2S9)$$

$$\text{Int11} = (2/(3k'^2a^{11}))(\text{dnu}1(\text{ncu}1^3)\text{snu}1^{11} + (6k^2 - 8)((1/k'^2)(\text{ncu}1\text{dnu}1\text{snu}1^{11} + (10k^2 - 10)A10 - 11k^2S12)) - 9k^2A10)$$

$$\begin{aligned} \text{Int12} = & (2/(5k'^2a^{11}))((\text{ndu}1^3)(\text{ncu}1^5)\text{snu}1^{11} \\ & (2k^2 + 6)((1/(3k'^2))((\text{ncu}1^3)(\text{ndu}1^3)\text{snu}1^{11} \\ & + (2k^2 - 8)((1/k'^2)(\text{ncu}1(\text{ndu}1^3)\text{snu}1^{11} + (6k^2 - 10)S5 - 7k^2S6)) - 5k^2S5)) - \\ & (3k^2/k'^2)(\text{ncu}1(\text{ndu}1^3)\text{snu}1^{11} + (6k^2 - 10)S5 - 7k^2S6)) \end{aligned}$$

$$\text{Int13} = (2/(5k'^2a^9))(\text{dnu}1(\text{ncu}1^5)\text{snu}1^9 - 4\text{Int6} - (5k^2/k'^2)(\text{ncu}1\text{dnu}1\text{snu}1^9 + (8k^2 - 8)A8 - 9k^2S11))$$

$$\begin{aligned} \text{Int14} = & (2/(5k'^2a^{11}))(\text{dnu}1(\text{ncu}1^5)\text{snu}1^{11} + (2k^2 - 6)((1/(3k'^2))((\text{ncu}1^3)\text{dnu}1\text{snu}1^{11} + (6k^2 - 8)((1/k'^2)(\text{ncu}1\text{dnu}1\text{snu}1^{11} + (10k^2 - 10)A10 - 11k^2S12)) - 9k^2A10)) - \\ & (7k^2/k'^2)(\text{ncu}1(\text{dnu}1)\text{snu}1^{11} + (10k^2 - 10)A10 - 11k^2S12)) \end{aligned}$$

$$\text{Int15} = (2/(k'^2a^{11}))(\text{dnu}1\text{ncu}1\text{snu}1^{11} - (10k^2 - 10)A10 - 11k^2S12)$$

$$\text{Int16} = (2/(k'^2a^{11}))(\text{ndu}1\text{ncu}1\text{snu}1^{11} - (8k^2 - 10)S7 - 9k^2S8)$$

$$\text{Int17} = (2/(k'^2a^{11}))((\text{ndu}1^3)\text{ncu}1\text{snu}1^{11} - (6k^2 - 10)S5 - 7k^2S6)$$

$$\text{Int18} = (2/a^9)S13$$

$$\text{Int19} = (2/a^{11})S14$$

$$\text{Int20} = (2/a^{11})S3$$

$$\text{Int21} = \text{Int17}$$

$$\text{Int22} = \text{Int16}$$

$$\text{Int23} = (2/a^7)A6$$

$$\text{Int24} = (2/a^9)S1$$

$$\text{Int25} = (2/a^{11})S7$$

$$\text{Int26}=\text{Int19}$$

$$\text{Int27}=(2/a^9)A8$$

$$\text{Int28}=(2/a^{11})A10$$

$$\text{Int29}=\text{Int15}$$

$$\text{Int30}=(2/a^7)S16$$

$$\text{Int31}=(2/a^9)S15$$

$$\text{Int32}=(2/a^{11})S17$$

$$\text{Int33}=(2/a^{11})S18$$

$$\text{Int34}=(2/(k^2a^{11}))((\text{ndu}1^7)\text{ncu}1\text{snu}1^{11}-(2k^2-10)S17-3k^2S19)$$

$$\text{Int35}=(2/a^9)S20$$

$$\text{Int36}=(2/a^7)S21$$

$$\text{Int37}=\text{Int20}$$

$$\text{Int38}=\text{Int18}$$

$$\text{Int39}=(2/a^7)S22$$

$$\text{Int40}=(2/(k^2a^3))(\text{dnul}1\text{tnul}-\text{Eu}1)$$

$$\text{Int41}=(2/(k^2a^5))((\text{snu}1^5)\text{ncu}1\text{ndu}1+(2k^2-4)S26-3k^2S27)$$

$$\text{Int42}=(2/(k^2a^7))((\text{snu}1^7)\text{ncu}1(\text{ndu}1)^3+(4k^2-6)S28-3k^2S29)$$

$$\text{Int43}=(2/(k^2a^7))((\text{snu}1^7)\text{ncu}1\text{ndu}1+(4k^2-6)S30-5k^2S31)$$

$$\text{Int44}=(2/(k^2a^9))((\text{snu}1^9)(\text{ncu}1^2)(\text{ndu}1)^3+(4k^2-8)S32-5k^2S33)$$

$$\text{Int45}=(2/(k^2a^9))((\text{snu}1^9)\text{ncu}1(\text{ndu}1)^5+(2k^2-8)S34-3k^2S35)$$

$$\text{Int46}=(2/(k^2a^{11}))((\text{snu}1^{11})\text{ncu}1(\text{ndu}1)^6+(4k^2-10)S3-5k^2S4)$$

$$\text{Int47}=(2/(k^2a^5))((\text{snu}1^5)\text{ncu}1\text{dnul}+(4k^2-4)A4-5k^2S36)$$

$$\text{Int48}=(2/(k^2a^9))((\text{snu}1^9)\text{ncu}1\text{ndu}1+(6k^2-8)S1-5k^2S2)$$

$$\text{Int49}=(2/(k^2a^7))((\text{snu}1^7)\text{ncu}1\text{dnul}+(6k^2-6)A6-5k^2S25)$$

$$\text{Int50}=(2/(k^2a^{11}))((\text{snu}1^{11})(\text{ncu}1^5)\text{ndu}1+(-8)\text{Int9}-$$

$$(5(k^2/k^2))((\text{snu}1^{11})\text{ncu}1\text{ndu}1+(8k^2-10)S7-9k^2S8))$$

$$\text{Int51}=(2/(k^2a^9))((\text{snu}1^9)\text{ncu}1\text{dnul}+(8k^2-8)A8-9k^2S11)$$

$$\text{Int52}=(2/(a^3))A2$$

$$\text{Int53}=(2/(a^5))S26$$

$$\text{Int54}=\text{Int39}$$

$$\text{Int55}=(2/(a^5))A4$$

$$\text{Int56} = (2 / (k^2 a^3)) (I2 - I0)$$

$$\text{Int57} = (2 / ((k^2 a^5)) (I4 - 2I2 + I0)$$

$$\text{Int58} = (2 / (k^2 a^3)) ((\text{sn}u1^{13}) \text{cn}u1 (\text{dn}u1^3) + (8k^2 - 12) S9 - 9k^2 S10)$$

The calculations of the Legendre elliptic integral of 1st kind $F(\phi, k) = u1$ and 2nd kind $E(u1)$ and Jacobian elliptic functions $\text{sn}u1$, $\text{cn}u1$, $\text{dn}u1$ are done numerically⁴². The Routines for calculating these terms in FORTRAN are as follows:

Elliptic Integral and Function calculation (excerpt from the main program for constructing the stress field)

YYY IS THE THICKNESS OF THE PLATE
 RT=BBB/YYY IS THE THICKNESS RATIO
 EMC=BBB/AAA IS THE RATIO OF THE SEMI-MINOR TO SEMI-MAJOR AXIS
 ELLIPSOIDAL COORDINATE LAMBDA is CLAMBDA

```

      BBB=YYY*RT
      AAA=BBB/EMC
c     CAA=(AAA/RC)
      caa=0.666667
      write(*,*)'AAA BBB CAA',AAA,BBB,CAA
      write(20,*)'AAA BBB CAA',AAA,BBB,CAA
      AK=sqrt((AAA**2 - BBB**2)/(AAA**2))
      PHI= ASIN(SQRT(AAA**2/(AAA**2+CLAMBDA)))
      U1 = ellf(PHI,AK)
      EU1= elle(PHI,AK)
      EMMC=1-(AK**2)
c     UU=U1
      CALL snendn(U1,EMMC,sn,cn,dn)
      SNU1=sn
      CNU1=cn
      DNU1=dn
      WRITE(20,*)'AK U1 EU1 SNU1 CNU1 DNU1'
      WRITE(20,*) AK,U1,EU1,SNU1,CNU1,DNU1
  
```

To calculate the Legendre elliptic integral of 1st kind $F(\phi, k)=u_1$

```
C-----  
      FUNCTION ellf(phi,ak)  
C-----  
      REAL ellf,ak,phi  
C      USES rf  
C      Legendre elliptic integral of the 1st kind  $F(\phi, k)$ , evaluated using  
C      Carlson's function RF.  
      REAL s,rf  
      s=sin(phi)  
      ellf=s*s*rf(cos(phi)**2,(1.-s*ak)*(1.+s*ak),1.)  
      return  
      END
```

To calculate the Legendre elliptic integral 2nd kind $E(u_1)$

```
C-----  
      FUNCTION elle(phi,ak)  
C-----  
      REAL elle,ak,phi  
C      USES rd,rf  
C      Legendre elliptic integral of the 2nd kind  $E(\phi, k)$ , evaluated using  
C      Carlson's function RD and RF.  
      REAL cc,q,s,rd,rf  
      s=sin(phi)  
      cc=cos(phi)**2  
      q=(1.-s*ak)*(1.+s*ak)  
      elle=s*(rf(cc,q,1.)-((s*ak)**2)*rd(cc,q,1.)/3.)  
      return  
      END
```

Function rd and rf that used to calculate $F(\phi, k)=u_1$ and $E(u_1)$

```

C-----
FUNCTION rf(x,y,z)
C-----
  REAL rf,x,y,z,ERRTOL,TINY,BIG,THIRD,C1,C2,C3,C4
  PARAMETER (ERRTOL=.08,TINY=1.5e-38,BIG=3.E37,THIRD=1./3.,
  * C1=1./24.,C2=.1,C3=3./44.,C4=1./14.)
C Computes Carlson's elliptic integral of the first kind, RF(x,y,z).
C x,y, and z must be nonnegative, and at most one can be zero. TINY
C must be at least 5 times the machine underflow limit, BIG at most
C one fifth the machine overflow limit.
  Real alamb,ave,dely,delx,delz,e2,e3,sqrtx,sqrty,sqrtz,xt,yt,zt
  if (min(x,y,z).lt.0..or.min(x+y,x+z,y+z).lt.TINY.or.
  * max(x,y,z).gt.BIG)pause ' invalid arguments in rf '
  xt=x
  yt=y
  zt=z
1 continue
  sqrtx=sqrt(xt)
  sqrty=sqrt(yt)
  sqrtz=sqrt(zt)
  alamb=sqrtx*(sqrty+sqrtz)+sqrty*sqrtz
  xt=.25*(xt+alamb)
  yt=.25*(yt+alamb)
  zt=.25*(zt+alamb)
  ave=THIRD*(xt+yt+zt)
  delx=(ave-xt)/ave
  dely=(ave-yt)/ave
  delz=(ave-zt)/ave
  if(max(abs(delx),abs(dely),abs(delz)).gt.ERRTOL)goto 1
  e2=delx*dely-delz**2
  e3=delx*dely*delz
  rf=(1.+(C1*e2-C2-C3*e3)/sqrt(ave))
  return
END

```

C-----

FUNCTION rd(x,y,z)

C-----

```

      REAL rd,x,y,z,ERRTOL,TINY,BIG,C1,C2,C3,C4,C5,C6
      PARAMETER (ERRTOL=.05,TINY=1.e-25,BIG=4.5E21,C1=3./14,
* C2=1./6.,C3=9./22.,C4=3./26.,C5=.25*C3,C6=1.5*C4)
C   Computes Carlson's elliptic integral of the second kind, RD(x,y,z).
C   x and y must be nonnegative, and at most one can be zero. z must be
C   positive. TINY must be at least twice the negative 2/3 power of the
C   machine overflow limit. BIG must be at most 0.1 x ERRTOL times
C   the negative 2/3 power of the machine underflow limit.
      REAL alamb,ave,delx,dely,delz,ea,eb,ec,ed,ee,fac,sqrtx,sqrty,
* sqrtz,sum,xt,yt,zt
      if (min(x,y).lt.0..or.min(x+y,z).lt.TINY.or.min(x+y,z).lt
* .TINY.or.max(x,y,z).gt.BIG)pause 'invalid arguments in rd'
      xt=x
      yt=y
      zt=z
      sum=0
      fac=1
1  continue
      sqrtx=sqrt(xt)
      sqrty=sqrt(yt)
      sqrtz=sqrt(zt)
      alamb=sqrtx*(sqrty+sqrtz)+sqrty*sqrtz
      sum=sum+fac/(sqrtz*(zt+alamb))
      fac=.25*fac
      xt=.25*(xt+alamb)
      yt=.25*(yt+alamb)
      zt=.25*(zt+alamb)
      ave=.2*(xt+yt+3.*zt)
      delx=(ave-xt)/ave
      dely=(ave-yt)/ave
      delz=(ave-zt)/ave
      if(max(abs(delx),abs(dely),abs(delz)).gt.ERRTOL)goto 1
      ea=delx*dely
      eb=delz*delz
      ec=ea-eb
      ed=ea-6.*eb
      ee=ed+ec+ec
      rd=3.*sum+fac*(1.+ed*(-C1+C5*ed-C6*delz*ee)
* +delz*(C2*ee+delz*(-C3*ec+delz*C4*ea)))/(ave*sqrt(ave))
      return
      END

```


To calculate Jacobian elliptic functions snu1, cnu1, dnu1

```

C-----
SUBROUTINE sncndn(uu,emmc,sn,cn,dn)
C-----
REAL cn,dn,emmc,sn,uu,CA
PARAMETER (CA=.0003)
C   The accuracy is the square of CA.
C   Returns the Jacobian elliptic functions sn(u,kc), cn(u,kc),
C   and dn(u,kc). Here uu=u, while emmc = kc^2
INTEGER i,ii,l
REAL a,b,c,d,emc,u,em(13),en(13)
LOGICAL bo
emc=emmc
u=uu
if(emc.ne.0.)then
  bo=(emc.lt.0.)
  if(bo)then
    d=1.-emc
    emc=-emc/d
    d=sqrt(d)
    u=d*u
  endif
  a=1
  dn=1
  do i=1,13
    l=i
    em(i)=a
    emc=sqrt(emc)
    en(i)=emc
    c=0.5*(a+emc)
    if(abs(a-emc).le.CA*a)goto 1
    emc=a*emc
    a=c
  enddo
1  u=c*u
  sn=sin(u)
  cn=cos(u)
  if(sn.eq.0.)goto 2
  a=cn/sn
  c=a*c
  do ii=1,1,-1
    b=em(ii)
    a=c*a
    c=dn*c
  
```

```
        dn=(en(ii)+a)/(b+a)
        a=c/b
    enddo
    a=1./sqrt(c**2+1)
    if(sn.lt.0)then
        sn=-a
    else
        sn=a
    endif
    cn=c*sn
2   if(bo)then
        a=dn
        dn=cn
        cn=a
        sn=sn/d
    endif
    else
        cn=1./cosh(u)
        dn=cn
        sn=tanh(u)
    endif
    return
END
```

APPENDIX E. List of Publications

- 1) Wibowo.H. N., W.K. Chiu, “ **Monitoring of the Severity of A Cracked Structure Using Discrete Point Measurements: A Numerical Study**”, published and presented for COMADEM’98 on December 8th – 11th 1998 at Launceston Tasmania, Australia
- 2) H.N. Wibowo, W.K. Chiu, “ **Crack Monitoring of A Structural Component** ”, accepted for The Third Workshop on Structural Health Monitoring, Stanford, CA USA, Sept. 12-14, 2001
- 3) Wibowo. H. N., W.K. Chiu, ” **Use of An Array of Sensor/Actuator for Location of Cracks in Structural Components**”, (to be submitted to Smart Materials & Structure Journal)
- 4) Wibowo. H.N., W.K. Chiu,” **In-situ Method for the Estimation of Residual Life of Structural Components**”, (to be submitted to Smart Materials & Structure Journal)



BIOGRAPHICAL NOTE

The Author was born in Jakarta, Indonesia in 1967, and graduated with;

- Ir degree (1990) in Naval Architecture and Shipbuilding Engineering, from Institut Teknologi Sepuluh nopember (ITS), Surabaya, Indonesia
- MSc degree (1994) in Engineering Mathematics, from University of Newcastle, Newcastle Upon Tyne, United Kingdom